# Load sequence effects and mixed-mode fatigue crack growth in offshore structures

by

Kristen Rege

Thesis submitted in fulfilment of
the requirements for the degree of
PHILOSOPHIAE DOCTOR
(PhD)


Faculty of Science and Technology
Department of Mechanical and Structural Engineering and Materials Science
2019

University of Stavanger
NO-4036 Stavanger
NORWAY
www.uis.no



ISBN: 978-82-7644-888-7
ISSN: 1890-1387
PhD: Thesis UiS No. 490

# Summary

An increasing number of the offshore structures in the North Sea are being operated in a life extension phase, which means that their original design life has been exceeded. As the structures age, they are deteriorating, mainly due to fatigue and corrosion. In order to ensure that the structural integrity is maintained during the life extension phase, the remaining fatigue life of the structures needs to be assessed. While simple and conservative approximations are used in fatigue design, it will often be necessary to use more advanced and accurate models when assessing the remaining fatigue life of an existing structure. Among the different effects that influence the fatigue life, load sequence effects and mixed-mode conditions are currently not explicitly included in relevant fatigue life assessment standards for offshore structures. Therefore, this thesis addresses how these effects can be accounted for in fatigue life evaluation.

The following three topics are investigated:

- Load sequence effects in variable amplitude fatigue crack initiation
- Mixed-mode fatigue crack propagation
- Load sequence effects in variable amplitude mixed-mode fatigue crack propagation

A number of experimental studies have previously demonstrated the influence of load sequence effects in variable amplitude fatigue crack initiation. In the present work, a model is proposed for estimating the fatigue life, in which the load sequence effects are taken into account. The model contains one material parameter, but a single value for this parameter is found to give reasonable agreement between predicted and experimental fatigue lives for four different steels from three different experimental studies. This indicates that the proposed model is able to predict the observed load sequence effects quite well and easily.

Mixed-mode fatigue crack propagation usually needs to be modelled using a computational method. Currently, the finite element method seems to be the most easily applicable method for practicing engineers. One of the main tasks when modelling mixed-mode fatigue crack propagation is the determination of the stress intensity factor, which is a measure of how severely a crack is loaded. Here, seven different techniques for obtaining the stress intensity factor from a finite element model are compared. It is found that the domain integral method is the most reliable technique. If this method is not readily available, the displacement extrapolation technique can be used as an alternative for plane cracks. Models for estimating the fatigue crack propagation rate and crack path of mixed-mode cracks are also evaluated. It is shown that the Richard effective stress intensity factor is more conservative than the Tanaka effective stress intensity factor for estimating the fatigue crack propagation rate in most practical cases. Furthermore, most of the existing criteria for predicting the crack path work reasonably well, but the criterion of maximum tangential stress is the easiest one to apply.

Very few experimental studies have previously considered variable amplitude mixed-mode fatigue crack propagation. In the present work, fatigue crack propagation tests have been carried out, in which the specimens were subjected to a mixed-mode overload, followed by mixed-mode constant amplitude cyclic loading. It is found that the fatigue crack growth retardation caused by the overload lasted longer than predicted by the models proposed in the literature. This demonstrates the need for new models, and the experimental results presented here may be used in the development of such a model.

# Acknowledgements

This thesis is submitted in fulfilment of the requirements for the degree of Philosophiae Doctor (PhD) at the University of Stavanger (UiS), Norway. The research presented has been carried out at the Department of Mechanical and Structural Engineering and Materials Science, Faculty of Science and Technology, UiS, in the period from October 2016 to September 2019. The research was funded by the Ministry of Education and Research.

I would like to express my sincere gratitude to my main supervisor, Professor Dimitrios G. Pavlou, for excellent guidance, support and advices throughout this period. His positivity has made me feel comfortable during this work. I would also like to thank my co-supervisor, Professor Tor Hemmingsen, for his support.

I am also grateful to all my colleagues at the Department of Mechanical and Structural Engineering and Materials Science during these three years, for providing a nice and friendly working environment. Especially, I would like to thank:

- Professor Hirpa G. Lemu and Professor Bjørn H. Hjertager, for teaching an interesting course on computational mechanics.
- Jørgen Grønsund, Martin Bae, Jonas O. Rydland, Dr. Xiaoping Huang, Emil S. Kristiansen, Ashish Aeran, Øyvind Karlsen and John C. Grønli, for their practical assistance in carrying out the fatigue tests.
- Mostafa A. Atteya, for his kind assistance with the fatigue tests, and many pleasant discussions.
- Dr. Ove Mikkelsen, for several pleasant and fruitful discussions.
- Professor Per Skjerpe, for making me feel very welcome at the department.
- Yaaseen A. Amith and Johan Andreas H. Thorkaas, for practical assistance.

Finally, I would like to thank my parents for their great encouragement and support.

# Table of Contents

# List of Papers

This thesis is written as a collection of the following six papers:

Paper I: Rege, K. and Hjertager, B.H. (2017) Application of foam-extend on turbulent fluid-structure interaction, *IOP Conference Series: Materials Science and Engineering*, 276, 012031. doi: 10.1088/1757-899X/276/1/012031

Paper II: Rege, K. and Pavlou, D.G. (2017) A one-parameter nonlinear fatigue damage accumulation model, *International Journal of Fatigue*, 98, pp. 234–246. doi: 10.1016/j.ijfatigue.2017.01.039

Paper III: Rege, K. and Lemu, H.G. (2017) A review of fatigue crack propagation modelling techniques using FEM and XFEM, *IOP Conference Series: Materials Science and Engineering*, 276, 012027. doi: 10.1088/1757-899X/276/1/012027

Paper IV: Rege, K. and Pavlou, D.G. (2019) Effect of stop holes on structural integrity of offshore structures: a numerical model, *Proceedings of the Institution of Civil Engineers – Maritime Engineering*, 172(1), pp. 3–14. doi: 10.1680/jmaen.2018.34

Paper V: Rege, K. and Pavlou, D.G. (2019) Stress intensity factors for circumferential through-wall cracks in thin-walled cylindrical shells subjected to tension and torsion, *Fatigue & Fracture of Engineering Materials & Structures*, 42(5), pp. 1062–1074. doi: 10.1111/ffe.12970

Paper VI: Rege, K., Grønsund, J. and Pavlou, D.G. (2019) Mixed-mode I and II fatigue crack growth retardation due to overload: An experimental study, *International Journal of Fatigue*, 129, 105227. doi: 10.1016/j.ijfatigue.2019.105227

The following paper is not included in the thesis, as its ideas and contents were revised and expanded into the form presented in Paper IV:

Mikkelsen, O., Rege, K., Hemmingsen, T. and Pavlou, D.G. (2017) Numerical estimation of the stop holes-induced fatigue crack growth retardation in offshore structures taking into account the corrosion effect, *Proceedings of the Twenty-seventh (2017) International Ocean and Polar Engineering Conference*. San Francisco, June 25–30, 2017. Cupertino: ISOPE, vol. 4, pp. 451–458.

## *List of supervised master's theses*

1. Rydland, J.O. (2018) *Design of loading devices for mixed-mode fatigue crack propagation testing*. Master's thesis, University of Stavanger.
   http://hdl.handle.net/11250/2562426

2. Bjørheim, F. (2019) *Practical comparison of crack meshing in ANSYS mechanical APDL 19.2*. Master's thesis, University of Stavanger.

# Abbreviations

| | |
|---|---|
| ALE | Arbitrary Lagrangian-Eulerian |
| BEM | Boundary element method |
| CA | Constant amplitude |
| CFD | Computational fluid dynamics |
| DCT | Displacement correlation technique |
| FE | Finite element |
| FEA | Finite element analysis |
| FEM | Finite element method |
| FPSO | Floating production, storage and offloading unit |
| FSI | Fluid-structure interaction |
| FV | Finite volume |
| FVM | Finite volume method |
| LEFM | Linear elastic fracture mechanics |
| LES | Large-eddy simulation |
| MCCI | Modified crack closure integral, = VCCT |
| QPDT | Quarter-point displacement technique |
| RANS | Reynolds-averaged Navier-Stokes |
| SGS | Sub-grid-scale |
| TNDE | Two-node displacement extrapolation |
| VCCT | Virtual crack closure technique, = MCCI |
| XFEM | Extended finite element method |

# 1 Introduction

## 1.1 Background

Since the discovery of the first commercial oil and gas field in the Norwegian sector of the North Sea in 1969, over 100 offshore platforms have been installed in the Norwegian sector (Ersdal, Sharp and Stacey, 2019), in order to facilitate the extraction of the petroleum resources. While the originally intended lifetime of these installations typically ranges from 20 to 30 years, an overview of existing installations presented by Ersdal, Sharp and Stacey (2019, p. 6) shows that 47 of them are already more than 30 years old. Since there is a continued possibility to produce oil and gas from the fields, and improved oil recovery techniques are being developed, it is likely that the ageing installations will remain operational for several years. The possibility for ageing platforms to serve as hubs for neighbouring subsea completions further actualises the continued operation of these structures. A recent example is the Njord A platform, which has been in operation for 20 years, and currently is being upgraded for continued production for another 20 years, thereby extending the total service life to twice the original design life (Andersen, 2017; Heyerdahl, 2017).

During the life extension phase of these structures, it is of great importance to ensure that the structural safety is maintained at an acceptable level. As a structure ages, it will deteriorate, mainly by fatigue and corrosion (Stacey, Birkinshaw and Sharp, 2008). These processes affect the structural integrity, increasing the risk of failure unless properly managed.

Fatigue is a progressive deterioration process, which is of major importance to the life of a structure. It is caused by cyclic loading applied to a component, e.g. due to environmental loads caused by waves, wind and current acting on an offshore structure. The cyclic load leads to repeated slip between planes of atoms, localized at the free surface or at

stress concentrators in the component. Over time, a sufficiently high cyclic load will lead to the initiation of a crack. Continued cyclic loading will cause the crack to propagate, eventually leading to fracture of the component. These three stages of the fatigue process are shown in Figure 1.1.

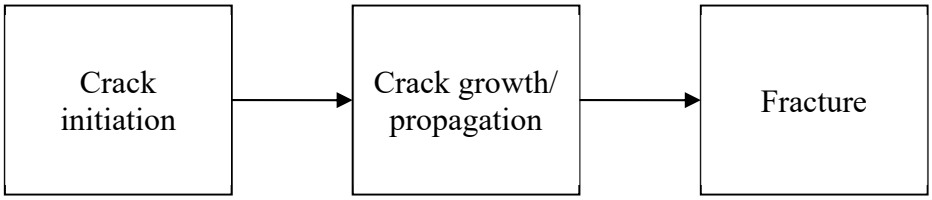


Figure 1.1 – The three stages of the fatigue process

Fatigue is one of the main causes of failure of structural and mechanical components (Suresh, 1998). The best known fatigue failure in Norway is probably the *Alexander L. Kielland* accident. The *Alexander L. Kielland* was a semi-submersible accommodation platform which capsized in the North Sea in March 1980 following fatigue cracking and subsequent severance of a main brace. 123 of the 212 persons on board lost their lives in the accident (Lotsberg, 2016, p. 7). The accident led to increased research efforts towards fatigue, revised design standards and stricter requirements of structural redundancy. Accidents of this extent have been avoided since then, but fatigue failures still occur. In March 2017, the 14.4 tonnes heavy boom of a pipe handling crane on the *Gullfaks B* platform fell 10 metres, and the direct cause was fatigue failure of the steel rope carrying its weight (Lie et al., 2017). No one was injured, but the material damage was estimated to NOK 66 million. Also, a fatigue failure of a gear led to the helicopter crash at Turøy at the west coast of Norway in April 2016, in which 13 persons lost their lives (Søndeland and Seglem, 2017; Dalløkken, 2018). These accidents indicate the seriousness of fatigue failures. As fatigue is a progressive and cumulative process, it is very important to take into account when operating structures beyond their initial design life.

Offshore structures made of steel contain numerous welded transitions, joints and connections. These details lead to stress concentrations, in which the stresses may be many times greater than the nominal stresses acting in the plate or member (Ersdal, Sharp and Stacey, 2019, p. 80). In addition, the welds often contain small fabrication defects, also called flaws. The combination of flaws and stress concentrations makes the welds the most common spot for fatigue crack initiation in welded structures. If the fatigue crack is allowed to grow, the member may be completely severed. When a member is severed, it cannot carry any loads, which means that the load is redistributed to the remaining structure. The intact members will be more heavily loaded, possibly leading to more rapid fatigue cracking. Newer structures are designed with a good degree of redundancy, which means that they are able to withstand loads even with one or a few severed members. Most of the early offshore structures were built with a relatively good degree of conservatism (Ersdal, Sharp and Stacey, 2019, p. 62), which means that it will take a longer time for fatigue cracks to initiate. In both cases, fatigue damage is accumulating over time, and it is therefore important to assess and possibly repair fatigue cracks as they are discovered, in order to maintain the structural integrity.

Structures are designed for a given design life, which means that they are designed in such a way that the likelihood of through-thickness fatigue cracks occurring during the design life is low. When a structure is operated beyond the design life, the probability of through-thickness fatigue cracks occurring increases. However, the fatigue process is associated with a number of uncertain factors. For instance, the exact material properties depend on the manufacturing process, and the microstructure of structural steels is not uniform. Furthermore, two welds will never be entirely equal, and will contain different flaws. In addition, welding leads to residual stresses which are difficult to quantify. The exact load distribution through a large structure may also be influenced by the construction process, to some degree. Finally, the

environmental loading history which will be acting on the structure cannot be known in advance, and has to be estimated based on statistical analysis of existing data. All these factors (and more) influence the fatigue life of a structural detail, making the prediction of a precise fatigue life impossible.

As it is impossible to precisely predict the fatigue life, additional information is needed in the assessment of existing structures for life extension, in order to reduce the uncertainties. First and foremost, additional information is gained by inspecting the structure for fatigue cracks. The results of an inspection can verify results from a fatigue analysis, and improve our confidence in the actual state of the structure (Ersdal, Sharp and Stacey, 2019, p. 144). Any detected cracks should be compared with expectations from previous fatigue analyses, and the proceeding growth of the crack should be estimated, in order to assess its influence on the structural integrity. Detected cracks may be repaired, for which multiple methods are available (Haagensen, 1994; Haagensen, Larsen and Vårdal, 2015). Furthermore, if historical data of the environmental loads are recorded during the lifetime of the structure, more accurate predictions of the fatigue life may be made, as the uncertainty related to the applied loading is reduced. In both cases, more accurate predictions may be obtained if models which take into account the multiaxial stress state and the irregularity of the stress histories, i.e. the real loading conditions, are applied.

## 1.2 Problem description

The environmental loads acting on offshore structures are irregular, thereby causing irregular stress histories, as illustrated in Figure 1.2. Fatigue caused by irregular stress histories is called variable amplitude fatigue. Current standards for fatigue design of structures, including NORSOK N-004 (Standards Norway, 2013) which covers the design of offshore steel structures in Norway, recommend the use of the linear damage hypothesis, also called the Palmgren-Miner rule. This

cumulative damage rule takes into account the magnitude of the stress amplitudes, but not their sequence, even though it is well-known that load sequence effects have a consistent influence on the fatigue life (Fatemi and Yang, 1998). However, as the exact sequence of waves and wind for thirty years into the future can never be known at the design stage, the application of this rule seems reasonable for design, as long as sufficiently large design fatigue factors are used. After all, fatigue design analyses are intended simply to ensure that the likelihood of fatigue cracking during the design life is kept to an acceptable level (Ersdal, Sharp and Stacey, 2019, p. 79), in which case the Palmgren-Miner rule works quite well for welded joints (Lotsberg, 2016, p. 114).

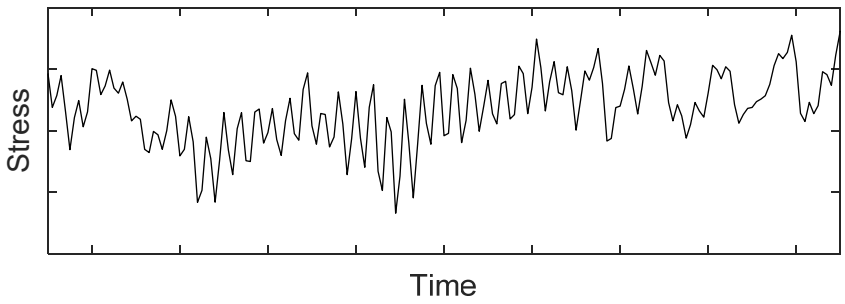


Figure 1.2 – An irregular stress history

While the load sequence effects may be ignored in design, it could be useful to take them into account in the assessment of ageing structures. At the design stage, simple and conservative approximations are often used. In the life extension phase of the structure, these approximations may not be able to document sufficient fatigue lives, in which case the use of more advanced and accurate assessments is justified. Reference is made to NORSOK standard N-006 on assessment of existing offshore structures (Standards Norway, 2015), where it is stated that 'the requirements for accurate fatigue assessments are even higher for assessment of a structure during its service life compared to the design stage'. Advances in monitoring techniques make it increasingly viable to monitor the environmental loads acting on offshore structures (Kajolli,

Siriwardane and Gudmestad, 2015; Vestli et al., 2017; Votsis et al., 2018). An analysis of the experienced environmental loads, combined with a nonlinear cumulative damage rule, which takes load sequence effects into account, may improve our confidence in the structure.

Changes in the use of a structure may also lead to a significant change in its experienced loads. Examples include relocation of a mobile offshore structure to a new location with different weather conditions (L'Hostis et al., 2013), and revamping and upgrading a structure for a different use (Haagensen, Larsen and Vårdal, 2015), thereby changing its weight distribution and geometry. Even though the detailed loading history may not be known, this kind of change in the typical loading pattern could possibly also be assessed using a nonlinear cumulative damage rule.

With the recent advances in monitoring techniques (Votsis et al., 2018), computational resources and efficient computational techniques (Knezevic et al., 2018), online monitoring of a structure's fatigue lifetime consumption is becoming increasingly more viable. Systems for monitoring the lifetime consumption have recently been proposed for general aviation aircraft (Keryk et al., 2018) and mechanical components (Heinrich et al., 2019). Such a system has also been installed on two floating production, storage and offloading units (FPSOs), as part of joint industry projects (L'Hostis et al., 2013). In this case, where the detailed loading history is available, a more realistic estimate of the lifetime consumption is expected to be obtained when using a nonlinear cumulative damage rule, instead of the Palmgren-Miner rule.

While cumulative damage rules are mainly used to estimate fatigue crack initiation (of a through-thickness crack, in the case of offshore structures), load sequence effects do also influence the fatigue crack propagation. Fatigue crack propagation analyses are used to assess the remaining fatigue life of joints with detected cracks, to assess the need to repair a crack, and to determine the optimal frequency of in-service inspection (Ersdal, Sharp and Stacey, 2019, p. 127). The NORSOK

standards contain few explicit procedures for crack growth analysis, but refer to recommended practices from DNV GL for fatigue design, DNVGL-RP-C203 (DNV GL, 2016), and probabilistic inspection planning, DNVGL-RP-C210 (DNV GL, 2015), in addition to the British standard for assessment of flaws, BS 7910 (British Standards Institution, 2015). None of these documents provide detailed guidelines on the assessment of load sequence effects on fatigue crack propagation, even though it would beneficial to predict how e.g. a storm (Taheri, Trask and Pegg, 2003) influences the fatigue crack propagation of a detected crack.

Fatigue crack propagation under mixed-mode conditions, i.e. the combination of tensile opening, in-plane and out-of-plane shear loading of the crack is not considered in the recommended practices mentioned above either. Still, cracks in offshore structures may propagate under mixed-mode conditions, due to the multidirectional nature of the environmental loads, the complex geometries and random defect orientations (Rhee, 1989; Pook, Kam and Mshana, 1992; Mshana, Kam and McDiarmid, 1992; Riahi et al., 2011; Mai, Sørensen and Rigo, 2016). It is therefore necessary to study the application of models for mixed-mode fatigue crack propagation life prediction, and their application to offshore structures.

In order to contribute to filling the gaps in the current methodologies mentioned above, the aim of this thesis is to study the effect of load sequence effects (variable amplitude fatigue) on fatigue crack initiation and mixed-mode fatigue crack propagation.

## 1.3 Objectives and thesis organisation

The three main objectives of this thesis may be summarized as follows:

1. To study load sequence effects on fatigue crack initiation, and, based on this study, formulate a nonlinear cumulative damage rule which more closely matches experimental data.
2. To study models for mixed-mode fatigue crack propagation, i.e. models for predicting the crack propagation path and the crack propagation rate under mixed-mode conditions, and give advice for choosing models for practical use.
3. To perform fatigue crack propagation tests, where mixed-mode overloads are applied, and their influence on proceeding mixed-mode constant amplitude fatigue crack propagation is studied. An overload followed by constant amplitude loading is one of the simple load cases which form the basis for developing models for variable amplitude fatigue crack propagation.

While the propagation of mode I fatigue cracks can often be modelled using analytical solutions, it is usually necessary to use computational methods, such as the finite element method (FEM), to model mixed-mode fatigue crack propagation. As part of addressing objectives 2 and 3, it was found necessary to model fatigue cracks computationally. Therefore, it was found useful to address a fourth objective:

4. To review methods for simulating fatigue crack propagation using finite element methods.

While planning the fatigue tests as part of objective 3, it was found that solutions for the stress intensity factor (a parameter for assessing the severity of a crack) for long circumferential through-wall cracks in cylindrical shells subjected to torsion were missing from the literature. This geometry is representable for the final stage of fatigue crack growth through the brace of the *Alexander L. Kielland* platform (Lotsberg, 2016, p. 416). A number of incidents of severed members in offshore structures

have been recorded (Ersdal, Sharp and Stacey, 2019, p. 78), indicating the importance of this crack geometry. Even though the torsional loading in many cases most likely is negligible, compared to tensile and bending loading, the crack cannot be fully assessed without considering the stress intensity factor due to torsion. This led to the formulation of a fifth objective:

5. To determine a solution for the stress intensity factor for long circumferential through-wall cracks in cylindrical shells subjected to torsion, using the finite element method.

Measurement of the stress history at critical spots of offshore structures is often not practical, in which case the stress history has to be predicted. The recent advances in computational techniques and resources make it increasingly viable to include complicated effects in such simulations. For instance, fully coupled fluid-structure interaction simulations for the analysis of flexible structures exposed to fluid flow, such as drilling risers, has recently become viable. The option of performing turbulent fluid-structure interaction simulations has been made available in the open source finite volume computational fluid dynamics (CFD) code foam-extend, but its application for fatigue analysis has earlier not been studied. It is likely that more accurate fatigue life estimations for flexible structures can be made if the fluid-structure interaction effect is included. A sixth objective was therefore included:

6. To investigate the practical applicability of foam-extend to derive stress histories for fatigue life estimation, from a fully coupled fluid-structure interaction analysis of a flexible structure.

Following this introduction, a literature review will be provided for the three main topics covered in this thesis; variable amplitude fatigue crack initiation, variable amplitude fatigue crack propagation and mixed-mode fatigue crack propagation. Then, the six papers of which this thesis consists are provided as individual chapters. An overview of the six

papers, and the objective each of them addresses, is provided in Figure 1.3.

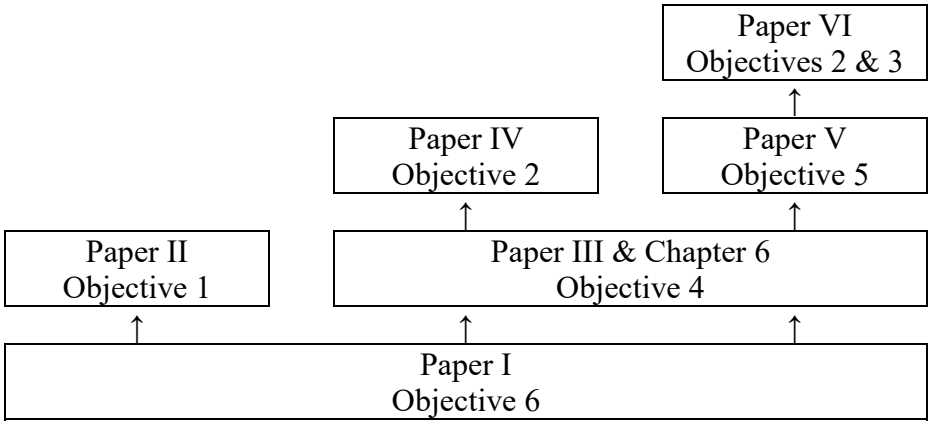


Figure 1.3 – Overview of the relationship between the papers included in the thesis

In Paper I, the viability of performing turbulent fluid-structure interaction simulations using foam-extend is studied, by analysing a simple test case. This simulation clearly illustrates that environmental loads cause an irregular stress history, which is the reason why variable amplitude effects in fatigue are important. In Paper II, a nonlinear cumulative damage rule for variable amplitude fatigue crack initiation is proposed, based on a study of existing experimental data. Then, different methods for analysing and modelling propagating fatigue cracks using FEM are reviewed in Paper III. In Chapter 6, which comes between Paper III and Paper IV, some of these techniques are applied to specific examples and compared, in order to choose the optimal techniques for use in Papers IV to VI.

In Paper IV, a procedure is presented for analysing the effect of a stop hole drilled through the tip of a mixed-mode fatigue crack, which is one of the repair techniques mentioned in NORSOK N-006 (Standards Norway, 2015). In the solution of this problem, methods for handling mixed-mode fatigue crack propagation are reviewed, and recommended choices are specified. Paper V addresses objective 5, i.e. the stress

intensity factor solution for a circumferential crack in a cylindrical shell subjected to torsion. In Paper VI, the results of mixed-mode fatigue crack propagation tests with overloads are presented. The tubular specimens used in the tests are analysed using the same methodology as used in Paper V. The experimental data are available in tabular format in an appendix following the thesis' conclusion.

## 1.4 Limitations

The fatigue analysis of an offshore structure may be divided into two stages, as indicated in Figure 1.4. In the first stage, hydrodynamic and structural analyses are carried out, in order to derive the stress history in critical spots from the predicted (or measured, in the case of online monitoring) environmental loads. In the second stage, the fatigue life is predicted from the stress history, using experimental data for the material and structural detail in question, together with fatigue models. The main focus of this thesis is this second stage, i.e. the fatigue modelling. The first stage is the topic of Paper I, but is not further addressed in this thesis.

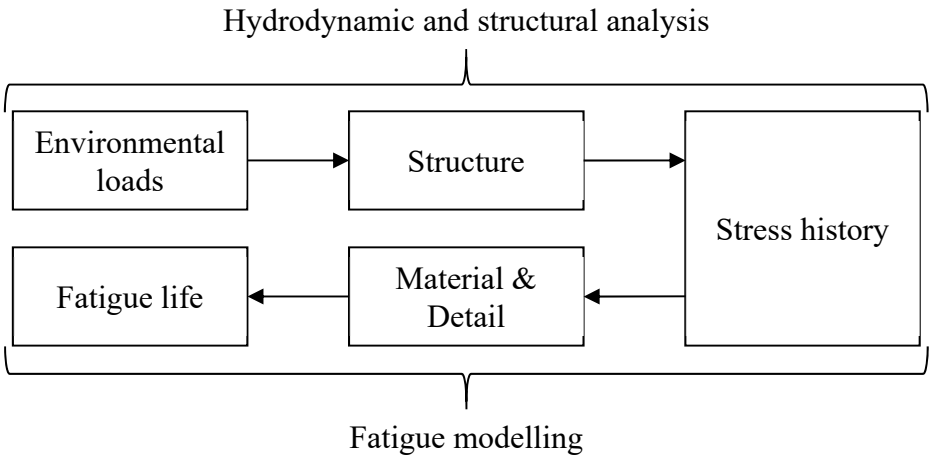


Figure 1.4 – Overview of a fatigue analysis of an offshore structure

As mentioned in Section 1.1, fatigue cracks usually initiate in the welded joints of offshore structures. Welds are not explicitly considered in this thesis however, as it is expected that models developed for the base materials also can be used for the welded connections, as long as appropriate material/detail data (*S*-*N* curve and Paris law parameters) are used for the welded connections.

In the same way as fatigue cracks may propagate under mixed-mode conditions, fatigue cracks may initiate under multiaxial loading conditions. However, multiaxial fatigue crack initiation is not included in the scope of this thesis. Similarly, probabilistic fatigue analysis, which can be used to estimate the evolution of the structure's probability of failure, is beyond the scope of this thesis.

# 2 Literature review

This chapter presents a literature review of the three major topics which are considered in this thesis, i.e. variable amplitude fatigue crack initiation, variable amplitude fatigue crack propagation, and mixed-mode fatigue crack propagation. This review focuses partly on classical models, and partly on recent research within each of these topics. Further literature reviews of specific topics are included in the papers of which this thesis consists.

For clarification, we will start this chapter by defining the way the terms fatigue crack initiation and fatigue crack propagation are used in this thesis.

## 2.1 Fatigue crack initiation and propagation

As indicated in Section 1.1, cyclic stresses can lead to the nucleation of microscopic cracks. These microscopic flaws may grow and coalesce, thereby forming a macrocrack. The macrocrack then propagates until fracture occurs. As the microscopic crack exists long before it is detectable by normal non-destructive crack detection equipment, there is a variety of definitions of when the fatigue crack initiation phase ends and the crack propagation phase begins (Suresh, 1998, p. 11). This is particularly true for welded structures, where some researchers claim that crack-like defects always exist, causing fatigue to be a problem solely of crack propagation (Cui, Wang and Huang, 2011), while other researchers claim that the crack initiation phase constitutes an important and finite part of the fatigue life (Lassen and Recho, 2009).

In the scope of this thesis, it was found convenient to define the fatigue crack initiation life as the fatigue life estimated by using an *S*-*N* curve. An *S*-*N* curve, also called a Wöhler curve, is indicated in Figure 2.1, and represents an experimentally determined relation between the applied cyclic stress, *S*, and the number of cycles to 'failure', *N*. Traditionally,

*S-N* curves have been established by subjecting small (typically 5 to 10 mm diameter) and smooth-surfaced axial test specimens to cyclic loading until they fracture, or until substantial cracking is visible (Boyer, 1986, p. 4; Dowling, 2013, p. 787). This corresponds to the initiation of an engineering size crack in the order of 1 to 5 mm in a component (Dowling, 2013, p. 787). In some cases, the existence of an initiated crack of this length may not be critical to the integrity of a structure, and its remaining fatigue crack propagation life may be estimated using fracture mechanics.

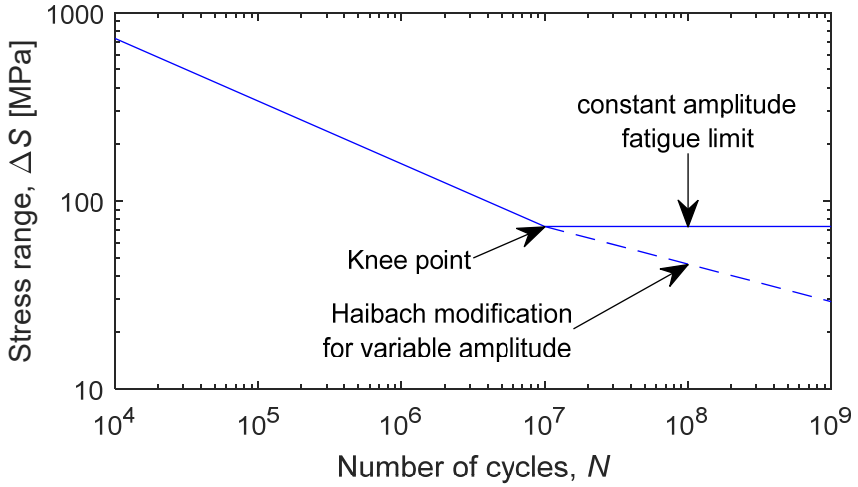


Figure 2.1 – An *S-N* curve

The *S-N* curves used in fatigue design of welded structures have been obtained from fatigue test data obtained from welded specimens, and represent the number of cycles required to produce a through-thickness fatigue crack (Maddox, 2011). For instance, in DNVGL-RP-C203 (DNV GL, 2016) the reference thickness is 25 mm for welded connections, except for tubular joints, for which it is 16 mm. It is obvious that the fatigue life given by these *S-N* curves contains a significant portion of fatigue crack propagation. Within this thesis, this fatigue life is still called fatigue crack initiation, simply because the models which are used

with *S-N* curves to take variable amplitude and multiaxial loading into account are based on fatigue crack initiation theories.

A crack with a finite length may be assessed using fracture mechanics. The fatigue crack propagation life may usually be estimated using linear elastic fracture mechanics (LEFM), while elastic-plastic fracture mechanics is needed in order to evaluate the crack size at which fracture will occur. In LEFM, a central parameter is the stress intensity factor, $K$, which is a measure of how severely a crack is loaded. A crack can experience three types of loading, which are called mode I, II and III, and represent tensile opening, in-plane shear and out-of-plane shear, respectively (Anderson, 2005). Each loading mode is quantified by its own stress intensity factor. A crack can also be subjected to a combination of the different modes. This is called mixed-mode loading. Under mode I conditions, the fatigue crack propagation rate may be related to the applied stress intensity factor range, $\Delta K_{\mathrm{I}}$. The simplest relation is the Paris law (Paris and Erdogan, 1963), which gives the fatigue crack propagation rate as

$$\frac{\mathrm{d}a}{\mathrm{d}N} = C\Delta K_{\mathrm{I}}^{m} \tag{2.1}$$

where $C$ and $m$ are material parameters. The Paris law is limited to a single load ratio $R = K_{\min}/K_{\max}$ and intermediate values of $\Delta K_{\mathrm{I}}$. A number of different relations have subsequently been proposed, where additional effects are taken into account (Anderson, 2005), which can be used if the associated material parameters are known. The fatigue crack propagation life is obtained by integration of the fatigue crack growth law.

While the *S-N* curves used in fatigue design of welded structures can be used to predict when a through-thickness crack will be present, they cannot be used to predict the remaining fatigue life of a detected fatigue crack. In this case, a crack propagation law based on fracture mechanics is required. This means that the interval from a macrocrack is formed

until it extends through the material thickness, is analysed using *S-N* curves and associated fatigue crack initiation theory in the design phase, while it is analysed as a propagating fatigue crack using fracture mechanics during the operation phase, as illustrated in Figure 2.2. Consequently there is an overlap in the regimes analysed by fatigue crack initiation theory and fatigue crack propagation theory for welded structures.

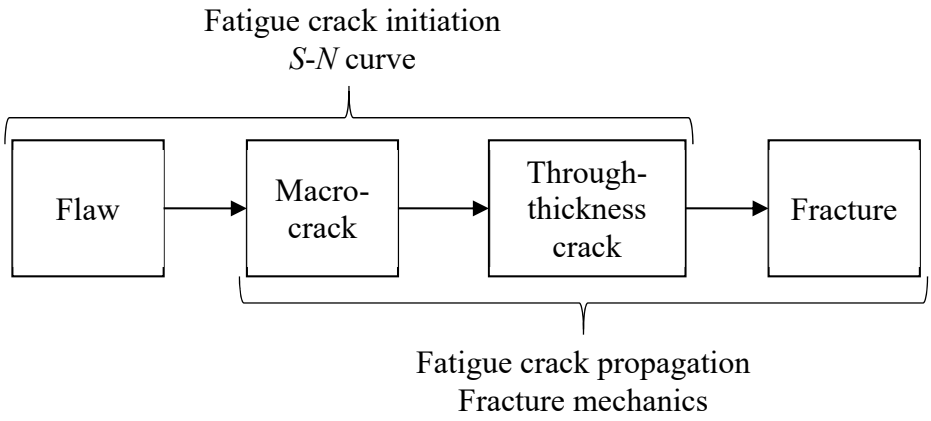


Figure 2.2 – Fatigue analysis regimes for welded structures

Summing up, we note that *S-N* curves are used together with fatigue crack initiation theory, and can be used to estimate the number of cycles until a specified event. This event could be the occurrence of a detectable fatigue crack of a given size, or the occurrence of a through-thickness crack. Meanwhile, fracture mechanics can be used to estimate the crack propagation rate and life of any crack, in the absence of extensive yielding (although special considerations are required for analysing small cracks with length below a couple of millimetres, see Suresh, 1998).

## 2.2 Variable amplitude fatigue crack initiation

If a component is subjected to a cyclic load, where the amplitude and mean value are constant for all the cycles, the fatigue crack initiation life of the component may easily be predicted using an *S*-*N* curve, as shown in Figure 2.1. This is rarely encountered in practice however. Usually, there is some variation in both the amplitude and the mean value. For instance, bridges are trafficked by cars, buses and lorries, each one having a different weight, thereby subjecting the bridge to different stress magnitudes. Similarly, the magnitude of the environmental loads acting on an offshore structure is naturally subject to variation. It is therefore necessary to have a procedure for predicting the fatigue life under variable amplitude loading.

Suppose that a component is subjected to a number of different loading blocks, where loading block $i$ contains $n_i$ cycles of stress amplitude $\sigma_i$. ($n_i = 1$ is allowed.) The constant amplitude fatigue life at stress range $\Delta\sigma_i = 2\sigma_i$ is found from an *S*-*N* curve to be $N_i$. In 1924, the Swede Palmgren proposed that the fatigue life could be estimated by the condition

$$\sum_i \frac{n_i}{N_i} = 1 \tag{2.2}$$

i.e. when the sum of the cycle ratios $n_i/N_i$ reaches unity. This criterion was also proposed by the American Miner in 1945 (Cotterell, 2010, p. 225), and is currently known as the Palmgren-Miner rule, or the linear damage hypothesis (see Figure 2.3).

Some materials, including steel, have a fatigue limit when subjected to constant amplitude loading. This means that if the applied stress amplitude is below this limit, the fatigue life is practically infinite ($>> 10^7$ cycles). Even though stresses below the fatigue limit are not able to nucleate a microcrack, they may be sufficiently high to propagate a microcrack which has already been nucleated by higher stress

amplitudes. Therefore, cycles below the fatigue limit need to be taken into account in variable amplitude fatigue. When the Palmgren-Miner rule is used for fatigue design of welded structures, the *S*-*N* curve is modified by extending it beyond its knee point, using a reduced slope, as shown in Figure 2.1 (Marquis, 2011). This modification was proposed by Haibach. It has been found that the Haibach modification can be non-conservative, and it may be better to extrapolate the *S*-*N* curve linearly beyond its knee point (Zhang and Maddox, 2009).

It has been known for a long time that the Palmgren-Miner rule has its deficiencies. For instance, if the stress amplitude shows a decreasing trend it generally makes non-conservative predictions of the fatigue life, whereas it can be very conservative if the stress amplitude shows an increasing trend (Manson, Freche and Ensign, 1967). It is assumed that lower stress amplitudes are more damaging if a microcrack has already nucleated (due to the application of higher stress amplitudes), than if the material is undamaged, thereby causing the observed load sequence effect. While this deficiency is very clear if the Palmgren-Miner rule is applied to a specimen subjected to only two loading blocks of different stress amplitudes (Manson, Freche and Ensign, 1967), its accuracy has been observed to improve as the number of loading blocks and randomness increase (Xia and Yao, 2013). Therefore, the Palmgren-Miner rule is generally considered acceptable for the design of offshore structures (Lotsberg, 2016, p. 114), even though it can be non-conservative for some loading spectra (Zhang and Maddox, 2009).

Due to the inability of the Palmgren-Miner rule to predict the observed load sequence effects, a number of alternative fatigue damage accumulation models have been proposed. While the Palmgren-Miner rule represents a linear relation between the 'fatigue damage' and $n_i$, most of the later models are nonlinear, as illustrated in Figure 2.3. Nonlinear models may more accurately represent the load sequence effects, but this comes at a computational cost. Some of the models associate the fatigue damage with measureable quantities, as reviewed

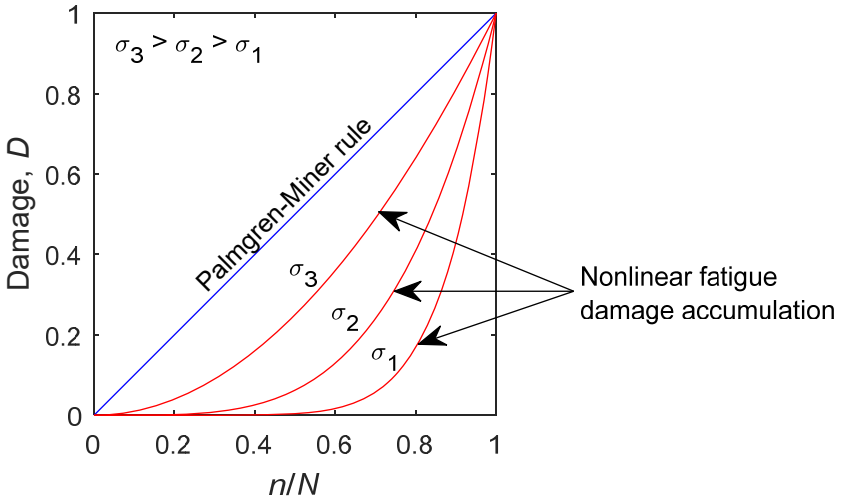


Figure 2.3 – Linear and nonlinear fatigue damage accumulation

by Yang and Fatemi (1998), some are based on mapping the damage in the region below the *S-N* curve, while others contain mathematical expressions with limited physical and conceptual explanation. The models based on physical measurement of the fatigue damage have not proved to be better or easier to apply than the rest. Most of the models contain one or more experimental fitting parameters, which may or may not depend on the material. The research up to 1998 has been reviewed by Fatemi and Yang (1998), and we will therefore only mention a couple of the most promising models from this period here.

An interesting alternative to the Palmgren-Miner rule is the double linear damage rule, first proposed by Manson (1966). He suggested that the crack initiation and crack propagation phases could be treated separately, even for small test specimens, applying a linear damage rule to each. This keeps the computation simple, while still including the load sequence effect. Manson, Freche and Ensign (1967) carried out an extensive test program of two-stress level fatigue tests, noting that the double linear damage rule was able to predict the fatigue life quite well. However, they also noted that no crack could be observed after their

defined crack initiation phase was completed, and they therefore chose to name the two phases simply phase I and phase II. Manson and Halford (1981) later associated the transition between phase I and phase II to a damage curve approach, presenting a final formulation of the double linear damage rule which is easy to use, and matched their experimental data very well. The double linear rule has been found to seem to be promising by Fissolo et al. (2015), and is recommended by Lee et al. (2005, p. 75).

A different model was proposed by Subramanyan (1976), who suggested that the damage accumulation could be mapped by the use of isodamage lines converging at the knee point of the *S*-*N* curve. This model was able to yield reasonable predictions, and is further studied in Paper II. Srivatsavan and Subramanyan (1978) later extended this model to also consider cycles below the constant amplitude fatigue limit, by implementing a fatigue limit which decreases as the material is subjected to fatigue loading. Hashin and Rotem (1978) suggested a similar kind of mapping, with isodamage curves extending between the knee point and the intersection between the *S*-*N* curve and the *S*-axis. They found it convenient to discretize these isodamage curves into two sets of straight lines, one set which converges at the intersection between the *S*-*N* curve and the *S*-axis, and another set which is equal to Subramanyan's isodamage lines.

Since Fatemi and Yang's (1998) review of fatigue damage accumulation models, many new models have been proposed. We will mention some of them here, in order to illustrate the variety of models existing.

Shang and Yao (1999) proposed a model based on continuum damage mechanics, where the influence of mean stress is included, but the determination of one material parameter is required. Continuum damage mechanics was also the basis for the model proposed by Dattoma et al. (2006), which contains four material parameters, which all can be determined from a normal *S*-*N* curve. Pavlou (2002) assumed that the

fatigue damage could be related to the measured hardness increase during fatigue, and showed that isodamage lines based on these hardness measurements converged to the knee point of the *S*-*N* curve, in agreement with Subramanyan's (1976) assumption. A simple mathematical expression for the fatigue damage accumulation was proposed by Košút (2002), who suggested quadratic addition of the cycle ratio. This expression requires a material parameter however, and it is not clear how it should be applied to a general variable amplitude loading history.

A number of models with no material parameter have recently been developed. For instance, a model which considered mapping of the fatigue damage using the *S*-*N* curve was proposed by Mesmacque et al. (2005), and further examined by Aid et al. (2011). The model requires no material parameter, but Siriwardane et al. (2009) found its results to deviate significantly from real fatigue lives. Therefore, they combined it with a grain-scale plasticity model, in order to improve the predictions for multiaxial variable amplitude fatigue. Another model, based on a 'fatigue driving stress' concept, was proposed by Kwofie and Rahbar (2013), and further analysed by Zuo et al. (2015), but its predictions do not match the trend observed in the two-stress level fatigue tests by Manson, Freche and Ensign (1967). Additional models include those by Gao et al. (2014) and Lv et al. (2015), which both are modifications of previous models.

More recently, Theil (2016) proposed a graphical method for mapping the damage evolution below the *S*-*N* curve, but due to the lack of analytical expressions for this method, it is difficult to apply in practice. Some researchers (Wu et al., 2017) do even suggest estimating the fatigue life of small specimens using solely variable amplitude fatigue crack propagation models (see the following section), even though it is well known that the crack initiation life can be as high as 80 % of the fatigue life of this kind of specimen (Suresh, 1998, p. 224).

It is clear that a variety of models have been proposed. However, it is often difficult to judge the quality of each model, as they are often compared only to the Palmgren-Miner rule and maybe one more model, and a limited amount of experimental data. Due to the scatter in fatigue life, relatively many test results are required in order to distinguish a trend in the data. This leaves it to the reader to assess the applicability of each model. Many good data sets are available in the literature, e.g. in the works of Manson, Freche and Ensign (1967)[1], Subramanyan (1976), Srivatsavan and Subramanyan (1978) and Pereira et al. (2008). Experimental data is also available in the works by Jeelani and Musial (1986) and Pavlou (2002), but these data sets do not include the knee point of the *S*-*N* curve, making them difficult to use for some of the models. Most of the cited data were obtained from two-stress level fatigue tests, which is the simplest variable amplitude load history for fatigue crack initiation, and also the history in which the deficiency of the Palmgren-Miner rule is most pronounced. It is obvious that the performance of nonlinear models should be assessed also for more realistic loading histories before they are used in practice.

## 2.3 Analysis of irregular stress histories

In the models for variable amplitude fatigue crack initiation, the fatigue damage accumulation is calculated from individual loading blocks. Each loading block $i$ contains $n_i$ cycles (i.e. complete load reversals) with constant stress range $\Delta\sigma_i$, where $n_i = 1$ is allowed. However, the wind and waves acting on offshore structures usually cause spectrum loading (Marquis, 2011), as illustrated in Figure 1.2, in which case the identification of individual cycles and their respective stress range is not obvious.

[1] The actual data in tabular format may be found in NASA TN D-3839, at https://ntrs.nasa.gov/archive/nasa/casi.ntrs.nasa.gov/19670013955.pdf (accessed 15 January 2018).

In the design of offshore structures, it is common to establish a long-term distribution of waves, and relate each wave height to a specific stress range, as explained by Fines (1985) and Lotsberg (2019). Thus, a long-term stress range distribution is obtained, i.e. a relation between each stress range and its expected yearly occurrence. In this case, the Palmgren-Miner rule may be directly applied.

If a more detailed loading history is available, as illustrated in Figure 1.2, it is necessary to identify individual cycles and their stress range, in order to use a fatigue damage accumulation model. The most common method for doing this is the rainflow cycle counting method, which is well explained in textbooks (Dowling, 2013). An alternative to the rainflow method is the reservoir method, which is mentioned in Eurocode 3 (Standards Norway, 2010). The cycle counting methods are used to transform the irregular stress history into a series of complete load reversals, each having a clear stress range and mean stress. When nonlinear fatigue damage accumulation models are used, it is important that the order of the stress ranges is maintained through the cycle counting process.

Cycle counting is also used in the modelling of variable amplitude fatigue crack propagation due to spectrum loading (Pavlou, 2000; Miranda et al., 2003).

## 2.4 Variable amplitude fatigue crack propagation

In fatigue crack initiation tests, one test specimen normally provides us with just a single piece of information, that is the number of cycles to failure (fracture or substantial cracking) for the load history applied. The influence of individual load cycles is difficult to assess, and will likely be concealed by the scatter associated with this kind of tests. Therefore, these specimens are usually subjected to block loading when investigating variable amplitude fatigue. On the other hand, in fatigue crack propagation tests, the specimens are typically larger, pre-cracked

plates (see e.g. ASTM International, 2016), allowing the entire crack propagation history, i.e. the crack length as a function of cycle number, to be recorded throughout the test. This provides us with detailed information, and the direct influence of changes in the applied load, e.g. on the fatigue crack propagation rate, may be assessed. Therefore, the basics of variable amplitude fatigue crack propagation are usually studied by subjecting cracked test specimens to a cyclic load (force) with constant amplitude, interrupted by a single load peak, which is either significantly higher or significantly lower than the base cyclic load. These load peaks are called overloads and underloads, respectively. Any variable amplitude loading history can, in principle, be represented as a sequence of overloads and underloads (Salvati et al., 2017), which is why the study of these configurations is interesting.

If a cracked geometry is subjected to a constant amplitude cyclic force, the instantaneous fatigue crack propagation rate may be estimated using a fatigue crack growth law, such as the Paris law, Equation (2.1). However, if the applied force amplitude suddenly changes, it has been found that the crack propagation rate deviates from the one predicted from the fatigue crack growth law. The application of a single overload causes a retardation in the proceeding crack propagation, while a single underload causes the crack propagation to accelerate. This means that the crack propagation rate does not depend only on the stress intensity factor range, $\Delta K_{\mathrm{I}}$, and the load ratio, $R$, but also on the prior loading history. Due to these observations, dedicated models are required for variable amplitude fatigue crack propagation, just as for variable amplitude fatigue crack initiation.

The first well-known model for variable amplitude fatigue crack propagation was proposed by Wheeler (1972). He suggested that the fatigue crack growth retardation following an overload could be related to the increased size of the crack tip plastic zone caused by the overload. As long as the plastic zone due to the current load peak is confined by the plastic zone due to the overload, the crack growth rate is assumed to

be reduced. The model contained one material parameter (in addition to an expression for the plastic zone size), and agreed quite well with experimental results. A second model was proposed by Willenborg, Engle and Wood (1971), where the residual stresses in the overload plastic zone were assumed to reduce the effective stress intensity factor range and load ratio acting at the crack tip, as long as the plastic zone due to the current load peak is confined by the plastic zone due to the overload. The Willenborg model does not have any material parameters, but it does not always match experimental data very well; see e.g. Pavlou (2000) and Taheri, Trask and Pegg (2003).

Two models developed at NASA were presented in 1981 by Johnson (1981) and Newman (1981). The Johnson model is an extension of the Willenborg model, in which the instantaneous acceleration during the overload cycle and the acceleration following an underload are also taken into account. The Newman model is based on the concept of crack closure proposed by Elber (1970). As a fatigue crack grows, the tensile plastic deformation left in the wake of the crack tip causes the crack faces to make contact during unloading, even before the applied loading reaches zero. This contact is called crack closure, and Elber suggested that this effect would decrease the crack propagation rate. The application of an overload necessarily causes increased plastic deformations, which leads to crack growth retardation, according to this theory. Newman (1981) developed a numerical model for predicting the crack-opening stress, and thereby also the load sequence effects in the fatigue crack propagation history. Johnson (1981) and Newman (1981) compared their predictions to the same set of test data from specimens subjected to aircraft-type spectrum loadings. For the 13 different load spectra tested, the average ratio between the predicted and experimental fatigue crack propagation lives were 0.97 and 0.98, with standard deviations 0.24 and 0.28, respectively. The performance of the two models was quite similar, but the Johnson model is much easier to apply. If the load sequence effects were entirely disregarded, the mean value

was 1.12, with standard deviation 0.64, indicating that the retardation and acceleration effects nearly cancelled each other in most of the spectra.

Over the years, a number of different mechanisms have also been suggested to be fully or partly responsible for the fatigue crack growth sequence effects, in addition to the two mentioned above. The suggested mechanisms include strain hardening, crack tip blunting and crack branching, and have recently been reviewed by Salvati et al. (2017). However, the models based on these mechanisms have not reached the same popularity as the ones based on the residual stresses in the overload plastic zone or on plasticity-induced crack closure.

The models based on the residual stresses in the overload plastic zone have been subject to continuous development. For instance, the Wheeler model has been studied and modified by several researchers. Sheu, Song and Hwang (1995) carried out a number of experiments in order to determine the normalized distance over which the overload-induced retardation lasts, and to investigate the material parameter in the Wheeler model. Both parameters were found to vary with the overload ratio and initial crack length, suggesting that the general applicability of the original Wheeler model is questionable. Yuen and Taheri (2006) modified the Wheeler model to take into account the initial acceleration and delayed retardation, which have been observed to follow an overload, and also the interaction between different overloads. Furthermore, Huang, Moan and Cui (2008) included the effect of an underload following an overload.

Research is still being conducted on the capability of the closure-based models, often involving finite element analyses for determining the crack-opening loads (Aguilar Espinosa et al., 2017b). In order to reduce the computational effort, Liu, Venkatesan and Zhang (2017) suggested to link the crack closure level to the crack tip plastic zone size. This is an interesting proposal, but they found it necessary to introduce an

empirical scaling factor to the crack tip plastic zone size, in order to obtain reasonable predictions, which currently limits the applicability of this suggestion. Salvati et al. (2017) suggested that both crack closure and residual crack tip stresses influence the overload-induced retardation, and demonstrated an experimental procedure for determining the contributions of each factor.

Different variable amplitude fatigue crack propagation models have been implemented in various simulation tools, like NASGRO and ESACRACK, and are used in practice, especially in aerospace and astronautics (Kuna, 2013, p. 123), even though the effects of overloads and underloads often cancel each other in typical flight-load spectra (DuPont et al., 2017).

The above discussion on variable amplitude fatigue crack propagation has been limited to mode I (tensile opening) conditions. In the next section, we will also consider mixed-mode variable amplitude fatigue crack propagation.

## 2.5 Mixed-mode fatigue crack propagation

The procedures for estimating the fatigue crack propagation life that have been mentioned so far in this chapter, only apply when the fatigue crack is propagating under mode I cyclic loading, i.e. when the applied cyclic stress is orthogonal to the crack. This is the normal condition if the geometry is simple, the material is homogeneous and initially defect-free, and the loading direction remains constant throughout the life of the component. The environmental loads acting on offshore structures, on the other hand, are multidirectional. This means that the cyclic stresses will not always be orthogonal to the crack, and mixed-mode conditions will occur (Pook, Kam and Mshana, 1992). When the crack is subjected to mixed-mode cyclic loading, its crack path will not remain straight. In some geometries, the local loss of stiffness due to crack propagation can also lead to mixed-mode conditions and curved crack paths, as illustrated

by He, Liu and Xie (2014). Examples of curved cracks found in an offshore structure are shown in Haagensen, Larsen and Vårdal (2015).

### 2.5.1 Prediction of the mixed-mode crack path

As the crack path does not remain straight under mixed-mode conditions, it is necessary to be able to predict the crack path in some way. A number of criteria have been proposed for estimating the deflection angle for a mixed-mode crack. Most of these criteria have been developed for monotonic loading (i.e. the fracture angle, instead of the fatigue crack propagation angle), but the crack growth direction has been found to be approximately the same for monotonic and cyclic loading (Sih and Barthelemy, 1980). Therefore, these criteria are also used for fatigue.

Erdogan and Sih (1963) proposed that for brittle materials, the crack will propagate in the direction in which the tangential stress at the crack tip is maximized. A simple formula for finding this direction has subsequently been derived, and is provided in Paper IV. For ductile materials, Erdogan and Sih (1963) suggested that the crack will propagate in the direction along which the energy release rate is maximized, but they did not address the mathematical derivation. This was later considered by Hussain, Pu and Underwood (1974), who showed that the criterion of maximum energy release rate predicted slightly larger fracture angles than the criterion of maximum tangential stress. A third criterion was proposed by Sih (1974), in which the crack is assumed to propagate in the direction of minimum strain energy density. A related criterion is the T-criterion, proposed by Theocaris and Andrianopoulos (1982b), in which the crack is assumed to propagate in the direction of maximum dilatational strain energy density, evaluated along the boundary of the crack tip plastic zone.

While the first three criteria mentioned above are the classical, well-known criteria, some additional criteria have been proposed in recent years. For instance, Pavlou et al. (2003) proposed that the crack will

propagate in the direction which results in the minimum accumulated elastic strain energy in the vicinity of the crack tip. Bian and Taheri (2011) suggested the direction in which the ratio between the tangential stress and the von Mises stress is maximized, while Salimi-Majd, Shahabi and Mohammadi (2016) suggested the direction which yields the maximum of an effective local stress intensity factor, which takes into account the ratios of in-plane and out-of-plane shear strength to tensile strength for different materials.

In most practical cases, the difference between the predictions of the various criteria is quite small. Demir, Ayhan and İriç (2017) have performed mixed-mode fracture tests of the Al 7075-T651 aluminum alloy, and all the three classical criteria (maximum tangential stress, maximum energy release rate and minimum strain energy density) agree reasonably well with the measured fracture angles. The difference between the criteria increase as $K_{II}$ rises above $K_I$ (Suresh, 1998, p. 371; Tanaka, 1974). In practical cases of fatigue crack propagation, the crack will quickly deflect to an angle where $\Delta K_{II}$ is low, in which case the predictions from the three criteria are similar. It has been demonstrated by Bittencourt et al. (1996) that the three classical criteria give nearly identical crack paths when used in practical mixed-mode fatigue crack propagation simulations. Therefore, the criterion of maximum tangential stress is most commonly used in practice, because of its simple implementation.

### 2.5.2 Prediction of the mixed-mode fatigue crack propagation rate

The various fatigue crack growth laws, including the Paris law (Equation (2.1)), have been developed for cracks growing under mode I conditions, and therefore relates the crack growth rate to $\Delta K_I$. When a crack is subjected to cyclic mixed-mode loading, it is obvious that the other stress intensity factor ranges, $\Delta K_{II}$ and $\Delta K_{III}$, will also contribute to the crack propagation. This has led to the development of ‘effective’ stress

intensity factor ranges, which takes into account $\Delta K_{II}$ and $\Delta K_{III}$, and which are used with the normal crack growth laws. The two most well-known effective stress intensity factor ranges are those of Tanaka (1974) and Richard (Richard, Schramm and Schirmeisen, 2014).

Mixed-mode fatigue crack propagation tests are usually performed using a specimen with an initial crack which is not orthogonal to the applied uniaxial cyclic load (e.g. Tanaka, 1974; Borrego et al., 2006), or a specimen with a non-symmetric geometry which causes mixed-mode conditions (e.g. Silva et al., 2017). In both cases, the crack very quickly deflects to an angle where $\Delta K_{II}$ is very low. It is therefore difficult to assess the influence of $\Delta K_{II}$ on the crack growth rate, except at the very beginning of a test with an initial high value for $\Delta K_{II}$. This is likely the reason why it has not been possible to find studies which clearly and convincingly compare the Tanaka and Richard effective stress intensity factor ranges. A limited comparison has therefore been added in Paper IV, but regrettably not with experimental data.

### 2.5.3 Variable amplitude mixed-mode fatigue crack propagation

It is obvious that in practice the load amplitude will change as well as the loading direction. Therefore, models for variable amplitude fatigue crack propagation should be extended to mixed-mode cracks. This has to some degree been done (Boljanović and Maksimović, 2014; 2017; Dirik and Yalçinkaya, 2018), but the existence of experimental results which can be used to verify these models is very limited. As will be further reviewed in Paper VI, a number of studies have considered the application of a single mixed-mode overload in an otherwise mode I cyclic loading history. In practice the load amplitude and direction may vary from cycle to cycle, in which case many of the cycles (both the small and the large) will act under mixed-mode conditions. The experiments mentioned above do not represent this situation. It is therefore necessary to conduct experiments where both the overload and

the constant amplitude cyclic loads act under mixed-mode conditions. It has only been possible to find one such study in the literature: Lee and Choi (2009) have performed experiments where a mixed-mode overload is followed by mode I constant amplitude loading, where a mode I overload is followed by mixed-mode constant amplitude loading, and where a mixed-mode overload is followed by mixed-mode constant amplitude loading. While this is an interesting data set, the applied overloads all had the same magnitude. However, in order to check whether a model is able to predict the effect of overloads, it is necessary to compare it with several overload magnitudes. This kind of tests is missing from the available literature, and is therefore the subject of Paper VI.

# 3 Paper I: Application of foam-extend on turbulent fluid-structure interaction

[*]Kristen Rege, Bjørn H. Hjertager

Department of Mechanical and Structural Engineering and Materials Science, University of Stavanger, Norway

**Abstract:** Turbulent flow around flexible structures is likely to induce structural vibrations which may eventually lead to fatigue failure. In order to assess the fatigue life of these structures, it is necessary to take the action of the flow on the structure into account, but also the influence of the vibrating structure on the fluid flow. This is achieved by performing fluid-structure interaction (FSI) simulations. In this work, we have investigated the capability of a FSI toolkit for the finite volume computational fluid dynamics software foam-extend to simulate turbulence-induced vibrations of a flexible structure. A large-eddy simulation (LES) turbulence model has been implemented to a basic FSI problem of a flexible wall which is placed in a confined, turbulent flow. This problem was simulated for 2.32 seconds. This short simulation required over 200 computation hours, using 20 processor cores. Thereby, it has been shown that the simulation of FSI with LES is possible, but also computationally demanding. In order to make turbulent FSI simulations with foam-extend more applicable, more sophisticated turbulence models and/or faster FSI iteration schemes should be applied.

[*] Previously published as: Rege, K. and Hjertager, B.H. (2017) Application of foam-extend on turbulent fluid-structure interaction, *IOP Conference Series: Materials Science and Engineering*, 276, 012031. doi: 10.1088/1757-899X/276/1/012031

## 3.1 Introduction

Fatigue is responsible for the majority of failures in structural and mechanical components (Suresh, 1998). One of the many causes of fatigue loading is the action of a turbulent flow field on a structure, e.g. turbulent flow through water turbines (Saeed, Galybin and Popov, 2010), wind turbines (Nebenführ and Davidson, 2017), or around flexible structures like marine risers (Trim et al., 2005; Holmes, Oakley and Constantinides, 2006; Kamble and Chen, 2016; Nguyen and Nguyen, 2016). In order to assess the safety and reliability of these structures, it is necessary to estimate their fatigue life, which depends on the actual stress history experienced at their critical spots.

While being subjected to the turbulent flow, the structures will vibrate. If the structure is very stiff compared to the fluid, the influence of its vibration on the fluid flow will be negligible (Shepherd and Inaba, 2010). Then, the stress history may be found by first evaluating the flow field around or through a rigid model of the structure, and then imposing the resulting fluid load history to a structural dynamics analysis of the structure (Tijsseling, 1996). This is called an uncoupled simulation. However, slender structures like marine risers are flexible. Therefore, they will be subjected to significant deformations, thereby influencing the fluid flow. In these cases, it will be necessary to perform coupled fluid-structure interaction (FSI) simulations, in which the deformed shape of the structure is explicitly taken into account when calculating the fluid flow, in order to obtain realistic estimations for the stress history (Benra et al., 2011; Woldemariam and Lemu, 2016).

Because of their complexity, FSI problems are normally solved using computational techniques. These techniques may be divided into two groups: Monolithic approaches and partitioned approaches. In monolithic approaches (Hübner, Walhorn and Dinkler, 2004; Richter, 2012), a unified mathematical model is formulated for the entire regime (fluid and structure), and solved as a single large system of equations

(Mehl et al., 2016) for each time step. Stability and convergence rate may be better in a monolithic approach, but the system matrices may become ill-conditioned, requiring appropriate preconditioners (Hübner, Walhorn and Dinkler, 2004).

In partitioned approaches (Campbell and Paterson, 2011; Cesur et al., 2014; Gillebaart et al., 2016; Mehl et al., 2016) on the other hand, the structure and fluid regimes are each solved independently by separate mathematical models, i.e. computational solvers. At the interface between the fluid and the structure, information is interchanged between the two solvers, thereby enabling the fluid-structure interaction to be taken into account. The FSI problem is solved sequentially, as shown in Figure 3.1. The partitioned approach makes it possible to use existing, well-developed solvers to compute each of the two regimes, e.g. to use a finite element solver to compute the structural vibrations and a finite volume solver to compute the fluid flow. Because of this flexibility, the partitioned approach is very popular, and is employed in the majority of the FSI research reported (Campbell and Paterson, 2011).

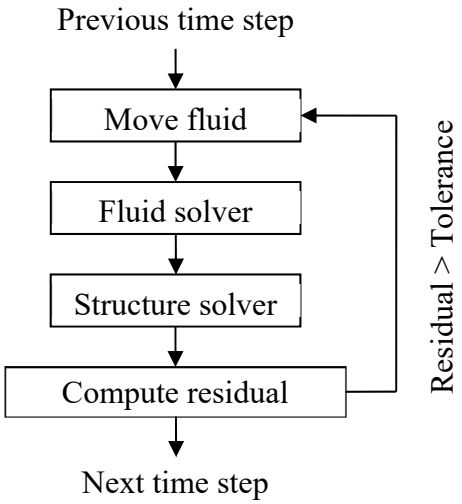


Figure 3.1 – Partitioned FSI approach with strong coupling

For the partitioned approaches, it is possible to employ either weak or strong coupling (Hübner, Walhorn and Dinkler, 2004; Campbell and Paterson, 2011). When weak coupling is employed, the fluid and structure regimes are each solved once at each time step. However, this scheme does not guarantee that the instantaneous equilibrium between the fluid and structure is fulfilled. In strong coupling, this is ensured by iteratively computing the fluid and structure fields until instantaneous equilibrium is satisfied, as indicated in Figure 3.1. According to Münsch and Breuer (2010), weak coupling leads to severe stability problems in most applications, and strong coupling should therefore be employed, especially for flexible structures.

Fluid-structure interaction has been studied for a number of flexible structures. Holmes, Oakley and Constantinides (2006) have simulated the vortex-induced vibration of marine riser models using the AcuSolve finite element (FE) computational fluid dynamics (CFD) solver. In these simulations, the motions of the riser are computed by combining the CFD results with the eigenvalues and eigenvectors of the riser. Holmes, Oakley and Constantinides propose to use a detached eddy simulation or an unsteady Reynolds averaged Navier-Stokes turbulence model, but do not specify which turbulence model they have used. The same riser model has also been simulated by Kamble and Chen (2016), using the finite volume (FV) CFD solver FANS3D, together with the chimera (overset) grid technique, in which a very fine mesh around the riser overlaps the mesh for the rest of the domain. Using a large eddy simulation (LES) model and about two millions cells, together with a finite difference scheme to simulate the curvature of the riser, good correlation with experimental results has been obtained.

Vortex-induced vibration of marine risers has also been simulated by Menter et al. (2006), by using the element-based finite volume software ANSYS-CFX to compute a laminar simulation of the flow, and the ANSYS structural FE software to compute the structural vibrations. Nguyen and Nguyen (2016) used the FV CFD solver OpenFOAM to

simulate vortex-induced vibration of rigid, elastically mounted circular cylinders, using a detached eddy simulation turbulence model.

Other simulations of offshore structures include the uncoupled simulation of wave actions on a simplified platform deck structure by Marzban et al. (2012), and the strongly coupled simulation of the movement of a closed riser filled with mud by Paczkowski et al. (2014).

In the case of turbulent FSI, several test cases have been simulated by Münsch and Breuer (2010), using strong coupling between a FV CFD solver and a FE structural solver, employing LES. The simulation results have only been compared to other computational results or laminar experimental data, however. Nilsson, Lillberg and Wikström (2012) have employed weak coupling and LES to simulate structural excitation of thin plate structures subjected to acoustics and gas flow in OpenFOAM, commenting on some short-comings. Recently, Cesur et al. (2014) studied the flow past a flexible cantilever beam, employing implicit large eddy simulation and strong FSI coupling, providing a thorough discussion of the results.

As indicated by the above literature review, the majority of FSI studies employ a finite element solver for the structural dynamics. However, recently a FSI toolkit was developed for foam-extend, a branch of the open source finite volume CFD code OpenFOAM (Weller et al., 1998), by Tuković et al. (2014). The toolkit employs the finite volume method (FVM) to solve both the fluid and structure regimes, in a partitioned approach, and is based on their previous works (Jasak and Tuković, 2006; 2010; Tuković and Jasak, 2007; 2012; Beaudoin and Jasak, 2008; Cardiff, 2012). The toolkit supports parallel computation of FSI problems with weak or strong coupling between a laminar or turbulent incompressible flow and an elastic structure subjected to large deformations. Ponweiser, Stadelmeyer and Karásek (2014) have investigated the scalability of this toolkit for multiple processors, and Šekutkovski et al. (2016) have used the toolkit together with a hybrid

RANS-LES turbulence model, in order to simulate flow around aircraft wings.

The objective of this paper is to investigate whether the FSI toolkit for foam-extend 4.0 is readily applicable to predict the fatigue life of flexible structures subjected to a turbulent flow. Available test cases for FSI are limited. Turek and Hron's (2006) test case is for laminar flow, while Pereira Gomes and Lienhart's (2010) turbulent test case employs two structural materials of different densities, which is currently not supported in the FSI toolkit. Therefore, it is chosen to implement a LES turbulence model to Richter's (2012) laminar test case of a flexible wall in an enclosed channel flow, which also is included as a tutorial in the toolkit. This test case has also been simulated by Gillenbaart et al. (2016) and Mehl et al. (2016).

LES is chosen as the turbulence model, because Reynolds-averaged Navier-Stokes (RANS) models do not resolve the turbulent fluctuations which may be important for fatigue evaluation, while direct numerical simulation has a high computational cost (Cesur et al., 2014). While previous FSI simulations with LES have often employed the Smagorinsky model (Münsch and Breuer, 2010; Nilsson, Lillberg and Wikström, 2012; Kamble and Chen, 2016), the one-equation $k_{SGS}$ eddy viscosity model is used in the current work. The goal is to obtain the stress history for a critical spot on the flexible structure. The stress history should be recorded for a sufficient amount of time, so that it is representative for the full fatigue life of the flexible structure, and be usable for fatigue life evaluation.

## *3.2 Governing equations*

The governing equation for a solid structure is normally stated in the Lagrangian formulation, in which the reference frame moves and deforms with the structural deformations. On the other hand, the governing equations for fluid flow are normally stated in the Eulerian

formulation, in which the reference frame remains stationary, independently of the fluid flow. Like the majority of partitioned FSI solvers (Campbell and Paterson, 2011), the FSI toolkit for foam-extend employs the Arbitrary Lagrangian-Eulerian (ALE) formulation for the fluid flow. This means that the reference frame for the fluid domain is independent of the fluid flow (Eulerian), but deforms according to the deformations of the structure (Lagrangian). In practice, this also means that the fluid mesh deforms according to, and conforms to, the deformed shape of the structure.

### 3.2.1 Governing equations for the fluid flow

The isothermal flow of an incompressible and Newtonian fluid may be fully described by the continuity equation and the Navier-Stokes equations. However, in order to solve these equations accurately with even the smallest turbulent eddies and fastest fluctuations resolved, an extremely fine spatial mesh and very small time steps would be required. Instead, we use large eddy simulation (LES), where only the large-scale turbulent eddies are resolved. This makes it possible to use a coarser mesh and larger time steps, decreasing the computational effort.

In LES, the small-scale turbulent eddies, which are smaller than the cutoff width, $\Delta$, (normally equal to the cell size), are not resolved (Versteeg and Malalasekera, 2007). Instead, they are modelled by sub-grid-scale (SGS) stresses, $\tau_{ij}$, which represent the effects of the unresolved motions. This spatial filtering decomposes the variables $\phi$ (pressure and velocity components) into a sum of a filtered component, $\overline{\phi}$, and a sub-grid-scale component, $\phi'$, i.e. $\phi = \overline{\phi} + \phi'$ (Tian et al., 2014). The governing equations for the fluid flow are solved for the filtered components, in which case the incompressible LES continuity equation in the ALE formulation becomes (Campbell and Paterson, 2011):

$$\operatorname{div}\left(\overline{\mathbf{u}}-\mathbf{u}_{\mathrm{m}}\right)=\frac{\partial\left(\overline{u}_i-u_{\mathrm{m}i}\right)}{\partial x_i}=0 \tag{3.1}$$

where $\overline{\mathbf{u}}=\left[\overline{u}_1,\,\overline{u}_2,\,\overline{u}_3\right]$ is the filtered fluid velocity field, $\mathbf{u}_{\mathrm{m}}$ is the velocity of the reference frame (i.e. the mesh), and $\mathbf{x} = [x_1, x_2, x_3] = [x, y, z]$ are the Cartesian coordinates. The filtered and incompressible Navier-Stokes equations in the ALE formulation are given as (Jasak and Tuković, 2006; 2010; Versteeg and Malalasekera, 2007; Tian et al., 2014; Cesur et al., 2014):

$$\rho_{\mathrm{f}}\frac{\partial\overline{u}_i}{\partial t}+\rho_{\mathrm{f}}\frac{\partial}{\partial x_j}\left(\overline{u}_i\left(\overline{u}_j-u_{\mathrm{m}j}\right)\right)=-\frac{\partial\overline{p}}{\partial x_i}+\mu_{\mathrm{f}}\frac{\partial^2\overline{u}_i}{\partial x_j^2}-\frac{\partial\tau_{ij}}{\partial x_j} \tag{3.2}$$

where $\rho_{\mathrm{f}}$ is the density of the fluid, $t$ is time, $\overline{p}$ is the filtered fluid pressure field, $\mu_{\mathrm{f}}$ is the dynamic viscosity of the fluid and $\tau_{ij}$ are the SGS stresses. For simplicity, the effects of gravitation are neglected in the simulation.

The SGS stresses are given as (Versteeg and Malalasekera, 2007):

$$\tau_{ij}=\rho_{\mathrm{f}}\overline{u_iu_j}-\rho_{\mathrm{f}}\overline{u}_i\overline{u}_j \tag{3.3}$$

The first term in this equation cannot be calculated from the solution of the filtered governing equations. Instead, it has to be modelled. The simplest SGS model is the Smagorinsky-Lilly model, which is often used, e.g. by Münsch and Breuer (2010), Nilsson, Lillberg and Wikström (2012), Tian et al. (2014) and Kamble and Chen (2016). However, this model contains a constant which needs to be adjusted on a case-to-case basis (Versteeg and Malalasekera, 2007). Therefore, the one-equation $k_{\mathrm{SGS}}$ eddy viscosity model will be used in the current work. This model includes one additional transport equation, which is solved for the SGS turbulent kinetic energy, $k_{\mathrm{SGS}}$ (Versteeg and Malalasekera, 2007):

$$\begin{aligned}&\frac{\partial\left(\rho_{\mathrm{f}} k_{\mathrm{SGS}}\right)}{\partial t}+\operatorname{div}\left(\rho_{\mathrm{f}} k_{\mathrm{SGS}}\left(\overline{\mathbf{u}}-\mathbf{u}_{\mathrm{m}}\right)\right)\\&\quad=\operatorname{div}\left(\frac{\mu_{\mathrm{SGS}}}{\sigma_k}\operatorname{grad}\left(k_{\mathrm{SGS}}\right)\right)+2\mu_{\mathrm{SGS}}\overline{S}_{ij}\cdot\overline{S}_{ij}-\rho_{\mathrm{f}}\varepsilon_{\mathrm{SGS}}\end{aligned}\tag{3.4}$$

where the SGS viscosity is given as $\mu_{\mathrm{SGS}}=\rho_{\mathrm{f}}C'_{\mathrm{SGS}}\Delta\sqrt{k_{\mathrm{SGS}}}$, the local strain rate of the resolved flow is given as $\overline{S}_{ij}=\frac{1}{2}\left(\partial\overline{u}_i/\partial x_j+\partial\overline{u}_j/\partial x_i\right)$, and the rate of dissipation is given as $\varepsilon_{\mathrm{SGS}}=C_\varepsilon k_{\mathrm{SGS}}^{3/2}/\Delta$. $C'_{\mathrm{SGS}}$, $C_\varepsilon$ and $\sigma_k$ are constants, while $\Delta$ is the filter cutoff width. With the SGS viscosity known, the SGS stresses may be calculated from:

$$\tau_{ij}=-2\mu_{\mathrm{SGS}}\overline{S}_{ij}+\frac{1}{3}\tau_{ii}\delta_{ij}\tag{3.5}$$

where $\delta_{ij}$ is the Kronecker delta. The van Driest (1956) damping function has been used in the simulations to reduce the near-wall eddy viscosity.

### 3.2.2 Governing equation for the structure

The governing equation for the structure is the conservation of linear momentum. For an isothermal structure in the total Lagrangian formulation, taking large deformations into account, this equation may be written as (Tuković and Jasak, 2007; Belytschko et al., 2014):

$$\int_{\Omega_0}\rho_{\mathrm{s}0}\frac{\partial\mathbf{u}_{\mathrm{s}}}{\partial t}\,\mathrm{d}\Omega_0=\int_{\Gamma_0}\mathbf{n}_0\cdot\left(\mathbf{S}\cdot\mathbf{F}^{\mathrm{T}}\right)\mathrm{d}\Gamma_0+\int_{\Omega_0}\rho_{\mathrm{s}0}\mathbf{f}_{\mathrm{b}}\,\mathrm{d}\Omega_0\tag{3.6}$$

where $\rho_{\mathrm{s}0}$ is the initial density of the structure, $\mathbf{u}_{\mathrm{s}}$ is its velocity vector, $\Omega_0$ is its initial volumetric domain, $\Gamma_0$ is its initial surface, and $\mathbf{n}_0$ is its outward pointing unit normal vector. $\mathbf{S}$ is the applied second Piola-Kirchhoff stress, $\mathbf{f}_{\mathrm{b}}$ is any body force acting, and $\mathbf{F}$ is the deformation gradient, given as:

$$\mathbf{F} = \mathbf{I} + \left(\nabla_0 \mathbf{d}_s\right)^T \tag{3.7}$$

where $\mathbf{d}_s$ is its displacement vector and $\nabla_0$ represents the gradient operator at the undeformed geometry.

The second Piola-Kirchhoff stress $\mathbf{S}$ may be related to the more commonly used Cauchy stress $\boldsymbol{\sigma}$ (current force acting on current geometry) by the following equation:

$$\boldsymbol{\sigma} = \frac{1}{\det \mathbf{F}} \mathbf{F}\mathbf{S}\mathbf{F}^T \tag{3.8}$$

For an elastic St. Venant-Kirchhoff material, the constitutive equation is:

$$\mathbf{S} = 2\mu_s \mathbf{E} + \lambda \operatorname{tr}\left(\mathbf{E}\right)\mathbf{I} \tag{3.9}$$

where $\mathbf{E}$ is the Green-Lagrangian strain and $\mu_s$ and $\lambda$ are the Lamé parameters (Belytschko et al., 2014):

$$\mathbf{E} = \frac{1}{2}\left(\mathbf{F}^T\mathbf{F} - \mathbf{I}\right) \tag{3.10}$$

$$\mu_s = \frac{E}{2\left(1+\nu_s\right)}, \ \lambda = \frac{\nu_s E}{\left(1+\nu_s\right)\left(1-2\nu_s\right)} \tag{3.11}$$

$E$ is the elastic modulus and $\nu_s$ is Poisson's ratio for the material.

### 3.2.3 Fluid-structure interface

At the fluid-structure interface, the following conditions must be met (Campbell and Paterson, 2011):

$$\begin{aligned} \mathbf{u}_f &= \mathbf{u}_s \\ \boldsymbol{\sigma}_s \cdot \mathbf{n} &= \boldsymbol{\sigma}_f \cdot \mathbf{n} \end{aligned} \tag{3.12}$$

Here, $\mathbf{u}_f$ is the fluid velocity field, $\mathbf{u}_s$ is the structural velocity, $\mathbf{n}$ is the unit normal vector of the interface, and $\boldsymbol{\sigma}_s$ and $\boldsymbol{\sigma}_f$ are the Cauchy stress matrices for the solid and fluid, respectively.

## 3.3 Discretisation of the equations

### 3.3.1 Discretisation of the fluid equations

The FSI toolkit for foam-extend 4.0 is used to solve the governing equations numerically, using the finite volume method. For the fluid flow, the PISO (Pressure Implicit with Splitting of Operators) scheme is used in the present study.

The SGS stresses calculated as part of the LES model are similar in magnitude to the numerical truncation errors (Versteeg and Malalasekera, 2007). It is therefore important to reduce these errors, so that they do not swamp the SGS stresses. This is done by using second-order or higher-order discretisation schemes in time and space.

The recommended temporal discretisation scheme for LES is the Crank-Nicolson scheme (Hjertager, 2014), while the backward scheme may give unacceptable dispersion (Nilsson, Lillberg and Wikström, 2012). The Crank-Nicolson scheme is an implicit scheme, which is second-order accurate in time, by weighting field variables at two succeeding time steps equally (Versteeg and Malalasekera, 2007). OpenFOAM (and foam-extend) allows the Crank-Nicolson scheme to be mixed with the first-order implicit Euler scheme. It is recommended to use a mix of 90 % Crank-Nicolson and 10 % Euler scheme in OpenFOAM, in order to bound/stabilise the scheme (Greenshields, 2016). However, investigations by the authors have shown that using 80 % Crank-Nicolson and 20 % Euler works better in foam-extend, as illustrated by pure CFD simulations in Figure 3.2.

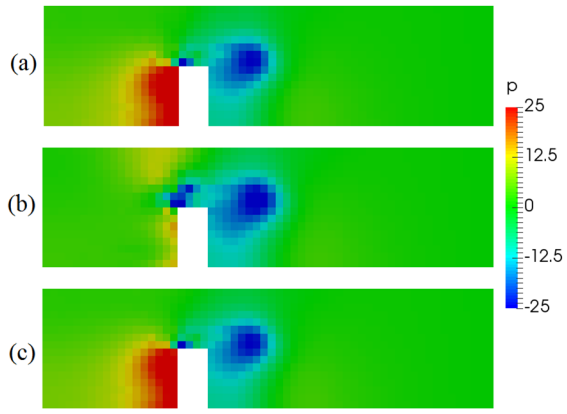


Figure 3.2 – Pressure fields [Pa] for identical cases at $t = 0.09$ s, computed by (a) OpenFOAM 4.0, Crank-Nicolson 0.9, (b) foam-extend 4.0, Crank-Nicolson 0.9 and (c) foam-extend 4.0, Crank-Nicolson 0.8. For (b), the pressure field in front of the obstruction suddenly disappears between $t = 0.08$ s and $t = 0.09$ s

The Courant number is given as $Co = |\mathbf{u}_f| \times \Delta t / \Delta x$, where $|\mathbf{u}_f|$ is the magnitude of the local velocity vector, $\Delta t$ is the length of the time step and $\Delta x$ is the length of the finite volume cell. The maximum Courant number should be kept below 1.0 when using the transient PISO scheme (Hjertager, 2009). Here, a constant time step length has been used to keep the maximum Courant number around 0.53.

For the spatial discretisation of the convection and diffusion terms, and the gradient, central differencing with Gaussian integration is used. More specifically, OpenFOAM's scheme 'Gauss filteredLinear2 1 0' was used for the div(phi,U) term, in order to remove staggering caused by pressure-velocity decoupling. Further details of the discretisation schemes (in the OpenFOAM branch) may be found in Greenshields (2016).

### *3.3.2 Discretisation of the structure equations*

The finite volume discretisation of Equation (3.6) contains one temporal term, one diffusive term and two source terms (Cardiff, 2012).

The first-order fully implicit Euler temporal discretisation scheme was first added to the FSI toolkit, and has been used in the current work. The second-order backward scheme has later been added to the FSI toolkit (Tuković et al., 2014), and should be used for increased accuracy (Gillebaart et al., 2016).

The diffusive term is discretised using central differencing with Gaussian integration, and gradients are computed using the least-squares approach. Further details of the discretisation of the governing equation for the structure may be found in Cardiff (2012).

### 3.3.3 Discretisation of the fluid-structure interaction

The fluid-structure interaction is solved in a partitioned approach, with strong coupling, as illustrated in Figure 3.1. The displacement increment and velocity of the structure are transferred to the fluid, by deforming the fluid mesh, while the pressure and viscous forces are transferred from the fluid to the structure. This is the most common procedure, as the reversed exchange of information might lead to instability (Campbell and Paterson, 2011). Hence, the fluid forces are applied on the structure as natural boundary conditions.

#### 3.3.3.1 Under-relaxation

As part of the iterative strong coupling, the fluid mesh is deformed at each iteration step. However, in order to stabilise the iterations and enforce convergence (Mehl et al., 2016), the fluid mesh is not moved the same distance as the predicted structural displacement at the last iteration step. Instead, the iteration is under-relaxed. This means that the displacement of the fluid mesh at iteration step $i$+1 is calculated as:

$$\mathbf{d}_{i+1} = \omega_i \overline{\mathbf{d}}_{i+1} + \left(1-\omega_i\right)\mathbf{d}_i \tag{3.13}$$

where $\mathbf{d}_i$ is the displacement of the fluid mesh at iteration step $i$, $\overline{\mathbf{d}}_{i+1}$ is

the structural displacement predicted in iteration step $i$, and $\omega_i$ is called the relaxation factor.

Three relaxation schemes are available in the FSI toolkit for foam-extend (Tuković et al., 2014): Fixed relaxation (i.e. $\omega_i$ = constant), Aitken dynamic relaxation and IQN-ILS. The fixed relaxation often leads to slow convergence (Mehl et al., 2016), and dynamic relaxation is therefore employed. The convergence rate of both the dynamic relaxation techniques has briefly been tested, but no significant difference was observed. The Aitken dynamic relaxation method is one of the most popular methods (van Zuijlen and Bijl, 2010), and has been employed in the current work. Details of the method may be found in Mok (2001). In the current work, an initial relaxation factor of 0.4 is used at each time step, and iterations are made until a relative tolerance of $10^{-5}$ is reached. If this tolerance is not reached within 200 iterations, the solver simply moves on to the next time step.

#### 3.3.3.2 Mesh movement

The motion of the fluid mesh is computed by a Laplacian approach, in which the points are moved according to the Laplace equation (Jasak and Tuković, 2006; Campbell and Paterson, 2011):

$$\nabla \cdot \left( \gamma \nabla \mathbf{u}_{\mathrm{m}} \right) = 0 \tag{3.14}$$

where $\gamma$ is the diffusion coefficient, which is chosen to be proportional to the squared inverse distance from the moving boundary. The solver 'refVelocityLaplacian' is chosen, with 2 non-orthogonal correctors.

## 3.4 Modelling approach

### 3.4.1 Geometry, properties and boundary conditions

The geometry of the problem chosen for this study is shown in Figure 3.3. It is based on Richter's (2012) laminar test case, but has been extended to full three-dimensionality, in order to allow turbulence modelling. The geometry of the problem consists of a flexible wall (structure) inside a rectangular duct. The duct has one inlet and one outlet. Its width is 0.8 m and its height is 0.4 m. The flexible wall is 0.4 m wide, 0.1 m thick and 0.2 m high, and is fixed to the floor of the duct, as shown in Figure 3.3. While Richter's case had an inlet length, *IL*, of 0.45 m, preliminary studies have shown that this is too short for the turbulent case, and therefore it has been increased to *IL* = 0.95 m (units are here added to Richter's non-dimensional measures).

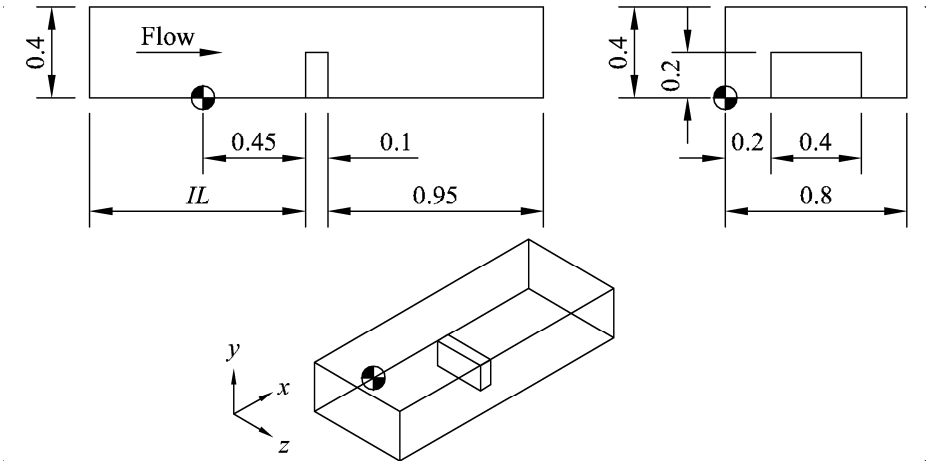


Figure 3.3 – Geometry of the problem. All dimensions are given in meters

As in Richter's case, the duct conveys an artificial fluid of density $\rho_f = 1000$ kg/m3 and kinematic viscosity $\nu_f = 10^{-3}$ m$^2$/s. In Richter's case, the fluid enters the duct with mean velocity $U = 0.15$ m/s. This velocity is here increased to $U = 5$ m/s, in order to get turbulence in the wake of the flexible wall. In this case, the Reynolds number, *Re*, for the flow

entering the duct is 2667, which is within the critical zone between fully laminar ($Re < 2000$) and fully turbulent ($Re > 4000$) flow (Finnemore and Franzini, 2002). This value should be sufficient to give turbulence in the wake of the flexible wall, however.

For simplicity, a laminar inlet velocity profile, i.e. a parabolic velocity profile, has been used as an approximation. The peak velocity in the middle of the cross-section is $u_{max} = 2U = 10$ m/s. The no-slip condition is applied for the bottom, top and sides of the fluid domain, as well as for the interface to the flexible wall. At the outlet, the zero gradient condition is imposed on the velocity, and the pressure has a Dirichlet boundary condition with zero pressure.

The properties of the flexible wall have been changed from those in the Richter's case, in order to obtain visible, but yet not extreme deformations. The wall is too thick to obtain significant vibrations with any realistic material. Its density, $\rho_s$, has been set equal to 8000 kg/m$^3$, Poisson's ratio, $\nu_s$, has been set to 0.3, while the elastic modulus has been chosen to be $E = 4$ MPa, which is very soft. The flexible wall is fixed ($\mathbf{d}_s = 0$) at the bottom, but is otherwise free to move.

### 3.4.2 Initial conditions

It is chosen to start the solution from a fully developed turbulent flow, and the structure at rest; a technique which has also been used by Münsch and Breuer (2010) and van Zuijlen and Bijl (2010). The chosen initial velocity field is shown in Figure 3.4. The structure is allowed to move during the first computational step. This initial condition is preferred, because it requires little computational effort, compared to the alternatives.

However, as illustrated in the works by Münsch and Breuer (2010) and van Zuijlen and Bijl (2010), the sudden exposure of the flexible structure to a fully developed fluid flow induces an initial transient to its vibration.

In the context of fatigue life estimation, we are mostly interested in the stabilised vibrations remaining when this transient effect has been damped out. In order to reduce the transient effect, the inlet velocity could have been slowly increased to the full flow. However, as very many FSI iterations are required even at low velocities, this procedure is computationally demanding. Furthermore, the PISO solver implemented in the FSI toolkit does not contain any ability to automatically adjust the time step to keep the Courant number within a given limit, meaning that the time step would have needed to be manually decreased as the velocity increased.

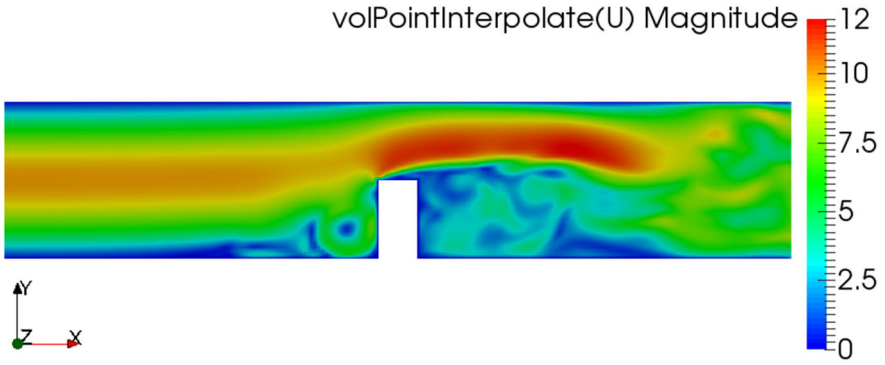


Figure 3.4 – Initial velocity field [m/s] at $t = 0$ (volume point interpolated)

### 3.4.3 Computational meshes

While Richter (2012) uses finite elements to discretise the computational domain, both Gillenbaart et al. (2016) and Mehl et al. (2016) use hexahedral finite volume cells which are approximately 2.5 cm long in each direction, for the flow domain. In a fully three-dimensional model, this corresponds to 40 448 finite volume fluid cells. This is quite a coarse mesh for a large eddy simulation. In the current study, the cell size has therefore been decreased to 1.0 cm in each direction, resulting in a total of 632 000 cells in the fluid domain. In Figure 3.5, the vibration history for the flexible wall, computed by both meshes, is plotted for 1.5 seconds, and it is clear that the coarser mesh is not able to capture all the

small eddies which significantly influence the vibration of the flexible wall. The fine mesh, which is used to obtain the remainder of the results presented, is shown in Figure 3.6.

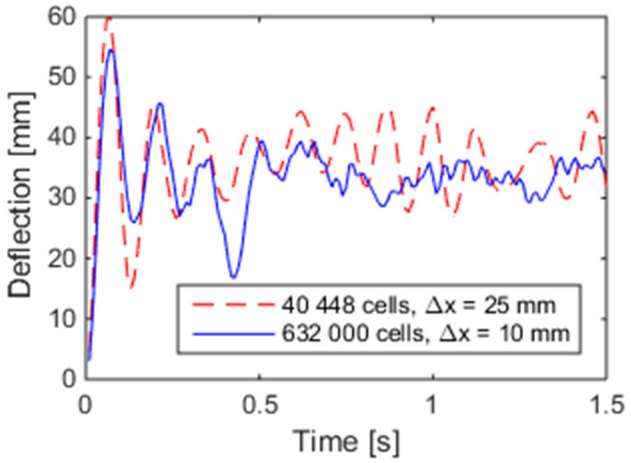


Figure 3.5 – Deflection history for the wall, for two different meshes

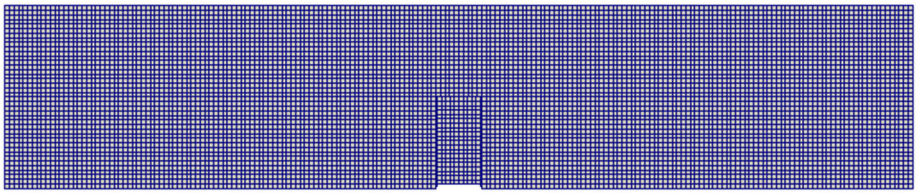

Figure 3.6 – Section of the mesh used in the simulations

The flexible wall has in all cases been discretised by 512 hexahedral finite volume cells, each 2.5 cm long in each direction. Both meshes have been decomposed for 20 processors using the metis algorithm. A computational time step $\Delta t$ of 250 µs has been used to keep the maximum Courant number around 0.53. Simulation results have been saved every 0.01 s, i.e. at a sampling frequency of 100 Hz.

In order to assess the quality of the simulation, the dependence of these parameters should be further investigated. Such studies could not be

conducted within the present work however, due to time and CPU constraints.

## 3.5 Simulation results

Results from the simulations are illustrated in this section, and further discussed in Section 3.6. If otherwise is not mentioned, the figures show the computed fields at the plane $z = 0.4$ (ref. Figure 3.3), which cuts through the middle of the flexible wall. Finite volume results are saved in the nodes in the centre of each cell, and the field values are thereby constant throughout each cell. However, volume point interpolation has been used to smooth out the fields shown in the figures.

### 3.5.1 Computation time

Due to time constraints, the simulation was run for 2.32 simulated seconds only. For the first 1.5 simulated seconds, the computation time was 96 hours (clock time) using 20 of 80 available Intel Xeon CPU E7-8870 @ 2.40 GHz processor cores. The remaining cores were idle. This corresponds to an average of 38 min 33 s computation time per 0.01 second simulated. On average, 17.7 FSI iterations had to be made for each time step of 250 µs, as shown in Figure 3.7. Simulation data was saved every 0.01 simulated second, each time step being composed of approximately 293 MB of data.

For the remainder of the simulation, the 80-core computer was subjected to an increased workload, and did also randomly crash. Continuous log files are therefore not available between $t = 1.5$ s and $t = 1.88$ s. Between $t = 1.88$ s and $t = 2.32$ s, the computation time was 96 hours (clock time) using 20 cores, i.e. 130 min 51 s per 0.01 second simulated, on average. As the average number of FSI iterations was more or less the same as for the first 1.5 s, the increased computation time is thought to result from the increased workload on the computer, which had around 120-150 concurrent jobs at this time.

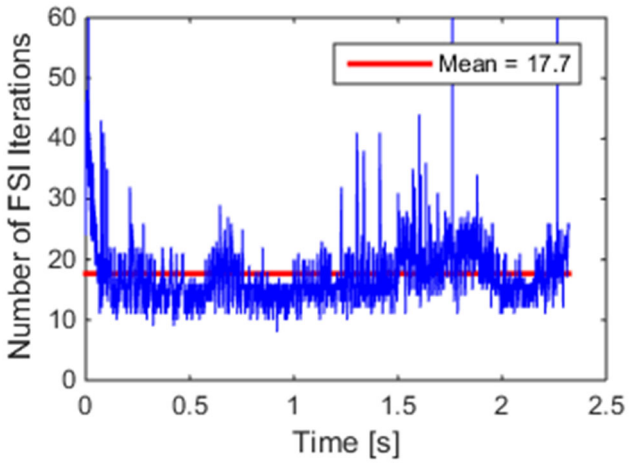


Figure 3.7 – Number of FSI iterations required at each time step to reach a relative FSI tolerance of $10^{-5}$

For reference, similar simulations without FSI did only require 33 s clock time per 0.01 second simulated, using 20 processor cores.

### 3.5.2 The fluid flow

The local velocity reaches its maximum at $t = 0.079$ s. The nearest time step which is saved is $t = 0.08$ s, and the velocity field at this time step is shown in Figure 3.8(a). It is clear that the flexible wall has become significantly curved, and that the relatively smooth flow path (continuous red field in Figure 3.4) has been disturbed.

The velocity field for the last time step is shown in Figure 3.8(b). The wall is not as curved as at $t = 0.08$ s, but the amount of turbulence has increased. A lot of mixing is taking place in the wake of the wall, and the velocity profile is no longer smooth upstream the wall either.

The time average (mean) velocity fields are shown in Figure 3.9 for $t = 1.80$ s and for $t = 2.32$ s. It is observed that these two fields look relatively similar; indicating that a stabilised flow has been reached.

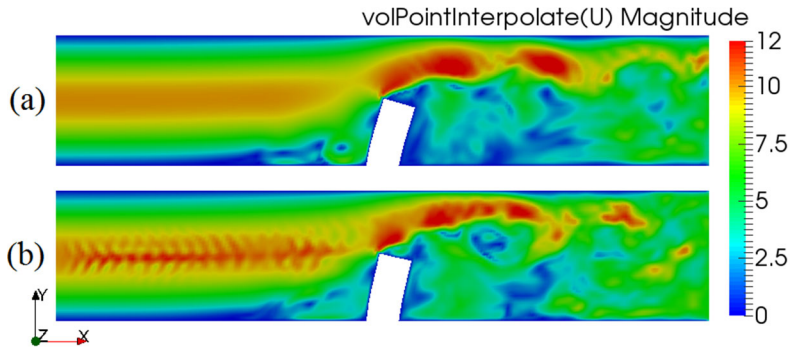


Figure 3.8 – Velocity field [m/s] at (a) $t$ = 0.08 s, and (b) $t$ = 2.32 s

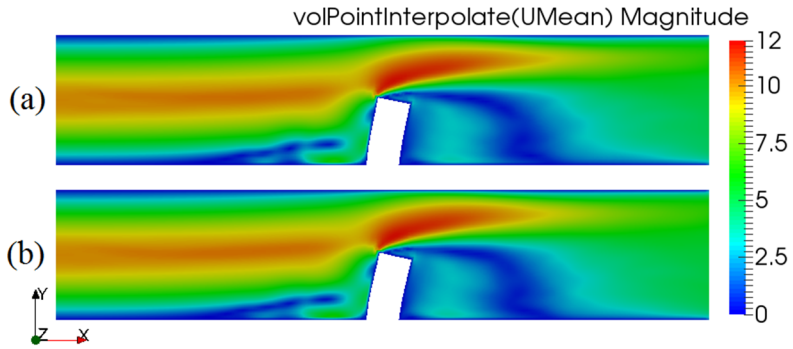


Figure 3.9 – Time averaged velocity field [m/s] up to (a) $t$ = 1.80 s, and (b) $t$ = 2.32 s

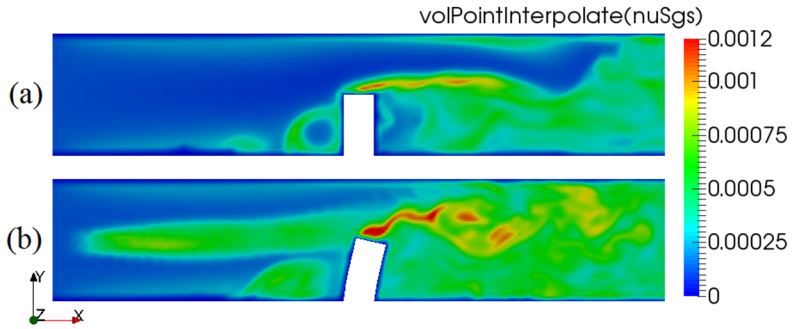


Figure 3.10 – The SGS kinematic viscosity fields [$m^2/s$] at (a) $t$ = 0, and (b) $t$ = 2.32 s

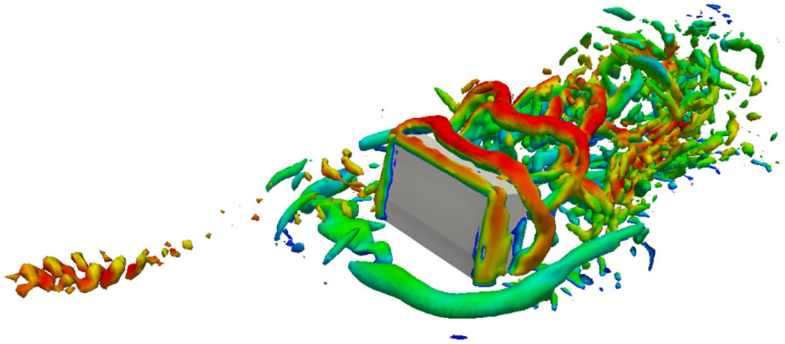

Figure 3.11 – Isosurfaces for $Q = 10^4$, at $t = 2.32$ s, coloured by velocity magnitude

The increase in turbulence due to the vibration of the flexible wall is also evident from Figure 3.10, where the SGS kinematic viscosity fields are shown for $t = 0$ and $t = 2.32$ s. The flow downstream the flexible wall is clearly turbulent, and the upstream turbulence has also been increased. The turbulent field at $t = 2.32$ s is illustrated by isosurfaces of the second invariant of the velocity gradient tensor, $Q$, in Figure 3.11. In addition to the turbulence downstream the flexible wall, it indicates that a spiralling flow pattern has developed near the inlet.

### 3.5.3 The vibration of the flexible wall

The deflection history for the point $(x, y, z) = (0.45, 0.2, 0.4)$, which is positioned at the middle of the upper front edge of the wall, is shown in Figure 3.12. The transient initial vibration due to the sudden freedom of the wall at $t = 0$ is clearly visible. The time history is too short to determine whether these transient effects have disappeared during the simulated interval, but the curves do indicate a possible stabilised vibration starting a bit before $t = 2$ s.

With a sampling frequency of 100 Hz, the deflection magnitude history has been found to be dominated by frequencies around 7.3 Hz, with lesser peaks at 2.2 Hz and 27 Hz.

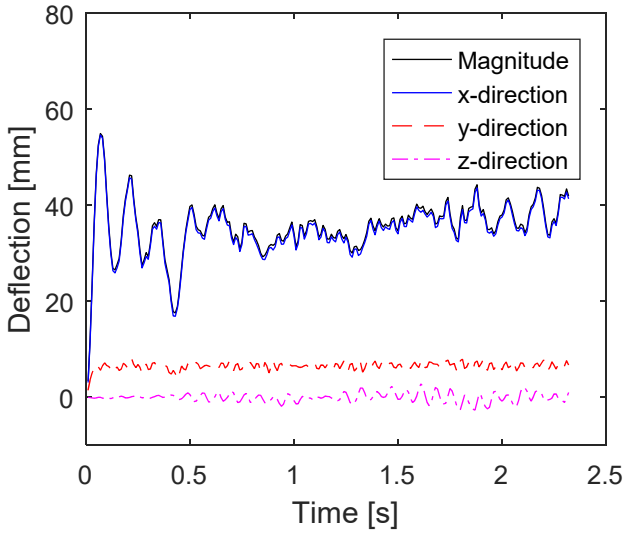


Figure 3.12 – Deflection history for the wall, at $(x, y, z) = (0.45, 0.2, 0.4)$. The difference between the histories of the component in $x$-direction, and the absolute value/magnitude of the displacement, is indistinguishable

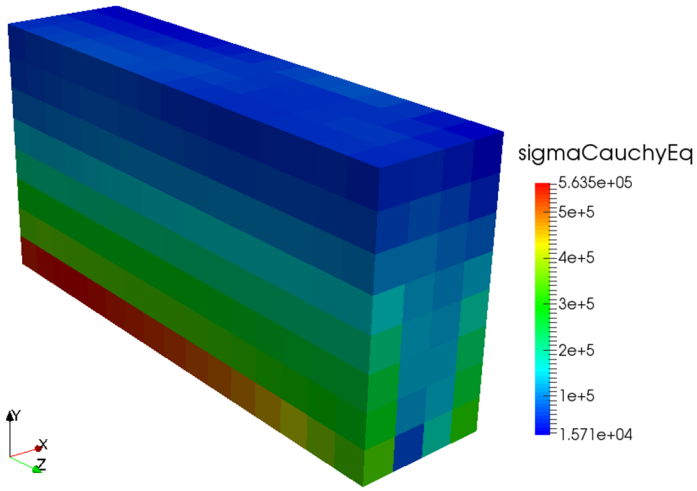


Figure 3.13 – Von Mises stress distribution [Pa] at $t = 2.32$ s

For the purpose of estimating the fatigue life of a structure, it is essential to know its stress history. The stress state at a point is often represented by the von Mises equivalent stress, which may be calculated as:

$$\sigma_{\mathrm{VM}} = \left\{ \frac{1}{2} \left[ \left( \sigma_{xx} - \sigma_{yy} \right)^2 + \left( \sigma_{yy} - \sigma_{zz} \right)^2 + \left( \sigma_{zz} - \sigma_{xx} \right)^2 \right] + 3 \left( \sigma_{xy}^2 + \sigma_{yz}^2 + \sigma_{xz}^2 \right) \right\}^{1/2} \tag{3.15}$$

The von Mises stress distribution in the wall at $t$ = 2.32 s is shown in Figure 3.13. The asymmetry along the $z$-axis is assumed to be a result of the turbulence of the flow.

As illustrated in Figure 3.13, the most critically loaded part of the wall is the strip along the front, close to the bottom. It is likely that any fatigue crack will nucleate along this strip. The time histories of the different stress components at the middle of the strip, $(x, y, z)$ = (0.45, 0.0125, 0.4) are shown in Figure 3.14.

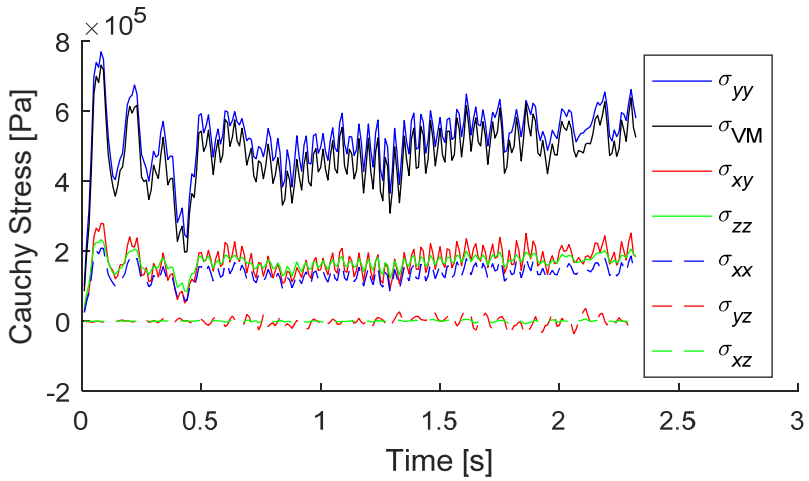


Figure 3.14 – Stress histories at $(x, y, z)$ = (0.45, 0.0125, 0.4)

## 3.6 Discussion

Figures 3.12 & 3.14 indicate that the FSI toolkit for foam-extend 4.0 is capable of producing a vibration history, which is appropriate for evaluating the fatigue life of the structure. However, some important aspects need to be taken into account, and will be addressed in this section.

### 3.6.1 The initial transient

As predicted in Section 3.4.2, the sudden application of fluid-structure interaction in the fully developed flow induces an initial transient to the vibration history, as observed in Figure 3.12. As momentum is dissipated from the structure to the fluid, the vibration of the wall, due to the sudden application, is damped, and will diminish over time. This means that a 'steady-state' or stabilised vibration will be reached after a certain time. If the wall is subjected to the turbulent flow for most of its life, it is this stabilised vibration which is interesting for fatigue purposes. When the vibration is stabilised, a relatively short vibration response may be extrapolated to represent the full vibration history of the wall. Then, its fatigue life may be estimated by using an *S-N* curve for the material and applying a cycle counting technique and a cumulative damage law (Suresh, 1998), like the well-known linear Palmgren-Miner rule (Miner, 1945) or more recent, nonlinear rules, e.g. by Rege and Pavlou (2017).

However, as shown in Figures 3.12 & 3.14, it is not possible to indisputably assess whether the transient effect has diminished completely within the 2.32 seconds simulated in the current work. There is still a lot of variation. Still, the last three major oscillations of the deflection magnitude shown in Figure 3.12 seem to have a relatively constant mean value and frequency, with only small deviations in the amplitude. This may indicate that the stabilised vibration either has been reached, or that it is coming. This indication is further strengthened by

the observation made of the time averaged velocity fields shown in Figure 3.9, where the flow seems to have stabilised at about $t = 1.80$ s.

This indicates that even though the simulated interval of 2.32 s is too short to make any sensible fatigue life estimations, we are not very far away from having sufficient data to make such estimations. It is absolutely possible that having results all the way up to $t = 3$ or 4 s would have made such estimations possible. The major problem is the time required to obtain these results. Based on the obtained results, somewhere between 44 and 148 hours of computation would be required to reach $t = 3$ s.

### 3.6.2 The need for simulation of the fluid-structure interaction

Throughout Section 3.5, it is noted that the amount of turbulence has increased during the time interval from $t = 0$ to $t = 2.32$ s, whereas the amount of turbulence stabilised in similar simulations where FSI was not employed. This turbulence increase may be directly related to the fluid-structure interaction. While the turbulence induces vibrations to the flexible wall, the vibrations of the wall do also induce additional disturbances and mixing, i.e. turbulence, to the flow. This illustrates the importance of applying (strong) fluid-structure interaction when simulating the vibration of flexible structures being subjected to a turbulent flow.

### 3.6.3 Assessment of the simulation results

As no experimental data is available for the case investigated, the validity of the simulation results cannot be confirmed. Furthermore, the authors are not aware of other implementations of LES to this case. The flexible wall is relatively thick and short, and can therefore be analysed neither as a plate nor as a cantilever beam. The next step would therefore be to perform simulations of a more realistic problem, where an analytical

solution of the natural frequencies of the structure, and preferably, experimental data, are available.

Several sources of errors exist for the computed results. First and foremost, a full convergence check with respect to mesh refinement and time step length has not been conducted within the present work, due to time and CPU constraints. The results may therefore be sensitive to these parameters. Secondly, while the influence of the inlet length has been investigated, it is possible that the length from the flexible wall to the outlet may be too short. Also, the sampling frequency of 100 Hz may be too low to resolve the highest vibration frequencies. Furthermore, the accuracy of the vibration history may have been increased by using the second-order backward temporal discretisation scheme for the structure.

In addition, as the flow is confined by the duct on four sides, the results rely on the quality of the $\nu_{SGS}$ wall function, which may be questionable. Further refinement of the mesh near the wall, so that the first cell centre would lie at a non-dimensional distance, $y^+$, of ~1 from the wall (instead of $y^+ \approx 12$, as used here), would make it possible to omit the use of the wall function (Hjertager, 2009). The spiralling flow developing from a unidirectional inlet may indicate that some numerical problem exists.

### 3.6.4 Computational effort

With the resolution and settings used in the current work, between 64 and 218 hours of computation are required to compute one simulated second, depending on the workload of the computer. The computational cost is therefore high. However, as indicated above, even three to four seconds of data may be sufficient to estimate the full fatigue life of the structure. For critical structures, performing FSI simulations in foam-extend may be a good alternative to the empirical and analytical tools often used today (Nguyen and Nguyen, 2016).

Within the current FSI toolkit for foam-extend, a couple of parameters could be tuned which could possibly further decrease the computational effort. In the current work, the computation has been performed in parallel using 20 processor cores, each core handling 31 600 fluid cells and 25–26 structure cells, decomposed by the metis algorithm. It is possible that this is a low amount of cells per core, meaning that excessive time is used to transfer information between the cells. However, computations with even fewer fluid cells per processor core are found in the literature, e.g. Tuković and Jasak's (2012) simulation of a droplet using 8 parallel processors, each handling about 7777 cells.

Nevertheless, some computation time could probably be saved by using fewer processor cores to compute the structure. Here, the toolkit's standard setting of using all of the same cores for the computation of both regimes was chosen for simplicity. The fluid and structure are usually computed in serial, i.e. in a staggered pattern, meaning that all the processor cores cannot be fully utilised when running a parallel computation, no matter how the structure is decomposed. Mehl et al. (2016) have proposed two techniques for simultaneous parallel computation of both regimes at each time step, which could be implemented to maximise the utilisation of each processor core.

A relatively large amount of the computation time is spent moving and deforming the fluid mesh (Ponweiser, Stadelmeyer and Karásek, 2014). In the current work, the FVM-based 'refVelocityLaplacian' solver with 2 non-orthogonal correctors has been used to deform the mesh. The FEM-based solver developed by Jasak and Tuković (2006) is also available. It is stated to be more robust, and may influence the computation time.

The number of FSI iterations does also contribute significantly to the computation time. With the Aitken scheme, an initial under-relaxation factor of 0.4 and required relative tolerance of $10^{-5}$, 17.7 FSI iterations were required at each time step, on average. This is a significant increase

from the laminar case. Changing any of these parameters would influence the number of FSI iterations, and thereby the computation time. Limiting the number of FSI iterations will be of major importance for reducing the computational effort for simulating turbulent FSI. van Zuijlen and Bijl (2010) have suggested a technique where the flow is solved on alternating coarse and fine meshes during the FSI iteration within each time step, in order to reduce the computational effort for RANS simulations. However, this technique has limited application to LES simulations, where the fine mesh always is required to give a sufficient resolution.

The last solution to reduce the computational effort we will mention is the use of a more sophisticated turbulence model. Implicit large eddy simulation (Cesur et al., 2014), hybrid RANS-LES models (Šekutkovski et al., 2016) and detached eddy simulation techniques (Nguyen and Nguyen, 2016) have all been used for this purpose to solve turbulent FSI problems.

## 3.7 Conclusions

In this paper, a large-eddy simulation (LES) turbulence model has been implemented to Richter's fluid-structure interaction (FSI) test case, and 2.32 seconds of turbulent fluid-structure interaction has been simulated, using the FSI toolkit for foam-extend 4.0. It has been shown that this toolkit is capable of producing a vibration history, which is appropriate for evaluating the fatigue life of a flexible structure.

The computational effort required to perform such simulations is large, however. Even for the relatively simple case investigated here, 632 000 cells were required to discretise the fluid domain. An average number of 17.7 FSI iterations were required at each time step, due to the relatively slow FSI convergence rate. The FSI convergence rate is significantly lower for turbulent flows modelled by LES, than for laminar flows.

Because of this, over 200 computation hours was required for the simulation of 2.32 seconds of turbulent FSI.

This indicates the need of applying more sophisticated turbulence models and/or faster FSI iteration schemes. The FSI toolkit for foam-extend could also require the possibility of automatically adjusting the time step according to the Courant number, and the implementation of additional solvers. Especially a two-phase solver for the simulation of ocean waves and a compressible solver to simulate water hammer induced vibrations of pipelines would be appreciated.

In future work, the factors influencing the computational effort, as mentioned in Section 3.6.4, should be further studied. The studies should also consider a more realistic problem, with experimental and/or analytical data available.

## *Acknowledgements*

This work was supported by the Norwegian Ministry of Education and Research. Dr. K.E. Giljarhus is acknowledged for constructive suggestions.

# 4 Paper II: A one-parameter nonlinear fatigue damage accumulation model

*Kristen Rege, Dimitrios G. Pavlou

Department of Mechanical and Structural Engineering and Materials Science, University of Stavanger, P.O. Box 8600 Forus, N-4036 Stavanger, Norway

**Abstract:** A nonlinear model for fatigue damage accumulation under variable amplitude loading is presented. The known assumption that the isodamage curves are converging at the knee point of the *S*-*N* curve of the material, has been adopted. The proposed model does only require one parameter, in addition to the *S*-*N* curve of the material, in order to calculate the remaining fatigue life. A single value for the parameter has been found to give satisfying agreement with experimental data for four arbitrary selected steels, indicating a general trend.

## 4.1 Introduction

In order to calculate the cumulative fatigue damage of steel structures subjected to variable amplitude loading, design standards like Eurocode 3 (Standards Norway, 2010) and DNVGL-RP-C203 (DNV GL, 2016) still recommend the use of the Palmgren-Miner rule (Palmgren, 1924; Miner, 1945), which was stated mathematically in 1945 (Fatemi and Yang, 1998). This rule is also commonly used in the European automotive industry (Schoenborn et al., 2015). However, it has been known for a long time that this linear damage rule predicts a longer fatigue life than normally experienced if the loading amplitude is decreasing, and a shorter life if the loading amplitude is increasing

* Previously published as: Rege, K and Pavlou, D.G. (2017) A one-parameter nonlinear fatigue damage accumulation model, *International Journal of Fatigue*, 98, pp. 234–246. doi: 10.1016/j.ijfatigue.2017.01.039

(Fatemi and Yang, 1998; Mesmacque et al., 2005; Fissolo et al., 2015; Theil, 2016). The conservatism of the Palmgren-Miner rule is therefore questionable. Probabilistic approaches to overcome this shortcoming are discussed in the works by Fernández-Canteli et al. (2014), Blasón et al. (2016) and Correia et al. (2016). Because of this problem, numerous cumulative fatigue damage rules have been proposed (Fatemi and Yang, 1998).

One model, which has shown excellent agreement with experimental results, is the double linear damage rule, developed by Manson et al. during the 1960s and ’70s (Manson and Halford, 1981; Lee et al., 2005; Fissolo et al., 2015). This rule divides the fatigue life into two phases; Phase I and Phase II, in which different mechanisms are assumed to dominate. The double linear rule assumes that the behaviour within each of these two phases may be modelled by a linear rule, thereby preserving some of the simplicity of the Palmgren-Miner rule.

The two phases were originally considered to represent crack initiation and crack growth, but Manson and co-workers did later abandon this phrasing for their model (Manson and Halford, 1981). However, other models differentiating between crack initiation and crack growth were developed, like the double exponential law by Miller and Zachariah (1977). These models typically require tests to be performed in order to determine the duration of each of these two stages at different stress levels.

Also developed in the 1970s was the concept of isodamage lines (Fatemi and Yang, 1998). Subramanyan (1976) provided a simple model, in which the isodamage lines were assumed to converge at the knee point of the *S*-*N* curve, as will be explained in Section 4.2.2. An alternative approach of the concept of isodamage lines was proposed by Hashin and Rotem (1978). In this work they assumed isodamage lines converging at the point where the *S*-*N* curve intersects the *S*-axis. Since these alternative isodamage lines become invalid at low stress amplitude

values (Hashin and Rotem, 1978), the selection of Subramanyan's model is preferable. Additional confirmation of the validity of the assumption of Subramanyan's model can be found in the work by Pavlou (2002), indicating the existence of isodamage lines converging at the knee point, by considering the evolution of surface hardness during fatigue damage accumulation. The model containing isodamage lines converging at the knee point shows a clear improvement from the Palmgren-Miner rule, but is still slightly non-conservative (Lee et al., 2005).

As shown in the reviews by Fatemi and Yang (1998) and Santecchia et al. (2016), many other cumulative damage rules have been proposed over the years. In order to account for more of the underlying mechanisms, the simplicity of the double linear rule and Subramanyan's model is often lost, but still none of them has reached universal acceptance yet (Santecchia et al., 2016). Many of the models require some material-dependent coefficient to be determined through extensive testing, e.g. Yuan et al. (2013). Such test data or testing facilities may not be available to a design engineer, causing fatigue calculation by these models to be difficult.

However, some models have recently been developed, which do not require extensive testing. One example is the damage curve approach by Gao et al. (2014), based on a similar approach by Manson and Halford (1981). Furthermore, a simple model, taking the mean stress of the cyclic loading into account, has been developed by Shang and Yao (1999), based on the continuum fatigue damage theory. Another recent damage rule is the sequential law, developed by Mesmacque et al. (2005) (see also Aid et al., 2011). This rule also does not need any experimentally determined constant, apart from the full *S-N* curve of the material, and has been applied in order to estimate the remaining fatigue life of railway bridges (Siriwardane et al., 2008). However, significant deviation between the sequential law and real fatigue life has been observed (Siriwardane et al., 2009). Therefore, a similar rule, where the plastic

meso-strain is used in the damage indicator, instead of the von Mises stress, has also been developed (Siriwardane et al., 2009).

In the present work, a fatigue damage accumulation model based on isodamage curves is proposed. The model is intended to be simple to use for practicing engineers, while also being more accurate than comparable models. The shape of the isodamage curves is based on experimental data for two-step fatigue tests of SAE 4130 steel, reported by Manson, Freche and Ensign (1967). The proposed model is then compared to the Palmgren-Miner rule, Subramanyan's model, the double linear damage rule, Shang and Yao's model and the sequential law, using experimental data for C-35 steel (Subramanyan, 1976), P355NL1 steel (Pereira et al., 2008) and 300 CVM steel (Manson, Freche and Ensign, 1967).

## 4.2 Fatigue damage accumulation

### 4.2.1 Isostress lines

Let us assume a constant stress amplitude ($\sigma_a$ = const.). The elementary percentage of the damage increment, d$D$/$D$, should be proportional to the elementary percentage of the increment of the loading cycles, d$n$/$n$:

$$\frac{\mathrm{d}D}{D} = m\left(\sigma_a\right)\frac{\mathrm{d}n}{n} \tag{4.1}$$

where $m(\sigma_a)$ is a parameter depending on the stress amplitude.

Integration of Equation (4.1) yields:

$$\int \frac{\mathrm{d}D}{D} = m\left(\sigma_a\right)\int \frac{\mathrm{d}n}{n} + C \tag{4.2}$$

or

$$\ln D = m\left(\sigma_a\right)\ln n + C \tag{4.3}$$

For $n = N$, failure of the material is occurring. Therefore, the damage function takes the value $D = 1$. Taking into account the above boundary condition, the constant of integration, $C$, can be obtained by Equation (4.3):

$$0 = m\left(\sigma_{\mathrm{a}}\right)\ln N + C \tag{4.4}$$

or

$$C = \ln N^{-m(\sigma_{\mathrm{a}})} \tag{4.5}$$

With the aid of Equations (4.5) and (4.3) yields:

$$\ln D = \ln n^{m(\sigma_{\mathrm{a}})} + \ln N^{-m(\sigma_{\mathrm{a}})} \tag{4.6}$$

or

$$D = \left(\frac{n}{N}\right)^{m(\sigma_{\mathrm{a}})} \tag{4.7}$$

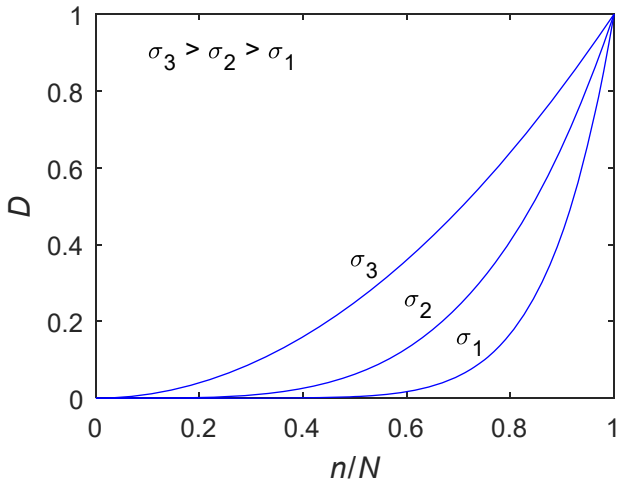


Figure 4.1 – Schematic demonstration of isostress curves according to Equation (4.7)

The above functional form for damage accumulation is illustrated in Figure 4.1, and has been proposed by many researchers, e.g. Manson and Halford (1981) and Gao et al. (2014; 2015).

### *4.2.2 Isodamage lines*

Subramanyan's (1976) model for cumulative fatigue damage is based on the assumption that the *S*-*N* curve of a material corresponds to a state of 100 % fatigue damage, while combinations of stresses and cycles ($n_i$, $\sigma_i$) below the endurance limit (fatigue limit) correspond to a state of 0 % fatigue damage. In between these two extremes, a set of straight isodamage lines were introduced, as shown in Figure 4.2. Earlier experimental results indicated that such isodamage lines converged near the knee point of the *S*-*N* curve, leading to the simplifying assumption that the mathematical description of the isodamage lines do converge to the knee point (Subramanyan, 1976; Fatemi and Yang, 1998).

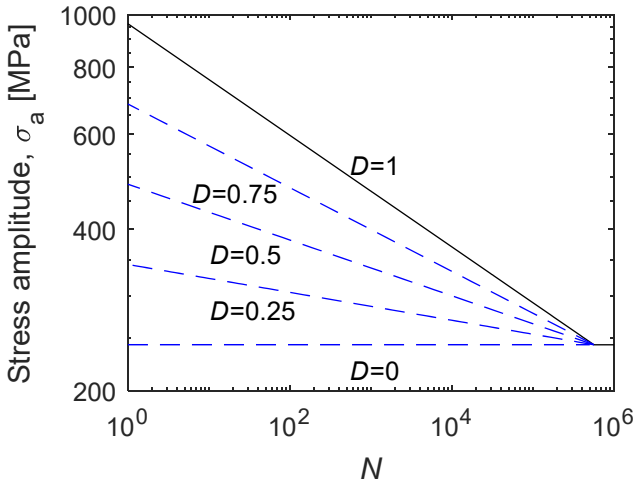


Figure 4.2a – Isodamage lines for soft SAE 4130 steel, by Equation (4.8)

We define a load step *i* as a load block containing $n_i$ cycles with constant stress amplitude $\sigma_i$. The accumulated damage due to load step *i* was in Subramanyan's model defined to be the ratio between the slope of an

isodamage line through this point ($n_i$, $\sigma_i$) in the *S-N* diagram, tan $\theta_i$, and the slope of the *S-N* curve, tan $\theta_f$ (Subramanyan, 1976);

$$D_i = \frac{\tan\theta_i}{\tan\theta_f} = \frac{\log N_e - \log N_i}{\log N_e - \log n_i} \tag{4.8}$$

Here, $N_e$ is the number of cycles at the knee point of the *S-N* curve, $n_i$ is the number of cycles with stress amplitude $\sigma_i$ applied in the load step $i$, and $N_i$ is the fatigue life for a constant stress amplitude $\sigma_i$.

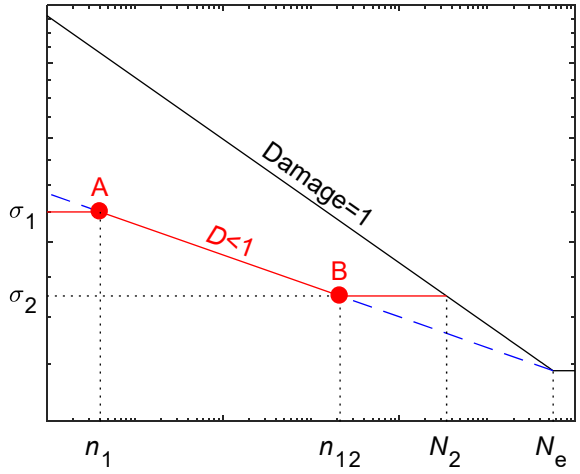


Figure 4.2b – Isodamage path for two-step cyclic loading from $\sigma_1$ to $\sigma_2$

When a new load step is applied, the damage introduced by the previous load step needs to be taken into account. This is done by following the isodamage line (Figure 4.2b) to the new stress amplitude. For a two-step cyclic loading, this makes it possible to model the $n_1$ load cycles experienced at stress amplitude $\sigma_1$ to be equivalent to $n_{12}$ cycles at stress amplitude $\sigma_2$. As it can be shown in Figure 4.2b, the points A and B are lying on the same isodamage line. Therefore, according to Equation (4.7) the damage for the point A is $D = \left(n_1 / N_1\right)^{m(\sigma_1)}$. For the point B, Equation

(4.7) yields $D = \left(n_{12}/N_2\right)^{m(\sigma_2)}$. Combination of these equations yields the equivalent number of cycles:

$$n_{12} = N_2 \cdot \left(\frac{n_1}{N_1}\right)^{\alpha_i} \tag{4.9}$$

where (Subramanyan, 1976)

$$\alpha_i = \frac{m\left(\sigma_i\right)}{m\left(\sigma_{i+1}\right)} = \frac{\log N_\mathrm{e} - \log N_{i+1}}{\log N_\mathrm{e} - \log N_i} \tag{4.10}$$

The remaining fatigue life at the second stress amplitude is then:

$$N_{2\mathrm{rem}} = N_2 - n_{12} \tag{4.11}$$

Let a cycle ratio be defined as $C_i = n_i/N_i$. In general, the remaining cycle ratio after a loading sequence containing $i$ steps may be calculated from the following formula (Subramanyan, 1976):

$$C_i = 1 - \left\{ C_{i-1} + \left[ C_{i-2} + \ldots + \left( C_2 + C_1^{\alpha_1} \right)^{\alpha_2} \ldots \right]^{\alpha_{i-2}} \right\}^{\alpha_{i-1}} \tag{4.12}$$

where $C_1$ to $C_{i-1}$ are the experienced cycle ratios at stress amplitudes $\sigma_1$ to $\sigma_{i-1}$, while $C_i$ is the estimated remaining cycle ratio for the last stress amplitude, $\sigma_i$.

In practice, cyclic loading histories are often irregular, with a continuously changing stress amplitude. However, cycle counting techniques may be used to convert an irregular load history to a series of load steps (Lee et al., 2005), allowing the above model to be used.

Fatemi and Yang (1998) note that Subramanyan's approach is not valid for stress amplitudes near the endurance limit of the material, both because *S-N* curves usually are nonlinear around the knee point, and

because you get a singularity at the knee point since all isodamage lines pass through this point.

## 4.3 The proposed model: Isodamage curves

As seen in the comparison with test data by Hashin and Rotem (1978), and mentioned by Lee et al. (2005), Subramanyan's model seems to be slightly non-conservative. This means that the model often predicts a longer remaining life than indicated by experimental two-step cyclic loading data. Therefore, a new damage accumulation model is proposed, in which nonlinear isodamage curves are used instead of isodamage lines. As an alternative to Equations (4.7) and (4.8), it is proposed that the fatigue damage due to load step $i$ may be described by the following expression:

$$D_i = \left( \frac{\tan\theta_i}{\tan\theta_\mathrm{f}} \right)^{q(\sigma_i)} = \left( \frac{\log N_\mathrm{e} - \log N_i}{\log N_\mathrm{e} - \log n_i} \right)^{q(\sigma_i)} \tag{4.13}$$

Here, the exponent $q(\sigma_i)$ is a function of the stress amplitude for the current load step $i$. The proposed model makes the isodamage curves nonlinear, while still conserving the main assumptions that $D_i(\theta_i = 0) = 0$ and $D_i(\theta_i = \theta_\mathrm{f}) = 1$. The function $q(\sigma_i)$ needs to be determined using experimental data. It is assumed that a function $q(\sigma_i)$ may be found, which is sufficiently accurate for a number of steels.

Note that in addition to the function $q(\sigma_i)$, the proposed model requires the full $S$-$N$ curve of the material, in order to find the constant-amplitude fatigue life $N_i$ for each stress amplitude $\sigma_i$, and also the knee point of the $S$-$N$ curve, $N_\mathrm{e}$. The model may be used regardless of whether the $S$-$N$ curve is linear in a log-log or semi-log diagram however.

### 4.3.1 Calculation of remaining fatigue life under two-step cyclic loading

As the new damage curves are not linear, a simple expression for the remaining fatigue life like Equation (4.12) cannot be used. When going from the first load step to the second, the damage remains the same, and we follow an isodamage path as shown in Figure 4.3:

$$D_1 = \left( \frac{\log N_e - \log N_1}{\log N_e - \log n_1} \right)^{q(\sigma_1)} = \left( \frac{\log N_e - \log N_2}{\log N_e - \log n_{12}} \right)^{q(\sigma_2)} \tag{4.14}$$

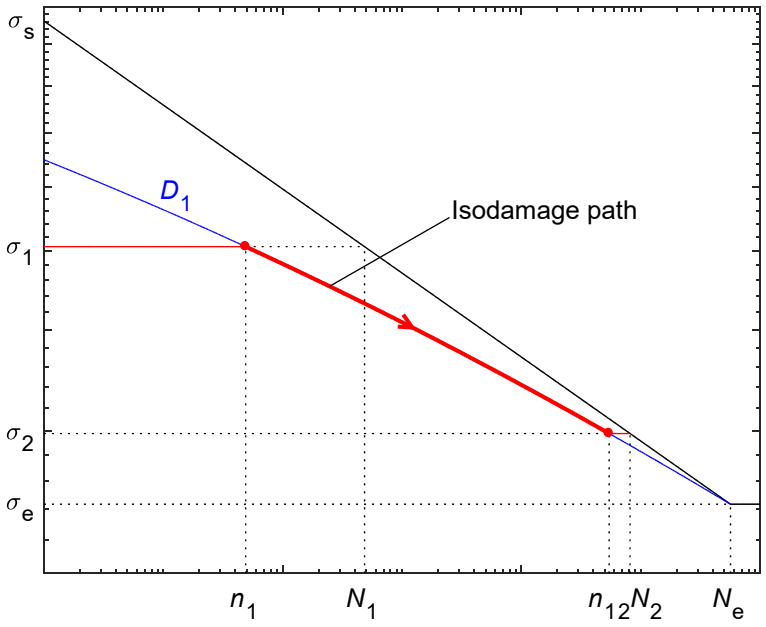


Figure 4.3 – Using the isodamage curve to find the remaining fatigue life under two-step cyclic loading

By reordering this equation, with respect to the equivalent number of experienced cycles at load step 2, the following expression is obtained:

$$\log n_{12} = \log N_e - \frac{\log N_e - \log N_2}{D_1^{\frac{1}{q(\sigma_2)}}} = \log N_e - \frac{\log N_e - \log N_2}{\left(\frac{\log N_e - \log N_1}{\log N_e - \log n_1}\right)^{\frac{q(\sigma_1)}{q(\sigma_2)}}} \quad (4.15)$$

The remaining fatigue life, if the component is subjected to the stress amplitude $\sigma_2$ for the rest of its life, is given by Equation (4.11). The estimated remaining cycle ratio may be found to be:

$$C_2 = \frac{N_2 - n_{12}}{N_2} \quad (4.16)$$

### 4.3.2 Calculation of remaining fatigue life under cyclic loading with multiple load steps

If the component is subjected to more than two load steps, the cumulative fatigue damage after the second load step is given as:

$$D_2 = \left( \frac{\log N_e - \log N_2}{\log N_e - \log\left(n_{12} + n_2\right)} \right)^{q(\sigma_2)} \quad (4.17)$$

This damage is then transferred to the third load step, in a similar way as described above.

The number of cycles at load step $i$ which is equivalent to all the previous cycles applied, may be expressed as:

$$\log n_{(i-1),(i)} = \log N_e - \frac{\log N_e - \log N_i}{D_{i-1}^{\frac{1}{q(\sigma_i)}}} \quad (4.18)$$

The cumulative damage up to and including load step $i$ may then be found by:

$$D_i = \left( \frac{\log N_e - \log N_i}{\log N_e - \log\left(n_{(i-1),(i)} + n_i\right)} \right)^{q(\sigma_i)} \tag{4.19}$$

The cumulative fatigue damage is calculated by first calculating the initial damage from Equation (4.14), followed by consecutive calculations by Equations (4.18) and (4.19) until $D_i = 1$, at which fatigue failure is estimated to occur.

## 4.4 Determination of the function $q(\sigma_i)$

Assuming that a general form for $q(\sigma_i)$ may be found, the experimental data for two-step fatigue tests of soft SAE 4130 steel, reported by Manson, Freche and Ensign (1967), were used to determine $q(\sigma_i)$. This data is clear, and includes the *S-N* curve for the actual test specimens, allowing easy interpretation of the fatigue life for any given stress amplitude, and vice versa. This data set is often used to test new cumulative damage theories, e.g. by Hashin and Rotem (1978). All the data are from two-step fatigue tests with a decreasing load.

The *S-N* curve for soft SAE 4130 steel, provided by Manson, Freche and Ensign (1967) is shown in a semi-log diagram. However, the curve is linear in a log-log diagram. The following representation of the *S-N* curve was found by a linear least-squares fit, based on the given data points:

$$\log \Delta\sigma = 3.2840 - 0.10374 \log N \tag{4.20}$$

Here, $\Delta\sigma = 2\sigma_a$ is the cyclic stress range, given in MPa. The endurance limit, given by the *S-N* curve, is $\sigma_e \approx 243.4$ MPa (stress amplitude), placing the knee point at $N_e \approx 5.6 \times 10^5$. This *S-N* curve, plotted for stress amplitude instead of stress range, is shown in Figure 4.2a.

In order to determine $q(\sigma_i)$, Equations (4.15) and (4.16) are combined, and the relation $n_1 = C_1 N_1$ is introduced, yielding:

$$C_2 = \frac{N_2 - 10^{\log N_e - \frac{\log N_e - \log N_2}{\left(\frac{\log N_e - \log N_1}{\log N_e - \log C_1 N_1}\right)^{\frac{q(\sigma_1)}{q(\sigma_2)}}}}}{N_2} \tag{4.21}$$

Solving this equation for $q(\sigma_1)/q(\sigma_2)$, we obtain:

$$\frac{q(\sigma_1)}{q(\sigma_2)} = \frac{\log \dfrac{\log N_e - \log N_2}{\log N_e - \log\left[(1-C_2)N_2\right]}}{\log \dfrac{\log N_e - \log N_1}{\log N_e - \log C_1 N_1}} \tag{4.22}$$

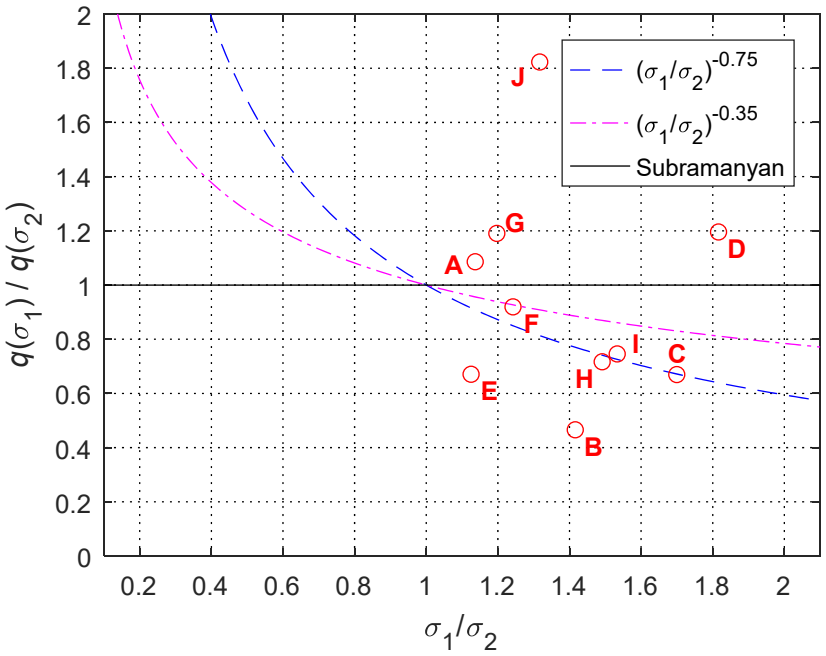


Figure 4.4 – Determination of $q(\sigma_i)$ from experimental data of SAE 4130 steel. Letters A–J refer to the experimental data, as shown in Figure 4.6

For all the data points for soft SAE 4130 steel given by Manson, Freche and Ensign (1967), 58 in total, defined by $N_1$, $N_2$, experienced $C_1$ and $C_2$, this fraction was calculated. For a given $\sigma_1/\sigma_2$ ratio, the resulting $q(\sigma_1)/q(\sigma_2)$ ratio was evaluated repeatedly applying Equation (4.22) for the different tested cycle ratios $C_1$ and $C_2$, to finally calculate the mean value for each $\sigma_1/\sigma_2$ ratio. These values are shown in Figure 4.4, and are mean values of the SAE 4130 data from Manson, Freche and Ensign (1967), which are also shown in Figure 4.6. The unbiased sample variances of this averaging operation for data sets A through J are equal to 0.044, 0.019, 0.037, 0.12, 0.031, 0.21, 0.10, 0.031, 0.041 and 0.58, respectively. There was not found any systematic dependency of applied cycle ratios $C_1$ and $C_2$ for the ratio $q(\sigma_1)/q(\sigma_2)$.

The data points in Figure 4.4 do not show any clear trend. However, by comparing Figure 4.4 with Figure 10 in Hashin and Rotem (1978) (see also Figure 4.6 here), it is observed that Subramanyan's model is non-conservative for the data points lying below the straight line $q(\sigma_1)/q(\sigma_2) = 1$. Therefore, a more conservative model may be obtained if a curve is fitted closer to the lower data points in Figure 4.4.

It is chosen to fit a power function to the data; $q(\sigma_i) = (a\sigma_i)^b$, as it then will be easy to separate the numerator of $q(\sigma_1)/q(\sigma_2)$ from the denominator. $a$ and $b$ may be material-dependent. Direct least-square curve fitting of the data points shown in Figure 4.4 to a power function yields the expression $q(\sigma_1)/q(\sigma_2) = 0.99(\sigma_1/\sigma_2)^{-0.36} \approx (\sigma_1/\sigma_2)^{-0.35}$, indicated by the dash-dotted curve in Figure 4.4. However, this representation is not very much more conservative than Subramanyan's model, as more than half the data points still lie below the curve. Taking this into account, the following curve was found to fit the data points in better agreement to the intention of the modification:

$$\frac{q(\sigma_1)}{q(\sigma_2)} = \left(\frac{\sigma_1}{\sigma_2}\right)^{-0.75} = \frac{(a\sigma_1)^{-0.75}}{(a\sigma_2)^{-0.75}} \tag{4.23}$$

This curve is indicated by the dashed curve in Figure 4.4.

The coefficient $a$ in Equation (4.23) may be calculated by taking the local evolution of material parameters like ductility or hardness during the fatigue damage accumulation into account (Pavlou, 2002; Yuan et al., 2013; Santecchia et al., 2016). This way, the accumulated damage $D_i$ may be related to the evolution of a measurable quantity. However, as shown in Equations (4.18), (4.19) and (4.21), only the ratio $q(\sigma_{i-1})/q(\sigma_i)$ is required to calculate the remaining fatigue life; therefore the value of $a$ does not matter in the calculation. For illustrative purposes (see Figure 4.5), the coefficient $a$ has been assigned the value $2/\sigma_s$, where $\sigma_s$ is the stress at which the straight $S$-$N$ curve intersects the stress axis. This value for the coefficient makes a single loading of amplitude $\sigma_s/2$ cause an accumulated damage of 0.5. The proposed function has therefore been found to be:

$$q(\sigma_i) = (a\sigma_i)^b = \left(\frac{2\sigma_i}{\sigma_s}\right)^{-0.75} \tag{4.24}$$

It is assumed that the value $b = -0.75$ will give satisfying results for many different steel grades, in which case the proposed model would be easily applicable. This assumption is tested in Section 4.6.

## 4.5 Visualization of the new isodamage curves

An illustration of the isodamage curves proposed in this work is shown in Figure 4.5. The deviation from straight lines is small, but significant. By comparison with Figure 4.2, it is observed that the proposed isodamage curves have a steeper angle near the knee point of the $S$-$N$ curve, and a lower angle for low values of $N$. This makes the high stresses cause higher damage than if straight isodamage lines are used as the damage indicator.

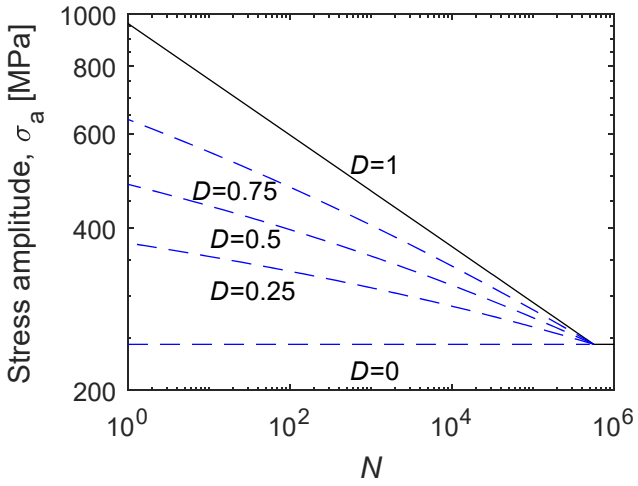


Figure 4.5 – Isodamage curves for soft SAE 4130 steel, by Equations (4.13) and (4.24).

In Figure 4.6, the remaining cycle ratio estimated by the proposed model is compared to the experimental data for two-step cyclic loading of soft SAE 4130 steel from Manson, Freche and Ensign (1967). Similar estimations based on Subramanyan's (1976) model, the double linear rule from 1981 (Manson and Halford, 1981), Shang and Yao's (1999) model and the sequential rule by Mesmacque et al. (2005) are also presented. The Palmgren-Miner rule would represent a straight line from $(1, 0)$ to $(0, 1)$ (Manson, Freche and Ensign, 1967; Hashin and Rotem, 1978), and all the five newer models suit the experimental data better. As expected, the proposed model is more conservative than Subramanyan's model.

For some loading programs, like those marked B and E, the proposed model is still non-conservative. This is in agreement to the observations made of Figure 4.4, where points B and E are far below the proposed curve. Another choice of exponent in Equations (4.23) and (4.24) could have brought the curve down to points B and E, but then the model would be very conservative for cases D and J. In order to determine a better value for the exponent, more tests for only a few loading programs

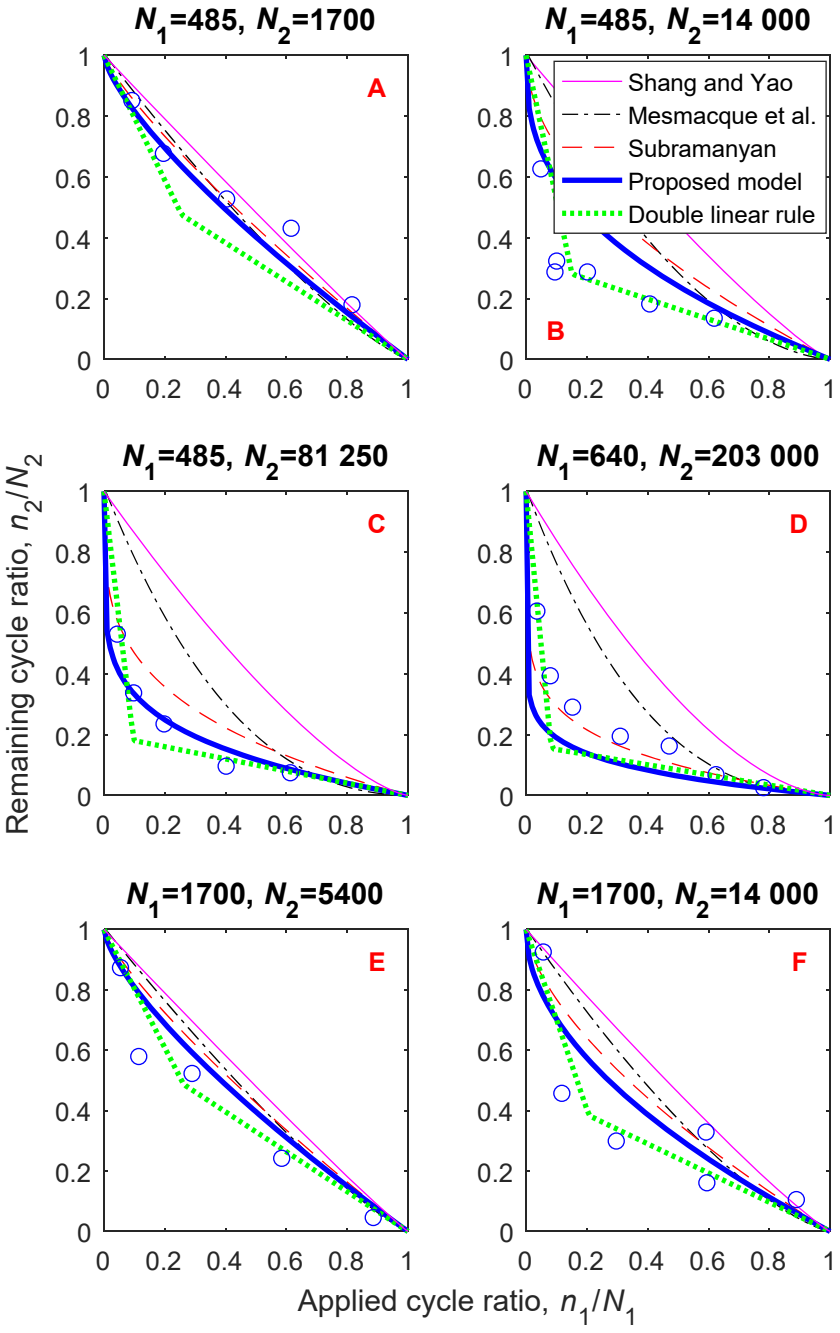


Figure 4.6a – Comparison of predicted fatigue life with experimental data for two-step cyclic loading of soft SAE 4130 steel. Data from Manson, Freche and Ensign (1967)

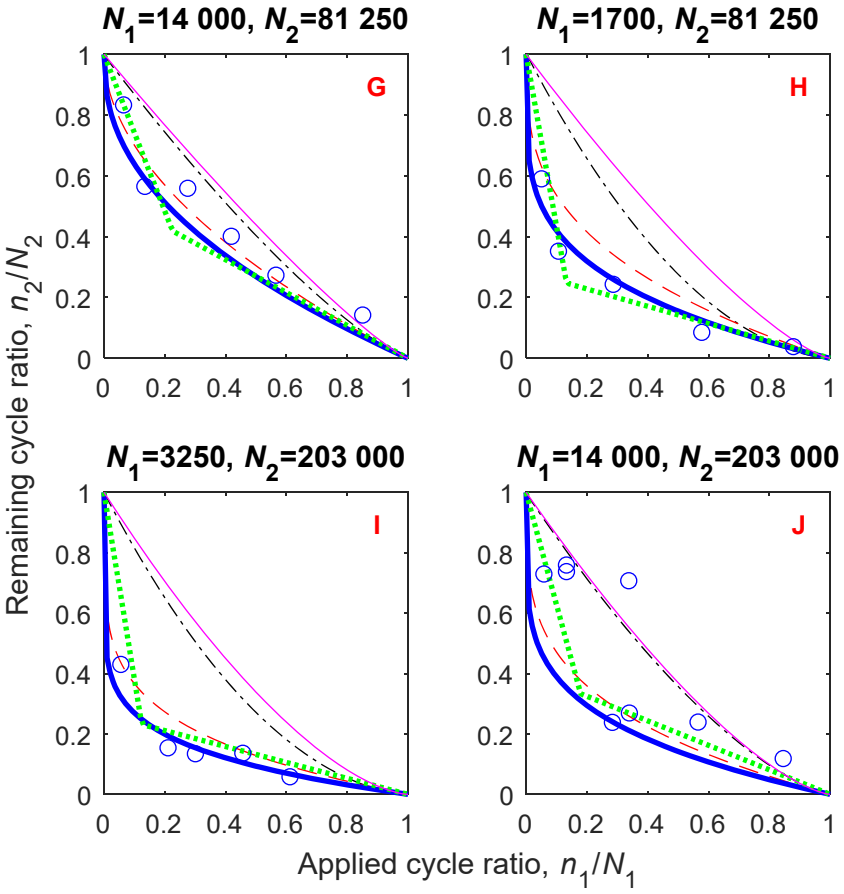


Figure 4.6b – Comparison of predicted fatigue life with experimental data for two-step cyclic loading of soft SAE 4130 steel. Data from Manson, Freche and Ensign (1967)

should be conducted, making it possible to quantify the scatter of the data. For instance, for loading sequence F, the experimental values show that an initial cycle ratio $C_1 \approx 0.60$ may give a remaining cycle ratio of $C_2 \approx 0.16$ or $C_2 \approx 0.33$. Similarly, for loading sequence J, $C_1 \approx 0.34$ gives both $C_2 \approx 0.27$ and $C_2 \approx 0.70$, indicating a significant scatter. As only one value of $C_2$ is given for most of the remaining loading histories, it is not known to what degree that value is representative for that specific loading history.

It is noted that in most cases both the proposed model and Subramanyan's (1976) model are more conservative, and give improved estimations compared to both Shang and Yao's (1999) model and the sequential law by Mesmacque et al. (2005). These two models are close to the other models when the difference between the load amplitudes is low (loading sequences A, E and F), but quickly become non-conservative when the difference becomes higher. In the current work, multiaxial fatigue has not been investigated, in which case the sequential law may perform better, but previous studies do also indicate deviations between the sequential law and experimental data (Siriwardane et al., 2009).

## 4.6 Comparison with test data

As Equation (4.24) was determined using the experimental SAE 4130 data, it was expected that the proposed model would give improved estimations compared to Subramanyan's model for this particular data set. It is therefore important to compare the proposed model to other data sets. The same value for the model parameter in Equation (4.24), $b = -0.75$, has been used for all the estimations. As discussed in Section 4.4, the value of $a$ is not needed for the calculations.

### 4.6.1 C-35 steel

In Figure 4.7, the model is compared to experimental data from two-step cyclic loading of C-35 steel, reported by Subramanyan (1976). The proposed model is observed to be slightly more conservative than Subramanyan's model for an increasing load amplitude, and slightly less conservative for a decreasing load amplitude. The difference between the two models is not significant when comparing them to these data. The sequential law shows poor performance however, presumably because the *S-N* curve for C-35 steel is linear in a semi-log diagram, while the sequential law was originally only tested for *S-N* curves which are linear

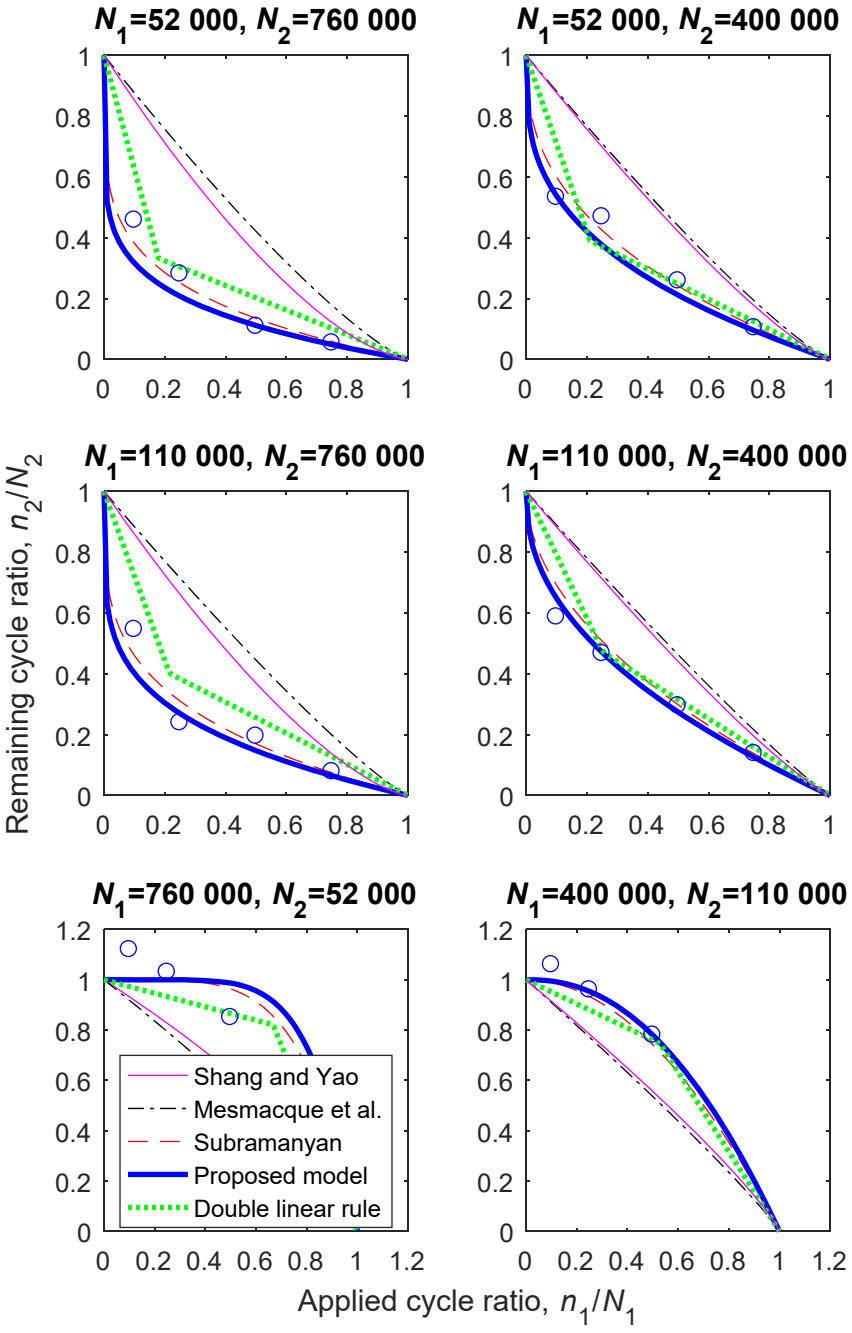


Figure 4.7 – Comparison of predicted fatigue life with experimental data for two-step cyclic loading of C-35 steel. Data from Subramanyan (1976)

in a log-log diagram. Shang and Yao's model is slightly closer to the experimental results, compared to the sequential law.

It is noteworthy that in the two plots in Figure 4.7 where $N_2$ = 760 000, the proposed model is even less non-conservative than the double linear rule by Manson and Halford (1981). For the four other plots, the estimations by these two models are quite similar to each other.

### 4.6.2 P355NL1 steel

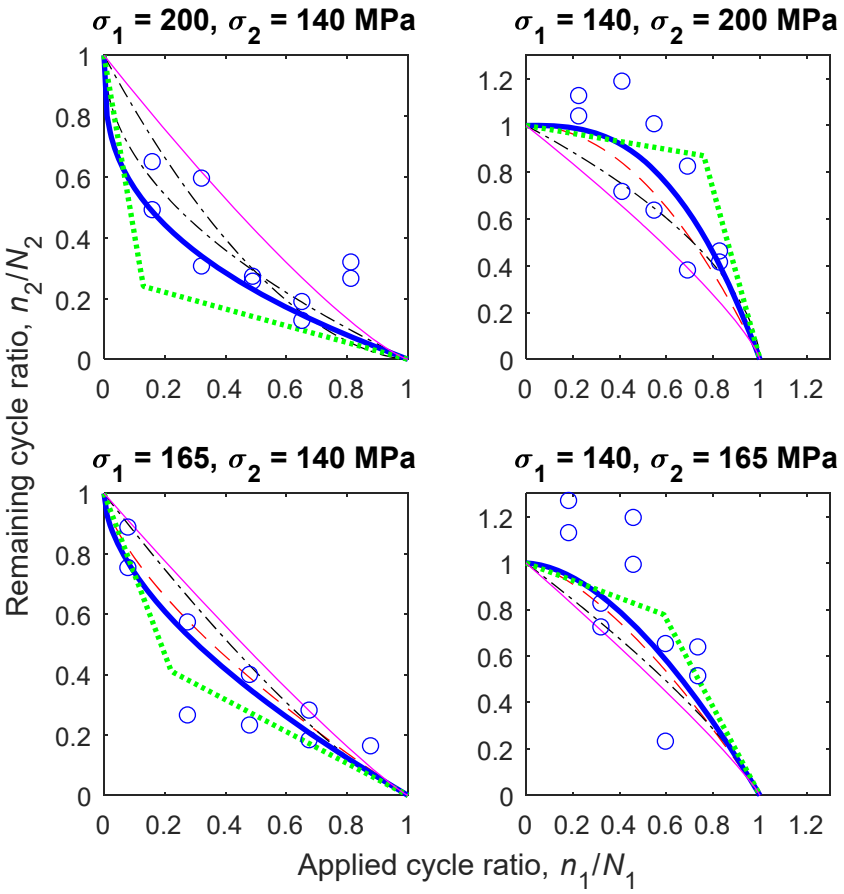


Figure 4.8 – Comparison of predicted fatigue life with experimental data for two-step cyclic loading of P355NL1 steel. Data from Pereira et al. (2008). For legend, see Figure 4.7

A comparison between predicted and experimentally observed fatigue life for the pressure vessel steel grade P355NL1 is shown in Figure 4.8. In this data set, two equal specimens have been tested for each value of $C_1 = n_1/N_1$. In 18 of 19 cases, the proposed model estimates a remaining life either between the two experimental results, or lower than both the experimental results, for a given value of $C_1$, indicating good agreement.

### 4.6.3 300 CVM maraging steel

There are few additional clear data sets which also report the full *S-N* curve for the test specimens. In general, the *S-N* curve will depend on the mean stress during the cyclic load, and the geometry and surface finish of the specimen, etc. (Boyer, 1986). Therefore, the *S-N* curve corresponding to the actual test specimens is required, in order to further verify the model for other materials.

In lack of other good data sets, the model has been compared to experimental data from two-step fatigue tests of 300 CVM maraging steel, reported by Manson, Freche and Ensign (1967). However, the *S-N* curves for these specimens are not shown beyond $N = 10^6$, and the knee point of the curves is not shown. The *Atlas of Fatigue Curves* (Boyer, 1986) indicates that the knee point of the *S-N* curve for smooth bars of grade 300 maraging steel lies approximately at $N_e = 10^7$. In order to obtain an indication of the performance of the proposed model, it has been assumed that the knee point for the test specimens also lies at $N_e = 10^7$, and that the *S-N* curve may be linearly extrapolated to this value in a log-log diagram. Estimated fatigue lives based on this assumption are illustrated in Figure 4.9. If $N_e$ is lower than $10^7$, the estimations for high to low stress histories become a little less non-conservative. If $N_e$ is higher than $10^7$, they become a little more non-conservative.

Overall, Figure 4.9 indicates that the proposed model has improved the estimations of the Palmgren-Miner rule, Subramanyan's model, Shang and Yao's model and the sequential law. The proposed model still gives

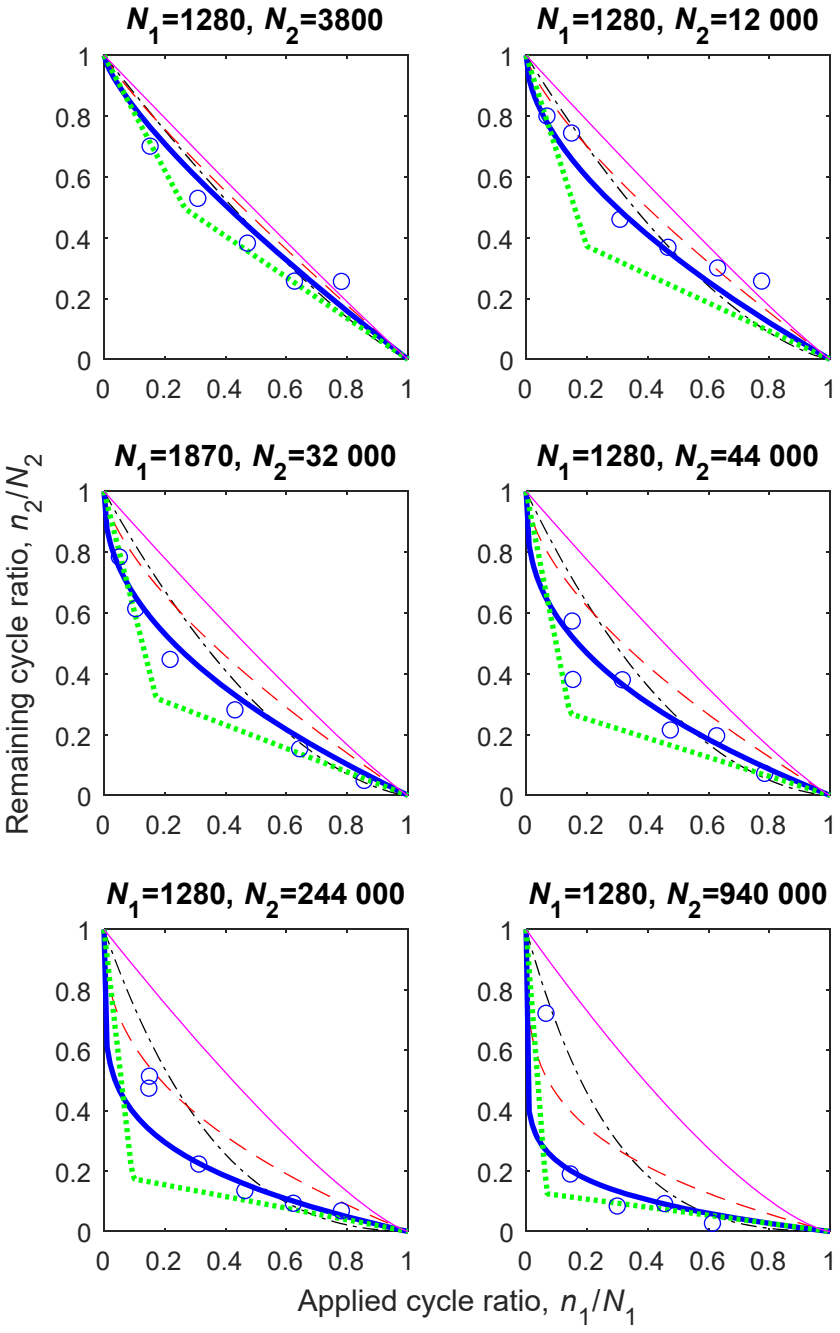


Figure 4.9a – Comparison of predicted fatigue life with experimental data for two-step cyclic loading of 300 CVM maraging steel. Data from Manson, Freche and Ensign (1967)

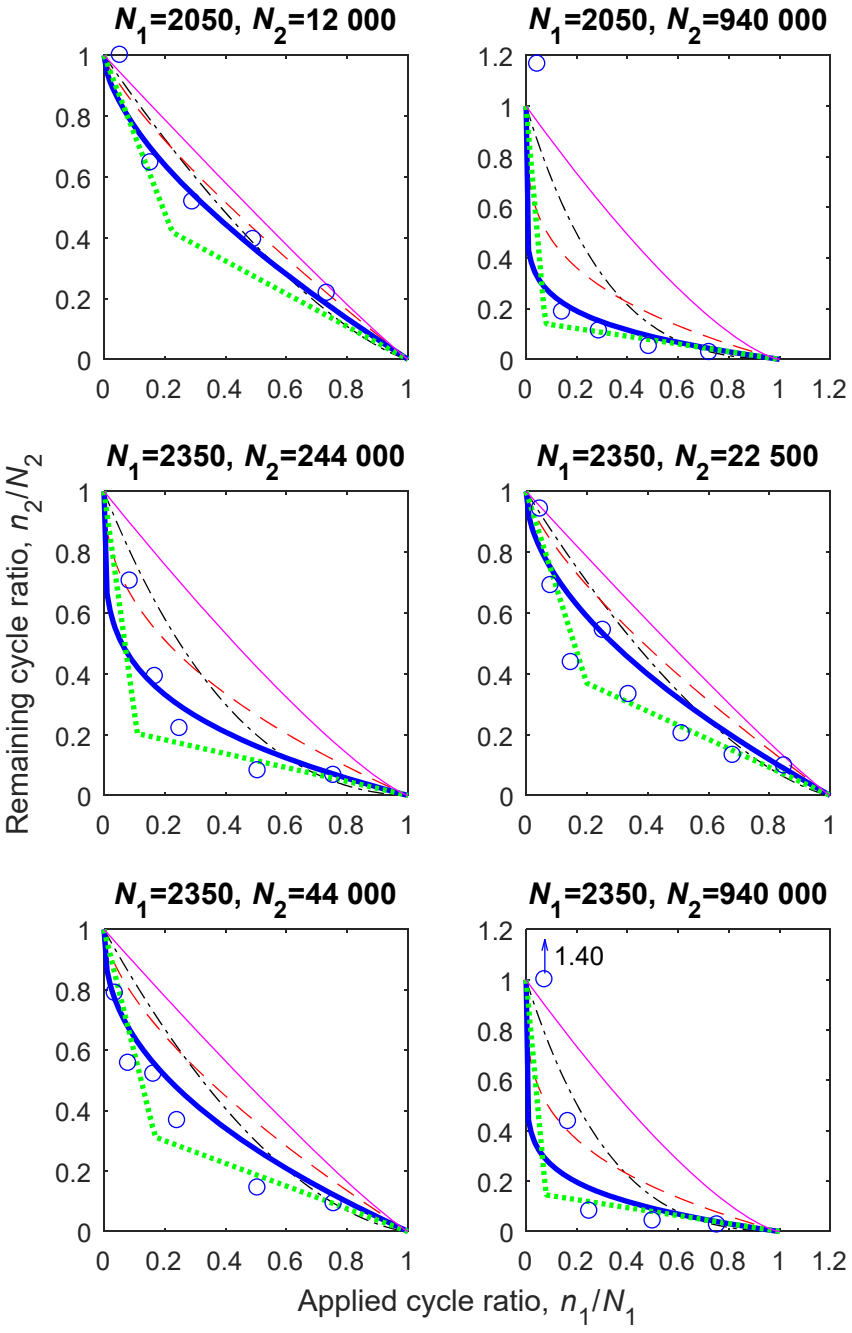


Figure 4.9b – Comparison of predicted fatigue life with experimental data for two-step cyclic loading of 300 CVM maraging steel. Data from Manson, Freche and Ensign (1967)

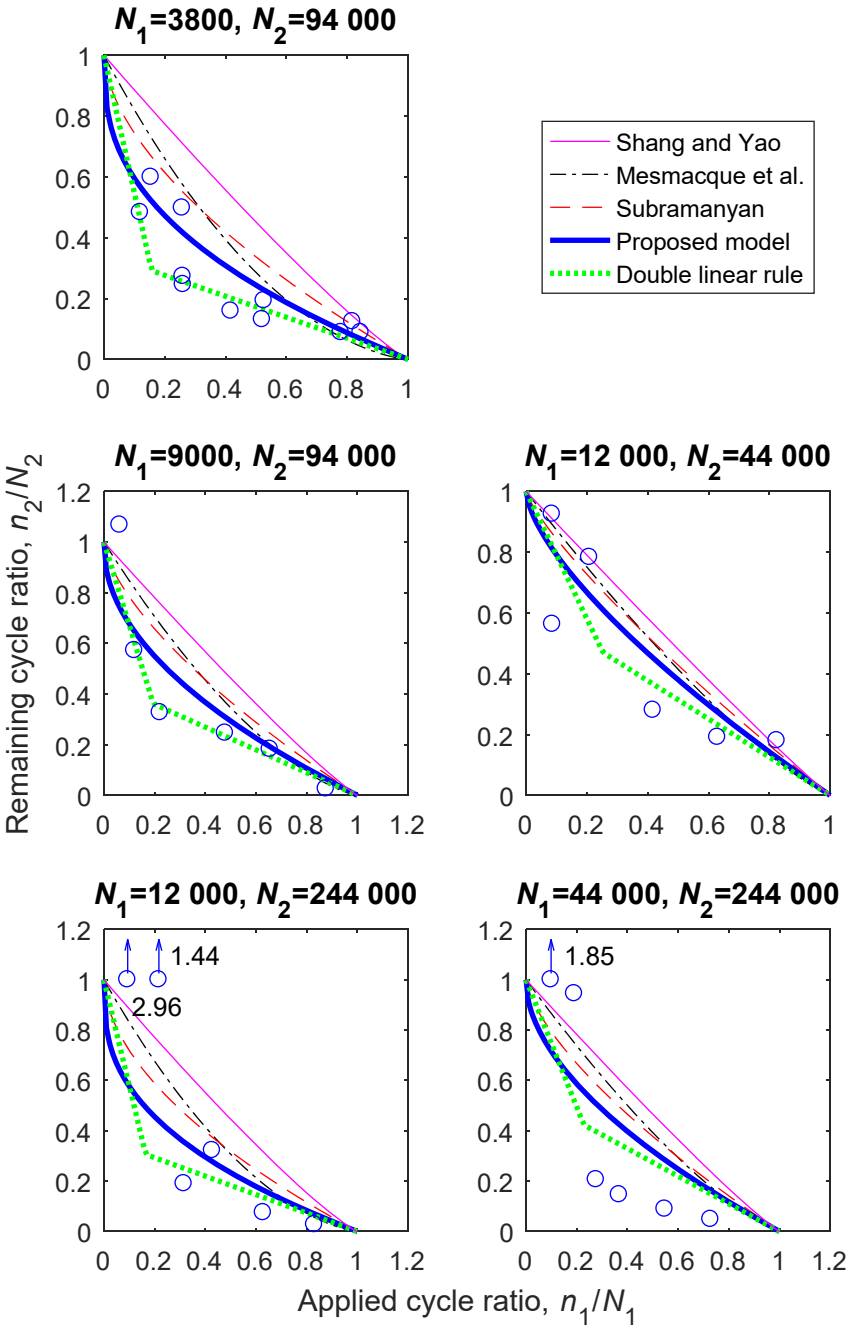


Figure 4.9c – Comparison of predicted fatigue life with experimental data for two-step cyclic loading of 300 CVM maraging steel. Data from Manson, Freche and Ensign (1967)

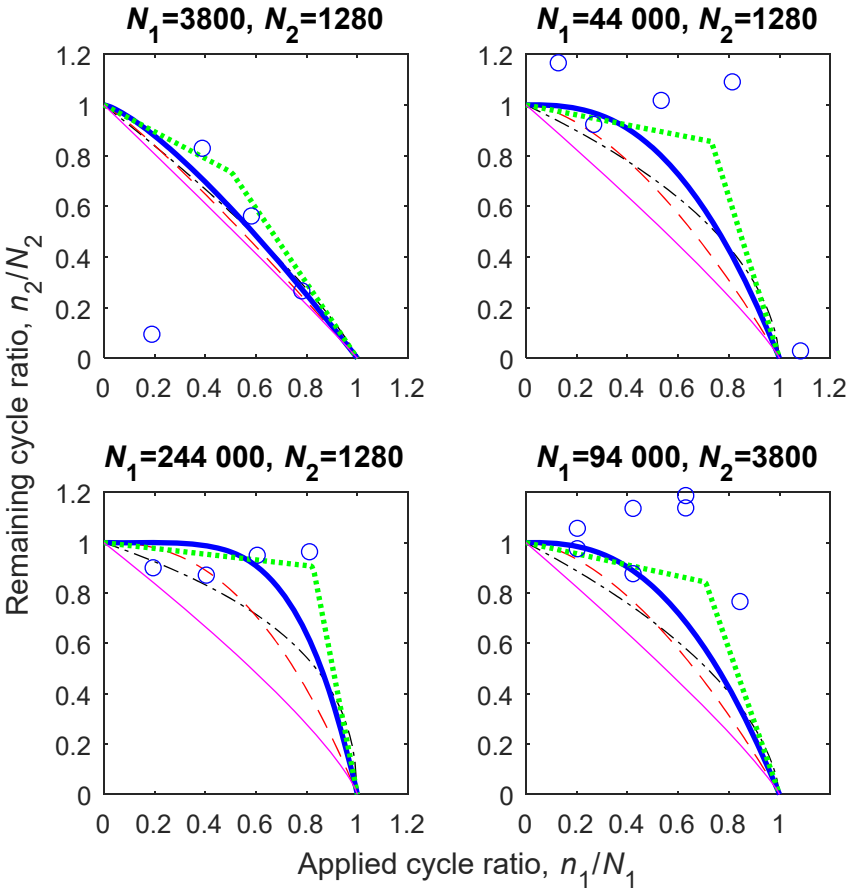


Figure 4.9d – Comparison of predicted fatigue life with experimental data for two-step cyclic loading of 300 CVM maraging steel. Data from Manson, Freche and Ensign (1967)

a little optimistic estimates in many of the tests, especially for the high to low stress histories with high initial life (Figure 4.9c). The double linear damage rule generally gives safer estimations. However, for the low to high stress histories, the estimations by the double linear damage rule and the proposed model are comparable.

The problem of the Palmgren-Miner rule is that the experienced cumulative fatigue damage at failure usually is less than one for high to low stress histories, and greater than one for low to high stress histories (Manson and Halford, 1981), while the rule predicts fatigue failure when

the cumulative damage is equal to one. For the experimental data considered in the current work, the experienced cumulative damage at fatigue failure, calculated by the Palmgren-Miner rule, is less than one in 91 % of the high-to-low loadings, and greater than one in 96 % of the low-to-high loadings. If calculated by the proposed model, these ratios become 51 % and 67 %, respectively. This shows that this bias is greatly reduced by the proposed model, as also observed in Figures 4.6–4.9.

## 4.7 Discussion

The comparison of the proposed model with other, comparable models, and experimental data, shows that the proposed model is able to predict the cumulative fatigue damage accumulation quite well. For the soft SAE 4130 steel (high-to-low loading), the estimations by the proposed model are more conservative than Subramanyan's model containing isodamage lines. The same trend was also observed for the high-to-low loading tests for the other materials, especially for the 300 CVM maraging steel. For the low-to-high loading tests, the proposed model is less conservative than Subramanyan's model, but the estimations are often closer to the majority of the experimental values. However, compared to the high amount of scatter in the low-to-high loading tests, the difference between the proposed model and Subramanyan's model is not very significant for these tests.

Furthermore, it has been shown that the predictions by the proposed model in general are closer to the experimental data considered, than equivalent predictions by the Palmgren-Miner rule, Shang and Yao's model and the sequential law.

The proposed model is comparable to the double linear damage rule, in terms of agreement with the experimental data. When applied to the C-35 steel, the proposed model tends to give less non-conservative estimations of the remaining fatigue life, while the double linear damage rule gives safer estimations when applied to the 300 CVM maraging steel.

However, as the knee point for the *S-N* curve for the 300 CVM test specimens had to be assumed, some uncertainty is related to the estimations based on the proposed model. Taking this uncertainty into account, the estimations by the proposed model seem acceptable.

Based on the *S-N* curves, it was possible to find a function $q(\sigma_i)$ yielding good prediction of experimental results for four different steels, using a single value for the model parameter, $b = -0.75$. This indicates that a general function $q(\sigma_i)$ may be used for cumulative fatigue damage for most steels, but evaluation of further experimental data is needed, in order to draw any conclusions. As the function is semi-empirical, there is no guarantee that it will perform well for all materials, and further tests of other materials are therefore required. As previously mentioned in Section 4.5, the scatter in the experimental data is also very large. It would therefore be interesting to perform a more systematic test program, where only a couple of stress amplitude levels were used, but where many more specimens were tested for the same combination of loading. This way it would be clearer whether the proposed model is able to represent the average fatigue behaviour of the material.

When determining the function $q(\sigma_i)$, it is also important to keep in mind whether one wants the cumulative fatigue damage model to fit the mean of the experimental data, or whether one wants it to be conservative, and in that case to what degree. When designing or evaluating real structures the *S-N* curves given in standards are used, and those are already quite conservative. For example, the *S-N* curves given in DNVGL-RP-C203 are associated with a 97.7 % probability of survival (DNV GL, 2016). If the conservatism in the cumulative damage rule is very high, you may end up with overly pessimistic fatigue life estimations. That is part of the reason why the model parameter $b$ of Equation (4.24) was not chosen to always estimate a longer fatigue life than the experiments show.

In this work, the proposed model has only been compared to two-step cyclic loading histories of specimens subjected to a uniaxial stress state.

In order to further verify the model, it should also be compared to experimental data based on more complex loading histories, and multiaxial fatigue.

The proposed model may be used regardless of whether the *S*-*N* curve is linear in a log-log or semi-log diagram. In Figure 4.7, it was seen that the sequential law yields poor estimates when the *S*-*N* curve is linear in a semi-log diagram. As *S*-*N* curves of both types exist, a cumulative damage model should be able to handle both types equally well.

One minor disadvantage of the proposed model is its need for consecutive calculation of Equations (4.18) and (4.19). This makes the calculation of the fatigue life due to a real-life loading history, in which the stress amplitude varies a lot, more tedious than the use of Subramanyan's model or the Palmgren-Miner rule, in which case simple expressions may be used (e.g. Equation (4.12)). However, the calculation process is not more complicated than that of the sequential law.

Another significant disadvantage of the proposed model is the need to know the knee point of the *S*-*N* curve. As we experienced in Section 4.6.3, the endurance limit for test specimens is not always given. This complicates the verification of the model. In addition, some materials, e.g. most nonferrous metals do not exhibit a clear endurance limit. Instead, their *S*-*N* curves continue to drop at a slow rate for high values of *N* (Boyer, 1986), making the proposed model unusable. Furthermore, the *S*-*N* curves in design standards, e.g. Standards Norway (2010) and DNV GL (2016), are often divided into two linear portions, each with a different slope, while the proposed model is based on *S*-*N* curves with a constant slope. Investigation of how the proposed model may be modified to suit bilinear *S*-*N* curves is proposed for further studies. With such a model, it may be possible to also model materials without a clear endurance limit.

## 4.8 Conclusions

A new cumulative fatigue damage model has been developed, based on the concept of isodamage curves. Only the *S*-*N* curve of the material, including the knee point of the curve, is needed to use the model. The comparison with experimental data has shown that a single expression for the empirical function $q(\sigma_i)$ is usable for four different steels. Comparison with further experimental results is still required, in order to optimize the function $q(\sigma_i)$, and to check how well the same function applies to other materials.

## Acknowledgements

This work was supported by the Norwegian Ministry of Education and Research.

# 5 Paper III: A review of fatigue crack propagation modelling techniques using FEM and XFEM

[*]Kristen Rege, Hirpa G. Lemu

Department of Mechanical and Structural Engineering and Materials Science, University of Stavanger, Norway

**Abstract:** Fatigue is one of the main causes of failures in mechanical and structural systems. Offshore installations, in particular, are susceptible to fatigue failure due to their exposure to the combination of wind loads, wave loads and currents. In order to assess the safety of the components of these installations, the expected lifetime of the component needs to be estimated. The fatigue life is the sum of the number of loading cycles required for a fatigue crack to initiate, and the number of cycles required for the crack to propagate before sudden fracture occurs. Since analytical determination of the fatigue crack propagation life in real geometries is rarely viable, crack propagation problems are normally solved using some computational method. In this review the use of the finite element method (FEM) and the extended finite element method (XFEM) to model fatigue crack propagation is discussed. The basic techniques are presented, together with some of the recent developments.

[*] Previously published as: Rege, K. and Lemu, H.G. (2017) A review of fatigue crack propagation modelling techniques using FEM and XFEM, *IOP Conference Series: Materials Science and Engineering*, 276, 012027. doi: 10.1088/1757-899X/276/1/012027

## 5.1 Introduction

Components which are subjected to fluctuating loads are found virtually everywhere: Vehicles and other machinery contain rotating axles and gears, pressure vessels and piping may be subjected to pressure fluctuations (e.g. water hammer) or repeated temperature changes, structural members in bridges are subjected to traffic loads and wind loads, while those in ships and offshore structures are subjected to the combination of wind loads, wave loads and currents. If the components are subjected to a fluctuating load of a certain magnitude for a sufficient amount of time, small cracks will nucleate in the material. Over time, the cracks will propagate, up to the point where the remaining cross-section of the component is not able to carry the load, at which the component will be subjected to sudden fracture (Boyer, 1986). This process is called fatigue, and is one of the main causes of failures in structural and mechanical components (Suresh, 1998). In order to assess the safety of the component, engineers need to estimate its expected lifetime. The fatigue life is the sum of the number of loading cycles required for a fatigue crack to nucleate/initiate, and the number of cycles required for the crack to propagate until its critical size has been reached (Suresh, 1998; Zhan et al., 2017). In this paper, computational methods to estimate the lifespan of a propagating crack whose initial geometry is known will be considered.

Estimations of the fatigue crack propagation rate, d$a$/d$N$, are normally based on a relation with the range of the stress intensity factor, $\Delta K$, which is a linear elastic fracture mechanics (LEFM) parameter for quantifying the load and geometry of the crack. Paris, Gomez and Anderson (1961) first proposed the existence of such a relation in 1961, and its simplest form is the Paris law (Paris and Erdogan, 1963):

$$\frac{\mathrm{d}a}{\mathrm{d}N} = C\Delta K^m \tag{5.1}$$

where $a$ is the length of an edge crack (or half the length of an internal crack), $N$ is the number of loading cycles, and $C$ and $m$ are scaling constants. Due to its simplicity, the Paris law is only applicable for intermediate values of $\Delta K$ (region II in Figure 5.1), under constant amplitude cyclic loading (Anderson, 2005). Furthermore, the constants $C$ and $m$ are influenced by the applied stress ratio $R = K_{\min}/K_{\max}$, and crack closure effects are not taken into account. Therefore, a number of different crack propagation laws have been proposed, each one taking different factors into account (Kłysz and Leski, 2012). One of the most detailed and commonly used is the so-called NASGRO equation (Forman and Mettu, 1992):

$$\frac{\mathrm{d}a}{\mathrm{d}N} = C\left[\frac{(1-f)}{(1-R)}\cdot\Delta K\right]^{m}\cdot\frac{\left(1-\dfrac{\Delta K_{\mathrm{th}}}{\Delta K}\right)^{p}}{\left(1-\dfrac{K_{\max}}{K_{\mathrm{c}}}\right)^{q}} \tag{5.2}$$

where $\Delta K_{\mathrm{th}}$ is the threshold value for fatigue crack propagation, $K_{\mathrm{c}}$ is the critical stress intensity factor at which fracture occurs, $\Delta K = K_{\max} - K_{\min}$,

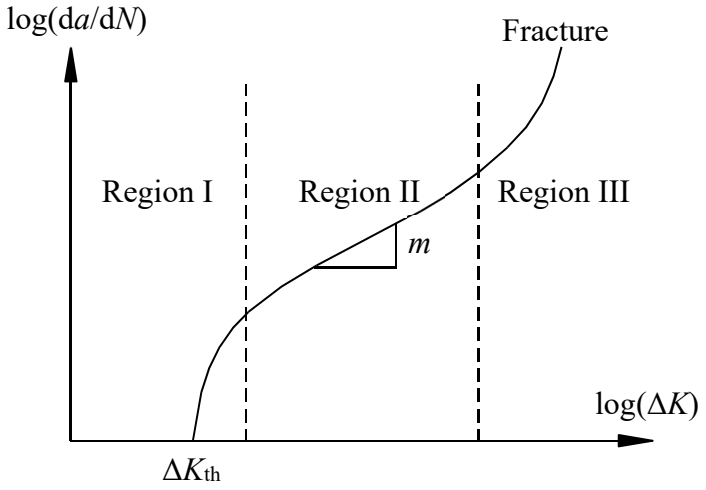


Figure 5.1 – Typical fatigue crack growth curve

$R = K_{min}/K_{max}$, $f$ is a crack opening function and $C$, $m$, $p$ and $q$ are empirical constants. Note that for a given material, $C$ and $m$ do not have the same numerical values in different crack propagation laws.

The loading and displacement of a crack can be described by the three modes of fracture, each with its own stress intensity factor; mode I (tensile opening, $K_I$), mode II (in-plane sliding, $K_{II}$) and mode III (tearing/out-of-plane shear, $K_{III}$) (Anderson, 2005). The different modes require different values for the constants in the crack propagation law. In the case of mixed-mode fatigue, it may be necessary to use an effective mixed-mode stress intensity factor (Alegre and Cuesta, 2010), for instance as given by Tanaka (1974), or a modified crack propagation law (Pavlou et al., 2003).

The crack propagation life can be estimated by integrating Equation (5.1) or (5.2). However, the stress intensity factors $K_{max}$ and $K_{min}$ are normally functions of the crack length $a$, and depend on the geometry of the structure. Analytical integration of Equations (5.1) and (5.2) is therefore rarely viable for complicated geometries. Instead, crack propagation problems are normally solved using some computational method, e.g. the Finite Element Method (FEM) (Colombo and Giglio, 2006). The crack propagation process is then solved in a step-wise manner. For each step, the crack is advanced a small length, and the number of cycles required for the next crack increment is estimated using one of the crack propagation laws. In order to accomplish this, the computational method needs to perform the following tasks within each step (Colombo and Giglio, 2006; Peng et al., 2017):

1. Computation of the minimum and maximum stress and displacement fields within the cracked component.
2. Evaluation of the minimum and maximum stress intensity factors for the crack.
3. Evaluation of the direction for further crack propagation.
4. Generation of a representation of the crack advancement.

This process is repeated until the critical stress intensity factor is reached; $K_{max} = K_c$, and the number of experienced cycles are summed to obtain the crack propagation life.

The main challenge when using the finite element method to estimate the fatigue crack propagation, lies in the fourth task in the list above (Colombo and Giglio, 2006). In order to evaluate stress intensity factors for the advanced crack, the finite element mesh needs to be updated, a process which has been shown to be challenging (Anderson, 2005). This has led to the development of alternative computational methods to handle propagating cracks, among them the eXtended Finite Element Method (XFEM) (Belytschko and Black, 1999; Fries and Belytschko, 2010), the Boundary Element Method (BEM) (Mi and Aliabadi, 1994), hybrids between finite and boundary element methods, e.g. the Symmetric Galerkin Boundary Element Method – Finite Element Method (SGBEM-FEM) (Nikishkov, Park and Atluri, 2001) and the scaled boundary finite element method (Yang, 2006), and meshless methods (Bordas, Rabczuk and Zi, 2008).

In this review, the use of the finite element method (FEM) and the extended finite element method (XFEM) to model fatigue crack propagation will be discussed. The basic techniques will be presented, together with some of the recent developments. The review will focus on the modelling techniques, and only to a less extent on their applications.

## 5.2 Crack propagation by the finite element method

### 5.2.1 Computation of stress and displacement fields, and the stress intensity factor

The first issue when estimating fatigue crack propagation rates using the finite element method is the computation of sufficiently accurate values for the stress intensity factor for the crack at the maximum and minimum applied loads during each cycle. In order to compute the stress intensity factor, the stress and displacement fields of the whole component are also needed. Three simple methods for computing the stress intensity factors of mode I cracks from a finite element stress field were presented by Chan, Tuba and Wilson (1970) already in 1970. These methods were called the stress method, the displacement method and the line integral method, and were all computed using ordinary linear (constant-strain) triangle elements, with a high degree of refinement at the crack tip.

#### 5.2.1.1 The stress method

In the stress method, nodal stress values are extrapolated to the crack tip. It is often easiest to do this extrapolation along the crack plane, in which case the stress intensity factor is related to the stress normal to the crack plane, $\sigma_{yy}$, by (Anderson, 2005):

$$K_{\mathrm{I}} = \lim_{r \to 0} \left[ \sigma_{yy} \sqrt{2\pi r} \right] \tag{5.3}$$

where $r$ is the distance from the crack tip. The nodal values of $K_{\mathrm{I}}$ are plotted as a function of $r$, and extrapolated to $r = 0$. As ordinary finite elements are not able to represent the stress singularity at the crack tip, the nodal values of $K_{\mathrm{I}}$ closest to the tip should be omitted when performing the extrapolation (Chan, Tuba and Wilson, 1970). The singularity of the stress field also causes this method to be one of the

least accurate methods available (Anderson, 2005). A similar approach is also possible for mode II and mode III cracks.

#### 5.2.1.2 The displacement method

The second method is called the displacement method, and involves a relation between the stress intensity factor and the crack-opening displacement $u_y$ (Chan, Tuba and Wilson, 1970). For mode I loading, this relation is given as (Chan, Tuba and Wilson, 1970; Anderson, 2005):

$$K_{\mathrm{I}} = \lim_{r \to 0} \left[ \frac{E^* u_y}{4} \sqrt{\frac{2\pi}{r}} \right] \tag{5.4}$$

where

$$E^* = \begin{cases} E, & \text{plane stress} \\ \dfrac{E}{1-\nu^2}, & \text{plane strain} \end{cases} \tag{5.5}$$

$E$ is the elastic modulus, while $\nu$ is Poisson's ratio. As the opening displacement $u_y$ is equal to zero at the crack tip, the nodal values of $u_y$ near the crack tip must be disregarded when performing the extrapolation of $K_{\mathrm{I}}$ to $r = 0$. The displacement method does generally give more accurate estimations than the stress method (Anderson, 2005).

#### 5.2.1.3 Finite elements at the crack tip

In order to reduce the mesh quality required for the displacement method, special crack tip elements were developed in the 1970's, which were able to describe the singularity which exists in the near-crack stress field. One of them was the isoparametric bilinear rectangle (quadrilateral) 4-node element with special shape functions, proposed by Tracey (1971), which should be used at the crack tip. Four years later, Henshell and Shaw (1975) declared in the title of their paper that 'Crack tip finite elements

are unnecessary'. They could show that the crack tip singularity could be represented by 8-node isoparametric quadratic rectangle elements, if the mid-side nodes closest to the crack tip were moved to the 'quarter points', i.e. ¼ of the element length away from the crack tip. Similar 2D elements, as well as three-dimensional elements, were independently developed by Barsoum (1976), and presented in the same journal, two issues later.

When used at the crack tip, these so-called 'quarter-point elements' (Bittencourt et al., 1996) have a reasonably accurate stiffness, but the local values of stress and displacement within the quarter-point elements are poor (Henshell and Shaw, 1975). The nodal displacements for these elements should therefore be omitted when calculating $K$. Recommendations for generating a suitable mesh with quarter-point elements for evaluating $K_I$ by the displacement method have been given by Menandro, Moyer and Liebowitz (1995) and Guinea, Planas and Elices (2000), and a typical example of the crack tip mesh is shown in Figure 5.2. Note that the quarter-point (8-node quadratic rectangle) elements are collapsed down to triangles, where each element has three nodes located at the crack tip.

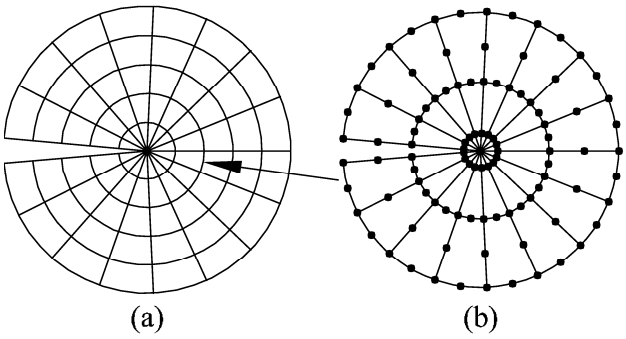


Figure 5.2 – (a) Typical rosette pattern for the FEM mesh at a LEFM crack tip, and (b) detail of the two inner rings, with nodes shown. Note the use of quarter-tip elements only in the innermost ring

#### 5.2.1.4 Energy release rate methods

The potential energy decrease per unit crack advance is called the energy release rate, $\mathcal{G}$, and may be used to characterise crack growth in a linear or nonlinear elastic body (Rice, 1968; Parks, 1974; deLorenzi, 1985). Rice (1968) showed that the energy release rate could be computed by a path independent line integral, which for a two-dimensional problem is defined by:

$$J = \int_{\Gamma} \left( W \, \mathrm{d}y - \mathbf{T} \cdot \frac{\partial \mathbf{u}}{\partial x} \mathrm{d}s \right) \tag{5.6}$$

where $\Gamma$ is a curve surrounding the crack tip, $W(x, y)$ is the strain-energy density field, and $x$, $y$ are the Cartesian coordinates being parallel and normal to the crack tip, respectively. $\mathbf{T}$ is the traction vector associated to the outward normal to $\Gamma$, $\mathbf{u}$ is the displacement vector, and d$s$ is an incremental arc length along $\Gamma$.

The third method to compute the stress intensity factors mentioned by Chan, Tuba and Wilson (1970) is the line integral method. This method consists of numerically evaluating the $J$ integral, Equation (5.6), for the finite element solution over an arbitrary path surrounding the crack tip. In the case of small-scale yielding, the energy release rate may be related to the mode I stress intensity factor by the following equation (Rice, 1968; Chan, Tuba and Wilson, 1970):

$$K_1 = \sqrt{\mathcal{G}E^*} = \sqrt{JE^*} \tag{5.7}$$

The $J$ integral may be evaluated at a remote contour, like the outer boundary of the geometry (Chan, Tuba and Wilson, 1970), which improves its numerical accuracy, compared with the stress method and the displacement method. The application of this method to three-dimensional problems is more difficult, however, because the integral becomes a surface integral. It is difficult both to define the surface and

to perform the numerical integration (deLorenzi, 1985). This led to the development of alternative methods to evaluate the energy release rate, e.g. the virtual crack extension methods developed by Parks (1974), Hellen (1975) and deLorenzi (1985). The most accurate and efficient (Anderson, 2005) method for the numerical evaluation of the energy release rate seems to be the domain integral method, formulated by Shih, Moran and Nakamura (1986). They compute the *J* integral by using the divergence theorem, in which the three-dimensional surface integral is transformed into a volume domain integral, which is evaluated using Gaussian quadrature.

For mixed mode I+II loading with small-scale yielding, the following relationship exists between the energy release rate and the stress intensity factors (Rice, 1968; Belytschko and Black, 1999):

$$J = \mathcal{G} = \frac{1}{E^*}\left(K_{\mathrm{I}}^2 + K_{\mathrm{II}}^2\right) \tag{5.8}$$

In order to extract the stress intensity factors from the *J* integral, Yau, Wang and Corten (1980) developed a technique using an interaction integral. The combination of the interaction integral with the domain integral method is shown by Shih and Asaro (1988) and Belytschko and Black (1999).

The main advantage of the energy release rate methods is that accurate estimations for the stress intensity factor may be obtained even with a relatively coarse mesh (Guinea, Planas and Elices, 2000). A finer mesh, with quarter-point elements at the crack tip, is required if determination of the stress field is part of the objective. The domain integral is often recommended for practical use. Some find it easier to implement in certain FE codes (because quarter-point elements are not needed) (Courtin et al., 2005), and others have found it to be more stable than the displacement method (Bittencourt et al., 1996). On the other hand, if quarter-point elements may easily be used in a FE code, the displacement

method does not need any specialised post-processing routine to obtain the stress intensity factor. Both the displacement method and the domain integral method are able to accurately predict the stress intensity factor (Bittencourt et al., 1996). The displacement method is still widely used (Miranda et al., 2003; Alegre and Cuesta, 2010), and Guinea, Planas and Elices (2000) question whether the domain integral actually is the most efficient.

### 5.2.2 Evaluation of the direction for further crack growth

If a crack is subjected to a mixed-mode loading, the propagating crack seeks the path of least resistance. Several theories have been proposed to choose this path. The three most used (Miranda et al., 2003) are the criteria of maximum tangential (circumferential) stress (Erdogan and Sih, 1963), maximum energy release rate (Hussain, Pu and Underwood, 1974) and minimum strain energy density (Sih, 1974). Other criteria include the criterion of maximum dilatational strain energy density (Theocaris and Andrianopoulos, 1982a) and the criterion of minimum accumulated strain energy (Pavlou et al., 2003). There is no general agreement about which criterion should be used for a given material, but Bittencourt et al. (1996) have shown that the three former criteria predict basically the same crack growth trajectory for poly(methyl methacrylate) (PMMA), which is a brittle material. The criterion of maximum tangential stress is often applied in FEM simulations of fatigue crack growth, because it is simple to implement, as it has an approximate explicit solution for the crack growth direction $\theta$ as a function of $K_{\mathrm{I}}$ and $K_{\mathrm{II}}$ (Belytschko and Black, 1999; Miranda et al., 2003; Alegre and Cuesta, 2010). To implement the evaluation of the direction for further crack propagation in FE codes is generally not a problem (Colombo and Giglio, 2006).

### 5.2.3 Representation of the crack advancement

When the stress intensity range and the crack growth direction have been found, the number of cycles required for the crack to propagate a distance $\Delta a$ may be estimated by the crack propagation law. As the crack propagation law is not linear with respect to $\Delta a$, the stress intensity factor range $\Delta K$ needs to be re-evaluated after the increment $\Delta a$. Reducing this increment will increase the accuracy of the solution, at the cost of increased computational effort.

In order to re-evaluate $\Delta K$, the crack increment needs to be represented by the finite element mesh. As noted in Section 5.2.1, some mesh refinement at the crack tip is normally needed. When the crack tip moves due to the crack increment, the focused region of the mesh should follow. The most common technique when modelling propagating fatigue cracks under LEFM conditions is to perform global or local re-meshing (Højfeldt and Østervig, 1986; Bittencourt et al., 1996; Miranda et al., 2003; Alegre and Cuesta, 2010). Local re-meshing is generally preferred, due to the lower computational effort, compared to global re-meshing.

Local re-meshing was employed already in 1986 by Højfeldt and Østervig (1986) to predict the shape and crack propagation life of fatigue cracks in shafts with a diameter transition. They employed the displacement method and quarter-point elements to estimate the stress intensity factors of the three-dimensional crack, and the criterion of minimum strain energy density to estimate the crack growth direction. Bittencourt et al. (1996) and Miranda et al. (2003) used the local re-meshing technique, together with quarter-point elements and the displacement technique, in their methodology for assessment of fatigue crack propagation in two-dimensional components. The re-meshing technique was also used by Alegre and Cuesta (2010) to model mode I+II crack propagation in a valve.

The local re-meshing technique generally consists of four steps (Bittencourt et al., 1996), as illustrated in Figure 5.3; (a) removing the

existing mesh around the crack, (b) advancing the length of the crack, (c) applying quarter-point elements in a uniform rosette pattern at the crack tip, and (d) generating a new mesh in the open area.

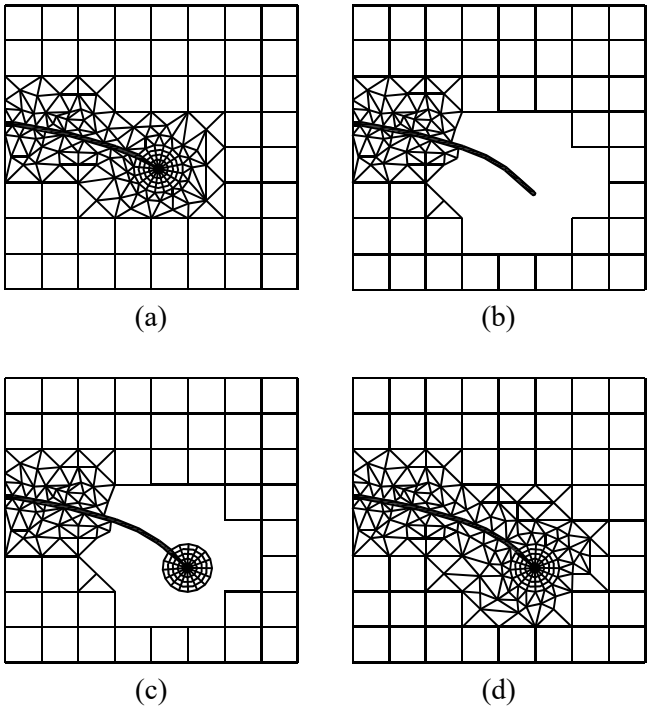


Figure 5.3 – Local re-meshing technique. (a) Existing mesh. (b) The mesh around the crack tip is removed, and the crack is advanced. (c) Rosette of elements are applied at the crack tip. (d) The remaining area is meshed

Recent research in crack propagation modelling by FEM often deals with plasticity induced crack closure, e.g. (Aguilar Espinosa et al., 2017a; García-Collado, Vasco-Olmo and Díaz, 2017; Hu et al., 2017), in which the material plasticity is explicitly taken into account in the finite element analysis. Re-meshing is then highly cumbersome, with respect to both computational and programming effort, because the plastic strain history needs to be mapped from the old mesh to the new one (Anderson, 2005). Furthermore, accuracy is lost during this mapping process. As an alternative, it is possible to create a single mesh which accommodates

crack growth, by being refined along the assumed crack propagation path. The disadvantage of this approach is that the crack path and shape are predetermined by the mesh (Anderson, 2005; Colombo and Giglio, 2006). In addition, the crack increment $\Delta a$ has to correspond to the element size, making the crack growth response mesh dependent. By employing micrometre-size elements, this approach is nevertheless widely used (García-Collado, Vasco-Olmo and Díaz, 2017; Hu et al., 2017).

In order to advance the crack through the refined mesh, the following techniques may be used (Anderson, 2005; Belytschko et al., 2014): (a) Removing elements along the crack front once a failure criterion is reached, (b) releasing the nodes at the crack tip at specific load steps or according to a failure criterion, so that these elements are no longer connected, or (c) using cohesive elements. The cohesive elements are zero-thickness elements which are placed in between the ordinary elements, and for which a certain force-displacement law is specified. When computing fatigue crack propagation with plasticity induced crack closure, the node release technique is the most common to use (Solanki, Daniewicz and Newman, 2004), but cohesive elements are also used by some researchers (Nguyen et al., 2001; García-Collado, Vasco-Olmo and Díaz, 2017; Hu et al., 2017). It should be noted that the plastic crack tip field does not contain the $1/\sqrt{r}$ singularity (Anderson, 2005), making quarter point elements unnecessary when studying plasticity induced crack closure.

Colombo and Giglio (2006) recently developed a crack advancement technique for LEFM conditions which is a combination of the local re-meshing and node release techniques. Their technique may be described by four steps: (a) the crack increment is projected on the FE mesh, (b) the elements touched by the crack increment are deleted, (c) the open area is re-meshed by debondable triangular elements which conform to the crack increment, and (d) the nodes along the crack increment are

released. This technique limits the re-meshing to the absolute minimum, while still keeping the crack growth mesh-independent. The resulting mesh is inadequate for evaluating the stress intensity factors using the displacement technique, however. Therefore, the submodelling technique (Knight et al., 1991; Cook et al., 2002) is used, in which the displacements from this mesh are imposed on an independent focused mesh which represents the crack tip using quarter-point elements (as shown in Figure 5.2(a)). The displacement field of this focused mesh is then used to estimate the stress intensity factor. The submodelling technique has also been used by Schöllmann, Fulland and Richard (2003) in their fatigue crack growth simulation software.

### 5.2.4 Current trends

In recent years the research focus seems to have shifted from simple geometries modelled under LEFM conditions towards three-dimensional cracks in complex geometries or with plasticity induced crack closure. A review of the literature on finite element analysis of three-dimensional fatigue cracks is provided by Branco, Antunes and Costa (2015), while an overview of the finite element analysis of plasticity induced crack closure is provided by Solanki, Daniewicz and Newman (2004). We will here limit our discussion to three of the latest works.

Aguilar Espinosa et al. (2017a) have used four-node quadrilateral elements with the node release technique in Abaqus, in order to estimate the crack opening and closing stress intensity factors for a crack in a four-point bending specimen subjected to fatigue loading. The contact of the crack flanks was simulated by using Abaqus' surface contact boundary condition. However, even with a mesh refined to 4 μm elements at the crack tip, the estimated crack opening and closing loads are significantly lower than the experimentally determined values.

Solanki, Daniewicz and Newman (2004) stated that the physics of fatigue crack growth is not taken into account when the node release

technique is used. García-Collado, Vasco-Olmo and Díaz (2017) illustrate some of the differences between the results obtained by using a physics-based cohesive element technique, and those obtained by using the node release technique, like differences in the plastic strain field around the crack tip. They used an element size of 15 μm at the crack tip, with 13 213 nodes in total to model a compact-tension specimen. In order to reduce the mesh refinement required at the crack tip, Hu et al. (2017) propose a special singular element to be used at the crack tip when considering plasticity induced crack closure in two-dimensional geometries. This single element covers the whole crack tip, and its radius should be equal to the plastic zone length. The element is based on a cohesive zone model, and is used to simulate variable amplitude propagation of a mode I fatigue crack.

## 5.3 Crack propagation by the extended finite element method

As indicated in Section 5.2.3, the methods for evaluating fatigue crack growth by the ordinary finite element method do normally contain one of two shortcomings: The methods are either mesh-dependent, or require re-meshing. In order to avoid both these shortcomings, Belytschko and Black (1999) published a mesh-independent method with minimal re-meshing in 1999. This method was further developed by Moës, Dolbow and Belytschko (1999) into a mesh-independent method without any re-meshing. The method has later become known as the eXtended Finite Element Method (XFEM) (Fries and Belytschko, 2010; Belytschko et al., 2014), and has become widely popular (Dong and Atluri, 2013a) for solving continuum mechanics problems containing discontinuities like cracks and material interfaces. In addition to crack propagation problems, XFEM has been employed to solve two-phase flows and fluid-structure interaction problems (Fries and Belytschko, 2010), and has even been proposed as an applicable tool to predict the deformation of a brain subjected to a surgeon's cut (Vigneron et al., 2009).

As illustrated in Figure 5.4, XFEM uses a non-conforming mesh to model the crack (or other discontinuities), i.e. the cracks are modelled independently of the mesh (Belytschko et al., 2014). This is made possible by 'enriching' the elements cut by the crack, by adding special shape functions to take care of the local discontinuities and singularities around the crack (Fries and Belytschko, 2010). The mesh-independency makes it possible to use the same mesh for all stages of a growing fatigue crack. Even though the modelling of the crack is said to be independent of the mesh, Ren and Guan (2017) clearly illustrate that the level of mesh refinement at the crack influences the accuracy of the representation of a three-dimensional crack. The mesh-independency does rather imply that the crack growth increment and orientation may be chosen independently of the mesh.

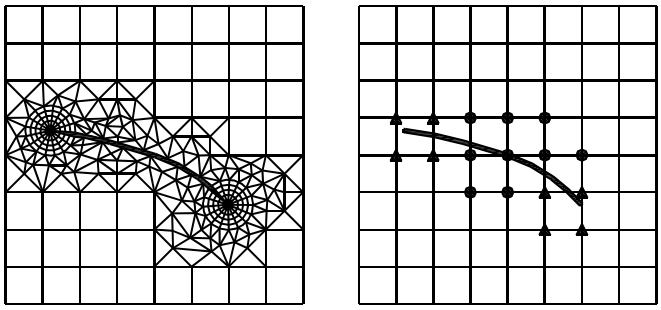


Figure 5.4 – Illustrative sketches of (a) a conforming FEM mesh and (b) a non-conforming XFEM mesh. ▲ indicates tip enriched nodes, while ● indicates step enriched nodes. Element sizes not to scale

We will here briefly review XFEM for the purpose of modelling fatigue cracks. An extensive review of XFEM in general is provided by Fries and Belytschko (2010), and some of its numerous applications have been reviewed by Yazid, Abdelkader and Abdelmadjid (2009).

### 5.3.1 Representation of the crack

As the extended finite element method mesh does not normally conform to the crack, it is necessary to formulate the position and shape of the crack face and the position of the crack tips mathematically. This is normally (but not necessarily) done using the level set method (Stolarska et al., 2001; Sukumar, Chopp and Moran, 2003; Fries and Belytschko, 2010; Belytschko et al., 2014). An arbitrary crack may be described by two level set curves. The first level set curve, $\phi(\mathbf{x}, t)$, is the signed-distance function, which is equal to zero along the whole crack surface, as well as at its tangential extensions at its ends, as shown in Figure 5.5(a) (Stolarska et al., 2001; Fries and Belytschko, 2010):

$$\phi\left(\mathbf{x},t\right) = \pm \min_{\mathbf{x}_\Gamma \in \Gamma(t)} \left\| \mathbf{x} - \mathbf{x}_\Gamma \right\|, \ \ \forall \mathbf{x} \in \Omega \tag{5.9}$$

where the sign is positive and negative on opposite sides of the crack. $\mathbf{x}_\Gamma$ is the closest point to $\mathbf{x}$ on the crack face $\Gamma(t)$. $\Omega$ represents the domain of the solid.

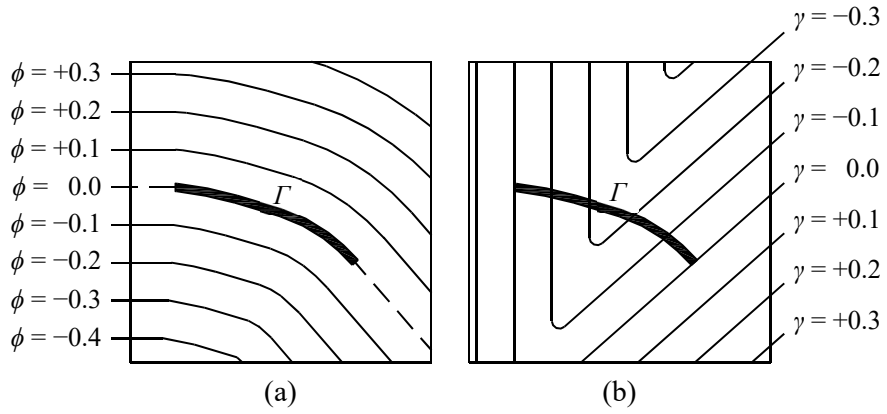


Figure 5.5 – Level set curves (a) $\phi(\mathbf{x}, t)$ and (b) $\gamma(\mathbf{x}, t)$ for a 2D crack

While $\phi(\mathbf{x}, t)$ represents the position and geometry of the crack face, it does not specify where the crack ends. This is accomplished by a second

level set curve, $\gamma(\mathbf{x}, t)$, which is orthogonal to $\Gamma(t)$ and equal to zero at the crack front (Fries and Belytschko, 2010), as shown in Figure 5.5(b). The crack front corresponds to the crack tip for a two-dimensional crack, or to the perimeter of a three-dimensional crack (Sukumar, Chopp and Moran, 2003).

Given these two level sets, the geometry and position of the crack is given by (Stolarska et al., 2001; Fries and Belytschko, 2010):

$$\Gamma(t) = \left\{ \mathbf{x} : \ \phi(\mathbf{x}, t) = 0 \wedge \gamma(\mathbf{x}, t) \leq 0 \right\} \tag{5.10}$$

As the crack grows, $\Gamma(t)$ is updated, based on the crack increment length and direction. One of the possible ways to update the crack representation is the fast marching method used by Sukumar, Chopp and Moran (2003). Alternative methods are mentioned by Fries and Belytschko (2010).

The values of the level sets are normally saved at the element nodes, and interpolated within the finite elements using standard shape functions (Fries and Belytschko, 2010). It should be noted that this interpolation makes the accuracy of the crack representation dependable on the element size and the number of nodes per element, as illustrated by Ren and Guan (2017).

### *5.3.2 The stress and displacement fields*

The fundamental requirement of any finite element method is its ability to represent the stress and displacement fields of the loaded solid. With a crack being defined by the level set method, the extended finite element method needs to be able to compute these fields with sufficient accuracy. In order to take the discontinuity and the singularity around the crack into account, the XFEM introduces an enrichment to the finite elements which are cut by the crack (Fries and Belytschko, 2010; Belytschko et al., 2014). More precisely, ‘a node is enriched if its support is cut by

the crack' (Moës, Dolbow and Belytschko, 1999). The nodes are enriched by the introduction of an additional set of degrees of freedom, **q**. The nodes do still contain their traditional degrees of freedom, **u**, meaning that the enriched nodes have a higher number of degrees of freedom than the ordinary nodes. The displacement field within the elements is then approximated by the following expression:

$$\mathbf{u}^{\mathrm{h}}\left(\mathbf{x}\right)=\underbrace{\sum_{i\in I}N_i\left(\mathbf{x}\right)\mathbf{u}_i}_{\text{standard FE approx.}}+\underbrace{\sum_{i\in I^*}N_i^*\left(\mathbf{x}\right)\cdot\left[\psi\left(\mathbf{x}\right)-\psi\left(\mathbf{x}_{\mathrm{i}}\right)\right]\mathbf{q}_i}_{\text{enrichment}} \tag{5.11}$$

which is the standard XFEM approximation (Fries and Belytschko, 2010). The enriched nodes *I** are a subset of all the nodes *I*, $N_i(\mathbf{x})$ are the standard FEM shape functions and $\psi(\mathbf{x})$ is called the enrichment function. $N_i^*(\mathbf{x})$ are some functions which have the partition of unity property (Fries and Belytschko, 2010):

$$\sum_{i\in I^*}N_i^*\left(\mathbf{x}\right)=1 \tag{5.12}$$

As the standard FEM shape functions $N_i(\mathbf{x})$ do have the partition of unity property (Belytschko et al., 2014), $N_i^*(\mathbf{x})$ are usually chosen to be equal to the $N_i(\mathbf{x})$. The term $-\psi(\mathbf{x}_i)$ is called shifting, and is used to remove the effects of $\mathbf{q}_i$ on the nodes and ensure compatibility across elements, i.e. to ensure that $\mathbf{u}^{\mathrm{h}}(\mathbf{x}_i) = \mathbf{u}_i$.

The enrichment function is responsible for introducing discontinuities and singularities to the displacement field. Belytschko and Black (1999) proposed the enrichment functions that describe the singular displacement field around the crack tip under LEFM conditions:

$$\psi_{\mathrm{tip}}\left(\mathbf{x}\right)=\sqrt{r}\left\{\cos\frac{\theta}{2},\quad\sin\frac{\theta}{2},\quad\sin\frac{\theta}{2}\sin\theta\quad\cos\frac{\theta}{2}\sin\theta\right\} \tag{5.13}$$

Here, $r$ and $\theta$ are the polar coordinates with the origin at the crack tip, and $\theta = 0$ along the parallel extension of the crack into the material.

The above enrichment is based on linear elastic fracture mechanics (LEFM), and is therefore only representative for cases where the crack tip plastic zone is considered to be small (Belytschko et al., 2014). For the case of significant plasticity, an alternative set of crack tip enrichment functions was developed by Elguedj, Gravouil and Combescure (2006). They still assume that the plasticity is confined to a region near the crack tip, and apply the Hutchinson-Rice-Rosengren solution for a power-law hardening material, proposing the following crack tip enrichment functions:

$$\psi_{\text{tip}}(\mathbf{x}) = r^{\frac{1}{n+1}} \left\{ \sin\frac{\theta}{2}, \quad \cos\frac{\theta}{2}, \quad \sin\frac{\theta}{2}\sin\theta, \right. \\ \left. \cos\frac{\theta}{2}\sin\theta \quad \sin\frac{\theta}{2}\sin 3\theta, \quad \cos\frac{\theta}{2}\sin 3\theta \right\} \tag{5.14}$$

$n$ is here the hardening exponent of the material.

Even though the enrichment functions, Equations (5.13) & (5.14), are discontinuous along $\theta = \pm\pi$ (Belytschko and Black, 1999), i.e. throughout the crack, they are not readily applicable to describe long, severely curved or three-dimensional cracks (Belytschko and Black, 1999; Moës, Dolbow and Belytschko, 1999). Hence, Belytschko and Black stated their method to require 'minimal re-meshing'. Moës, Dolbow and Belytschko (1999) removed the need of re-meshing altogether, by introducing an additional enrichment, to be used for the enriched nodes along the crack, away from the crack tip. This enrichment models the discontinuous displacement field over the crack by using the sign function (Moës, Dolbow and Belytschko, 1999; Fries and Belytschko, 2010):

$$\psi_{\text{step}} = \text{sign}\left(\phi\left(\mathbf{x},t\right)\right) = \begin{cases} -1 & \text{if } \phi\left(\mathbf{x},t\right) < 0, \\ 0 & \text{if } \phi\left(\mathbf{x},t\right) = 0, \\ 1 & \text{if } \phi\left(\mathbf{x},t\right) > 0. \end{cases} \tag{5.15}$$

This enrichment function is equal to −1 and +1 on opposite sides of the crack, which is normally represented by the level set $\phi(\mathbf{x}, t)$. Moës, Dolbow and Belytschko (1999) used the symbol $H(\mathbf{x})$ for this enrichment function, and subsequent authors have often referred to it as the Heaviside function, e.g. Sukumar, Chopp and Moran (2003), Yazid, Abdelkader and Abdelmadjid (2009), Vigneron et al. (2009) and Bergara et al. (2017), even though the Heaviside step function formally has the property $\text{H}(\phi(\mathbf{x})) = 0$ if $\phi(\mathbf{x}) \leq 0$ (Fries and Belytschko, 2010). However, the sign and the Heaviside step functions do actually lead to identical results because they span the same approximation space (Fries and Belytschko, 2010).

By using the crack tip and step enrichments, an appropriate approximation for the stress and displacement fields may be obtained, both for two-dimensional (Moës, Dolbow and Belytschko, 1999; Nasri and Zenasni, 2017) and three-dimensional (Sukumar, Chopp and Moran, 2003; Bergara et al., 2017) cracks. If we divide the additional degrees of freedom, **q**, into those around the crack tip, **b** (indicated by ▲ in Figure 5.4(b)), and those remaining, **a** (indicated by ● in Figure 5.4(b)), we can rewrite Equation (5.11) (Fries and Belytschko, 2010):

$$\begin{aligned} \mathbf{u}^{\text{h}}\left(\mathbf{x}\right) = & \sum_{i\in I} N_i\left(\mathbf{x}\right)\mathbf{u}_i \\ & + \sum_{i\in I^*_{\phi,\gamma}} N^*_i\left(\mathbf{x}\right)\cdot\left[\psi_{\text{step}}\left(\mathbf{x}\right) - \psi_{\text{step}}\left(\mathbf{x}_i\right)\right]\mathbf{a}_i \\ & + \sum_j \sum_{i\in I^*_{\text{tip}}} N^*_i\left(\mathbf{x}\right)\cdot\left[\psi^j_{\text{tip}}\left(\mathbf{x}\right) - \psi^j_{\text{tip}}\left(\mathbf{x}_i\right)\right]\mathbf{b}^j_i \end{aligned} \tag{5.16}$$

It should be noted that integration of the weak form of the finite element formulation is not straight forward when the elements contain

singularities and discontinuities, because the standard Gauss quadrature requires a smooth integrand and a finite order polynomial (Belytschko et al., 2014). Special integration techniques have therefore been developed for this purpose (Moës, Dolbow and Belytschko, 1999; Elguedj, Gravouil and Combescure, 2006; Fries and Belytschko, 2010; Belytschko et al., 2014).

### 5.3.3 Evaluation of the stress intensity factor and the direction for further crack growth

The stress intensity factor is commonly extracted from the extended finite element solution by employing the domain form of the interaction integral (Belytschko and Black, 1999; Moës, Dolbow and Belytschko, 1999; Sukumar, Chopp and Moran, 2003; Elguedj, Gravouil and Combescure, 2006; Ren and Guan, 2017), as explained in Section 5.2.1.4. It is likely that this method is preferred over the displacement method, because the crack tip displacements are less readily available in the XFEM results than in corresponding FEM results. Moës, Dolbow and Belytschko (1999) used a proper mesh and demonstrated computation of the stress intensity factors for two-dimensional mode I+II cracks within 1–2 % deviation from the analytical values. The XFEM enrichment takes care of the near-crack singularity, and linear elements can therefore be used even for the LEFM analyses.

The direction for further crack growth is often evaluated using the criterion of maximum tangential stress (Erdogan and Sih, 1963), e.g. by Belytschko and Black (1999), Moës, Dolbow and Belytschko (1999), Nasri and Zenasni (2017) and Ren and Guan (2017), just like in fatigue analyses using the ordinary FEM. The angle of propagation is estimated using a function of $K_{\mathrm{I}}$ and $K_{\mathrm{II}}$, and the level sets describing the crack are updated accordingly. The relation between the angle of propagation and the level set updates are illustrated by Belytschko et al. (2014).

### 5.3.4 Fatigue crack propagation and current trends

The first application of the extended finite element method to fatigue crack growth propagation was illustrated already by Moës, Dolbow and Belytschko (1999). They modelled the propagation of mode I+II fatigue cracks propagating from two holes in a two-dimensional plate with 2650 nodes. Two different values for the crack increment size are used, but the numerical results are not compared to any experimental ones.

Sukumar, Chopp and Moran (2003) presented the first XFEM simulation of planar fatigue cracks propagating through a three-dimensional solid (i.e. pure mode I cracks). They use the level set method to track the position of the crack front, and the fast marching method to advance the crack front. Using three-dimensional meshes of 24×24×24 eight-node (linear) hexahedral elements, they compute the stress intensity factors for a planar penny-shaped crack with errors between 0.4 % and 2.9 %, while for a planar elliptical crack the errors are between 0.6 % and 3.7 %. The fatigue simulations correctly predicted an initially elliptical crack to develop into a penny-shaped crack, but the crack propagation life is not compared to any experimental results.

Comparisons of XFEM fatigue simulations to experimental results have recently been published by Bergara et al. (2017). In this work, they have used the XFEM-based LEFM approach which is implemented in Abaqus to simulate the growth of a semi-elliptical crack located at the side of a beam specimen subjected to four-point bending. The specimen is completely modelled in three dimensions by 8-node hexahedral elements, with refinements around the crack and the boundary condition sites. With 173 892 nodes in total, approximately one week was required to run one fatigue crack propagation simulation using three 3.40 GHz processors. Bergara et al. report excellent correspondence between the numerical and experimental crack propagation histories, as well as good agreement for the evolution of the crack geometry. However, there are large differences between the experimental and numerical stress

intensity factor ranges; up to approximately 40 %. This seems remarkable given the fine mesh and good correspondence in the crack propagation histories.

Zhan et al. (2017) have proposed an entire framework for the fatigue life prediction of metallic components, where the crack initiation life is evaluated using FEM with continuum damage mechanics, while the crack propagation life is evaluated using XFEM. The initiated crack is set to be 0.1 mm long. Computational and experimental results have been compared for a mode I crack in a fuselage structure, modelled by 8-node hexahedral elements, using 20 106 nodes for half the model. The predicted crack propagation life was 28 % shorter than the experimental one, indicating a potential for improving the technique.

A new method for reducing the required structural mesh density near the crack has recently been proposed by Ren and Guan (2017). Their method is intended for the crack growth analysis of three-dimensional and arbitrarily shaped cracks subjected to mixed mode loading. They note that the level set method is not able to fully represent the crack front surface if the crack has a complicated geometry or if the mesh is relatively coarse. It is therefore proposed to use an individual mesh for the crack, and let the crack geometry in the XFEM model of the structure be described by this mesh, instead of the level set method. It is shown that this method makes the values for the stress intensity factor range more uniform along the crack front, and they are also less dependent on the structural mesh. However, the crack mesh is shown to be very fine in the illustrations, and necessarily needs to be updated (re-meshed) as the crack propagates. It has not been shown whether the computation time saved by using a coarser overall mesh makes up for the time required to re-mesh the crack for each propagation increment. Still, it is possible that this technique is more efficient for analysing fatigue crack propagation in large and complex components.

## 5.4 Discussion

The studies reviewed in Section 5.3.4 indicate that even though XFEM is capable of accurately predicting stress intensity factors for simple 'handbook' geometries, further development is required in order to make accurate predictions of stress intensity factors and fatigue crack propagation lives for more complex geometries. It should be noted that the accuracy of the predicted crack propagation life will always be limited by the fracture mechanics assumptions and the crack propagation law which is used, however. On the other hand, even though the XFEM was developed to reduce the computational effort required to simulate fatigue crack propagation, none of the studies reviewed do actually compare computation times between FEM and XFEM. This is remarkable.

Højfeldt and Østervig (1986) were able to predict the fatigue crack propagation life of shafts with shoulder fillets, with errors below 20 % in just 20 400 s (CPU-time). These results were obtained using the ordinary FEM with a three-dimensional mesh and the local re-meshing technique. By exploiting symmetry, only half the shaft was modelled, using only 1160 nodes. One would expect that after 30 years of research, either the accuracy of the computational results would increase, or the computation time would decrease, especially with the introduction of XFEM. The works considered in this review are inconclusive in this regard, mainly because computation times (with processor frequencies) are rarely stated. In order to choose between the various computational techniques for modelling fatigue crack propagation, and their variants, such information is essential.

Yazid, Abdelkader and Abdelmadjid (2009) state that 'about the only drawback' of the present XFEM 'is the need for a variable number of degrees of freedom per node.' This is mainly a challenge when XFEM is incorporated into existing FEM codes (Fries and Belytschko, 2010). A more important drawback, as indicated above, for both FEM and XFEM,

seems to be the large number of nodes and long computation time required. FEM and XFEM are challenged by methods requiring significantly fewer nodes, like the boundary element method (BEM) (Mi and Aliabadi, 1994) and the SGBEM-FEM by Nikishkov, Park and Atluri (2001). Recent comparisons by Dong and Atluri (2013a; 2013b) indicate that the SGBEM-FEM is both more accurate and more efficient than XFEM to analyse propagating fatigue cracks under LEFM conditions.

## 5.5 Conclusions

Both the ordinary Finite Element Method (FEM) and the eXtended Finite Element Method (XFEM) are able to provide good predictions for the fatigue crack growth propagation in simple geometries. While the FEM mesh conforms to the fatigue crack, the crack is only implicitly modelled in XFEM, independently of the mesh.

In FEM, the domain integral method is often recommended for evaluating the stress intensity factors, while the displacement method is still often used in practice. The domain integral method is commonly used also in XFEM. The criterion of maximum tangential stress is chosen for determining the crack propagation path in the majority of the analyses. Under linear elastic fracture mechanics (LEFM) conditions, local re-meshing is used to advance the crack in FEM, whereas either the node release technique or cohesive elements are used under elastic-plastic fracture mechanics conditions. In XFEM, it is common to use the level set method to describe the crack geometry.

As the complexity of the problem increases, the accuracy of both methods decreases. The latest research therefore focuses on applying and improving these techniques to complex problems, like three-dimensional crack propagation under mixed-mode loading. In the current literature, there is also an increasing focus on modelling plasticity induced closure and fatigue propagation under variable amplitude loading using FEM.

For both methods, there is also a focus on improving their efficiency, by introducing new techniques. Even though the XFEM was developed to reduce the computational effort required for crack propagation problems, none of the studies reviewed do actually compare computation times between FEM and XFEM. This is remarkable, and should be considered for later studies.

## *Acknowledgements*

This work is part of a PhD study supported by the Norwegian Ministry of Education and Research. The financial support is acknowledged.

# 6 Choosing computational techniques for crack analysis

Determining the evolution of the stress intensity factors as a fatigue crack propagates is an essential step in estimating its fatigue crack propagation life. For basic crack geometries, handbook solutions for the stress intensity factors exist (Tada, Paris and Irwin, 2000). These solutions are rarely readily applicable for cracks in real structures however, especially not if the crack is subjected to mixed-mode loading, in which case the crack path will be curved. In most cases, it is therefore necessary to compute the stress intensity factors using computational methods.

In the following chapters, several cracks are analysed, for which handbook solutions do not exist. It was therefore necessary to apply a computational method in order to determine their stress intensity factors. Several techniques were tested and assessed, in order to choose the most appropriate techniques for the considered geometries. In this chapter, some of the tests which formed the basis for these choices are presented. Seven different techniques for computing the stress intensity factors from a finite element model are presented, and applied to two different cracked geometries for which handbook solutions exist. The convergence of each technique, as the mesh density near the crack tip is increased, is studied. The scope of the presented convergence study is not sufficiently wide that general conclusions for choosing computational techniques for crack analysis may be made. Yet, it clearly shows strengths and weaknesses with the different techniques.

The considered geometries are an angled crack in an infinite plate, and a circumferential through crack in a long, thin-walled cylindrical shell subjected to tension and torsion. The geometries are analysed using plane and shell elements, respectively. The study does not include fully three-dimensional modelling, which requires significantly more computational resources.

## 6.1 Computational techniques

In the previous chapter, several computational techniques for analysing fatigue cracks using the finite element method (FEM) and the extended finite element method (XFEM) were reviewed. Due to the convenient availability of FEM and XFEM in commercial software, other alternatives were not considered for use in the present work. However, the XFEM capabilities of the two major commercial FEM software packages ANSYS (ANSYS, Inc., 2015) and Abaqus (Dassault Systèmes, 2016) are limited. They do not support XFEM neither for second-order elements (except for tetrahedron elements in Abaqus), nor for shell elements. Due to these limitations, it was chosen to analyse cracks using FEM in the present work. All analyses were performed using ANSYS® Academic Research Mechanical, Release 17.0.

In the following, seven different techniques for computing the stress intensity factors from a finite element model are briefly discussed, and later compared.

### 6.1.1 The domain integral method

The domain integral method (Shih, Moran and Nakamura, 1986) consists of computing the $J$ integral by using the divergence theorem, as explained in Section 5.2.1.4. The stress intensity factors for the different modes of fracture are extracted from the solution using an interaction integral (Yau, Wang and Corten, 1980; Shih and Asaro, 1988). The domain integral method is considered to yield accurate estimates for the stress intensity factors, but it is difficult to implement for the average FEM user if it is not already available in the software. The method is readily available in ANSYS, but only for plane and solid elements, not for shell elements.

For a two-dimensional problem, the domain integral is evaluated over an area. In the absence of thermal strain, body force and crack face traction, any annular domain centred at the crack tip can be chosen for evaluating

the *J* integral (Shih, Moran and Nakamura, 1986). In ANSYS, these domains are called contours. The first contour covers the elements connected to the crack tip node, the second contour covers the elements adjacent to the first contour, and so on (ANSYS, Inc., 2015), as illustrated in Figure 6.1.

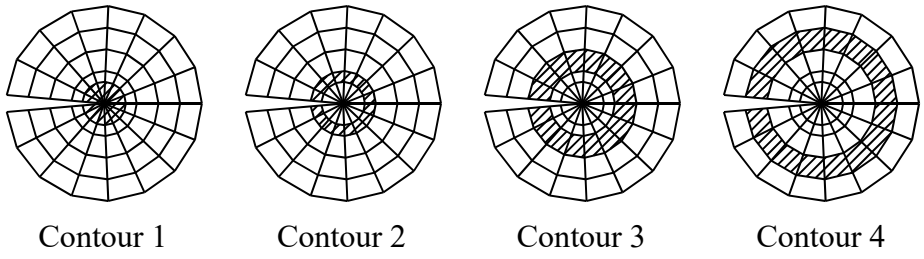


Figure 6.1 – Elements over which the domain integral is evaluated in ANSYS

Even though the *J* integral theoretically should be independent of the domain used for integration, the approximate nature of the finite element solution causes some domain dependence (Dassault Systèmes, 2016), as indicated in Figure 6.2. The contours close to the crack tip should be ignored, and the solution for the stress intensity factors should be taken from the contours in which domain independence has been reached. The results shown in Figure 6.2 are for an embedded through-thickness crack (not an edge crack). From contour number 39 and up, the radius of the integration domain is larger than half the crack length. Therefore, the computed results for these contours are influenced by the opposite crack tip, making them unusable.

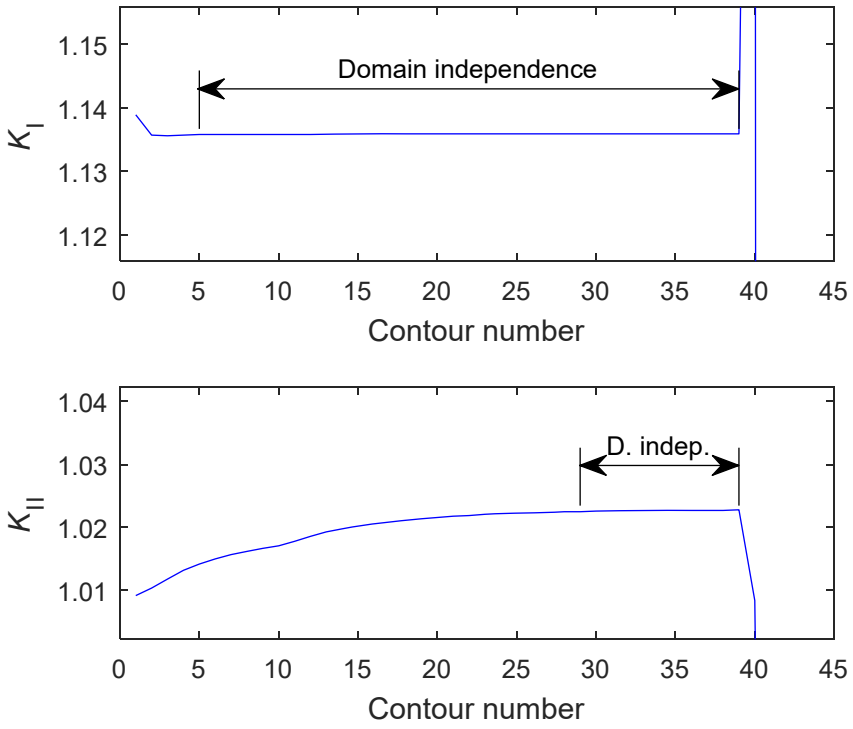


Figure 6.2 – Stress intensity factors $K_I$ and $K_{II}$ for an angled crack in a large plate, computed by the domain integral for different contours around the crack tip

### 6.1.2 The displacement extrapolation technique

The displacement extrapolation technique (Chan, Tuba and Wilson, 1970; Henshell and Shaw, 1975) was described in Section 5.2.1.2. In this technique, nodal values for the stress intensity factor are computed from the nodal displacements, and linearly extrapolated to the crack tip. It is most convenient to consider the nodal displacements along the length of the crack.

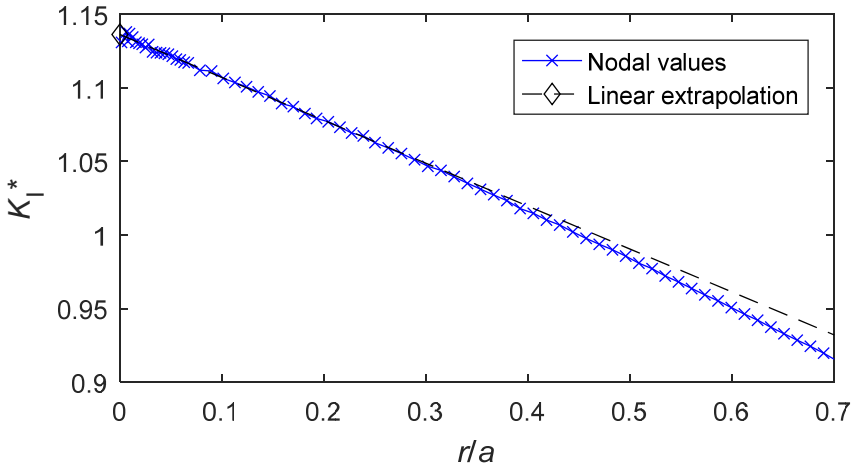


Figure 6.3 – Mode I displacement extrapolation for an angled crack in a large plate. The stress intensity factor is extrapolated to be $K_I = 1.1362$

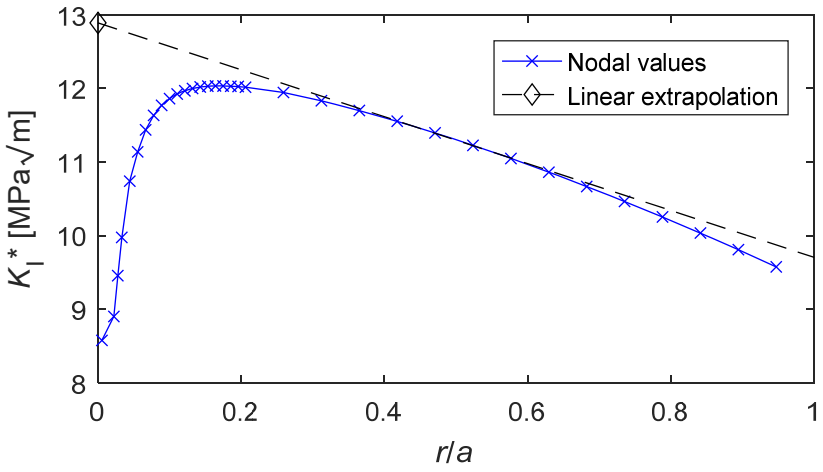


Figure 6.4 – Mode I displacement extrapolation for a circumferential crack in a long cylinder. The stress intensity factor is extrapolated to be $K_I = 12.890$ MPa√m

The application of the displacement extrapolation technique for two different cracked geometries is shown in Figures 6.3 & 6.4. The crack length is $2a$, and $r$ is the distance from the crack tip, along the crack faces. For the case shown in Figure 6.3, the linear trend near the crack

tip is evident, and it is straightforward to extrapolate the values to the crack tip ($r = 0$). For the case shown in Figure 6.4, it is more difficult to distinguish a linear trend. Close to the crack tip, the analytical stress field contains the sum of a singular term and a finite term which varies nonlinearly with the distance (Harrop, 1982). Due to the finite elements' inability to accurately represent this stress field, the nodal values $K_I$* fall too short (Kuna, 2013, p. 195). This is the case even when quarter-point elements are used at the crack tip, as can be seen in the analyses by Anderson (2005, p. 581) and Henshell and Shaw (1975). In these cases, the choice of where to extrapolate depends on the experience of the user. Some insight may be gained by analysing similar solutions, for which a stress intensity factor solution already exists.

### 6.1.3 The quarter-point displacement technique

As described in Section 5.2.1.3, the use of quarter-point elements was proposed independently by Henshell and Shaw (1975) and Barsoum (1976), in order to more accurately model the stress field near the crack tip. While Henshell and Shaw (1975) demonstrated this advantage by applying the displacement extrapolation technique, Barsoum (1976) chose to use only the displacement of the node closest to the crack tip, i.e. the quarter-point node, to compute the stress intensity factor. This was noted by Shih, deLorenzi and German (1976), who formulated a simple expression for computing the stress intensity factor from this node:

$$K_{\mathrm{I}}^{\mathrm{QPDT}} = \frac{2G\sqrt{2\pi}}{\kappa+1} \times \frac{2u_{y,\mathrm{B}}}{\sqrt{l_1}} \tag{6.1}$$

where the shear modulus $G = E/[2(1+\nu)]$, $\kappa$ is Kolosov's constant, which is equal to $(3-4\nu)$ for plane strain and $(3-\nu)/(1+\nu)$ for plane stress, $E$ is the elastic modulus, $\nu$ is Poisson's ratio, $l_1$ is the length of the quarter-point element, and $u_{y,\mathrm{B}}$ is the opening displacement of the quarter-point node. A similar expression for the mode II stress intensity factor may be

obtained by replacing $u_{y,B}$ with the displacement component $u_{x,B}$, which is parallel to the crack (Lim, Johnston and Choi, 1992). This technique has later been named the quarter-point displacement technique (QPDT).

### 6.1.4 The displacement correlation technique

Instead of using just the quarter-point node, Shih, deLorenzi and German (1976) suggested that the stress intensity factor should be computed by matching the $\sqrt{r}$ term of the displacement's variation within the quarter-point elements, to the analytical displacement field in the vicinity of the crack tip. The following expression was obtained:

$$K_{\mathrm{I}}^{\mathrm{DCT}} = \frac{2G\sqrt{2\pi}}{\kappa+1} \times \frac{4u_{y,\mathrm{B}} - u_{y,\mathrm{C}}}{\sqrt{l_1}} \tag{6.2}$$

$u_{y,B}$ and $u_{y,C}$ are the opening displacements of the first and second nodes along the crack, as indicated in Figure 6.5. A similar expression for the mode II stress intensity factor may be obtained by replacing $u_y$ with $u_x$ (Lim, Johnston and Choi, 1992). This technique has later been named the displacement correlation technique (DCT). It is noted that the application of Equations (6.1) and (6.2) is easier than applying the displacement extrapolation technique. The displacement correlation technique is therefore often used when simulating fatigue crack propagation, see e.g. Miranda et al. (2003) and Alegre and Cuesta (2010).

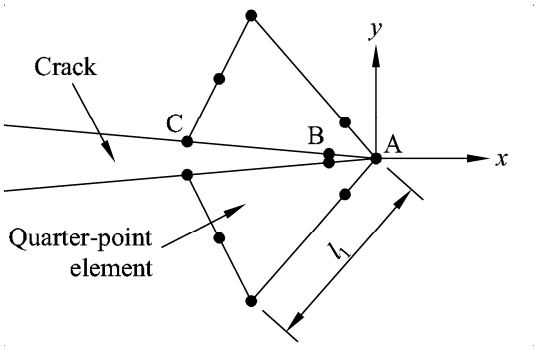


Figure 6.5 – The two quarter-point elements at the crack faces

### 6.1.5 Two-node displacement extrapolation

In their evaluation of the QPDT and the DCT, Guinea, Planas and Elices (2000) suggested yet another method to compute the stress intensity factor from the displacements of the quarter-point element nodes. They suggested to extrapolate the stress intensity factor from the two first nodes along the crack front. This extrapolation may be directly computed by the following expression:

$$K_{\mathrm{I}}^{\mathrm{TNDE}} = \frac{E^*}{12}\sqrt{\frac{2\pi}{l_1}}\left(8u_{y,\mathrm{B}} - u_{y,\mathrm{C}}\right) \tag{6.3}$$

where $E^*$ is equal to $E$ for plane stress, and $E/(1-\nu^2)$ for plane strain. They concluded that this expression yielded better results than QPDT and DCT for large element sizes.

### 6.1.6 The stress extrapolation technique

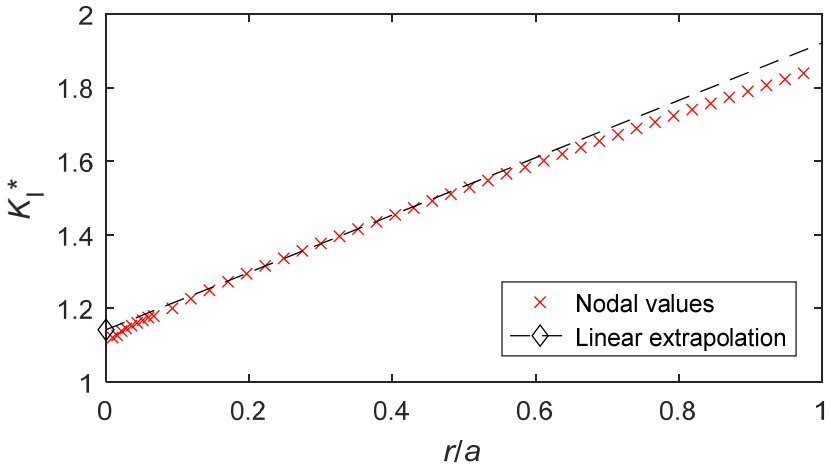


Figure 6.6 – Mode I stress extrapolation for an angled crack in a large plate. The stress intensity factor is extrapolated to be $K_{\mathrm{I}} = 1.1417$

The stress extrapolation technique (Chan, Tuba and Wilson, 1970), as described in Section 5.2.1.1, is similar to the displacement extrapolation

technique, except that the nodal values of the stress in front of the crack tip are used, instead of the nodal values of displacement behind the crack tip. Its application is demonstrated in Figure 6.6. In finite element analyses, the stress field is obtained by differentiation of the displacement field, and the computed stresses are therefore less accurate than the displacements. Therefore, it is likely that the stress extrapolation technique will give greater errors than the displacement extrapolation technique.

### *6.1.7 The modified crack closure integral*

The modified crack closure integral (MCCI), also called the virtual crack closure technique (VCCT), was proposed by Rybicki and Kanninen (1977) as a way of obtaining rough estimates for the stress intensity factors from a coarse mesh. The crack closure technique is based on the assumption that the energy released when the crack propagates an increment $\Delta a$, is equal to the energy required to close the crack over the same distance. The energy release rate $\mathcal{G}$ (= $J$) may therefore be obtained by computing the crack closure integral. This integral may be computed from the nodal forces and displacements of the crack tip elements. The modification proposed by Rybicki and Kanninen (1977) involves the further assumption that the stress state near the crack tip does not change significantly when the crack propagates a small increment $\Delta a$. This allows the computation of the crack closure integral from a single FEM analysis (instead of two).

Raju (1987) extended the MCCI to second-order and quarter-point elements. His simplified formulae for quarter-point elements are easy to apply, and have been used in the present work. For additional information on MCCI, the reader is referred to the review by Krueger (2004).

### 6.1.8 Published comparisons of different techniques

Several comparisons of the different techniques have been published in the literature (Lim, Johnston and Choi, 1992; Guinea, Planas and Elices, 2000; Anderson, 2005; Courtin et al., 2005; Miranda et al., 2012; Zhu and Leis, 2014; Han et al., 2015; Qian et al., 2016). The studies which have included the domain integral in their comparison (Anderson, 2005; Courtin et al., 2005; Zhu and Leis, 2014; Qian et al., 2016) do all agree that it is the best method (due to its high accuracy and low mesh dependency). Anderson (2005) and Zhu and Leis (2014) also agree that the displacement extrapolation method is more accurate than the stress extrapolation method. None of the studies considers all the seven techniques considered in this chapter, and only Lim, Johnston and Choi (1992) and Miranda et al. (2012) consider mixed-mode cracks. Therefore, further comparison of the techniques is required if the domain integral method cannot be used.

## 6.2 Description of the numerical study

As part of the evaluation of the different techniques, two cracked geometries were analysed. The geometries and their finite element models are presented in this section. For both the geometries, an initial study was performed to determine the overall mesh density required. This initial study is not presented here. The focus of this presentation is the length of the quarter-point elements at the crack tips, which was found to influence the computed stress intensity factors considerably. All the finite element analyses were performed using ANSYS Mechanical APDL. MATLAB R2016b was used to generate the input files, and to post process the output files.

### 6.2.1 Angled crack in an infinite plate

The most basic mixed-mode problem is a through crack in an infinite plate, subjected to a tensile nominal stress which is not orthogonal to the

crack, as indicated in Figure 6.7. The stress intensity factors for this crack are well known:

$$K_{\mathrm{I}} = \sigma \cos^2(\beta)\sqrt{\pi a} \tag{6.4}$$

$$K_{\mathrm{II}} = \sigma \sin(\beta)\cos(\beta)\sqrt{\pi a} \tag{6.5}$$

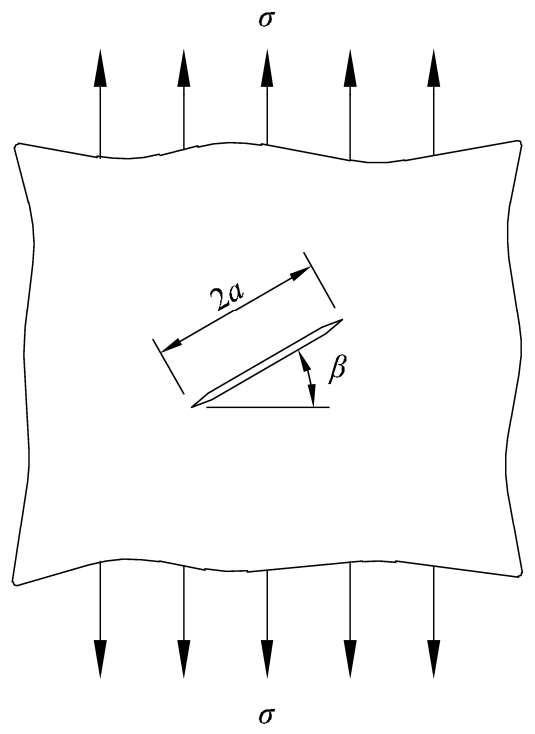


Figure 6.7 – Angled crack in an infinite plate

The crack tip coordinates were set to (1, 0.9) and (−1, −0.9), as earlier analysed by Stazi et al. (2003) and Dong and Atluri (2013a). The material properties were taken as $E = 207 \times 10^9$, $\nu = 0.25$, and the load was set to $\sigma = 1$. The analytical solution for this problem is found from Equations (6.4) & (6.5) to be $K_{\mathrm{I}} \approx 1.13584$ and $K_{\mathrm{II}} \approx 1.02225$. In a finite element model, the infinite plate needs to be truncated to a finite size. As shown

by Bjørheim (2019), the edge effects for this geometry become negligible when the finite size is set to 400 × 400 or larger. Therefore, a finite size of 400 × 400 was used here. The stress was applied on the two opposite edges of the plate, as shown in Figure 6.7. In order to avoid rigid-body translations and rotations, the horizontal and vertical displacement components were set to zero in the lower left corner of the plate, and the vertical displacement component was set to zero in the lower right corner of the plate.

The ANSYS documentation (ANSYS, Inc., 2015) recommends that the crack faces should be coincident in the finite element model. This is difficult to accomplish in practice, if the user wishes to generate the crack tip mesh manually, because the coincident crack faces will merge when the crack tip mesh is connected to the global mesh. Therefore, a small but finite gap of $a/200$ between the crack faces has been used in this thesis, as recommended by Phan (no date) (see also Anderson, 2005, p. 570). At the crack tip, the crack faces have been modelled with a slope of 1:100, also as recommended by Phan (no date).

The geometry was modelled using eight-node quadrilateral plane elements. At the crack tip, elements were placed in a rosette pattern (ref. Figure 5.2 or 6.1), with quarter-point elements in the inner ring. The length (radius) of the quarter-point element, $l_1$, is the main variable in this study. The length of the elements in the second ring was kept equal to half the length of the quarter-point elements, as this is the default choice in ANSYS. Additional rings of elements were included as required, in order to have a smooth transition to the element size used beyond the crack tip. If included, the length of the third through fifth rings of elements was kept equal to the length of the quarter-point element. For the angled crack, the number of rings was adjusted in such a way that the outer radius of the manually defined rosette was minimum 0.1. The element size beyond the rosette was set to match the size of the elements in the outer ring of the rosette.

The circumferential extent of each element in the rosette pattern has been set to 22.5 ° (i.e. 16 elements in each ring of the rosette) for all analyses presented in this thesis, except for the analysis in Paper IV, where this value was set to 30 °. The ANSYS documentation (ANSYS, Inc., 2015) recommends this value to be between 30 ° and 40 ° in general, while Guinea, Planas and Elices (2000) recommend it to be 30 ° or lower, when DCT, QPDT or two-node displacement extrapolation is used. Menandro, Moyer and Liebowitz (1995) stated that 22.5 ° is optimal when the displacement extrapolation technique is applied. A rosette with elements extending over 22.5 ° also allows a simple transition to a structured mesh beyond the crack tip, as shown in Papers V & VI.

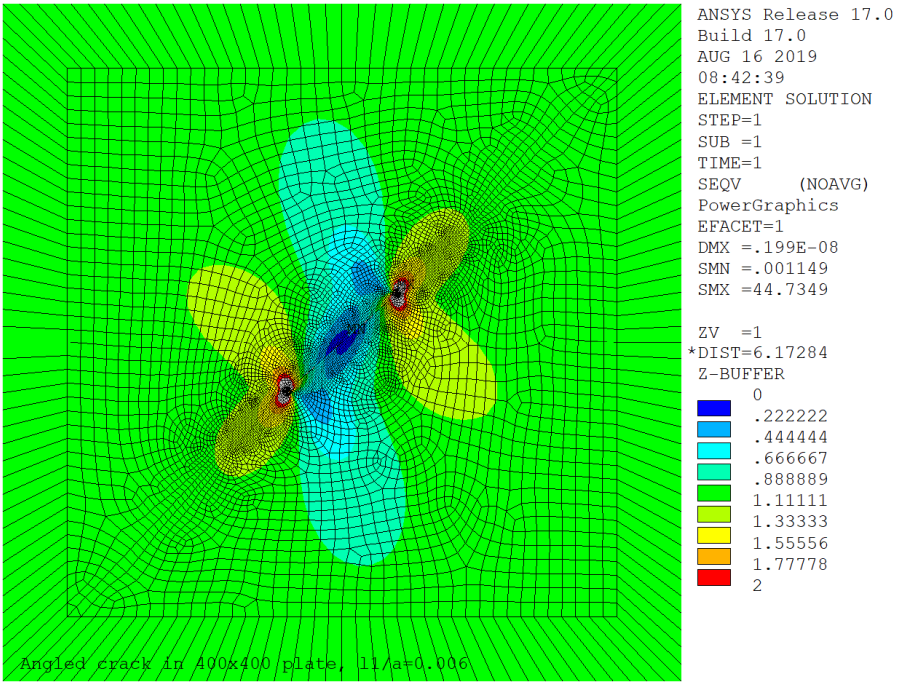


Figure 6.8 – Mesh and von Mises stress distribution for the angled crack, with quarter-point element length $l_1 = a/160$. The crack tip rosette consists of 10 rings

Beyond the crack tips, a fine and unstructured mesh was generated within a square of size 10 × 10. An example of the mesh within this square is

shown in Figure 6.8[2]. Beyond this square, the mesh was kept very coarse, as it did not influence the computed stress intensity factors (Bjørheim, 2019).

The geometry was analysed for several different quarter-point element lengths, $l_1$. The mesh beyond the crack tip rosette was kept similar in all the analyses, and for $l_1/a \leq 0.01$ it was kept identical. For all the analyses, the displacement extrapolation was taken from the nodes within a distance, $r$, between 0.07 and 0.30 units from the crack tip (i.e. the interval $0.052 \leq r/a \leq 0.223$ in Figure 6.3), for both modes. The stress extrapolation was taken from the interval $0.25 \leq r \leq 0.50$ ($0.186 \leq r/a \leq 0.372$ in Figure 6.6) for mode I, and the interval $0.30 \leq r \leq 0.75$ for mode II. The results are presented in Section 6.3.

### 6.2.2 Circumferential through crack in a cylindrical shell

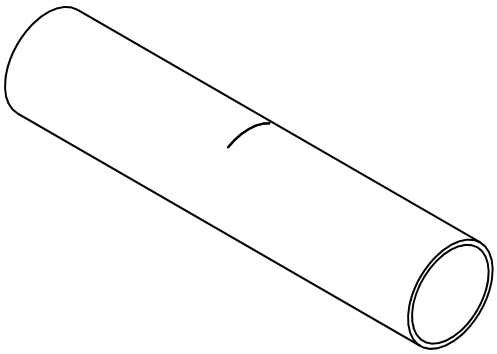

Figure 6.9 – Thin-walled cylinder with a circumferential through-crack

The second geometry considered is a circumferential through crack in a long, thin-walled cylindrical shell, as indicated in Figure 6.9. The cylinder is subjected to a tensile and a torsional load in each end, loading

[2] An expression which was used to generate this mesh is derived in Appendix A of this thesis.

the crack in mode I and mode II, respectively. This geometry is also analysed in Papers V & VI.

Analytical solutions for the stress intensity factor under tensile loading have been derived for both short and long cracks, and an interpolation of these two solutions, thereby covering both regimes, has been presented by Sanders (1982). An analytical solution does also exist for torsional loading when the crack is small (Erdogan and Ratwani, 1972).

The dimensions and loads for the cylinder have been taken from paper VI. The outer diameter is 63.609 mm, the inner diameter is 60.055 mm, the elastic modulus is 200 GPa, Poisson's ratio is 0.285, the tensile load is 25.2 kN, and the applied torsion is 234 Nm. The analytical solutions are valid for long cylinders, where end effects are negligible. Forman, Hickman and Shivakumar (1985) showed that the computed stress intensity factor for tension is equal for cylinder lengths $2L = 5.34\pi R_m$ and $2L = 10.34\pi R_m$, where $R_m$ is the mid-thickness radius. The cylinder length has therefore been set to $2L = 10\pi R_m$ here. The crack length is set to $2a = 15$ mm, measured along the mid-thickness cylindrical surface. Cracks in shells are characterized by the shell parameter, given by the following equation (Folias, 1965; Erdogan and Ratwani, 1972; Kumosa and Hull, 1989):

$$\lambda = \left[12\left(1-\nu^2\right)\right]^{1/4} \frac{a}{\left(R_m t\right)^{1/2}} \tag{6.6}$$

For the crack considered here, $\lambda \approx 1.8$, and it may therefore be considered as a short crack (see Section 8.4.2, and Sanders, 1982). The analytical solution by Erdogan and Ratwani (1972) is therefore valid for the considered crack. The analytical stress intensity factors are found to be $K_I \approx 12.909$ MPa$\sqrt{\text{m}}$ and $K_{II} \approx 3.8015$ MPa$\sqrt{\text{m}}$.

The cylinder was modelled using eight-node isoparametric shell elements. Due to the symmetric/anti-symmetric property of the problem,

only half the cylinder was modelled, and the tension and torsion load cases were analysed individually. A rosette with quarter-point elements was used at the crack tips. The local element size beyond this rosette was set to $0.025R_m$. An example of the mesh is shown in Figure 6.10. Further details about the mesh and boundary conditions may be found in Section 8.3.2.

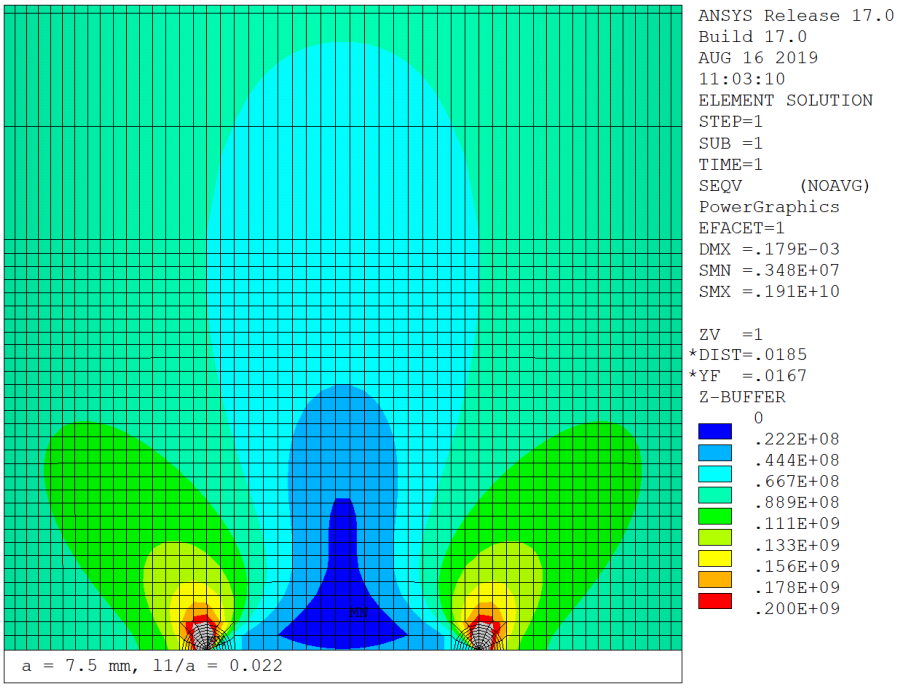


Figure 6.10 – Mesh and von Mises stress distribution for the cracked cylinder subjected to tension, with quarter-point element length $l_1 = a/45$. The crack tip rosette consists of 9 (half) rings. The lower edge is the plane of symmetry

The geometry was analysed for several different quarter-point element lengths, $l_1$. The mesh beyond the crack tip mesh was kept equal in all the analyses. For all the analyses, the displacement extrapolation was taken from the nodes within a distance, $r$, between 3.09 and 4.64 mm from the crack tip (i.e. the interval $0.412 < r/a < 0.619$ in Figure 6.4) for mode I, and the interval $2.4 < r < 3.6$ mm for mode II. The stress extrapolation

was taken from the interval $3 < r < 5$ mm for mode I, and the interval $2 < r < 4.5$ mm for mode II. The results are presented in the following section.

## 6.3 Results and discussion

The results from the analyses of the angled crack in the infinite plate, and the circumferential through crack in the cylindrical shell, are shown in Figures 6.11 and 6.12, respectively. For each technique, the error between the computed and the analytical stress intensity factor has been plotted as a function of the quarter-point element length, $l_1$, divided by the half-crack length, $a$. Please note that the two figures have different scales. The stress intensity factors computed using the domain integral method were extracted using the CINT command in ANSYS. The remaining techniques were manually implemented by analysing the computed nodal solution for displacement, stress and force, in MATLAB.

Of all the techniques used to analyse the plane geometry, the domain integral method is observed to be the best. As shown in Figure 6.11, the stress intensity factors computed by this method were equal for all the quarter-point element sizes used in this study. Compared with the analytical solutions, $K_{\mathrm{I}}$ was computed within an error of 0.006 %, and $K_{\mathrm{II}}$ within 0.05 %. These errors are negligible, and may possibly be related to the truncation of the infinite plate to a finite size. This result agrees with the general view in the published literature (Anderson, 2005; Courtin et al., 2005; Zhu and Leis, 2014; Qian et al., 2016), that the domain integral method is the preferred technique. Unfortunately, this method is not available for shell elements in ANSYS.

The second best technique for the two considered problems is the displacement extrapolation technique. As the quarter-point element size is reduced, this technique converges to the analytical value within ±1 % for all the four stress intensity factors. This complies with the expected

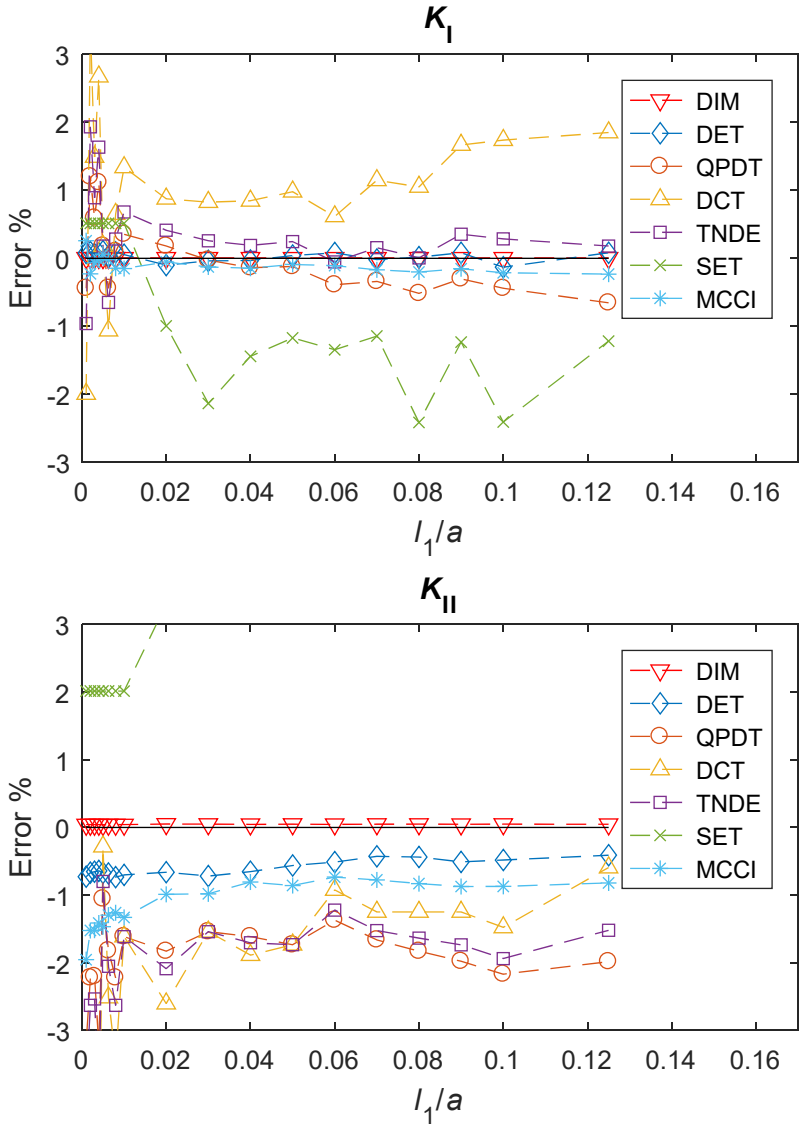


Figure 6.11 – Error between computed and analytical solutions for the stress intensity factors for the angled crack, as a function of the normalized quarter-point element length, for seven different computational techniques: Domain integral method (DIM), displacement extrapolation technique (DET), QPDT, DCT, two-node displacement extrapolation (TNDE), stress extrapolation technique (SET) and MCCI

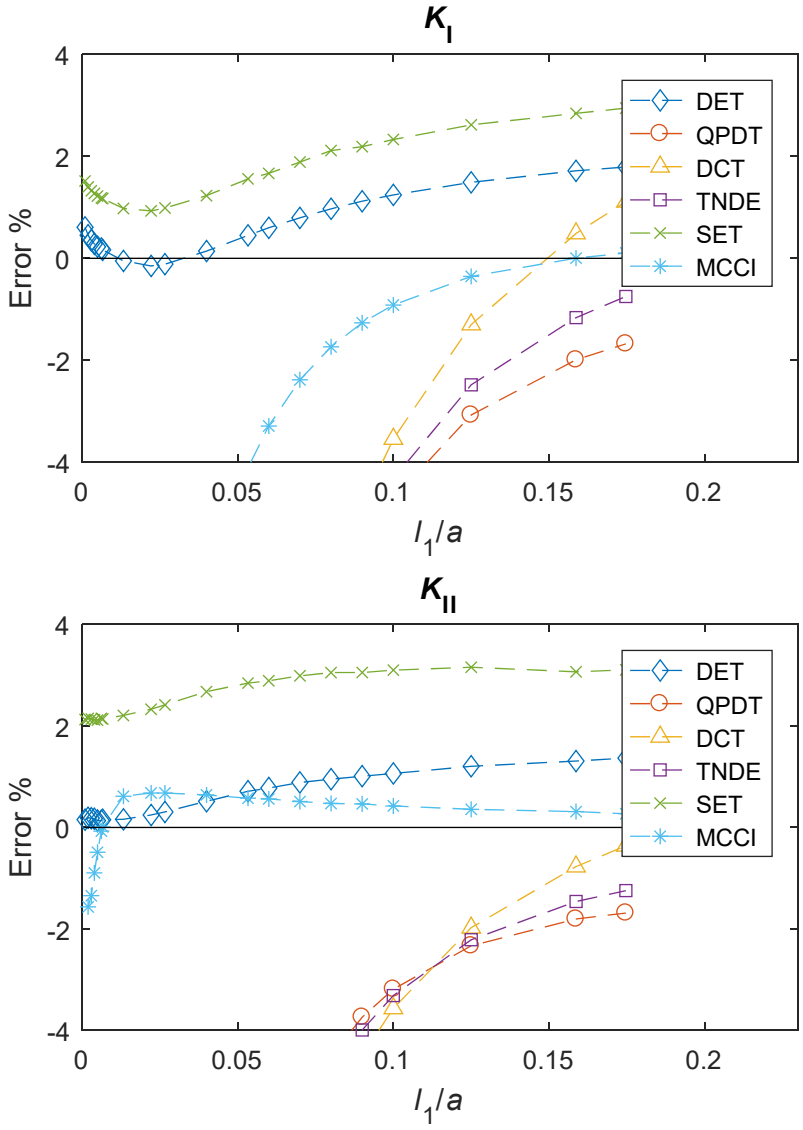


Figure 6.12 – Error between computed and analytical solutions for the stress intensity factor for the cracked cylinder, as a function of the normalized quarter-point element length, for six different computational techniques: Displacement extrapolation technique (DET) , QPDT, DCT, two-node displacement extrapolation (TNDE), stress extrapolation technique (SET) and MCCI

behaviour in the finite element method; that a finer mesh will lead to a more accurate answer. This technique is also the only one besides the domain integral method whose results remain within an error of ±2 % for all the quarter-point element lengths analysed. As mentioned above, the drawback of the displacement extrapolation technique is the more or less arbitrary choice of nodes from which to extrapolate. This can to some degree be compensated by comparison to an existing and similar analytical solution, comparison to results obtained by a different technique, or by experience.

The stress extrapolation technique is also observed to converge with decreasing element sizes, but not to a very accurate value. It typically converges to a result with an error of ±2 %. Also, the accuracy of this technique depends strongly on the mesh beyond the crack tip rosette. For the angled crack, the mesh beyond the crack tip rosette was kept identical for $l_1/a \leq 0.01$, in which case the stress intensity factors computed by the stress extrapolation technique remained constant as well, as shown in Figure 6.11. Beyond this value, there were slight variations in the mesh, which strongly influenced the computed results. There seems to be no reasons to use the stress extrapolation technique instead of the displacement extrapolation technique.

The three techniques based on the nodal displacements within the quarter-point elements, QPDT, DCT and two-node displacement extrapolation (TNDE), show a peculiar behaviour. They do not converge to a constant value as the element size is decreased. Instead, their results for low values of $l_1/a$ are entirely random for the angled crack (Figure 6.11), while they diverge from the analytical solution for the cracked cylinder (Figure 6.12). The reason for this strange behaviour is the finite elements' inability to accurately model the stress and displacement fields near the crack tip. It is clear from Figure 6.4 that using only the two nodes closest to the crack tip will yield an inaccurate solution. This is not surprising, as it was noted already in the first paper presenting the quarter-point elements (Henshell and Shaw, 1975) that the local values

of stress and displacement within these elements are poor. This shortcoming is further discussed in Section 8.4.3 of this thesis. For the larger quarter-point element sizes analysed, their predictions are within an error of ±2 %. This implies that QPDT, DCT and TNDE may be used to compute a rough estimate for the stress intensity factors from a coarse mesh. The results presented here do not indicate that one of these three techniques is consistently better than the others.

The last technique applied is the MCCI. This technique does also diverge when the quarter-point elements become very small. MCCI is based on the assumption that the stress state near the crack tip does not change significantly if the crack propagates a small increment, which is equal to the crack tip element length. One would therefore expect that its predictions would converge towards the correct solution as the crack tip element length is reduced, not diverge. However, the divergence may probably also be related to the inaccurate values of nodal displacements and forces within the quarter-point elements. Anyhow, it is clear that MCCI performs quite well when the quarter-point element is large, with its error staying within ±1 % when $l_1/a \geq 0.1$. In all the four cases shown in Figures 6.11 & 6.12, the MCCI does also follow a consistent trend (as opposed to the QPDT, DCT and TNDE). Therefore, MCCI is considered to be more reliable than the QPDT, DCT and TNDE.

It is noted that there is a large difference between how the different techniques behave for the two geometries. The conclusions reached in this study can therefore not be expected to be valid for other geometries. It is clear that several different geometries and load configurations should be analysed, in order to properly evaluate the different techniques. However, the problems analysed within this thesis are similar to the ones presented in this chapter. Therefore, this study justifies the choice of computational techniques made in the following chapters.

## 6.4 Conclusions

Seven different techniques for computing the stress intensity factors from a finite element model have been applied to two different cracked geometries. The following conclusions were drawn from this limited study:

- The domain integral method was the best technique, but it is not available for shell elements in ANSYS. It is difficult to implement if it is not already available.
- The displacement extrapolation technique converged to the correct solution (within ±1 %), as long as the correct nodes were used for extrapolation. The choice of nodes needs to be based on previous experience, comparison with a different technique applied to the same problem, or comparison with the analytical solution for a similar problem.
- The stress extrapolation technique converged, but not to a very accurate value.
- The techniques based on the nodal displacements within the quarter-point elements (QPDT, DCT and TNDE) did not converge, and were considerably influenced by the choice of quarter-point element length. They could still be used to compute a rough estimate from a coarse mesh.
- The modified crack closure integral (MCCI) could be used together with a coarse mesh, but its dependence on the quarter-point element length needs to be assessed on a case-by-case basis.

These conclusions may not necessarily be valid for different geometries, but they are valid for the crack problems considered within this thesis. Based on this study, it was chosen to use the domain integral method in Paper IV, the displacement extrapolation technique in Paper V, and both the displacement extrapolation technique and MCCI in Paper VI.

# 7 Paper IV: Effect of stop holes on structural integrity of offshore structures: A numerical model

[*]Kristen Rege, Dimitrios G. Pavlou

Department of Mechanical and Structural Engineering and Materials Science, University of Stavanger, Stavanger, Norway

**Abstract:** As offshore structures are reaching their original design life, effective repair and life extension techniques are required, in order to ensure continued safe operation. A stop hole may be drilled at the end of a crack, in order to delay further fatigue crack propagation. In order to compare the stop hole technique with other relevant repair techniques, its effect needs to be modelled. Here, a procedure for modelling the stop hole-induced fatigue crack growth delay for a crack propagating under mixed-mode I+II conditions is presented. The procedure combines the *S*-*N* curve for fatigue crack initiation and the Paris law for fatigue crack propagation, with models for mixed-mode crack propagation and finite element analysis of the cracked geometry. The failure criterion inherent in the *S*-*N* curves is used to define the transition between initiation and propagation. The procedure is implemented on an example, and the importance of considering the mixed-mode conditions is indicated.

[*] Previously published as: Rege, K. and Pavlou, D.G. (2019) Effect of stop holes on structural integrity of offshore structures: a numerical model, *Proceedings of the Institution of Civil Engineers – Maritime Engineering*, 172(1), pp. 3–14. doi: 10.1680/jmaen.2018.34

## 7.1 Introduction

A considerable number of offshore structures, both on the Norwegian and the UK continental shelves are approaching or have exceeded their original design life (Hörnlund et al., 2011; Stacey, 2011; Aeran et al., 2017). Due to the continued possibility of producing oil or gas from these fields, combined with improved oil recovery techniques and the possibility of serving as a base for neighbouring subsea completions, the installations are likely to remain operational for several years. During the extended life of these structures it is likely that fatigue cracks will occur, which may require repair in order to ensure the continued safety of the structure (Haagensen, 1994).

One of the many repair methods which are used for offshore structures is the so-called stop hole technique (Haagensen, 1994; Chen, 2016; Lotsberg, 2016). By drilling a hole through the tip of a through-thickness fatigue crack, the crack is transformed into a blunt notch, and the fatigue crack growth is effectively delayed, or in some cases completely stopped. This can often be a relatively inexpensive and easy solution, compared with the alternative of repair welding. The beneficial effect of stop holes applied to cracks under pure mode I (tensile opening) loading has been thoroughly analysed in the literature, see e.g. Wu et al. (2010), Castro et al. (2012), Ayatollahi, Razavi and Chamani (2014), Ayatollahi et al. (2016), Chen (2016), Razavi et al. (2017) and Malekan and Carvalho (2018).

In offshore structures, members and details are commonly subjected to a multiaxial stress state. Tubular members may, for instance, be subjected to a combination of bending, axial and torsional loading. Therefore, fatigue cracks may propagate under mixed-mode conditions, e.g. due to the multi-directional nature of the environmental loads acting on the structures, complex geometries or random defect orientations (Rhee, 1989; Mshana, Kam and McDiarmid, 1992; Riahi et al., 2011; He, Liu and Xie, 2014; Pavlou, 2017). During the life extension phase, it is likely

that modifications will be made to the topside process facilities (Stacey, 2011), which may also alter the load distribution through the structure, possibly leading to mixed-mode fatigue crack propagation. Still, few studies have considered the stop hole technique applied to mixed-mode cracks. In a study by Ayatollahi, Razavi and Yahya (2015), the effect of a stop hole applied to a modified compact tension specimen was investigated. The stop hole was modelled at the tip of a straight crack, which was then subjected to combined tensile and shear fatigue loading. Similar analyses were carried out by Miao, Zhou and He (2017) for a compact tension-shear specimen, but they did only consider fracture due to monotonic loading, instead of fatigue crack propagation. Analyses of a stop hole drilled through a crack already propagating under mixed-mode I+II conditions have been performed by Pavlou (2018) and Mikkelsen et al. (2017). They approximated the resulting curved crack path as a kinked crack, so that handbook solutions for the stress intensity factors of the crack could be used.

In this paper, a procedure for modelling the effect of the stop hole technique applied to fatigue cracks propagating under mixed-mode conditions is proposed. The propagating crack is modelled using the finite element method (FEM). While earlier works estimate only the crack re-initiation phase (Wu et al., 2010; Castro et al., 2012; Ayatollahi et al., 2016; Chen, 2016), or assign a fixed value to the length of the crack initiated at the stop hole edge (Ayatollahi, Razavi and Chamani, 2014; Ayatollahi, Razavi and Yahya, 2015; Razavi et al., 2017; Mikkelsen et al., 2017; Malekan and Carvalho, 2018; Pavlou, 2018), the length of the initiated crack is here related to the failure criterion inherent in the crack re-initiation estimate. Furthermore, the influence of the mean stress or any corrosive environment is taken into account. The proposed procedure is demonstrated for an illustrative example.

## 7.2 Procedure for analysing the effect of the stop hole

In order to properly assess the effect of a stop hole, both the crack re-initiation at the stop hole edge, and the proceeding fatigue crack propagation should be compared to the crack propagating without any stop hole. Therefore, the two different phases need to be modelled, and the transition between the two phases needs to be clearly defined.

### 7.2.1 Fatigue crack re-initiation at the stop hole edge

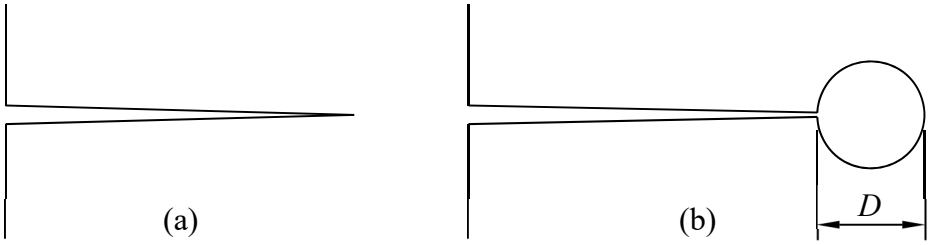


Figure 7.1 – (a) Crack and (b) crack repaired by a stop hole

When a stop hole with diameter $D$ is drilled at the tip of a crack, Figure 7.1, the crack is effectively transformed into a blunt notch with radius $D/2$. The fatigue crack initiation life of a notched member is normally estimated by using either a strain-life curve (typically when local yielding is involved; low cycle fatigue), or a stress-life curve combined with the stress concentration factor $k_t$ and the notch sensitivity $q$ for the geometry in question (high cycle fatigue) (Dowling, 2013). As offshore structures are normally designed for high cycle fatigue, the fatigue life of offshore structural steels (e.g. different variations of S355 to S500 acc. to EN 10225; see also NORSOK M-120) are generally presented using stress-life ($S$-$N$) curves. For the case of stop hole drilling, the stop hole should also be drilled sufficiently large for elastic conditions to prevail, in order to yield a significant effect. Therefore, analysis by the use of $S$-$N$ curves is considered in this work.

#### 7.2.1.1 Crack re-initiation based on standardised *S-N* curves

Well-documented *S-N* curves for offshore steels are found in standards and recommended practices, like DNVGL-RP-C203 (DNV GL, 2016). These *S-N* curves are given for different detail categories, with the majority representing different kinds of welded joints. The stop hole technique is mostly relevant for through-thickness cracks which have propagated away from the high stress concentration (Haagensen, 1994), i.e. away from the welds. Therefore, the *S-N* curves for non-welded details are applicable for crack initiation at the stop hole.

The failure criterion inherent the *S-N* curves of DNVGL-RP-C203 is the existence of a through-thickness crack in a 25 mm plate. By using stress intensity factor solutions for a corner crack in a uniformly stressed plate (Newman and Raju, 1986), it is possible to estimate the aspect ratio of the crack predicted by the *S-N* curve (see e.g. Toribio, Matos and González, 2017), which can then be used as the initiated crack for a fatigue crack propagation analysis. However, the detail considered in the *S-N* curves is that of a plate loaded in uniform tension, while at the edge of a stop hole the stress field will have a high gradient. Therefore, the aspect ratio evolution of the crack in the two cases would be different. In the case of a high stress gradient, crack propagation in the thickness direction is more dominant than in the case of a uniform stress field. This means that a crack at the stop hole which is equivalent to the through-thickness crack in a 25 mm uniformly loaded plate is needed, in order to define the transition between the crack initiation defined by the *S-N* curve and the proceeding crack propagation. This is possible by first estimating the initial defect size which would propagate to a through-thickness crack in a 25 mm uniformly loaded plate during the same number of cycles as estimated by the *S-N* curve (Lotsberg et al., 2016). Then, this initial defect could be implemented in a three-dimensional finite element model of the stop hole repaired geometry, and a crack propagation simulation could be carried out for the same number of cycles, in order to obtain the transition size. This makes it necessary to

perform time-consuming three-dimensional analyses for a problem which is normally analysed using a plane two-dimensional model.

#### 7.2.1.2 Crack re-initiation based on specimen *S-N* curves

The *S-N* curves given in DNVGL-RP-C203 have been constructed to represent fatigue failure, i.e. the combination of fatigue crack initiation, and the propagation of the crack through the thickness. However, in the analysis of the effect of the stop hole, it is convenient to separate the crack initiation and propagation phases. This is possible by making use of stress-life (or strain-life) curves derived directly from small specimens. Such curves are available in the literature (Chen, 2016; Micone and De Waele, 2017a), and represent mainly the crack initiation phase. These curves need to be adjusted to take into account the effects of size, surface finish, stress state and mean stress, along with the desired probability of failure, as described in e.g. Dowling (2013) or Budynas and Nisbett (2015). A study by Dowling, Calhoun and Arcari (2009) suggested that the Smith-Watson-Topper (SWT) method (Smith, Watson and Topper, 1970) is a good choice for taking the mean stress into account, as long as data for fitting are not available. According to the SWT method, a stress cycle with amplitude $\sigma_a$, maximum value $\sigma_{max}$ and load ratio $R$ may be transformed into an equivalent completely reversed stress amplitude $\sigma_{ar}$ given by:

$$\sigma_{ar} = \sqrt{\sigma_{max}\sigma_a} = \sigma_a \sqrt{\frac{2}{1-R}} \tag{7.1}$$

Variable amplitude loading may be taken into account by applying linear or nonlinear models (Rege and Pavlou, 2017). Methods for taking the full-range *S-N* curve into account and for performing probabilistic analyses are also available in the literature, see e.g. Sanches et al. (2015), Correia et al. (2017) and Raposo et al. (2017).

A finite element analysis of the crack, repaired by the stop hole technique, may be used to obtain the amplitude and mean value of the maximum principal stress at the edge of the stop hole. These values are used with the *S-N* curve in order to determine the crack re-initiation life, at the point where the accumulated fatigue damage is maximized. It should be noted that the stop hole is normally drilled with its centre somewhat ahead of the visible crack tip, in order to ensure that the crack tip is completely removed.

#### 7.2.1.3 Length of re-initiated crack, based on specimen *S-N* curves

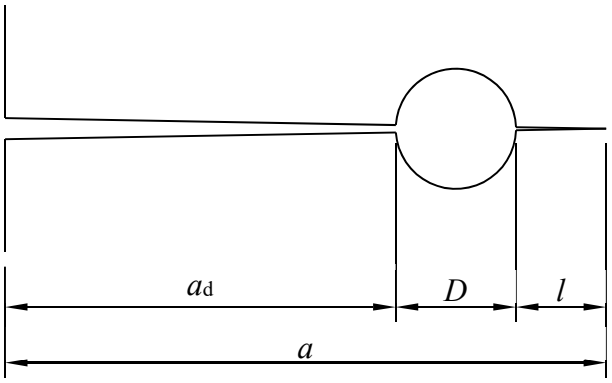


Figure 7.2 – Fatigue crack re-initiated from stop hole

The fatigue crack initiated at the edge of the stop hole is illustrated in Figure 7.2. Mode I conditions have been assumed for clarity, but the discussion to follow may be directly transferred to mixed-mode conditions. The total crack length, including the stop hole, is $a$, while $l$ is the length of the crack re-initiated at the stop hole edge. While the re-initiated crack is short, its stress intensity factor corresponds to that of a free surface crack, which is given by

$$K_s = 1.12\sigma_{loc}\sqrt{\pi l} \tag{7.2}$$

where $\sigma_{loc}$ is the maximum principal stress at the edge of the stop hole

prior to crack re-initiation. As the stop hole surface is a free surface, $\sigma_{loc}$ will be equal to the maximum circumferential stress at the edge of the hole, and the initial angle of the crack will therefore be in the radial direction. As the re-initiated crack grows, the influence of the stop hole gradually disappears, and only its total length $a$ is relevant to its stress intensity factor, given by

$$K_I = FS\sqrt{\pi a} \tag{7.3}$$

where $F$ is the relevant geometry factor and $S$ is the applied nominal stress. The evolution of the crack's behaviour from a free surface crack with length $l$ to a long crack with length $a$ is illustrated in Figure 7.3.

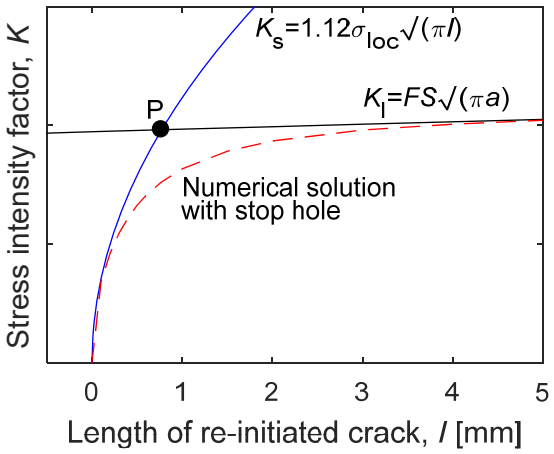


Figure 7.3 – Numerically computed stress intensity factor of the re-initiated crack, together with the short free surface crack solution $K_s$ and the long crack solution $K_I$

When $S$-$N$ curves representing the fatigue failure of small specimens are used to estimate the fatigue crack initiation life, it is necessary to estimate the corresponding initiated crack length in the structural component, $l_0$. If the initiated crack length is chosen to be too small, part of the crack propagation will be counted twice; both in the crack initiation life and in the crack propagation life, thereby leading to non-conservative total fatigue life estimations. This is also related to which one of the stress

intensity factor solutions shown in Figure 7.3 is used to estimate the proceeding crack propagation.

In earlier works, the length of the initiated crack at the edge of the stop hole has been handled in two different ways. Ayatollahi, Razavi and Yahya (2015), Razavi et al. (2017) and Malekan and Carvalho (2018) assumed that after the life estimated by a strain-life curve, the length of the re-initiated crack is $l_0 = 0.2$ mm. Then, they used the numerical solution (see Figure 7.3) for the stress intensity factor for the crack initiated at the stop hole to calculate the crack propagation life. On the other hand, Mikkelsen et al. (2017) and Pavlou (2018) assumed that after crack re-initiation, the crack can be modelled as a long crack with length $a = a_d + D$, i.e. that $l_0 = 0$. They used the long crack solution, $K_l$, which is higher than the numerical solution, to calculate the crack propagation life. This technique has been shown to agree reasonably well with experimental results from notched specimens (Socie, Dowling and Kurath, 1984).

A more conservative choice for the initiated crack length was proposed by Dowling (1979). He defined the initiated crack length by point P in Figure 7.3, i.e. where the stress intensity factor for a free surface crack of length $l$ is equal to that for the long crack of length $a$; $K_s = K_l$. Then, the long crack solution $K_l$ for a crack with length $a$, disregarding the geometry effect of the stop hole, is used to estimate the proceeding crack propagation. This method was found to agree well with experimental data on notched members (Dowling, 1979), and has been implemented for handling the transition between the crack initiation and the crack propagation phases in the current study. In this case, the notch sensitivity $q$ should be set equal to one when estimating the fatigue crack initiation life (Dowling, 2013).

### 7.2.2 Fatigue crack propagation

After the estimation of the fatigue crack initiation life and the corresponding initiated crack length, the proceeding fatigue crack propagation should be analysed. The stress intensity factor components, $K_{\mathrm{I}}$ and $K_{\mathrm{II}}$, of the propagating crack are required, and may either be approximated by analytical solutions (Pavlou, 2018), or found by computational analysis, like the finite element method (Ayatollahi, Razavi and Yahya, 2015; Rege and Lemu, 2017).

Relevant standards for offshore structures, e.g. DNVGL-RP-C210 (DNV GL, 2015) and BS 7910 (British Standards Institution, 2015), recommend the use of the Paris law for the calculation of the fatigue crack propagation rate:

$$\frac{\mathrm{d}a}{\mathrm{d}N} = C\left(\Delta K_{\mathrm{I}}\right)^{m} \text{ for } \Delta K_{\mathrm{I}} \geq \Delta K_{\mathrm{th}} \tag{7.4}$$

where $\Delta K_{\mathrm{I}} = K_{\mathrm{I,max}} - K_{\mathrm{I,min}}$ is the mode I stress intensity factor range, $\Delta K_{\mathrm{th}}$ is the threshold below which the crack propagation rate is assumed to be zero, and $C$ and $m$ are material parameters. For structural steel in marine environment, i.e. under free corrosion, DNVGL-RP-C210 suggests $m = 3.0$, and a characteristic value (mean value plus two standard deviations) of $C$ of $2.30 \times 10^{-12}$, for $\mathrm{d}a/\mathrm{d}N$ in mm/cycle and $\Delta K$ in N/mm$^{3/2}$. The mean value of $C$ is given to be $8.35 \times 10^{-13}$. While the characteristic value should be used for design, Marquis (2011) suggests that it may be more appropriate to use the mean value of $C$ for the crack propagation assessment of a specific component. More accurate models for the fatigue crack propagation rate may also be used (Cui, Wang and Huang, 2011), but they require a larger number of material parameters. The crack propagation rate is influenced by the load ratio $R$, for instance, and this effect is often included in variations of the crack propagation law (Huffman et al., 2017; Lesiuk et al., 2018).

For mixed-mode crack propagation, it is common to use an effective stress intensity factor range, $\Delta K_v$ in the Paris law:

$$\frac{da}{dN} = C\left(\Delta K_v\right)^m \text{ for } \Delta K_v \geq \Delta K_{th} \tag{7.5}$$

The two most well-known effective stress intensity factors are those proposed by Tanaka and Richard. For mixed-mode I+II (in plane) conditions, the Tanaka (1974) effective stress intensity factor range is given by:

$$\Delta K_v = \left(\Delta K_I^4 + 8\Delta K_{II}^4\right)^{1/4} \tag{7.6}$$

According to the Richard criterion (Richard, Schramm and Schirmeisen, 2014), the effective stress intensity factor range can be taken as:

$$\Delta K_v = \frac{\Delta K_I}{2} + \frac{1}{2}\sqrt{\Delta K_I^2 + 4\left(\alpha_1 \Delta K_{II}\right)^2} \tag{7.7}$$

where $\alpha_1$ is the ratio of the material's fracture toughness in mode I to mode II. $\alpha_1$ is usually set to 1.155 for isotropic materials. Both these effective values have been shown to agree well with experimental results

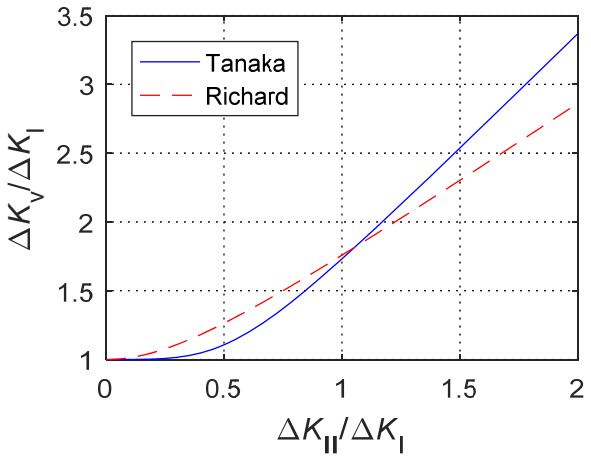


Figure 7.4 – Influence of mode mixity on effective stress intensity factor ranges

(Borrego et al., 2006; Silva et al., 2017), but few comparative studies exist. In Figure 7.4 the two proposals are compared. It is observed that Richard's $\Delta K_v$ is higher for $\Delta K_I > \Delta K_{II}$, while Tanaka's $\Delta K_v$ is higher for $\Delta K_I < \Delta K_{II}$. In many practical cases, the mode I component will dominate, in which case Richard's $\Delta K_v$ will be more conservative. For additional proposals for $\Delta K_v$, the reader is referred to the literature survey by Qian and Fatemi (1996).

Under mixed-mode conditions, a propagating crack will also change its direction of propagation. Several criteria have been proposed for estimating this direction (Rege and Lemu, 2017), with the three most well-known being the criteria of maximum tangential stress (Erdogan and Sih, 1963), maximum energy release rate (Hussain, Pu and Underwood, 1974) and minimum strain energy density (Sih, 1974). Despite the many proposed criteria, experimental results (e.g. Tanaka, 1974; Borrego et al., 2006; Peixoto and de Castro, 2017; Rozumek et al., 2018) can often be predicted by the criterion of maximum tangential stress (Erdogan and Sih, 1963) within a reasonable accuracy. This is also one of the simplest criteria to apply, as an explicit expression for the propagation angle is available (Ayatollahi, Razavi and Yahya, 2015; Spagnoli, Vantadori and Carpinteri, 2015):

$$\theta_c = 2\arctan\left\{\frac{1}{4}\left[\frac{\Delta K_I}{\Delta K_{II}} \pm \sqrt{\left(\frac{\Delta K_I}{\Delta K_{II}}\right)^2 + 8}\right]\right\} \tag{7.8}$$

## 7.3 Implementation of the methodology

The structural detail considered in this example (Figure 7.5) is taken from DNVGL-RP-C203 (DNV GL, 2016; Chen and Landet, 2001). It consists of a circular cut-out (manhole) in a plate, which is commonly found in ships and offshore structures, e.g. in floating production, storage and offloading units (FPSOs). The diameter of the cut-out is 600 mm,

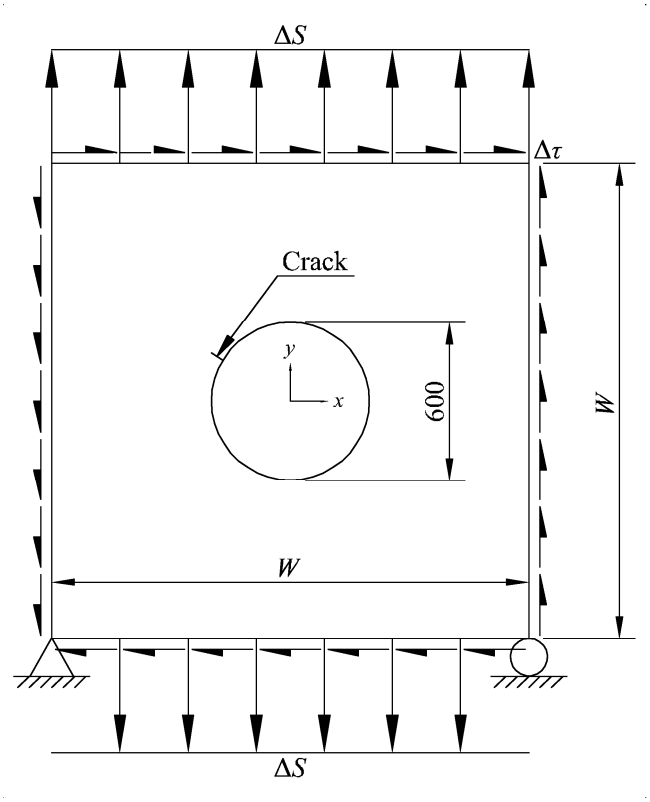


Figure 7.5 – Geometry and boundary conditions of the problem

and the plate thickness is 20 mm. No reinforcement is considered at the edge of the cut-out, but this could also be included in the analysis.

As operational conditions and environmental loads vary, the detail may be subjected to a varying combination of cyclic tensile and shear stresses. Here, a simplified case will be considered, in which a crack has been initiated to a through-thickness length of 20 mm under combined tension and shear, while further fatigue crack propagation proceeds under a pure tensile cyclic stress history, equivalent to a stress range $\Delta S = 31$ MPa at $R = S_{min}/S_{max} = \sigma_{min}/\sigma_{max} = 0.1$. When the crack has reached a length of 25 mm (i.e. 8.3 % of the radius of the cut-out), it is detected, and repaired by the stop hole technique. Cracks of this length may be found in ageing

offshore structures (Haagensen, Larsen and Vårdal, 2015). Three stop hole diameters have been considered; 10, 16 and 20 mm.

A two-dimensional analysis is carried out, using specimen *S-N* curves as described in Sections 7.2.1.2 and 7.2.1.3.

### 7.3.1 Material properties

The considered material is an offshore steel with yield strength $\sigma_y$ = 560 MPa, ultimate tensile strength $\sigma_{UTS}$ = 635 MPa, elastic modulus $E$ = 210 GPa and Poisson's ratio $\nu$ = 0.3. Its *S-N* curve under laboratory conditions at load ratio $R$ = 0.1 and frequency 10 Hz has been determined by Micone and De Waele (2017a), and is shown in Figure 7.6. The tests were performed until failure of mirror polished axial specimens with diameter 8 mm. By using the direct current potential drop technique to correlate *S-N* curves at different loading frequencies and corrosive conditions, Micone and De Waele (2017b) also estimated the *S-N* curve for the steel in seawater under typical offshore conditions (temperature

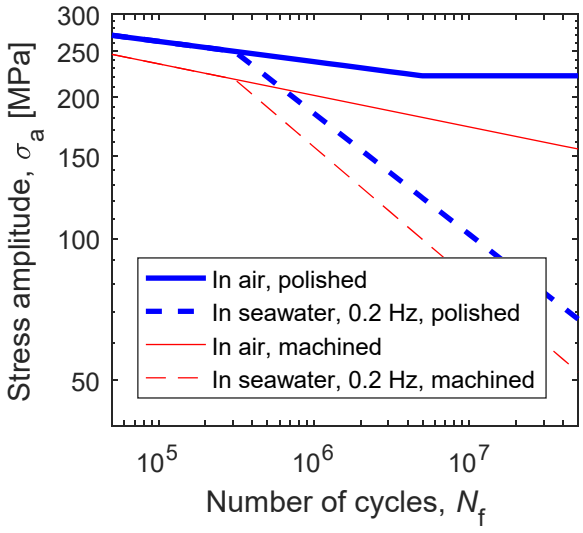


Figure 7.6 – *S-N* curves for fatigue in air and seawater at $R$ = 0.1 for polished surface (experimentally determined by Miconne and De Waele (2017a; 2017b)) and for machined surface (estimated)

8 °C and frequency 0.2 Hz). This curve is also shown in Figure 7.6. The portion of an *S-N* curve which is linear on a log-log scale may be expressed by the Basquin equation:

$$\frac{\Delta\sigma}{2} = \sigma_a = \sigma'_f \left(2N_f\right)^b \tag{7.9}$$

$\Delta\sigma$ is the stress range, $\sigma_a$ is the stress amplitude, $N_f$ is the number of cycles to fatigue failure (of the specimen), and $\sigma'_f$ and $b$ are material parameters. From Figure 7.6 it can be found that the parameters for laboratory conditions (air) are $\sigma'_f$ = 444 MPa and $b = -0.0431$, while for corrosion-fatigue in seawater the parameters are $\sigma'_f$ = 7680 MPa and $b = -0.257$ for $N_f > 3.06 \times 10^5$.

While the experimentally determined *S-N* curves represent fatigue failure of polished specimens, the surface roughness will be higher in the stop hole. Therefore, the fatigue limit should be lowered. First, an *S-N* curve for $R = -1$ which is equivalent to the *S-N* curve determined experimentally at $R = 0.1$ is constructed, using the SWT method, Equation (7.1). The fatigue limit at $R = -1$ is then multiplied by a surface factor of 0.816, determined using the recommendation for a machined surface by Budynas and Nisbett (2015). The *S-N* curve for the machined surface at $R = -1$ is constructed between this new endurance limit, and the original stress amplitude at $N_f = 10^3$ cycles. For shorter fatigue lives, the surface roughness has little influence. An equivalent *S-N* curve for the machined surface at $R = 0.1$ is then constructed using the SWT method. The resulting *S-N* curve has parameters $\sigma'_f$ = 533 MPa and $b = -0.0670$, and is also plotted in Figure 7.6. As offshore structures are subjected to variable amplitude fatigue, the fatigue limit should be disregarded. The *S-N* curve is therefore extended linearly beyond the knee-point (here: $N_e = 5 \times 10^6$), as recommended by Dowling (2013), which is more conservative than the more common Haibach modification (see e.g. Marquis, 2011).

The influence of the surface roughness on corrosion-fatigue is a more complex phenomenon, and few studies exist. However, a study by Abosrra et al. (2009) showed that the corrosion rate of a mild steel (in the absence of fatigue) decreased with increasing surface roughness. This finding makes it reasonable to keep the same number of cycles ($N_f = 3.06 \times 10^5$) for the mergence between the *S-N* curves in air and in seawater, while the surface factor of 0.816 is applied on the stress amplitude at $N_f = 5 \times 10^6$, as recommended by Dowling (2013). The parameters $\sigma_f' = 9270$ MPa and $b = -0.281$ for $N_f > 3.06 \times 10^5$ are obtained, and the *S-N* curve is shown in Figure 7.6.

It should be noted that the modified *S-N* curves are only able to give a rough estimation of the fatigue crack initiation life. More accurate predictions would be made by performing fatigue testing for the actual conditions experienced (load ratio, surface roughness, frequency and environment). The load ratio is particularly relevant for corrosion-fatigue, as mean stress relationships like the SWT method do not take stress corrosion cracking mechanisms into account.

For fatigue crack propagation, the mean material parameters given by DNV GL (2015) are used; $m = 3.0$ and $C = 8.35 \times 10^{-13}$, for $da/dN$ in mm/cycle and $\Delta K$ in N/mm$^{3/2}$.

### *7.3.2 Finite element modelling*

The structural detail was modelled by finite elements using ANSYS APDL 17.0, with boundary conditions as indicated in Figure 7.5. The length and width of the plate, *W*, was taken to be 7 times the diameter of the cut-out, as analysed by Chen and Landet (2001). The plate was discretised using eight-node quadrilateral elements. These elements can describe a quadratic displacement field, and thereby the strains and stresses can vary linearly within the elements. They may easily be made into quarter point elements (see below), which makes them optimal for crack analysis. An example of the finite element mesh is shown in

Figure 7.7. Convergence tests for the determination of the maximum principal stress at the edge of the stop hole were performed, as shown for $D$ = 10 mm in Figure 7.8. Convergence was reached with an element length of 0.05 mm at the edge of the stop hole. The corresponding mesh at the stop hole edge is shown in Figure 7.9.

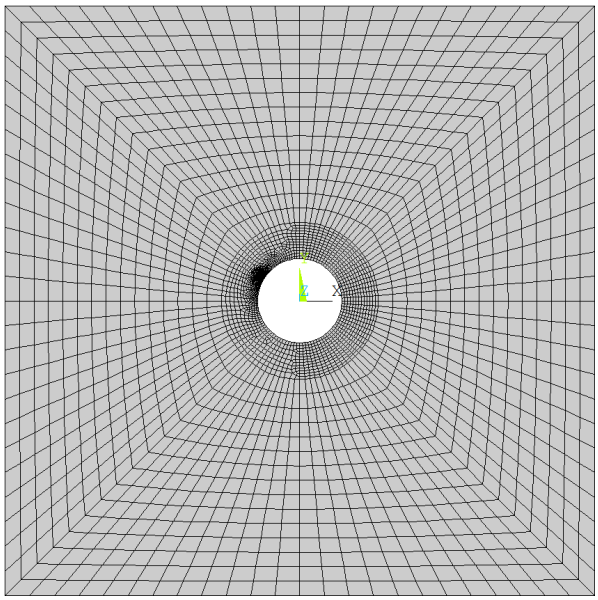

Figure 7.7 – Finite element mesh of plate

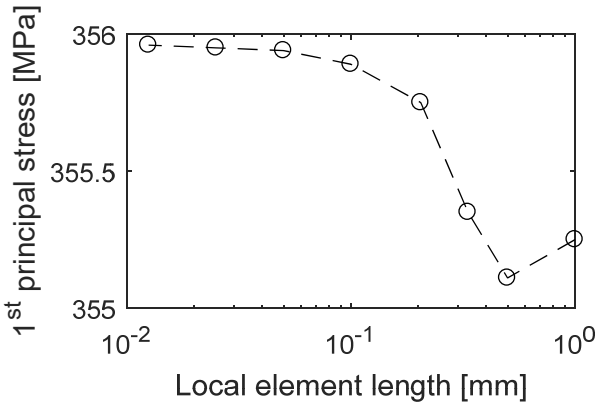


Figure 7.8 – Convergence test for $D$ = 10 mm

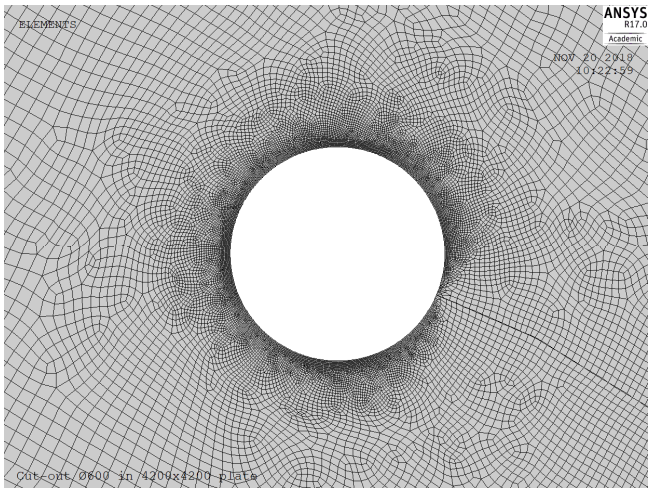


Figure 7.9 – Local mesh around 10 mm stop hole

For the evaluation of the stress intensity factor for the fatigue crack propagation analysis, a similar mesh was used. Along the length of the crack, an element length of 0.33 mm was used. At the crack tip, quarter point elements were placed in a rosette pattern, in order to represent the singularity in the linear elastic stress field at the crack tip. The interaction integral method was used to extract the stress intensity factor from the finite element solution, using the average of the values extracted from the second through the seventh ring of elements around the crack tip. The length of the quarter point elements was set to 0.1 mm. Varying their length between 0.05 and 0.3 mm resulted in a variation in the stress intensity factor of 0.02 %, indicating that convergence has been reached.

In order to confirm the suitability of the stress intensity factor computation and meshing techniques, a radial crack at the edge of a circular hole in an infinite plate subjected to axial loading was analysed. The hole radius is $R_H$, and the crack length from the edge of the hole is $a$, as shown in Figure 7.10. An analytical solution for the dimensionless stress intensity factor $F = K_I / S\sqrt{\pi a}$ was obtained by Tweed and Rooke (1973). In Table 7.1 the analytical solution is compared to those obtained

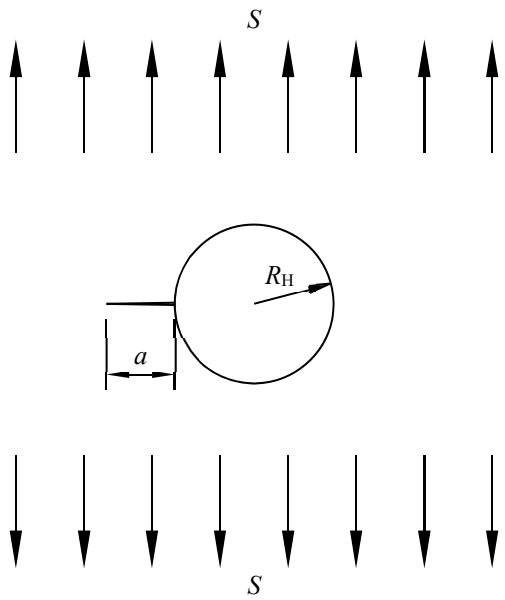


Figure 7.10 – Radial crack at the edge of a circular hole in an infinite plate

by finite element (FE) analysis here, truncating the width of the plate, $W$, to 80 times the diameter of the hole. The two solutions are found to agree within 0.13 %. This difference may be attributed to the truncation of the width of the plate. The stress intensity factor computation and meshing techniques are therefore considered to be suitable for the problem in question.

The fatigue crack propagation analysis was carried out using the global re-meshing technique (Rege and Lemu, 2017). A crack propagation increment length of 1 mm was found to be suitable. The crack increment

Table 7.1 – Comparison of FE results and analytical solution (Tweed and Rooke, 1973) for the dimensionless stress intensity factor $F$ of a radial crack at the edge of a circular hole

| $a/R_H$ | 0.01 | 0.02 | 0.06 | 0.10 | 0.14 | 0.18 | 0.20 | 0.25 | 0.30 | 0.40 | 0.50 |
|---|---|---|---|---|---|---|---|---|---|---|---|
| **Ana.** | 3.291 | 3.223 | 2.978 | 2.771 | 2.594 | 2.442 | 2.373 | 2.221 | 2.092 | 1.884 | 1.727 |
| **FE** | 3.295 | 3.226 | 2.981 | 2.774 | 2.596 | 2.444 | 2.376 | 2.223 | 2.094 | 1.886 | 1.729 |

was added in the direction of maximum tangential stress (Equation 7.8). The Paris law (Equation 7.5) was used together with the Richard effective stress intensity factor (Equation 7.7) to estimate the crack propagation life up to a total crack length of 75 mm. If the fracture toughness of the steel is known, the critical crack length for fracture may be found from the procedure given in BS 7910 (British Standards Institution, 2015).

### 7.3.3 Results and discussion

The results for the fatigue crack re-initiation at the stop hole edge are shown in Table 7.2. If the stop hole is not coated after drilling, it is exposed to the marine atmosphere, and corrosion-fatigue conditions are assumed. If the stop hole is completely coated however, the condition is considered to correspond that of fatigue in air, as long as the coating remains unbroken (Lotsberg, 2016). From Table 7.2, it is seen that the application of coating has a significantly larger influence on the efficiency of the stop hole than its diameter. This is particularly pronounced in this example, due to the large difference between the slopes of the *S-N* curves in air and in seawater.

The distribution of the first principal stress range around the 10 mm stop hole is presented in Figure 7.11. The maximum value of the first principal stress occurs at an angle of 185 ° away from the existing crack. The proceeding crack path is therefore relatively unaffected by the stop hole. This is true for all the three stop hole diameters investigated, as illustrated in Figure 7.12.

Table 7.2 – Range of maximum principal stress at stop hole edge, and estimated crack growth delay

| Stop hole diameter, $D$ [mm] | 10 | 16 | 25 |
|---|---|---|---|
| Maximum principal stress range, $\Delta\sigma_{loc}$ [MPa] | 356 | 304 | 267 |
| Crack growth delay (uncoated) [million cycles] | 0.643 | 1.13 | 1.79 |
| Crack growth delay (coated) [million cycles] | 6.43 | 67.9 | 471 |
| Initiated crack length, $l_0$ [mm] | 0.77 | 1.21 | 1.84 |

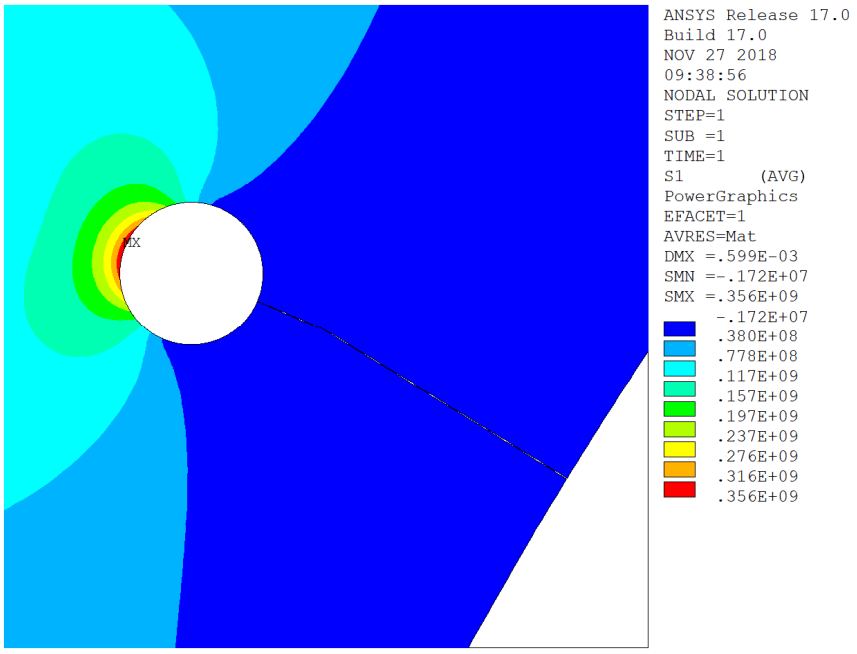


Figure 7.11 – First principal stress range near 10 mm stop hole

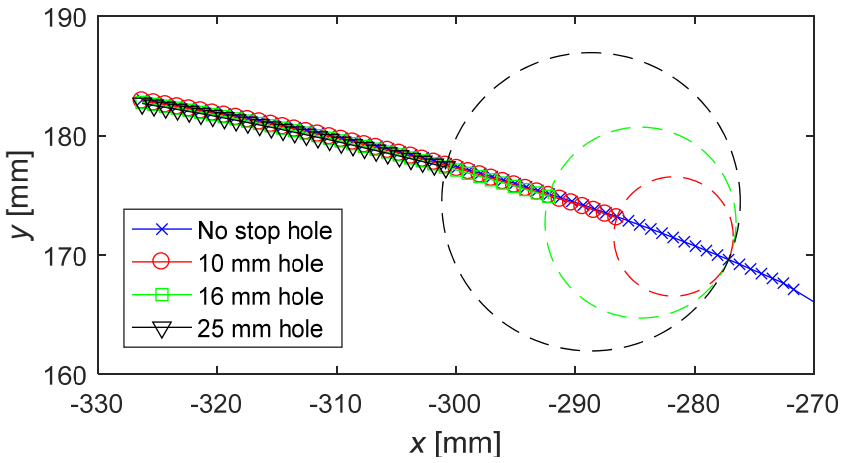


Figure 7.12 – Predicted fatigue crack propagation paths

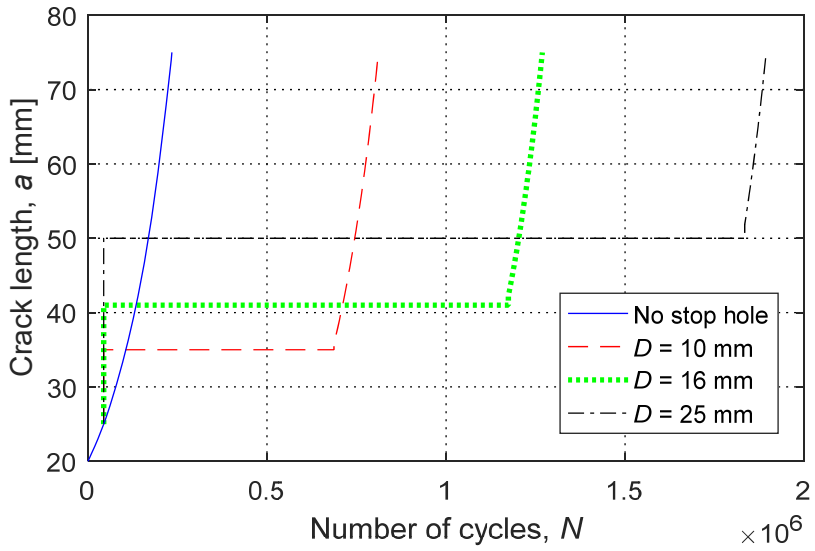


Figure 7.13 – Fatigue crack propagation and delay under corrosive conditions

In Figure 7.13 the estimated fatigue crack propagation up to a total length of 75 mm, both in the presence and absence of stop holes, is illustrated for the case where the stop hole is not coated, i.e. for fatigue-corrosion in a marine atmosphere. It is clear that even in the absence of coating, the stop hole significantly increases the total fatigue life of the detail. The life to 75 mm is estimated to increase by 246 %, 441 % and 707 %, by the 10, 16 and 25 mm stop holes, respectively, when compared with the alternative of not drilling a stop hole.

As the loading direction in this example is changed only once, the curvature of the crack path is small. It could be argued that it would be sufficiently accurate to model the curved crack as a straight crack, thereby allowing handbook solutions to be used. By combining the solution of a straight crack at the edge of a circular hole under uniaxial loading (Figure 7.10) (Tweed and Rooke, 1973) with the modification for an angle between the crack and the uniaxial stress presented by Anderson (2005), the stress intensity factor and fatigue crack propagation may be estimated, as shown in Figure 7.14. It is seen that if

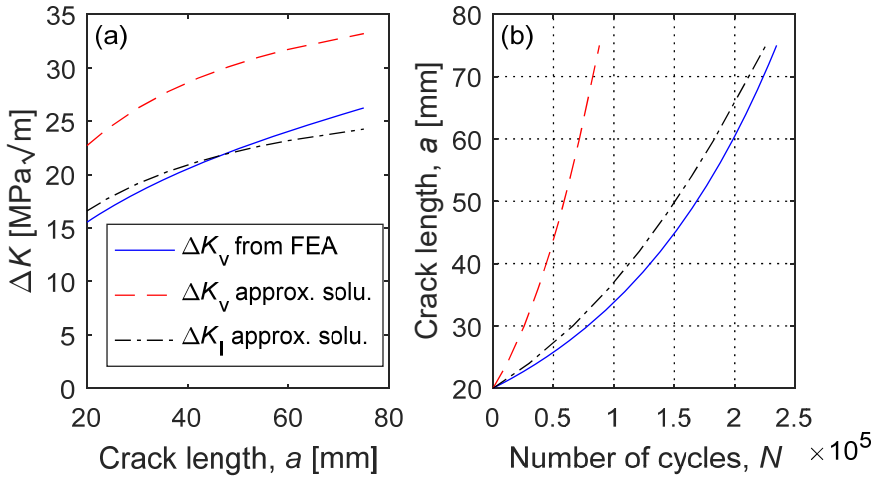


Figure 7.14 – (a) Stress intensity factor and (b) crack length evolution estimated by finite element analysis (FEA) and by the straight crack approximated solution. $\Delta K_v$ is calculated using the Richard criterion (Equation 7.7)

the mode II component of this approximation is taken into account in the effective stress intensity factor, the estimation becomes excessively conservative, because in reality the crack would quickly deflect to an angle in which mode I conditions dominate. If only the approximated mode I component is considered however, the estimated crack propagation is reasonably well approximated, but as the crack grows long, the approximated mode I stress intensity factor becomes increasingly non-conservative, thereby leading to a non-conservative estimation of the critical crack length. This justifies the application of a numerical model for the fatigue crack propagation analysis.

## 7.4 Conclusions

In this paper a procedure for modelling the fatigue crack growth delay induced by drilling a stop hole has been proposed for mixed-mode I+II conditions. Both fatigue crack initiation and fatigue crack propagation phases are modelled, and the transition between the two phases is explicitly considered. The procedure has been implemented on an example, and the following findings were made:

- A significant increase in the life extension may be obtained if the surface of the stop hole can be protected against the corrosive marine environment, e.g. by coating. It is often more effective to coat a small stop hole than drilling a larger stop hole.
- When the mode II component of the stress intensity factor range is low, the proceeding crack propagation path is left relatively unchanged by the stop hole.

The proposed procedure may be used to evaluate the application of the stop hole technique in a practical situation, and thereby to compare it to other life extension techniques. In order to make accurate estimations, it is necessary to have access to reliable fatigue crack initiation data (*S*-*N* curves) for the material under the actual operating conditions (load ratio, surface roughness, frequency and environment).

## Acknowledgements

The authors thank O. Mikkelsen for useful discussions of the finite element model. This work was supported by the Norwegian Ministry of Education and Research.

# 8 Paper V: Stress intensity factors for circumferential through-wall cracks in thin-walled cylindrical shells subjected to tension and torsion

[*]Kristen Rege, Dimitrios G. Pavlou

Department of Mechanical and Structural Engineering and Materials Science, University of Stavanger, Stavanger, Norway

**Abstract**: In order to assess the structural integrity of tubular members or pipes containing circumferential through-wall cracks, their stress intensity factor solutions are required. While stress intensity factors for tension and bending are available, few solutions exist for the case of torsion, even though these components may also be subjected to torque. In this paper, the finite element method is used to compute the stress intensity factors for this geometry under tension and torsion. Shell elements are employed to compute the results for thin shells by the means of the displacement extrapolation technique. The computed results indicate that the available analytical solution for torsional loading, which is based on shallow shell theory, is non-conservative for long cracks in thin shells. Shallow shell theory is in general not applicable to long cracks, and the present work is therefore able to provide solutions for a wider range of crack lengths than what is currently available.

[*] Previously published as: Rege, K. and Pavlou, D.G. (2019) Stress intensity factors for circumferential through-wall cracks in thin-walled cylindrical shells subjected to tension and torsion, *Fatigue & Fracture of Engineering Materials & Structures*, 42(5), pp. 1062–1074. doi: 10.1111/ffe.12970

## 8.1 Introduction

Flaws may develop in tubular members in offshore structures and in piping components, due to corrosion and fatigue crack initiation. In order to ensure the safety of these structures, their integrity needs to be monitored and assessed (Aeran et al., 2017; Moan, 2017). If flaws/cracks are observed, a stress intensity factor solution for the geometry in question is required, in order to assess the remaining fatigue life of the component (Keprate, Ratnayake and Sankararaman, 2017b). In the design phase, fatigue failure is normally defined as the presence of a crack extending through the thickness of the wall (Moan, 2017), and a significant amount of research is therefore focusing on the stress intensity factor solution for surface cracks (Predan, Močilnik and Gubeljak, 2013; Qian, Gonzalez-Albuixech and Niffenegger, 2014; Zareei and Nabavi, 2016; Keprate, Ratnayake and Sankararaman, 2017b). However, through-wall cracks may still be developed in tubular members in offshore structures, in connection with girth welds (Pereira, 2004) or other stress raisers (Lotsberg, 2016). Knowledge of the stress intensity factor for circumferential through-wall cracks is also required for the evaluation of leak-before-break behaviour (Takahashi, 2002; Huh et al., 2008), stress corrosion cracking and crack stability (Shim, Xu and Lee, 2014) for piping, e.g. in nuclear power plants.

While stress-intensity factor solutions for circumferential through-wall cracks in cylindrical shells subjected to tension and bending have been extensively studied in the past (Takahashi, 2002; Shim, Xu and Lee, 2014), few solutions exist for a shell subjected to torsion, even though both tubular members in offshore structures (e.g. jacket structures) (Rhee, 1989) and power plant piping (Hasegawa, Li and Osakabe, 2014; Hojo et al., 2014; Guzman-Leong and Udyawar, 2017; Li et al., 2017) may be subjected to torsional loads. A jacket or fixed steel platform is a trusswork tower consisting of tubular members with piles into the seabed, and a topside, used e.g. for oil and gas production. A jacket structure may also be used as the support structure for an offshore wind

turbine (Adedipe, Brennan and Kolios, 2016). Accurate stress intensity factor solutions for cracks under axial/torsional loading conditions are necessary for the prediction of mixed-mode fatigue crack growth, which may occur, e.g. due to the multi-directional nature of the environmental loads acting on offshore structures (Mshana, Kam and McDiarmid, 1992). The solutions may also be useful in the preliminary design of mixed-mode fatigue crack propagation tests (Yu, Li and Proust, 2017).

The objective of this study is to obtain solutions for the stress-intensity factor for circumferential through-wall cracks in thin-walled cylindrical shells subjected to torsion, using the finite element method (FEM). The developed finite element (FE) model is verified for cracks under tensile loading as well.

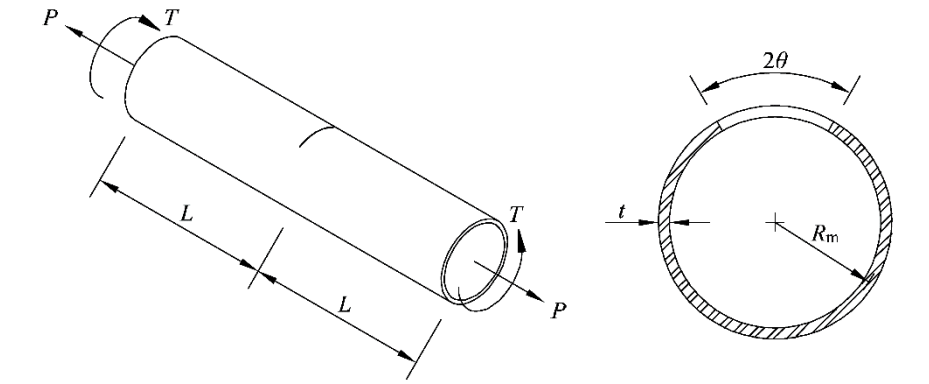


Figure 8.1 – Circumferential through-wall crack in a cylindrical shell subjected to tension $P$ and torque $T$

Expressions for the stress intensity factor for circumferential through-wall cracks (Figure 8.1) in cylindrical shells subjected to tension may be found in handbooks. *The Stress Analysis of Cracks Handbook* by Tada, Paris and Irwin (2000) gives the analytical solution obtained by Sanders (1982). This analytical solution is based on a complete shell analysis for elastic shells with long cracks. According to *The Stress Analysis of Cracks Handbook* (Tada, Paris and Irwin, 2000), this solution is accurate

within 1 % for $\theta/\sqrt{t/R_m} = a/\sqrt{R_m t} > 5$, where $2\theta$ is the circumferential angle of the crack, $R_m$ is the mean radius of the cylinder, $t$ is its thickness, as illustrated in Figure 8.1, and $2a = 2R_m\theta$ is the crack arc length measured along the mid-thickness. While Sanders' analytical solution is applicable to long cracks, earlier analytical solutions based on the shallow shell theory are applicable to short cracks. In the same paper, Sanders (1982) developed an interpolated solution by combining his own analytical solution with that of the shallow shell theory, thereby obtaining a single solution valid for all crack lengths. This interpolated solution has been shown to agree very well with FE results by Forman, Hickman and Shivakumar (1985), and extended finite element method (XFEM) results by Zarrinzadeh, Kabir and Deylami (2017). Zahoor (1985) generated an alternative, conservative version of Sanders' interpolated solution, limited to $5 \leq R_m/t \leq 20$, which was included in Zahoor's (1989) *Ductile Fracture Handbook*.

In 2002, Takahashi (2002) reviewed various solutions for tensile and bending loading, and recommended an interpolation of FE results by Lacire, Chapuliot and Marie (1999) for general use for $R_m/t$ between 1.5 and 100, and crack angles $2\theta$ below 220 °. Takahashi (2002) focused on FE results, and did not compare these results with Sanders' (1982) interpolated solution. More recently, three solutions from the literature, including the solution by Lacire, Chapuliot and Marie (1999), were compared with new finite element analyses by Shim, Xu and Lee (2014). They found the results by Lacire, Chapuliot and Marie to be a little conservative, and proposed an extension of an earlier closed-form solution by interpolating results from fully three-dimensional finite element analyses.

The case of bending loading has been thoroughly discussed by others (Forman, Hickman and Shivakumar, 1985; Takahashi, 2002; Shim, Xu and Lee, 2014), and will therefore not be considered in the current work.

For the case of torsional loading, an analytical solution for the stress intensity factor was derived using Marguerre shallow shell theory, and presented in tabular and graphical form, by Erdogan and Ratwani (1972). In the Marguerre shallow shell theory, it is assumed that the squares and products of the slopes of the middle surface with regard to a reference plane are negligible, compared to unity (Elias, 1967). Due to this assumption, as discussed by Sanders (1982) for the case of tension, the shallow shell theory is not applicable to long cracks. Lakshminarayana and Murthy (1976) did also apply shallow shell theory and a perturbation technique to solve the case of an arbitrarily oriented through-wall crack. Analytical solutions which are not based on the shallow shell theory seem not to be available. In 1989 a finite element analysis (FEA) of the problem was performed by Kumosa and Hull (1989), indicating that the shallow shell theory (Erdogan and Ratwani, 1972) gave too low values for the stress intensity factor. However, relatively few combinations of radii, thicknesses and crack lengths were considered, and the results are only available in the format of graphs, making them difficult to use. The same geometry was also analysed using FEA with shell elements by Xing and Zhou (2018), but only for short cracks. The computational results by Xing and Zhou (2018) were generally a little lower than those of Kumosa and Hull (1989).

In this paper the finite element method is used to compute the stress intensity factors for circumferential through-wall cracks in cylindrical shells subjected to tension and torsion. The analyses are limited to thin to moderately thick shells which may be modelled by shell elements, thereby reducing the computation cost compared to performing fully three-dimensional finite element analyses. Analyses are performed for thickness ratios $R_m/t$ between 10 and 80. Tubular sections in offshore jacket structures do typically have a thickness ratio $R_m/t$ between 10 and 20 (Lotsberg, 2009). The displacement extrapolation technique is used to obtain the stress intensity factor from the finite element results.

The solutions are tabulated as dimensionless geometry factors, allowing for interpolation.

## 8.2 Description of the problem

The geometry in question is illustrated in Figure 8.1. A cylindrical shell, with mean radius $R_m$, wall thickness $t$ and length $2L$, contains a circumferential through-wall crack extending over an angle $2\theta$. The crack arc length measured along the mid-thickness is $2a = 2R_m\theta$. The cylinder is subjected to a tensile force $P$, and/or a torque $T$ applied at each end. The tensile force corresponds to a uniform remote tensile stress:

$$\sigma_0 = \frac{P}{2\pi R_m t} \tag{8.1}$$

The torque leads to a remote shear stress distribution $\tau = TR/J$, where $R$ is radial distance and $J = \pi R_m t\left(4R_m^2 + t^2\right)\big/2$ is the polar moment of inertia for the cross-section. The remote mid-thickness shear stress is:

$$\tau_0 = \frac{2T}{\pi\left(4R_m^2 + t^2\right)t} \tag{8.2}$$

The tensile load will lead to mode I loading of the crack, while the torsional load will lead to mode II loading. It is convenient to define the membrane component of the stress intensity factors for the circumferential through-wall crack as follows, with $F_I$ and $F_{II}$ being dimensionless geometry factors:

$$K_I = F_I\sigma_0\sqrt{\pi a} \tag{8.3}$$

$$K_{II} = F_{II}\tau_0\sqrt{\pi a} \tag{8.4}$$

The stress intensity factors do also have a bending component (Viz et al., 1995), because of the through-thickness variation of the stresses near the crack tip. These bending components have been shown to be very small in both tension and torsion according to the shallow shell theory (Erdogan and Ratwani, 1972), and are usually neglected in the case of tensile loading (Sanders, 1982; Forman, Hickman and Shivakumar, 1985; Zahoor, 1985; Lacire, Chapuliot and Marie, 1999; Takahashi, 2002; Shim, Xu and Lee, 2014). Finite element results (Kumosa and Hull, 1989) suggest that these bending components are significant for the case of torsion however. But these results were obtained by a finite element model containing only one layer of twenty-node rectangular solid elements. It is questionable whether such a model is capable of accurately representing the through-thickness variation of the stress, considering that more recent fully three-dimensional models (Lacire, Chapuliot and Marie, 1999; Ghaffari and Hosseini-Toudeshky, 2013; Shim, Xu and Lee, 2014; Gintalas, Ainsworth and Scenini, 2017) use between 8 and 24 layers of solid elements through the thickness of the shell. In the current study, the membrane components were the main focus, and therefore shell elements were applied. This choice excludes the investigation of the through-thickness variation, which is suggested for later study.

It has been shown by Forman, Hickman and Shivakumar (1985) that the stress intensity factor depends on the length and boundary conditions of the shell. The stress intensity factor does generally increase as the shell is shortened. Analytical solutions are normally obtained for the case of a very long shell, where the crack is not influenced by end effects. Stress intensity factors in tension for half lengths $L = 2.67\pi R_m$ and $L = 5.17\pi R_m$ were shown to be indistinguishable by Forman, Hickman and Shivakumar (1985). The half-length $L = 5\pi R_m$ has therefore been used in the current work, in order to avoid end effects.

## 8.3 Finite element analysis

Lacire, Chapuliot and Marie (1999) showed that the difference between using shell elements and solid elements to model the problem with a tensile load was small for $R_m/t \geq 10$. As the bending component of the stress intensity factor for torsion is claimed to be negligible by Erdogan and Ratwani (1972), it was chosen to use shell elements to perform finite element analyses for thickness ratios $R_m/t$ between 10 and 80 in the current study. Shell elements have been used in the literature to analyse this problem, both for tensile (Forman, Hickman and Shivakumar, 1985; Zarrinzadeh, Kabir and Deylami, 2017) and torsional (Xing and Zhou, 2018) loading.

The finite element analyses were performed using ANSYS Mechanical APDL 17.0. The cylinder was modelled using the element type SHELL281, which is an eight-node isoparametric quadrilateral shell element. It includes the effects of transverse shear deformation, and is suitable for analysing thin to moderately-thick shell structures. Therefore, the cases of $R_m/t = 10$ and 20 have been analysed, even though a shell is usually considered to be thin-walled when $R_m/t > 20$ (Cook et al., 2002).

### 8.3.1 Evaluation of the stress intensity factor

The interaction integral method (Shih and Asaro, 1988) is generally considered to be the best method for determining the stress intensity factor from a finite element solution for the stress and displacement fields (Anderson, 2005; Banks-Sills, 2010; Zhu and Leis, 2014; Rege and Lemu, 2017). However, the interaction integral method is not available for shell elements in the current version of ANSYS. As an alternative, a displacement method may be used, but requires a finer mesh at the crack tip (Anderson, 2005; Banks-Sills, 2010; Zhu and Leis, 2014; Rege and Lemu, 2017).

According to the original displacement method, which is called the displacement extrapolation technique, the following quantities should be computed for each node along the crack face (Chan, Tuba and Wilson, 1970; Lim, Johnston and Choi, 1992):

$$K_{\mathrm{I}}^{*} = \frac{E^{*} u_y}{4}\sqrt{\frac{2\pi}{r}} \tag{8.5}$$

$$K_{\mathrm{II}}^{*} = \frac{E^{*} u_x}{4}\sqrt{\frac{2\pi}{r}} \tag{8.6}$$

$E^* = E$ for plane stress and $E/(1-\nu^2)$ for plane strain. $E$ is Young's modulus, $\nu$ is Poisson's ratio, $u_x$ and $u_y$ are nodal values of displacement parallel and normal to the crack, respectively, and $r$ is the node's distance from the crack tip, as illustrated in Figure 8.2. For the case of a circumferential crack considered in the current work, $r$ is measured along the mid-thickness circumference of the cylinder. $u_x$ and $u_y$ are displacements relative to the crack tip node. $K^*$ is computed for each node along the crack face, and extrapolated to $r = 0$. This intercept is used as the $K$ estimate.

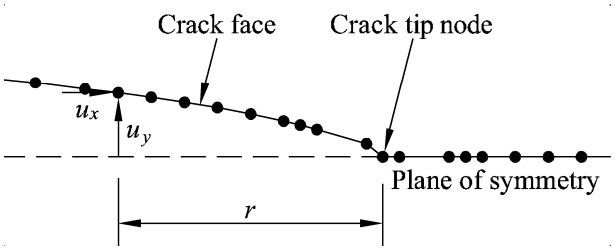


Figure 8.2 – Nodes along the crack face and plane of symmetry. The displacement is scaled by a factor of 25

The stress method (Chan, Tuba and Wilson, 1970) is another technique, in which $K^*$ is computed from the computed stress field instead of the nodal displacements. This method is more sensitive to changes in the mesh than the displacement extrapolation technique, but was used in the

current study to confirm the choice of range which was used for extrapolation of $K^*$ computed from nodal displacements.

### 8.3.2 Finite element modelling

The finite element analyses were carried out for a cylindrical shell with mean radius $R_m = 100$ mm, half-length $L = 5\pi R_m$, Young's modulus $E = 200$ GPa and Poisson's ratio $\nu = 0.33$. The cylinder is subjected to a remote tensile stress $\sigma_0 = 50$ MPa, and a remote mid-thickness shear stress $\tau_0 = 50$ MPa, each applied individually. Analyses were performed for $R_m/t = 10$, 20, 40 and 80. The circumferential crack angle $2\theta$ was varied between 20 ° and 180 °.

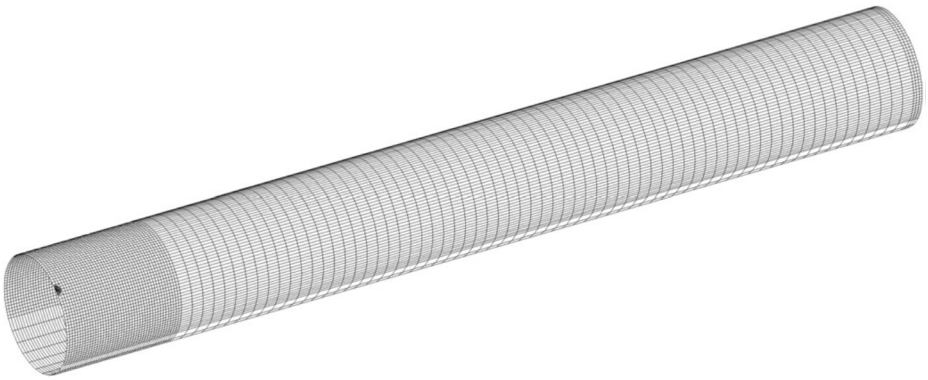

Figure 8.3 – Finite element mesh for $R_m/t = 40$ and $\theta = 40$ °

The finite element mesh employed in the current study is illustrated in Figure 8.3. As the problem is symmetric or antisymmetric when the cylinder is subjected to tension or torsion, respectively, only half the cylinder was modelled. Quarter-point elements (Henshell and Shaw, 1975; Barsoum, 1976) were used in a rosette pattern at the crack tip, in order to model the singularity in the stress field. These elements have their mid-side node moved to one quarter of the element length away from the crack tip. This modification makes the stress field within the element vary inversely with the square root of the distance from the crack tip, as predicted by linear elastic fracture mechanics. If the interaction

integral method is used to extract the stress intensity factor, the crack tip mesh may be relatively coarse, and sizing recommendations may be found, e.g. in Cook et al. (2002). However, when the displacement extrapolation technique is used, a finer crack tip mesh is required, and few general recommendations exist. Menandro, Moyer and Liebowitz (1995) optimized the crack tip mesh design for this technique for three basic problems, and some of those recommendations were taken into account here.

Eight elements were used in each half ring in the crack tip mesh, as stated to be optimal by Menandro, Moyer and Liebowitz (1995). This also enables an effective transition to the structured mesh away from the crack tip, as shown in Figure 8.4. The number of rings was adjusted to keep a smooth transition in element size. The shortest length of the transition element, $l_2$ in Figure 8.4, was kept equal to 20 % of the length of the square elements, $l_e$. It was found that varying this value between 10 % and 60 % did not influence the value of the extracted stress intensity factor.

The stress field at the crack tip will generally be the sum of a singular term, and a finite term varying nonlinearly with position (Harrop, 1982). Neither the quarter-point elements nor the eight-node quadrilateral

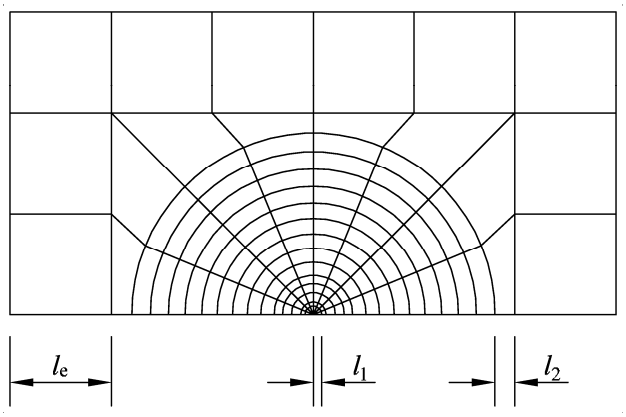


Figure 8.4 – Crack tip mesh

elements are able to represent both these terms. Therefore, the quarter-point element needs to cover the range where the singular term dominates. In this study, the radial length of the quarter-point element was chosen so as to yield a relatively smooth transition in the stress field between the quarter-point elements and the normal elements, when the cylinder is subjected to tension. This is illustrated in Figure 8.5. It was found that the radial length $l_1 = a/160$ fulfilled this criterion for the geometries considered here, and has therefore been used for all cases. The same mesh was also used for the torsional load.

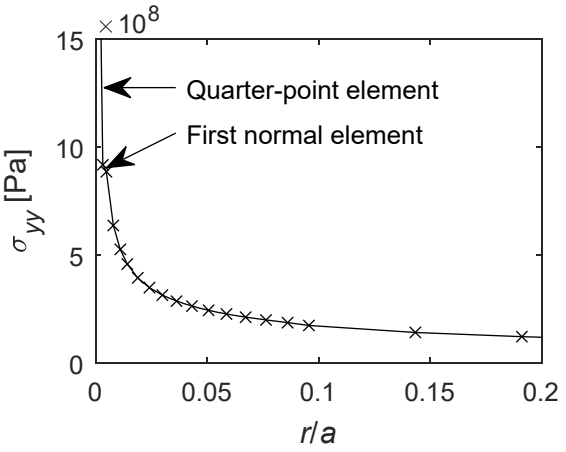


Figure 8.5 – Nodal values of stress along the circumference of the cylinder ($R_m/t = 20$ and $\theta = 30$ °), measured from the crack tip

Beyond the crack tip mesh, a structured mesh of quadrilateral shell elements was used. Each element was approximately $0.05R_m$ wide (along the circumference) and high. Further away from the crack, element lengths of $0.2R_m$ were used. If either element length was halved, the difference in the computed dimensionless geometry factor was less than 0.5 %. The structured mesh was therefore considered to be suitable for the problem. At the loaded end of the cylinder, three rows of elements were used within the axial distance $\sqrt{R_m t}$ from the end, as recommended

by Cook et al. (2002). The finite element meshes used contained between 13 663 and 57 612 elements.

The tensile stress was applied as a surface load on the circumference of one end of the cylinder, while the symmetric boundary condition available in ANSYS was applied to the other end, excluding the crack face. All degrees of freedom were locked in one node directly opposite to the middle of the crack, in order to disable rigid-body translations and rotations. The tensile surface load was automatically transformed to nodal loads by ANSYS. For the torsional load, this feature is not available; therefore consistent nodal loads (Cook et al., 2002) were computed, and applied directly to each node. In this case the antisymmetric boundary condition available in ANSYS was applied to the other end of the cylinder. MATLAB R2016b was used to generate input commands to ANSYS APDL, specifying the crack tip mesh and consistent nodal loads, and also to post process the computed stress and displacement fields.

## 8.4 Results and discussion

For all the cases analysed, the quantities $F_{\mathrm{I}}^{*} = K_{\mathrm{I}}^{*} \big/ \sigma_0 \sqrt{\pi a}$ and $F_{\mathrm{II}}^{*} = K_{\mathrm{II}}^{*} \big/ \tau_0 \sqrt{\pi a}$ were computed for all the nodes along the crack face, assuming plane stress conditions, and plotted against the circumferential distance $r$ from the crack tip, as shown in Figures 8.6 and 8.7. As also noted by Lim, Johnston and Choi (1992) the resulting plots are curved, and it may be relatively difficult to choose which nodes to use for extrapolation. However, for some crack angles, e.g. $\theta = 60\,°$ in Figure 8.6 and $\theta = 40\,°$ in Figure 8.7, the linear portion of the curve is clearly visible. By studying the shape of each curve, it was found that for a given value of $R_{\mathrm{m}}/t$, if the linear portion was clearly distinguishable, it would lie at the same distance from the crack tip, independently of the crack angle. It was assumed that this observation could be valid for all crack angles (above $\theta = 10\,°$). Therefore, nodes within the same range of $r$ were

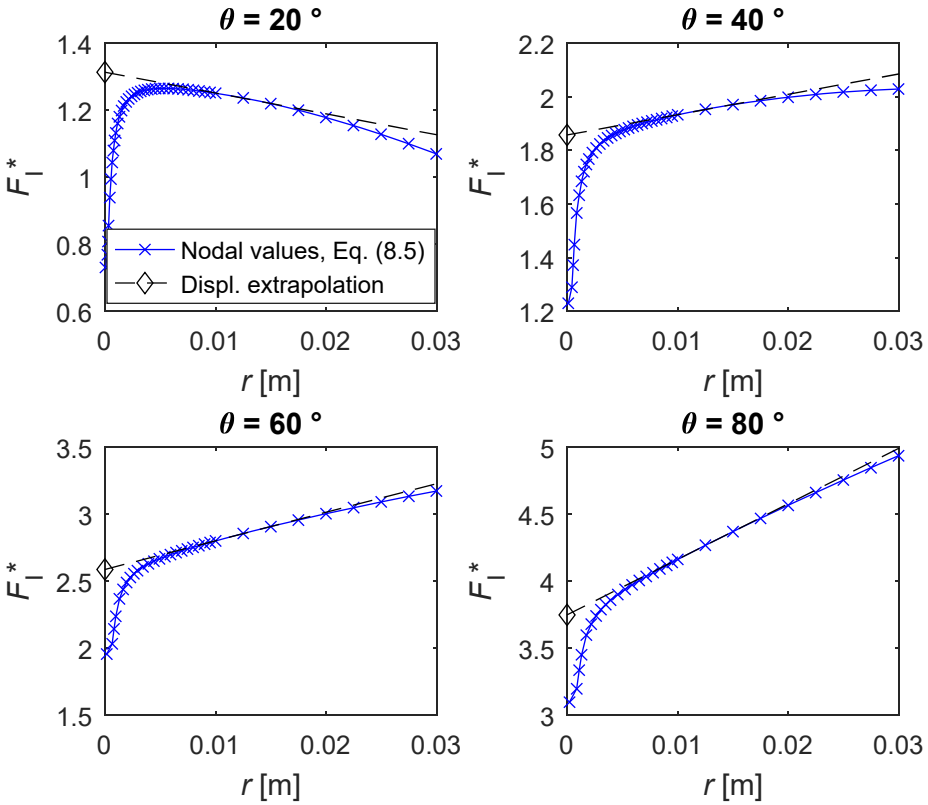


Figure 8.6 – Displacement extrapolation for mode I (tensile loading). $R_m/t = 20$

used for the extrapolation to $r = 0$, for all crack angles, for a given value of $R_m/t$. This range was not equal for mode I and mode II loading however. The ranges of $r$ used for extrapolation are specified in Table 8.1. This assumption was further strengthened by comparison with stress intensity factors computed by the stress method, which generally agreed very well with those computed by the displacement extrapolation technique from these ranges.

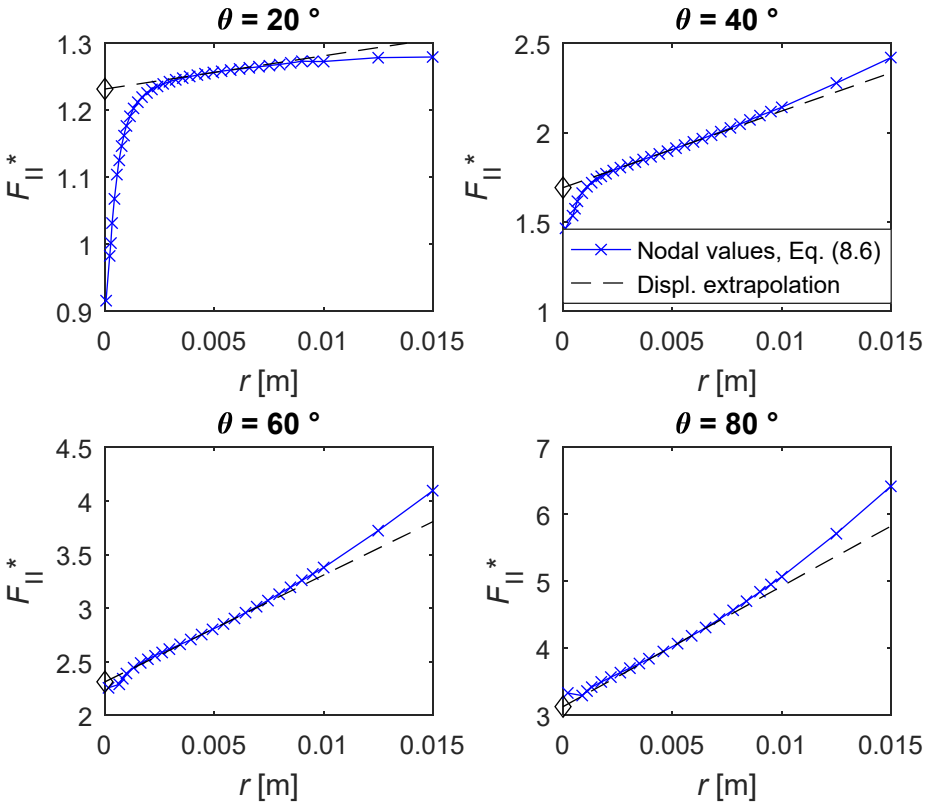


Figure 8.7 – Displacement extrapolation for mode II (torsional loading). $R_m/t = 20$

Table 8.1 – Ranges of $r$ used for extrapolation of $F_I$* and $F_{II}$*

| $R_m/t$ | 10 | 20 | 40 | 80 |
|---|---|---|---|---|
| **Range of *r* [mm] for mode I** | 10–15 | 10–15 | 5–10 | 5–10 |
| **Range of *r* [mm] for mode II** | 5–7 | 4–6 | 2.5–4.5 | 1.5–3.5 |

### 8.4.1 Tensile loading

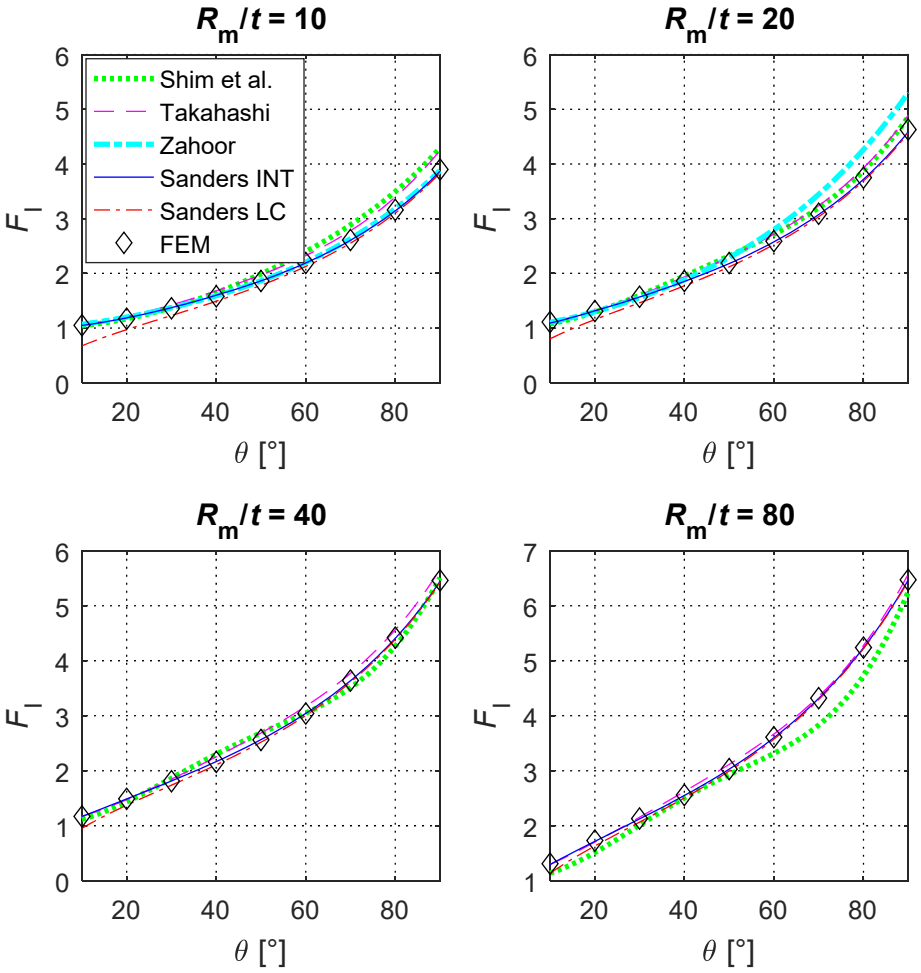


Figure 8.8 – Dimensionless shape factor $F_I$ for tensile loading. Comparison between closed-form solutions by Shim, Xu and Lee (2014), Takahashi (2002) and Zahoor (1985), Sanders' (1982) interpolated (INT) and long crack (LC) solutions, and FEM results obtained here

The dimensionless shape factors, computed by the displacement extrapolation technique using the ranges given in Table 8.1, are shown in Figure 8.8 for tensile loading. Their values are also given in Table 8.2. The FEM results are compared with five solutions found in the literature. Sanders' (1982) long crack solution and Zahoor's (1985) solution are

included because they are given in handbooks (Zahoor, 1989; Tada, Paris and Irwin, 2000). Takahashi (2002) and Shim, Xu and Lee (2014) performed extensive reviews of available solutions, each proposing an interpolation of certain finite element solutions. Neither review considered Sanders' (1982) interpolation of two analytical solutions, which was found to agree with finite element solutions by Forman, Hickman and Shivakumar (1985).

It is observed that the FEM results obtained here agree very well with Sanders' interpolated solution, and therefore also the FEM results by Forman, Hickman and Shivakumar (1985) and XFEM results by Zarrinzadeh, Kabir and Deylami (2017), both using shell element models. Sanders' long crack solution, given in the handbook (Tada, Paris and Irwin, 2000), agrees well for long cracks (as intended), but seems to be non-conservative for short cracks, especially for thicker cylinders. Zahoor's solution is only intended for $5 \leq R_m/t \leq 20$. For $R_m/t = 10$ it agrees with the FEM results, while for long cracks in thinner cylinders it becomes increasingly more conservative, also as intended (Zahoor, 1985).

Table 8.2 – Dimensionless shape factor $F_I$ for tension

| $\theta$ [°] | $R_m/t$ | | | |
|---|---|---|---|---|
| | **10** | **20** | **40** | **80** |
| **10** | 1.05 | 1.11 | 1.17 | 1.31 |
| **20** | 1.17 | 1.31 | 1.49 | 1.73 |
| **30** | 1.36 | 1.57 | 1.81 | 2.13 |
| **40** | 1.58 | 1.86 | 2.16 | 2.56 |
| **50** | 1.86 | 2.19 | 2.56 | 3.03 |
| **60** | 2.19 | 2.59 | 3.04 | 3.61 |
| **70** | 2.61 | 3.09 | 3.64 | 4.32 |
| **80** | 3.16 | 3.75 | 4.42 | 5.24 |
| **90** | 3.90 | 4.63 | 5.46 | 6.47 |

While the above solutions are based on shell theory or shell finite element models, the solution by Shim, Xu and Lee (2014) is based on interpolation of fully three-dimensional finite element analyses. Their solution predicts higher values for long cracks when $R_m/t = 10$, but lower when $R_m/t = 80$. Takhashi's (2002) solution is an interpolation of finite element results using shell elements for $R_m/t > 10$ and a fully three-dimensional model for $R_m/t \leq 10$. This explains why it is closer to Shim, Xu and Lee for $R_m/t = 10$, while for $R_m/t = 80$ it agrees with the other solutions.

The finite element model used in the current study agrees well with the other solutions based on shell formulations. It should be noted that for $R_m/t = 20$ and $R_m/t = 40$ all the solutions considered agree reasonably well. For $R_m/t = 10$ and $R_m/t = 80$ the solution deviates from those from fully three-dimensional finite element analysis, possibly due to effects of the through-thickness variation of the stresses. Shim, Xu and Lee (2014) averaged the stress intensity factor over the thickness of the cylinder, but its actual variation through the thickness was not shown. This should be considered in future works.

### *8.4.2 Torsional loading*

Due to the finite element model's excellent agreement with comparable solutions for the case of tensile loading, it has also been used to analyse the case of torsional loading. The results for the dimensionless shape factor $F_{II}$ are shown in Figure 8.9, and are also given in Table 8.3. The results are compared with the analytical shallow shell solution by Erdogan and Ratwani (1972), which is available for values of $\lambda = \left[12\left(1-\nu^2\right)\right]^{1/4} a/\left(R_m t\right)^{1/2}$ between 0 and 10. It is observed that for $\lambda \leq 5$ the two solutions agree quite well, while for $\lambda > 5$, the FEM results are considerably higher. This was expected, as the shallow shell theory is only suitable for short cracks (Sanders, 1982). This means that the

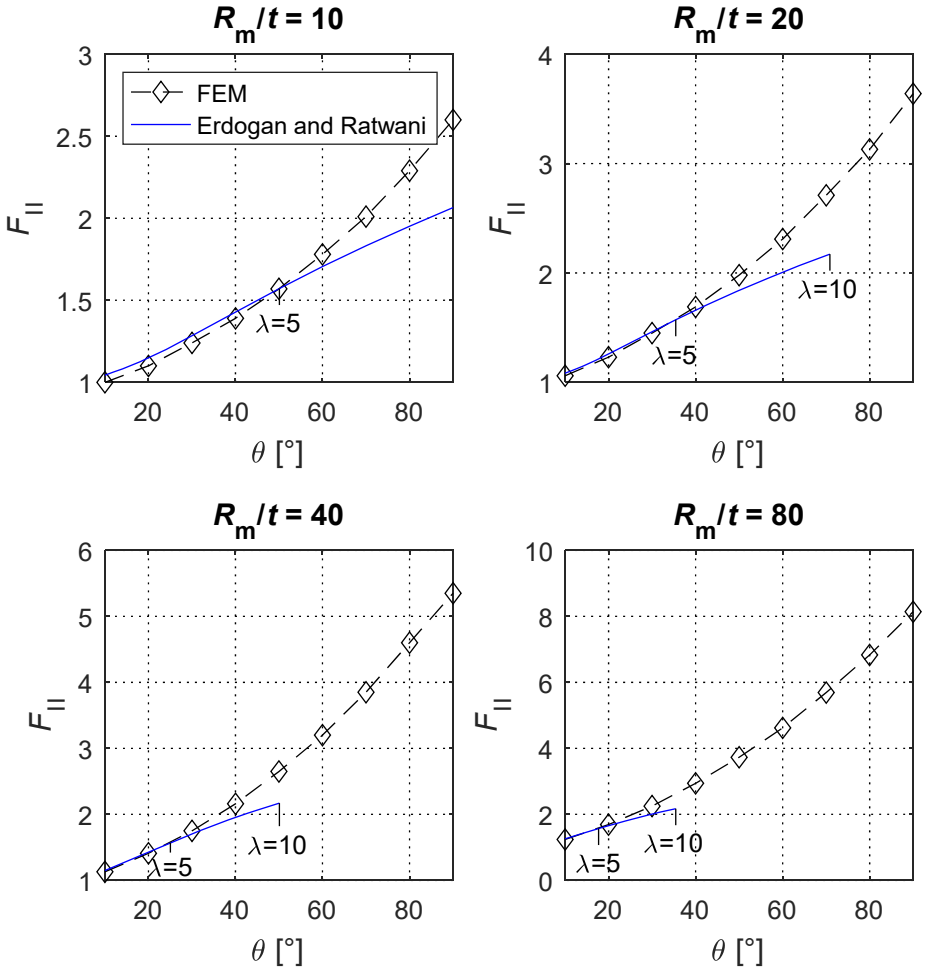


Figure 8.9 – Dimensionless shape factor $F_{II}$ for torsional loading. Comparison between analytical solution by Erdogan and Ratwani (1972) and FEM results obtained here

stress intensity factors predicted by Erdogan and Ratwani (1972) are likely non-conservative for long cracks.

In Figure 8.10 the FEM results obtained in the current study are compared with those obtained by Kumosa and Hull (1989), assuming plane stress conditions. Their results are even higher than those computed by FEM in the current study. A possible explanation for this

discrepancy may be that the displacement correlation technique (DCT) was used by Kumosa and Hull (1989). This is further investigated in the following subsection.

Table 8.3 – Dimensionless shape factor $F_{II}$ for torsion

| $\theta$ [°] | $R_m/t$ | | | | |
|---|---|---|---|---|---|
| | 10 | 20 | 25 | 40 | 80 |
| **10** | 1.00 | 1.06 | 1.08 | 1.13 | 1.24 |
| **20** | 1.10 | 1.23 | 1.28 | 1.41 | 1.69 |
| **30** | 1.24 | 1.45 | 1.53 | 1.75 | 2.25 |
| **40** | 1.39 | 1.69 | - | 2.16 | 2.94 |
| **50** | 1.57 | 1.98 | - | 2.65 | 3.73 |
| **60** | 1.78 | 2.31 | 2.52 | 3.20 | 4.62 |
| **70** | 2.01 | 2.71 | - | 3.85 | 5.69 |
| **80** | 2.29 | 3.13 | - | 4.60 | 6.83 |
| **90** | 2.60 | 3.64 | - | 5.35 | 8.14 |

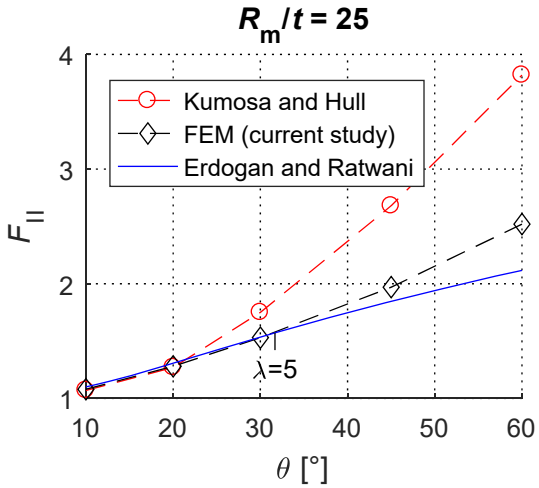


Figure 8.10 – Dimensionless shape factor $F_{II}$ for torsional loading for $R_m/t$ = 25. Comparison between analytical solution by Erdogan and Ratwani (1972), FEM results by Kumosa and Hull (1989) and FEM results obtained here

### 8.4.3 Comparison with the displacement correlation technique

Due to the discrepancy observed in Figure 8.10, an assessment of the two methods for obtaining the stress intensity factor is required. When quarter-point elements (Henshell and Shaw, 1975; Barsoum, 1976) are used at the crack tip, several authors advocate the use of the quarter-point displacement technique (QPDT) (Barsoum, 1976; Shih, deLorenzi and German, 1976) or the displacement correlation technique (DCT) (Shih, deLorenzi and German, 1976) instead of the displacement extrapolation technique (Shih, deLorenzi and German, 1976; Lim, Johnston and Choi, 1992; Guinea, Planas and Elices, 2000; Alegre and Cuesta, 2010; Fu

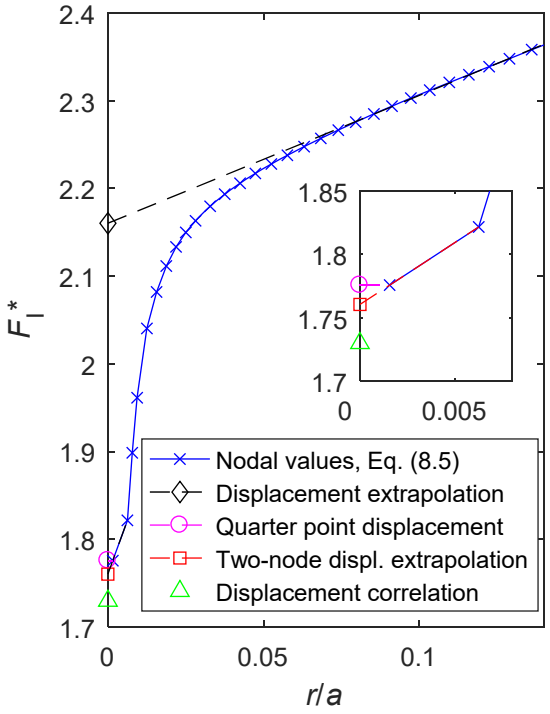


Figure 8.11 – Different displacement techniques applied with a fine crack tip mesh. Dimensionless stress intensity factor estimations: 2.16 by displacement extrapolation technique, 1.78 by quarter point displacement technique, 1.76 by two-node displacement extrapolation, and 1.73 by displacement correlation technique

et al., 2012). These techniques use simple mathematical expressions to estimate the stress intensity factor directly from the displacement of the quarter-point node, or as an extrapolation from the two first nodes away from the crack tip only.

For the case of $R_m/t = 40$ and $\theta = 40$ °, the three techniques are compared for a mesh with very small quarter-point elements (radial length = $a/160$) at the crack tip in Figure 8.11, and for a mesh with larger quarter-point elements (radial length = $a/12$) in Figure 8.12. Nodal values of $F_I$* are plotted as a function of $r/a$. The mesh beyond the distance $r/a = 0.2$ from the crack tip is equal in both cases.

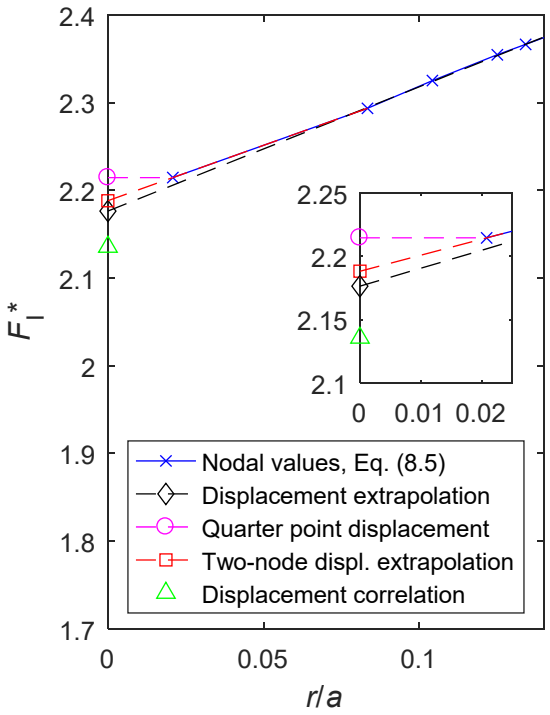


Figure 8.12 – Different displacement techniques applied with a coarse crack tip mesh. Dimensionless stress intensity factor estimations: 2.18 by displacement extrapolation technique, 2.21 by quarter point displacement technique, 2.19 by two-node displacement extrapolation, and 2.14 by displacement correlation technique

From Figure 8.11 it is observed that for the fine crack tip mesh, the curve has a sudden drop near $r/a = 0$, as also shown in other studies (Chan, Tuba and Wilson, 1970; Henshell and Shaw, 1975; Anderson, 2005). While the displacement extrapolation technique disregards this drop, it highly influences the results of the QPDT and the DCT. When the length of the quarter-point elements is increased into the range which is used for extrapolation in the displacement extrapolation technique (Figure 8.12), the sudden drop disappears, and all three techniques yield similar results. However, the location of this range is different from problem to problem, and therefore it is difficult to choose in advance the quarter-point element length allowing the QPDT or the DCT to be used. Furthermore, the length of the quarter-point element should rather be chosen so that the mesh is able to represent the crack tip stress field (Harrop, 1982).

The stress field in the vicinity of a crack tip contains a singular term and a finite term which varies nonlinearly with the distance (Harrop, 1982). Neither the quarter-point element nor normal quadratic elements can model both these terms. Therefore, the representation of the near-tip stress field and the nodal estimations $F^*$ are inaccurate near the crack tip (Henshell and Shaw, 1975), causing the well-known sudden drop in $F^*$ observed in Figure 8.11. This drop is therefore disregarded in the displacement extrapolation technique. On the other hand, the QPDT and the DCT assume that a mesh with quarter-point elements accurately models the crack tip fields, and that the nodal estimations of $F^*$ vary linearly with distance near the crack tip. For the coarse crack tip mesh (Figure 8.12) the variation is nearly linear, and the estimations by QPDT and DCT are therefore better than for the fine mesh (Figure 8.11). However, this cannot be known without producing these plots, and the results by QPDT and DCT could therefore be less reliable, if they are not compared with the displacement extrapolation technique. This is assumed to be the reason for the discrepancy between the results obtained here and the results obtained by Kumosa and Hull (1989).

### 8.4.4 Assessment of the computed results

In the finite element analyses, the same mesh was used for both tensile and torsional loading. While this mesh gave a smooth stress field in the vicinity of the crack tip for the tensile loading (see Figure 8.5), a discontinuity occurred in the transition between the quarter-point elements and the normal mesh for the torsional loading. It was found that in order to avoid this discontinuity, the quarter-point elements would need to be extended far into the region which was used for extrapolation (see Table 8.1). For instance, for the case of $R_m/t = 40$ and $\theta = 40$ °, the shear stress distribution ahead of the crack tip was found to become increasingly smoother at this transition as the crack tip element size was increased from 0.44 to 4.19 mm, while the displacement was extrapolated from nodes between 2.5 and 4.5 mm from the crack tip. In this case we would not have a sufficient number of nodes available for extrapolation, thereby making it impossible to use a displacement method to obtain the stress intensity factor. For the sake of consistency, the same mesh was therefore used for both the tensile and torsional loading. Using larger quarter-point elements would lead to a difference in the computed stress intensity factor estimated to be less than 2 %. As no general guideline or criterion for determining the size of the quarter-point element exist, this choice was considered to be acceptable.

As can be seen in Figure 8.7, the curve $F_{II}^{*}(r)$ has a very high gradient for large crack angles. This means that small changes in the choice of nodes for extrapolation can cause a large change in the estimated shape factor $F_{II}$. It was here assumed that the same range of nodes could be used for all crack angles (procedure A), but this is not necessarily true. If the range of nodes rather was chosen on a case-to-case basis (procedure B), it would in some cases be difficult to determine exactly where linear extrapolation should be performed. While for crack angle $\theta = 10$ °, procedure B would lead to deviations less than ±2 % compared to procedure A, the deviations could reach values between +7 % and

−30 % for $\theta = 90\,°$. These deviations are extreme values, estimated by arbitrarily choosing extrapolation ranges which could possibly be considered as linear, as shown in Figure 8.13. Due to the excellent agreement with other solutions for the tensile load, and the reasonable agreement with the stress method, the proposed procedure A is considered to be successful. The possible errors due to the choice in extrapolation range are therefore most likely considerably lower than those mentioned above. This indicates a considerable weakness in the displacement extrapolation technique however, which is rarely emphasised in relevant reviews (e.g. Menandro, Moyer and Liebowitz, 1995; Anderson, 2005; Banks-Sills, 2010; Zhu and Leis, 2014; Branco, Antunes and Costa, 2015; Rege and Lemu, 2017).

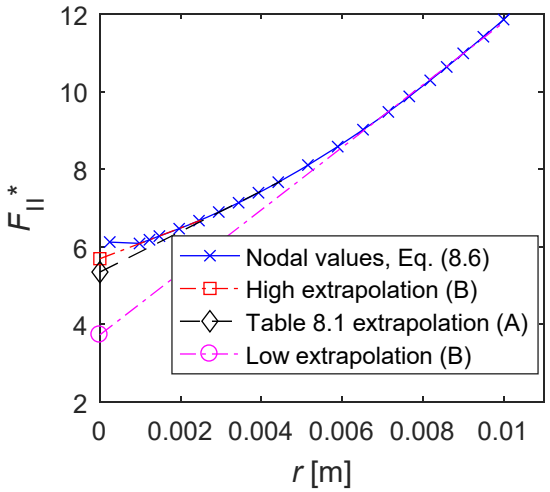


Figure 8.13 – Different extrapolation choices for $R_m/t = 40$, $\theta = 90\,°$

The accuracy of the results which are reported in this work is limited by the choices of using a shell model and the displacement extrapolation technique. Still, the accuracy for the torsional loading is judged to be higher than the two available solutions, i.e. those by Erdogan and Ratwani (1972) and Kumosa and Hull (1989). In order to obtain more accurate results, a fully three-dimensional model needs to be analysed

and the interaction integral technique applied. For practical applications, it should be taken into account that the stress intensity factors depend on the length and support conditions of the shell.

## 8.5 Conclusions

The stress intensity factors for a circumferential crack in a long cylindrical shell have been computed for both tensile and torsional loading, using FEM with shell elements. The computed results for tensile loading were found to agree very well with available results in the literature which are also based on the shell theory. For long cracks the available analytic solution for torsional loading was found to be non-conservative. Comparisons with fully three-dimensional FEM results from the literature indicated that the through-thickness variation of the crack tip stresses may be important. In order to further investigate this finding, fully three-dimensional finite element analyses should be carried out, applying the interaction integral technique to compute the stress intensity factor. Such analyses would require a significantly higher amount of preparatory and computational efforts however.

## Acknowledgements

This work was supported by the Norwegian Ministry of Education and Research.

# 9 Paper VI: Mixed-mode I and II fatigue crack growth retardation due to overload: An experimental study

[*]Kristen Rege, Jørgen Grønsund, Dimitrios G. Pavlou

Department of Mechanical and Structural Engineering and Materials Science, University of Stavanger, P.O. Box 8600 Forus, NO-4036 Stavanger, Norway

**Abstract:** Environmental loads acting on structures usually cause fatigue crack propagation under variable amplitude mixed-mode conditions. In order to better estimate the remaining fatigue life, the fatigue crack growth behaviour under these conditions needs to be studied. In this paper, an experimental study where mixed-mode I and II overloads are applied to a fatigue crack propagating under mixed-mode I and II constant amplitude loading, is presented. The overloads are found to cause fatigue crack growth retardation, lasting over a length which is more than two times longer than the overload crack tip plastic zone extent estimated using a linear elastic solution.

[*] Previously published as: Rege, K., Grønsund, J. and Pavlou, D.G. (2019) Mixed-mode I and II fatigue crack growth retardation due to overload: An experimental study, *International Journal of Fatigue*, 129, 105227. doi: 10.1016/j.ijfatigue.2019.105227

## 9.1 Introduction

Due to the fluctuating behaviour of environmental loads, offshore structures are subjected to variable amplitude fatigue. The fatigue loading may lead to the initiation and propagation of cracks, especially at critical spots, such as welded tubular joints in jacket structures. As environmental loads are also multi-directional in nature, the fatigue cracks may propagate under mixed-mode conditions (Rhee, 1989; Mshana, Kam and McDiarmid, 1992; Riahi et al., 2011; He, Liu and Xie, 2014; Rege and Pavlou, 2019a). Accurate modelling of the fatigue crack propagation life is important when evaluating detected fatigue cracks, and when planning inspection intervals (Riahi et al., 2011; Lotsberg et al., 2016; Mai, Sørensen and Rigo, 2016; Keprate, Ratnayake and Sankararaman, 2017a) for these structures. However, there is a lack of models and experimental studies for mixed-mode variable amplitude fatigue crack propagation.

The qualitative behaviour of variable amplitude fatigue crack propagation under pure mode I conditions, i.e. tensile opening, is well known from experimental studies. A single tensile overload in an otherwise constant amplitude load history causes a retardation in the proceeding crack propagation, while a single underload causes an acceleration (Ding et al., 2017). As any loading history in principle can be represented as a sequence of overloads and underloads (Salvati et al., 2017), these simple load cases form the basis for developing models for variable amplitude fatigue. Most of these models may be divided into two groups; those which assume that residual stresses in the plastic zone in front of the crack tip are responsible for the load interaction effects (Willenborg, Engle and Wood, 1971; Wheeler, 1972; Johnson, 1981; Yuen and Taheri, 2006; Huang, Moan and Cui, 2008; Cui, Wang and Huang, 2011; Li et al., 2018), and those which assume plasticity-induced closure due to plastic stresses in the wake of the crack tip to be responsible (Elber, 1970; Newman, 1981; DuPont et al., 2017; Liu, Venkatesan and Zhang, 2017; Aguilar Espinosa et al., 2017b). The latter

type of model typically requires time-consuming elastic-plastic finite element computations to be carried out, while the former employs analytical or semi-analytical expressions for the crack tip plastic zone size to predict the retardation and acceleration. A number of models emphasizing other mechanisms, e.g. the strain hardening effect on the crack growth retardation (Pavlou, 2000), do also exist. An overview of the different mechanisms which have been proposed to contribute to fatigue crack growth retardation may be found in the study by Salvati et al. (2017).

Some experimental studies have considered the application of a mixed-mode I and II (combination of tensile opening and in-plane shear) overload to an otherwise purely mode I constant amplitude load history. Richard (1989) demonstrated that a pure mode II overload resulted in very little retardation of the proceeding mode I fatigue crack propagation in an aluminium alloy, compared to the application of a mode I overload. This was further demonstrated by Sander and Richard (2006), who applied mixed-mode I and II overloads. They showed that by increasing the ratio of the mode I to the mode II overload stress intensity factor, the retardation effect on the proceeding mode I fatigue crack propagation was increased. In order to compare the applied overload under different mode mixity ratios, they kept Richard's equivalent stress intensity factor (Richard, Schramm and Schirmeisen, 2014) equal for all the overloads. Sander and Richard's finding was confirmed by similar experiments carried out by Mohanty, Verma and Ray (2009). Meanwhile, Decreuse et al. (2009) found that applying 10 or 50 cycles of overload in pure mode II actually accelerated the proceeding mode I fatigue crack propagation in S355NL steel.

Mokhtarishirazabad et al. (2017) applied an overload to a crack propagating through a carbon steel cylinder subjected to non-proportional constant amplitude tensile and torsional cyclic loading, and observed retardation. Gates and Fatemi (2017) subjected aluminium cylinders to non-proportional variable amplitude tensile and torsional

cyclic loading, and found the fatigue crack propagation lives to be longer than those predicted using mode I models. However, due to the complexity of non-proportional multiaxial fatigue, it is challenging to use these results in the early development of a predictive model.

Some models for variable amplitude fatigue crack propagation under mixed-mode conditions have been proposed. Sander and Richard (2006) simulated the influence of mixed-mode overloads on mode I crack propagation quite well by considering plasticity-induced closure. A framework for non-proportional mixed-mode plasticity at the crack tip has been presented by Fremy et al. (2012), but further development is needed in order to apply it to variable amplitude mixed-mode fatigue crack propagation. Boljanović and Maksimović (2014; 2017), and Dirik and Yalçinkaya (2018) have directly applied the Wheeler (1972) and Willenborg (Willenborg, Engle and Wood, 1971) models to mixed-mode conditions, implicitly assuming that the plastic zone is circular, with its centre at the crack tip. It is evident that the crack tip plastic zone is not circular for general mode I, mode II, or mixed-mode I and II loading (Banks and Garlick, 1984; Golos and Wasiluk, 2000; Subramanya, Viswanath and Narasimhan, 2005; Ding and Wang, 2017), and the crack growth retardation effects are therefore still worth studying. Other models have also been proposed (Dekker et al., 2019; Lesiuk, 2019), but further comparison with experimental results is clearly necessary.

Experimental results for proportional mixed-mode fatigue crack propagation after a mixed-mode overload are found in the work by Lee and Choi (2009). However, they did only consider a single overload ratio. In the present paper, the effect of a single mixed-mode I and II overload on proceeding mixed-mode I and II constant amplitude fatigue crack propagation is studied for two different overload ratios. Fatigue crack propagation tests are carried out using tubular specimens made of austenitic stainless steel, subjected to proportional (in-phase) tensile and torsional cyclic loading. The finite element method (FEM) is used to obtain the stress intensity factor of the propagating crack, in order to

relate it to the crack propagation rate. The observed retardation following the overload is compared to estimates of the crack tip plastic zone size, which forms the basis of most of the existing models for predicting the retardation.

## 9.2 Material and methods

### 9.2.1 Specimen and material

In this study, tubular specimens are subjected to proportional tensile and torsional cyclic loading. Tubular specimens are often used to study fatigue crack propagation under biaxial loading (Yokobori et al., 1985; Richard, 1989; Yu, Li and Proust, 2017). Their main advantages are the possibility of continuously adjustable mode mixity, and the possibility to apply non-proportional biaxial loading.

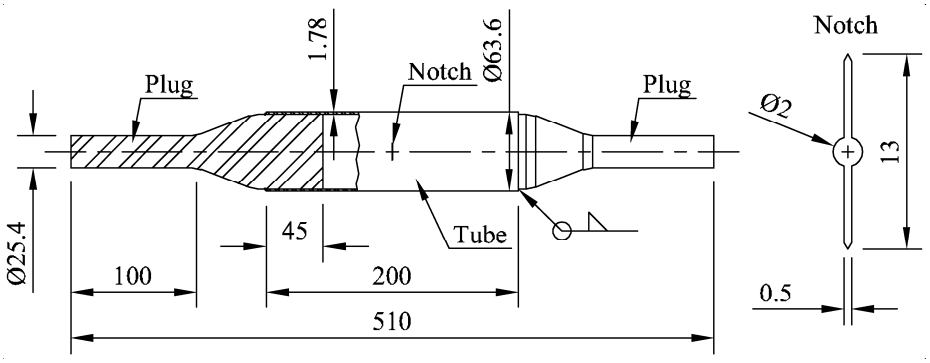


Figure 9.1 – Specimen geometry. All dimensions are given in mm

The geometry of the specimen is shown in Figure 9.1. It consists of a welded austenitic stainless steel tube according to ASTM A269/A270, and two custom-made steel plugs which facilitate the installation of the specimen into the fatigue testing machine. Twelve equal specimens were made from a single tube. The average diameter over the cross-section of the tube was measured at three points along the length of the tube, using a coordinate measuring machine. The outer diameter was measured to be

63.609 ± 0.005 mm, while the inner diameter was measured to be 60.055 ± 0.006 mm, where the deviations refer to the maximum difference between the three cross-sections. This means that the mean radius $R_m \approx 30.9$ mm, while the wall thickness $t \approx 1.78$ mm. The diameter was chosen to be this large, in order to allow observation of macroscopic crack propagation, while the thickness was kept low, in order to minimize the through-thickness variation of shear stress.

The tubing material is 316L austenitic stainless steel, satisfying both EN 10088 grade 1.4404 and ASTM A269/A270 grade TP316L. This steel grade is commonly used in topside process facilities on offshore platforms, and as a structural material in power plants (Nilsson et al., 2016). The chemical composition and mechanical properties obtained from the 3.1.B material certificate for the tube are given in Tables 9.1 and 9.2.

A notch was prepared in each specimen to facilitate crack initiation, as shown in Figure 9.1. The notch was made directly opposite of the longitudinal welding seam, in order to avoid crack propagation through the heat-affected zone, using die-sinking electrical discharge machining.

The plugs shown in Figure 9.1 were made for installing the larger tube into the 1 inch grip of the fatigue testing machine. They were machined

Table 9.1 – Chemical composition (wt%) of the steel tube. The balance is Fe

| C | Si | Mn | P | S | Cr | Ni | Mo |
|---|---|---|---|---|---|---|---|
| 0.023 | 0.40 | 0.88 | 0.027 | 0.006 | 17.39 | 11.12 | 2.04 |

Table 9.2 – Mechanical properties of the steel tube

| Test no. | 0.2 %-proof strength (yield strength), $\sigma_y$ | Tensile strength, $\sigma_{TS}$ | Elongation after fracture | Hardness |
|---|---|---|---|---|
| **1** | 366 MPa | 588 MPa | 45 % | 85 HRB |
| **2** | 347 MPa | 575 MPa | 50 % | 83 HRB |

from a round bar of 520M carbon steel (a variant of S355J2), and welded to the stainless steel tube.

### 9.2.2 Experimental setup

The 12 specimens were loaded using a servohydraulic MTS 809 axial/torsional test system, model 319.25. All specimens were pre-cracked in cyclic tension with $P_{max,PC} = 28$ kN and load ratio $R = 0.1$, except specimen I-A, whose $P_{max,PC}$ was increased stepwise from 20 to 25 to 30 kN. The pre-cracking load was applied as a tapered sinusoidal wave with a frequency of 10 Hz. The pre-cracking was stopped when cracks of approximately 2 mm length were observed at each side of the notch shown in Figure 9.1. This corresponds to an initial crack length $2a_0 \approx 17$ mm. The exact pre-crack length for each specimen is given in Table 9.3.

Table 9.3 – Overview of loads applied to each specimen

| Specimen name | Pre-crack length, $2a_0$ [mm] | Tension overload, $P_{OL}$ [kN] | Torsion overload, $T_{OL}$ [Nm] | Max. of cyclic tension, $P_{max}$ [kN] | Max. of cyclic torsion, $T_{max}$ [Nm] | Fre-quency [Hz] |
|---|---|---|---|---|---|---|
| **I-A** | 25.7 | 0 | 0 | 30 | 0 | 10 |
| **I-B** | 18.3 | 0 | 0 | 28 | 0 | 10 |
| **I-C** | 17.9 | 0 | 0 | 28 | 0 | 10 |
| | | | | | | |
| **I+II-A** | 17.3 | 0 | 0 | 23 | 250 | 2 |
| **I+II-B** | 16.0 | 0 | 0 | 25 | 260 | 4 |
| **I+II-C** | 17.0 | 0 | 0 | 25 | 260 | 5 |
| | | | | | | |
| **I+II+1.25OL-A** | 19.3 | 31.25 | 325 | 25 | 260 | 5 |
| **I+II+1.25OL-B** | 17.7 | 31.25 | 325 | 25 | 260 | 5 |
| **I+II+1.25OL-C** | 17.2 | 31.25 | 325 | 25 | 260 | 5 |
| | | | | | | |
| **I+II+1.50OL-A** | 18.6 | 37.5 | 390 | 25 | 260 | 5 |
| **I+II+1.50OL-B** | 16.5 | 37.5 | 390 | 25 | 260 | 4 |
| **I+II+1.50OL-C** | 17.3 | 37.5 | 390 | 25 | 260 | 5 |

In this study, four different load cases were studied; the application of cyclic tension only, the application of cyclic tension and torsion, the application of cyclic tension and torsion following a 25 % tension+torsion overload, and the application of cyclic tension and torsion following a 50 % tension+torsion overload. The overload was applied immediately after the pre-cracking. Three specimens were tested for each load case. The detailed loading of each specimen is documented in Table 9.3. All torsion loads were applied in the negative direction, causing a clockwise mean angle of twist. The cyclic loading was applied proportionally in tapered sinusoidal waveform, and the load ratio, $R$, was kept equal to 0.1 for both tension and torsion, for all the specimens. Most of the tests were stopped when the circumferential projection of the crack was approximately 30 mm.

Specimen I-A was used to figure out a suitable pre-cracking load for the specimens, and was therefore ultimately run at a higher cyclic load than the rest of the specimens. Similarly, specimen I+II-A was used to study the specimen's behaviour in combined cyclic tension and torsion. In order not to disturb the transition from a mode I crack to a mixed-mode I and II crack, slightly lower loads were used for this specimen, together with a low loading frequency. After finishing the data acquisition for this specimen, trials were made to figure out that the fatigue testing machine could accurately apply the higher loads used for the rest of the specimens, at a higher frequency. The cyclic tensile and torsional loads were chosen so that the Richard equivalent stress intensity factor (Richard, Schramm and Schirmeisen, 2014) would increase slightly in the transition from the pre-cracking load to the test load. As the steel is stainless, and was tested in air at room temperature, the effect of changing the frequency between 2 and 10 Hz is considered to be negligible.

The overloads were applied by slowly increasing the tension and torsion through the following discrete steps: 25 kN, 290 Nm, 28 kN, 325 Nm, 31.25 kN, 360 Nm, 34 kN, 390 Nm, 37.5 kN. Unloading followed the

same steps backwards. This stepwise approach was chosen in order to avoid unintentional overshoot. The steps were chosen so that the plastic zone at the crack tip, as estimated by the expression derived from linear elasticity by Golos and Wasiluk (2000), would monotonically increase ahead of the crack tip.

A digital camera was used to monitor the length of the crack. This solution has also been used previously by researchers to monitor the crack length, especially under mixed-mode conditions (Miranda et al., 2003; Gao, Shen and Yun, 2012; Demir, Ayhan and İriç, 2017). A millimetre scale was taped to the specimen in the vicinity of the crack, allowing measurement of the crack on the cylindrical surface. Measurements between each millimetre mark were made by analysing the photos at a computer. These measurements were too time-consuming to carry out on-site during pre-cracking, which is why there is some variation in the pre-crack lengths shown in Table 9.3. During the testing, the crack length was also observed visually, in order to confirm the crack lengths measured from the photos. For all the specimens subjected to combined tension and torsion, tap water was sprayed onto the cracked area of the specimens during testing to penetrate into the crack. The water would enter the crack during the loading phase of a cycle, and then emerge as small water droplets on the specimen surface during the unloading phase of the cycle. This enabled real time detection and measuring of the crack length during testing. As the specimen material is stainless steel, this infrequent application of tap water was not considered to influence its fatigue behaviour considerably.

## 9.3 Computations

### 9.3.1 Determination of stress intensity factors

In order to determine the stress intensity factors for the crack propagating through the tubular specimen, finite element (FE) models of the specimen were made. Existing analytical solutions, e.g. by Sanders (1982), are valid only for long cylinders, and may therefore not be directly applied to the short specimens considered here.

The FE analyses were performed using ANSYS® Academic Research Mechanical, Release 17.0. The tubular specimen was modelled using eight-node isoparametric quadrilateral shell elements called SHELL281. When the combined tensile and torsional cyclic load is applied, the crack will get a kink in both ends, and the proceeding crack path will be curved. However, the curvature observed from the tested specimens was very small, and the crack was therefore modelled as three straight lines on the cylinder surface, as shown in Figure 9.2. Quarter-point elements (Henshell and Shaw, 1975) were placed in a rosette pattern at the crack tips, in order to model the singularity in the stress field near the crack tip (Rege and Lemu, 2017). The geometry of the notch (Figure 9.1) was not included in the finite element models, as the fatigue pre-cracks were longer than the minimum requirements given in ASTM E647 (ASTM International, 2016) for disregarding the effect of the notch. A typical mesh used for a specimen with a kinked crack is shown in Figures 9.3 and 9.4.

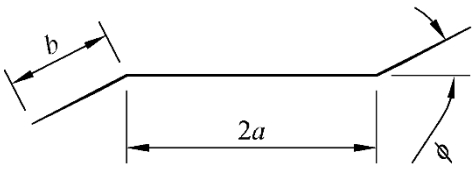


Figure 9.2 – Model of the mixed-mode fatigue crack

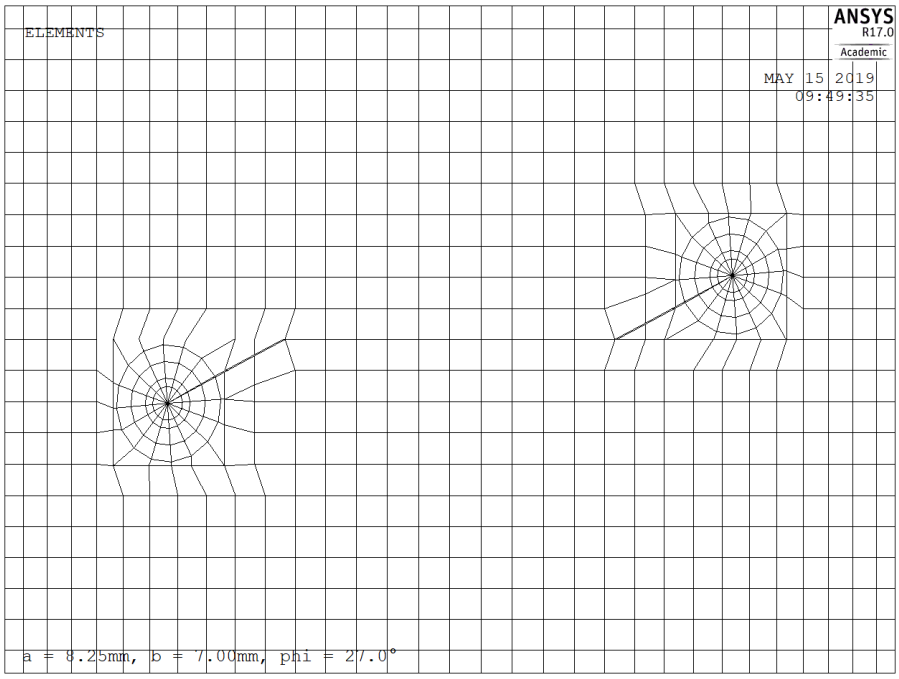


Figure 9.3 – Typical finite element mesh around the mixed-mode fatigue crack. Images used courtesy of ANSYS, Inc.

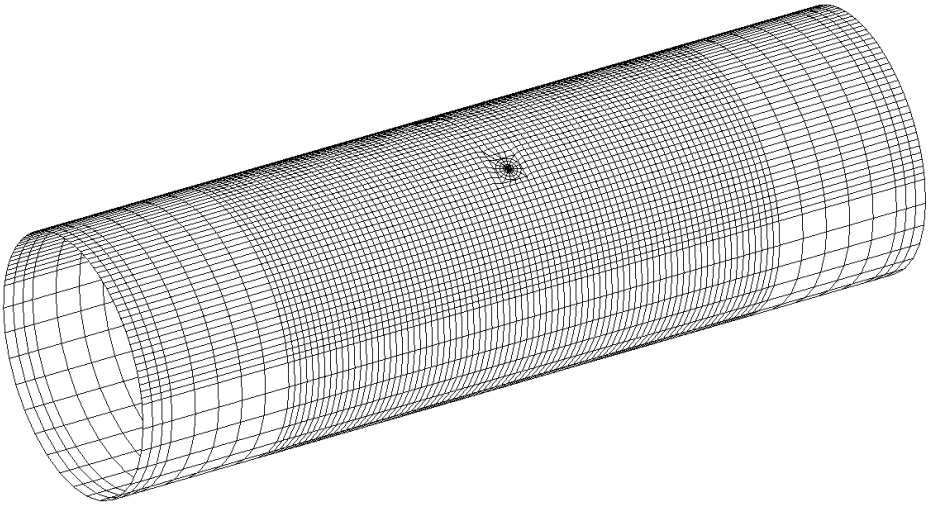

Figure 9.4 – Typical finite element mesh of the tubular specimen. Images used courtesy of ANSYS, Inc.

For 316L steel, typical values for the elastic modulus, $E$, and Poisson's ratio, $v$, are 200 GPa, and 0.27 to 0.30, respectively. $v$ = 0.285 was therefore used in the finite element model. The tensile load was applied on the circumference of each end of the tube as a surface load in ANSYS, while consistent nodal loads representing the torsional load were computed using MATLAB R2016b, and applied to each node along the ends of the tube individually. All degrees of freedom were locked in one node directly opposite of the middle of the crack, in order to disable rigid-body translations and rotations. The radial displacement of all nodes along the first 45 mm from each end of the tube was also set to zero, in order to model the constraint caused by the plugs (see Figure 9.1), denying radial contraction of the tube.

As the domain integral technique is not directly available for shell elements in ANSYS 17.0, the displacement extrapolation technique (Chan, Tuba and Wilson, 1970; Henshell and Shaw, 1975) was used to obtain the stress intensity factors, for the case of a plane circumferential crack. This technique was shown to be suitable for this problem in a previous study (Rege and Pavlou, 2019b). In this case, the symmetric/ antisymmetric properties of the problem were utilized, and only half the tube was modelled. Beyond the crack tip rosette pattern, the local element size was set to 2.5 % of the mean radius, $R_m$, of the tube, while further away an element size of $0.2R_m$ was used. The length of the quarter-point elements was set equal to 1/6 mm. This mesh was tested by applying it to a long, unconstrained tube, and comparing the computed mode I stress intensity factor to the one obtained using the analytical solution derived by Sanders (1982) (see also Rege and Pavlou, 2019b). It was found that the difference between the computed and analytical values was less than 0.15 % for crack lengths $2a$ between 15 and 60 mm. When applying the same mesh to the specimen actually considered here, the mode I geometry factor, $F_I$, was obtained as shown in Figure 9.5. The relation between the stress intensity factor, $K_I$, and the geometry factor, is:

$$K_{\mathrm{I}} = F_{\mathrm{I}}\sigma_0\sqrt{\pi a} \tag{9.1}$$

where $\sigma_0 = P/(2\pi R_{\mathrm{m}}t)$ is the remotely applied tensile stress, $t$ is the wall thickness of the tube, and $a$ is the half crack length. A fifth degree polynomial was fitted to the computed values using the least squares method, and is also shown in Figure 9.5:

$$\begin{aligned} F_{\mathrm{I}} = {} & 1.007 - 0.08737\left(\frac{a}{R_{\mathrm{m}}}\right) + 3.663\left(\frac{a}{R_{\mathrm{m}}}\right)^2 \\ & - 5.729\left(\frac{a}{R_{\mathrm{m}}}\right)^3 + 3.665\left(\frac{a}{R_{\mathrm{m}}}\right)^4 - 0.8656\left(\frac{a}{R_{\mathrm{m}}}\right)^5 \end{aligned} \tag{9.2}$$

This polynomial was used in the analysis of the specimens subjected to pure cyclic tension.

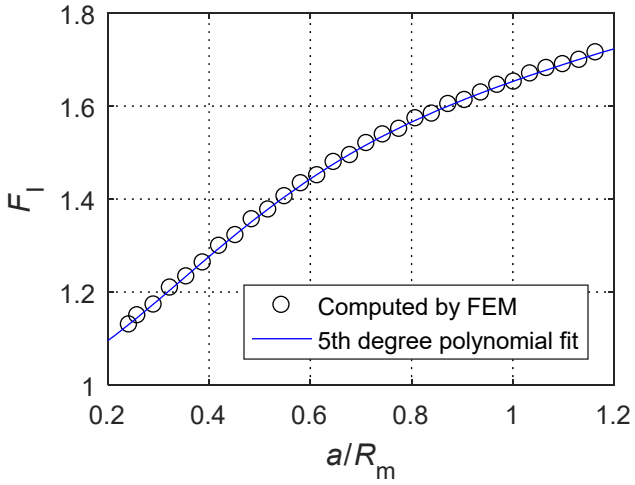


Figure 9.5 – Geometry factor $F_{\mathrm{I}}$ for the tubular specimen loaded in tension

For the kinked cracks developed in the specimens subjected to combined tension and torsion, it was not possible to use the displacement extrapolation method for kink lengths, $b$, shorter than 6 mm, due to the lack of nodes in the interval from which to extrapolate. Instead, the

modified crack closure integral (MCCI; also called the virtual crack closure technique) (Raju, 1987) was used as an alternative. This is a commonly used method, but in this study, it was found to diverge with decreasing crack tip element size, when used together with a rosette pattern with quarter-point elements at the crack tip, as shown in Figure 9.6 for a circumferential crack in a very long, unconstrained tube. Still, by comparing results by MCCI to the analytical solution (Sanders, 1982) for a long, unconstrained tube, it was possible to find a linear relation between the crack length and the quarter-point element length providing accurate stress intensity factors. This calibrated quarter-point element length was applied with MCCI to the kinked crack in the specimen (Figure 9.3), and provided excellent agreement with the displacement extrapolation technique for long kink lengths, as shown in Figure 9.7.

Due to the finite quarter-point element length required for the application of MCCI, this technique could only be used for kink lengths of 2.5 mm and longer. For shorter kink lengths, the stress intensity factors were

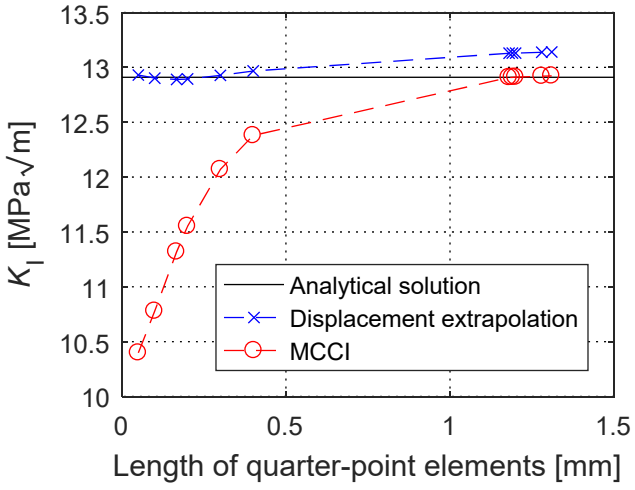


Figure 9.6 – Influence of the quarter-point element length on the stress intensity factor determined by the displacement extrapolation technique and MCCI, for a circumferential crack in a long, unconstrained tube subjected to tension. Compared with the analytical solution by Sanders (1982)

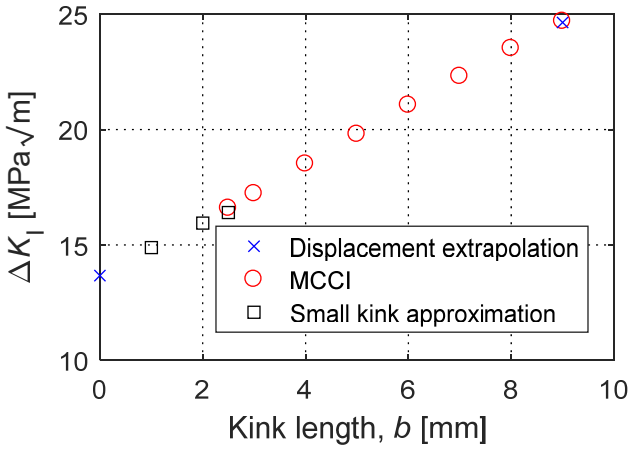


Figure 9.7 – Mode I stress intensity factor range solutions for a kinked crack (Figure 9.2) with $2a = 16.5$ mm and $\phi = 27$ °, computed using three different techniques. The stress intensity factor range at $b = 0$ is the Richard effective stress intensity factor range for the plane crack subjected to tension and torsion (mixed-mode)

computed from those obtained for the plane main crack, using the analytical relations for an infinitesimally small kink provided by Cotterell and Rice (1980). The resulting mode I stress intensity factor range, $\Delta K_\mathrm{I}$, as a function of the kink length, $b$, is illustrated in Figure 9.7. The results from the three methods follow a smooth curve, indicating that this modelling approach is appropriate. The solution based on an infinitesimally small kink is observed to deviate when a finite length of $b = 2.5$ mm is reached, as would be expected. For $b = 0$ the Richard effective stress intensity factor range (Richard, Schramm and Schirmeisen, 2014) has been plotted in Figure 9.7, in order to include the mode II component of the loading. For mixed-mode I and II loading, the Richard effective stress intensity factor range is given by:

$$\Delta K_\mathrm{v} = \frac{\Delta K_\mathrm{I}}{2} + \frac{1}{2}\sqrt{\Delta K_\mathrm{I}^2 + 4\left(\alpha_1 \Delta K_\mathrm{II}\right)^2} \tag{9.3}$$

where $\alpha_1$ generally can be set to 1.155. An example of the computed mid-thickness von Mises stress distribution near the crack tip is illustrated in Figure 9.8.

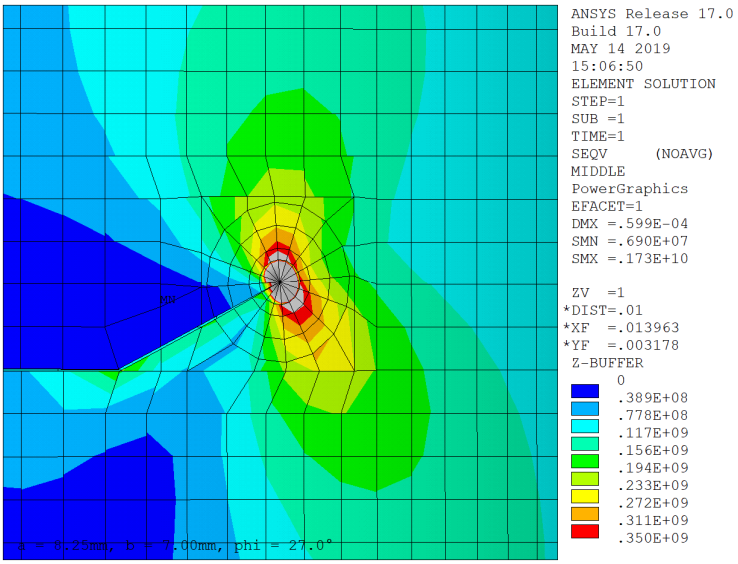


Figure 9.8 – Computed mid-thickness von Mises stress distribution of a kinked crack with $2a$ = 16.5 mm, $b$ = 7.0 mm and $\phi$ = 27 °, subjected to $P$ = 25 kN and $T$ = 260 Nm. Images used courtesy of ANSYS, Inc.

The kink angle, $\phi$, used in the models was chosen to be equal to the one experimentally observed. As the kink was modelled as a straight line, small mode II stress intensity factors were present in the model. If the curvature of the crack path had been included in the finite element model, these mode II stress intensity factors would have caused the crack path to curve, quickly making their effect on the crack growth rate negligible. Due to the diminishing mode II stress intensity factor, it was shown in Rege and Pavlou (2019a) that only the mode I stress intensity factor should be taken into account when approximating a curved crack under near-mode I conditions as a straight line. Therefore, the mode II stress intensity factor was only taken into account when combined tension and torsion is applied at $b$ = 0, by using the Richard effective stress intensity factor in this case.

### 9.3.2 Predicting the retardation length

As described in the introduction, the extents and degree of plasticity around the crack tip is an important parameter in models for variable amplitude fatigue crack propagation. The Wheeler (1972) model and its variants are based on the assumption that retardation lasts as long as the length of the plastic zone due to the current load peak is confined by the plastic zone due to the previously applied overload. For mode I, analytical solutions exist for the extent of the plastic zone in front of the crack tip, $r_p = \alpha(K_I/\sigma_y)^2$, where $\sigma_y$ is the yield strength, and $\alpha$ depends on the model and stress state. The most well-known models are the Irwin approach ($\alpha \approx 0.159$ for plane stress) (Irwin, 1960), based on linear elastic material behaviour, the modified Irwin approach ($\alpha \approx 0.318$ for plane stress) (Rice, 1967) and the strip-yield model ($\alpha \approx 0.393$ for plane stress) (Rice, 1966), both based on elastic-perfectly plastic material behaviour. Real ductile materials exhibit considerable strain-hardening, and their plastic zone size would therefore lie in between the estimates from linear elasticity and elastic-perfectly plastic behaviour. Experimental studies for mode I fatigue crack propagation (Guerra-Rosa, Moura Branco and Radon, 1984; Sheu, Song and Hwang, 1995; Yuen and Taheri, 2006) have also shown that the retardation length in most cases lies in between these estimates.

For a crack propagating under mixed-mode conditions, it is not sufficient to know the extent of the plastic zone along the crack plane. As the crack deviates from a straight path, the shape of the plastic zone is also important. Analytical expressions for the shape of the plastic zone under linear elastic material behaviour have been derived by Banks and Garlick (1984) for mode I conditions, and by Golos and Wasiluk (2000) for mixed-mode I and II conditions, from the leading (singular) term of the stress field near the crack tip. Some numerical analyses have been performed for determining the plastic zone shape in an elastic-plastic material under mixed-mode I and II conditions (Subramanya, Viswanath

and Narasimhan, 2005; Ding and Wang, 2017), but they are not readily applicable to a general problem.

Due to the lack of applicable estimates of the shape of the plastic zone in an elastic-plastic material under mixed-mode conditions, we compare the observed retardation length to the plastic zone determined using the linear elastic finite element models. A finite element model approximates the full stress field of the actual geometry, and is therefore considered to be a more relevant solution than the analytical expression by Golos and Wasiluk (2000). As austenitic stainless steels exhibit considerable strain-hardening (Arrayago, Real and Gardner, 2015), we also compare the retardation length to twice the linear elastic plastic zone size (due to the factor of two between the Irwin and modified Irwin approaches for mode I conditions, as mentioned above). These results are shown in Section 9.4.2.

## 9.4 Results and discussion

### 9.4.1 Fatigue crack propagation under tensile constant amplitude loading

The fatigue crack propagation data for the circumferential crack in the three specimens subjected to constant amplitude cyclic tensile loading are shown in Figure 9.9. The crack propagation rates have been determined using the incremental polynomial method, using seven points to fit each parabolic curve. A minimum crack size measurement interval $\Delta(2a) = 0.5$ mm was used when analysing the data. As shown in Figure 9.10, the crack propagation path was horizontal, as expected, and the stress intensity factors were computed using Equations (9.1) and (9.2).

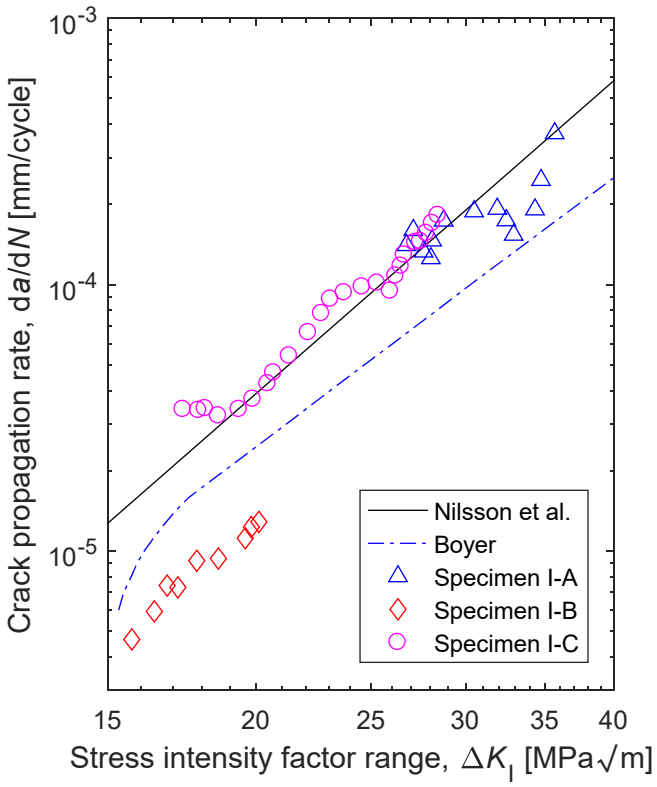


Figure 9.9 – Experimental crack propagation rates for tensile cyclic loading at $R$ = 0.1, determined using the 7-point incremental polynomial method, compared with literature data from Nilsson et al. (2016) and Boyer (1986)

Figure 9.10 – Fatigue crack in specimen I-C

Two fatigue curves from the literature are also included in Figure 9.9. One curve represents the Paris law parameters (for $R$ = 0.1) presented by Nilsson et al. (2016) for 316L steel in room temperature, which are based on a literature study. The second curve is found in Boyer (1986), and is based on tests of 20 % cold worked 316 steel at a frequency of 3 Hz, load ratio $R$ = 0.05, and a temperature of 24 °C. The experimental results from

specimens I-A and I-C match the curves from the literature very well, while the crack propagation rates for specimen I-B are quite low. This will be discussed in the next sub-section.

### *9.4.2 Fatigue crack propagation under combined tensile and torsional cyclic loading*

Applying a proportional tensile and torsional cyclic loading to a specimen with a circumferential pre-crack caused a kink in the crack path, as shown in Figure 9.11. The average angle of the kink over its length was measured within an error limit of ±2 °, and is given in Table 9.4 for each specimen. The measured angles are lower than those predicted using the criterion of maximum tangential stress. The reason for this is that the crack path is slightly curved, with its slope becoming gradually lower further away from the kink. The predictions apply only to the initial slope of the kink, which is slightly higher than the measured angle. In the finite element model, the kink is approximated to be straight. At a finite kink length of 8 mm, the kink angles which minimize the mode II stress intensity factor in the finite element model agree very well with the measured angle, as shown in Table 9.4. This implies that the straight kink representation is a suitable approximation of the crack path.

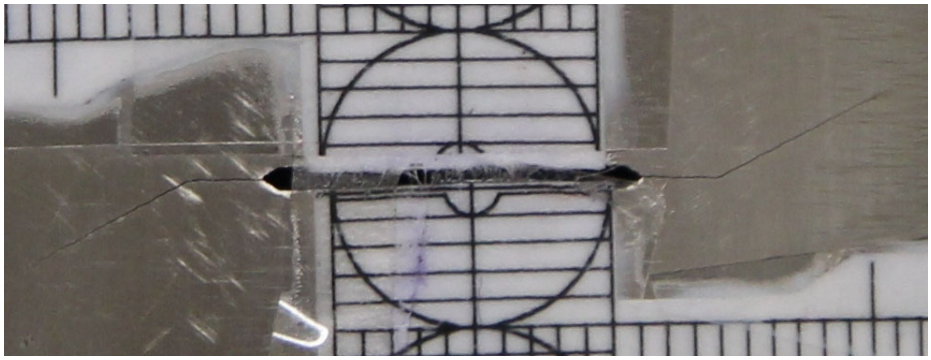

Figure 9.11 – Fatigue crack in specimen I+II+1.25OL-A

Table 9.4 – Measured (within an error limit of ±2 °) and predicted crack propagation angles, $\phi$

| Specimen name | Measured angle [°] | Predicted angle acc. to criterion of max. tangential stress [°] | Angle yielding $\Delta K_{II} = 0$ when $b = 8$ mm [°] |
|---|---|---|---|
| **I+II-A** | 31 | 32 | 27 |
| **I+II-B** | 29 | 31 | 26 |
| **I+II-C** | 24 | 31 | 26 |
| **I+II+1.25OL-A** | 25 | 31 | 27 |
| **I+II+1.25OL-B** | 28 | 31 | 27 |
| **I+II+1.25OL-C** | 26 | 31 | 26 |
| **I+II+1.50OL-A** | 27 | 31 | 27 |
| **I+II+1.50OL-B** | 27 | 31 | 26 |
| **I+II+1.50OL-C** | 25 | 31 | 26 |

In order to investigate any retardation following the applied overloads, the secant method (ASTM International, 2015) was used to obtain the crack propagation rates for the cracks propagating under combined tension and torsion. As this method does not smooth out the data points as the incremental polynomial method does, crack length intervals, $\Delta b$, of approximately 0.5 mm or larger were used in the data analysis. The stress intensity factors were determined for a symmetric model, where the kink length, $b$, was taken as the average of the two kink lengths observed at a given time. The resulting crack propagation data is shown in Figure 9.12.

The crack propagation data are observed to form a band, with most of the data lying below the curve given by Nilsson et al. (2016). A significant scatter between specimens subjected to the same loading is observed. The diameter and thickness of specimens I-B (low propagation rate) and I+II+1.25-OL-A (high propagation rate) were measured and found to differ by 0.01 mm, making it unlikely that variations in these factors were responsible for the observed scatter. The tube has been heat-treated after its cold-forming, so it is also unlikely that the forming

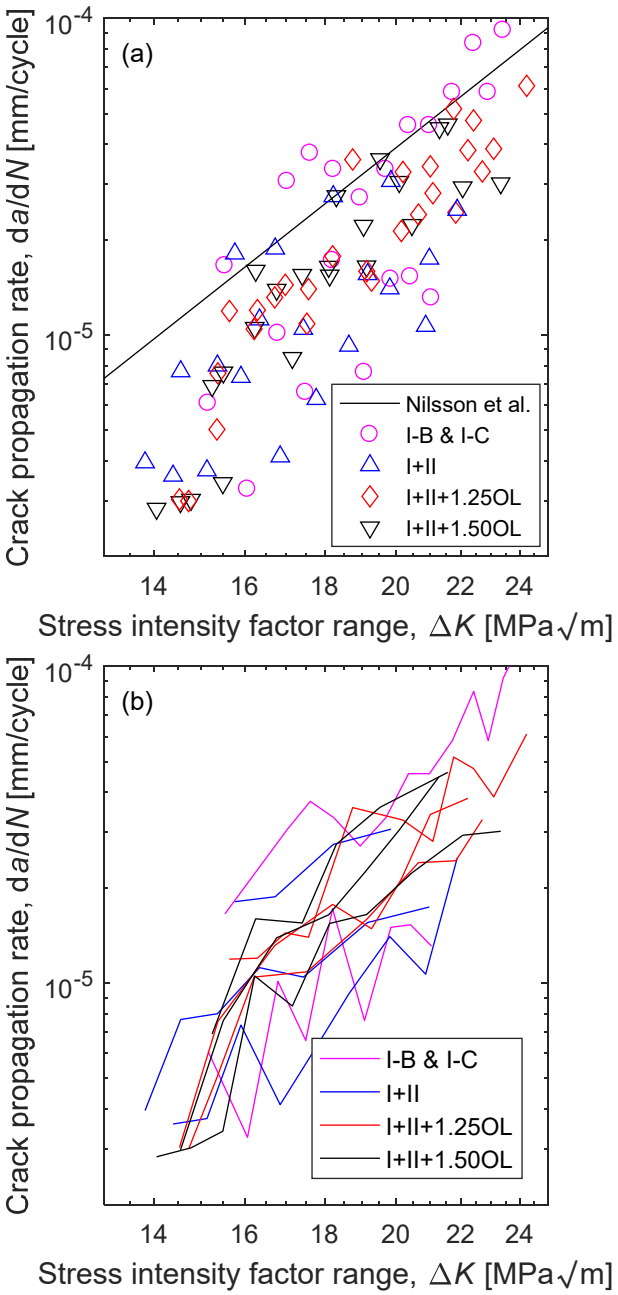


Figure 9.12 – Experimental crack propagation rates for cyclic loading at $R$ = 0.1, determined using the secant method, compared with literature data from Nilsson et al. (2016). Each curve shown in (b) is drawn between the data points from (a) belonging to a single specimen

process should increase the scatter. A possible reason for increased scatter could be tolerances in the fabrication and installation of the plugs in each end of the specimen (Figure 9.1), which could have caused slightly different constraints for each specimen.

Despite the scatter, it was possible to divide the mixed-mode specimens into three groups, A, B and C, where the constant amplitude crack propagation behaviour was similar within each group, as shown in Figure 9.13. As the kinks on the left- and the right-hand side of the crack in specimen I+II-C propagated at very different rates, this specimen has not been included in the further analysis. The constant amplitude crack propagation trends (ignoring the data points influenced by the overloads) in each group were fitted to the Paris law:

$$\frac{\mathrm{d}a}{\mathrm{d}N} = C\Delta K^m \tag{9.4}$$

The parameters $C$ and $m$ for each of the groups A, B and C are provided in Table 9.5. The correlation coefficients for the data points used from each group are included in Table 9.5 as well.

In Figure 9.13, the retardation due to the overloads is clearly visible. The first data point for each specimen subjected to an overload indicates the crack propagation rate directly after the overload, and is clearly below the trend in the rest of the crack propagation data. This is especially clear for specimen I+II+1.50OL-B, where the first three data points have a lower crack propagation rate than the rest.

Table 9.5 – Correlation coefficients and Paris law parameters $C$ and $m$ for the constant amplitude trend of each specimen group shown in Figure 9.13

| Group | Correlation coefficient | $C$ | $m$ |
|---|---|---|---|
| **A** | 0.90 | $4.681\times10^{-12}$ | 2.956 |
| **B** | 0.96 | $5.741\times10^{-13}$ | 3.474 |
| **C** | 0.90 | $9.951\times10^{-14}$ | 4.163 |

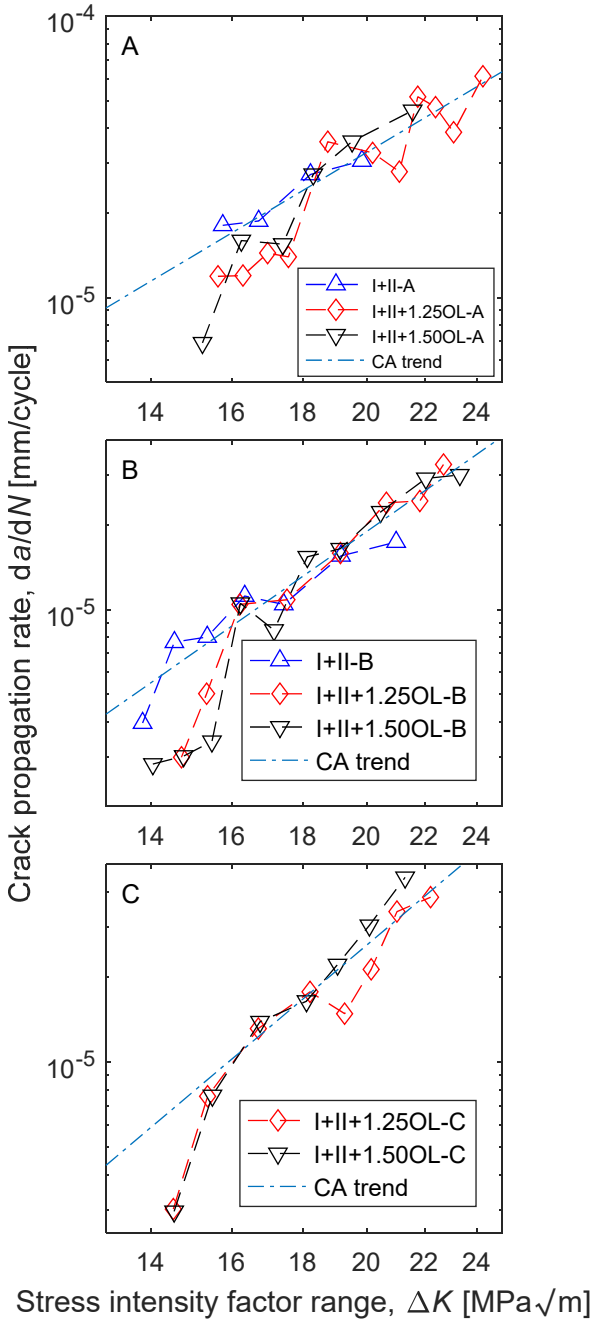


Figure 9.13 – Experimental crack propagation rates for cyclic loading at $R$ = 0.1, determined using the secant method

The actual crack propagation histories for each specimen are plotted in Figures 9.14 and 9.15[3]. As the initial crack length is different for each specimen, their crack propagation histories are not directly comparable to each other. Furthermore, specimen I+II A was subjected to a lower load than the rest of the specimens (see Table 9.3), and is therefore not directly comparable to the rest.

In order to compare the experimental crack growth histories, constant amplitude crack growth histories were estimated, using the Paris law parameters from Table 9.5. These constant amplitude (CA) trends were fixed to the last few data points in Figures 9.14 and 9.15, where the crack growth rate is not influenced by the overload (ref. Figure 9.13). For specimens I+II-A and I+II-B, which were not subjected to an overload, there is an excellent agreement between the estimated and experimental crack propagation histories, as expected. For the specimens which were subjected to an overload, it is clear that the predicted crack propagation histories match the experimental ones quite well when the kink is long, while the retardation is evident for short kink lengths. The duration of the overload-induced retardation was interpreted as the intersection of the predicted constant amplitude crack growth histories and the average of the left and right side experimental crack growth histories. The retardation lengths may also be found by analysing the crack growth rates in Figure 9.13. The two methods gave the same retardation lengths within a difference of 0.2 mm.

The fatigue crack propagation curve from Boyer (1986), which is shown in Figure 9.9, may suggest that the observed retardation is due to the applied stress intensity factor range being close to the threshold value for the material. However, other studies have found the threshold value for the 316 and 316L steel grades to lie in the range between 3.3 and 5.7 MPa√m for $R$ = 0.1 (Priddle, 1978; Sarrazin-Baudoux, Petit and

[3] The measured fatigue crack propagation histories are also provided in tabular format in Appendix B of this thesis.

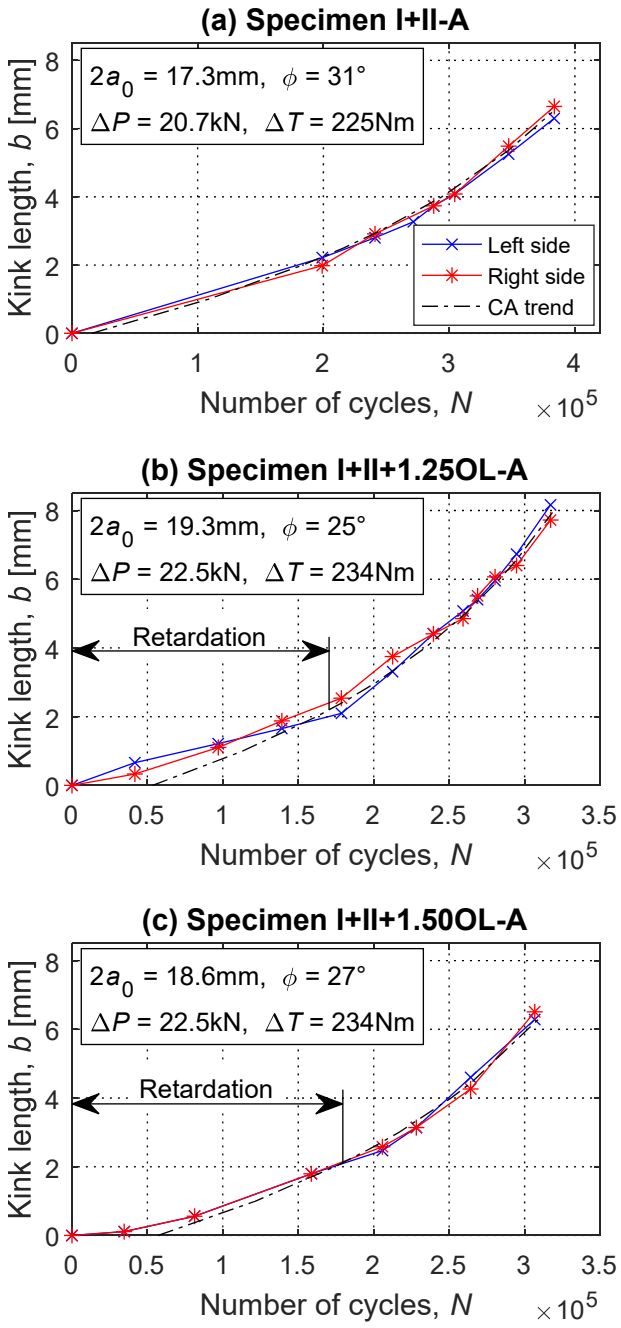


Figure 9.14 – Fatigue crack propagation histories for specimen group A

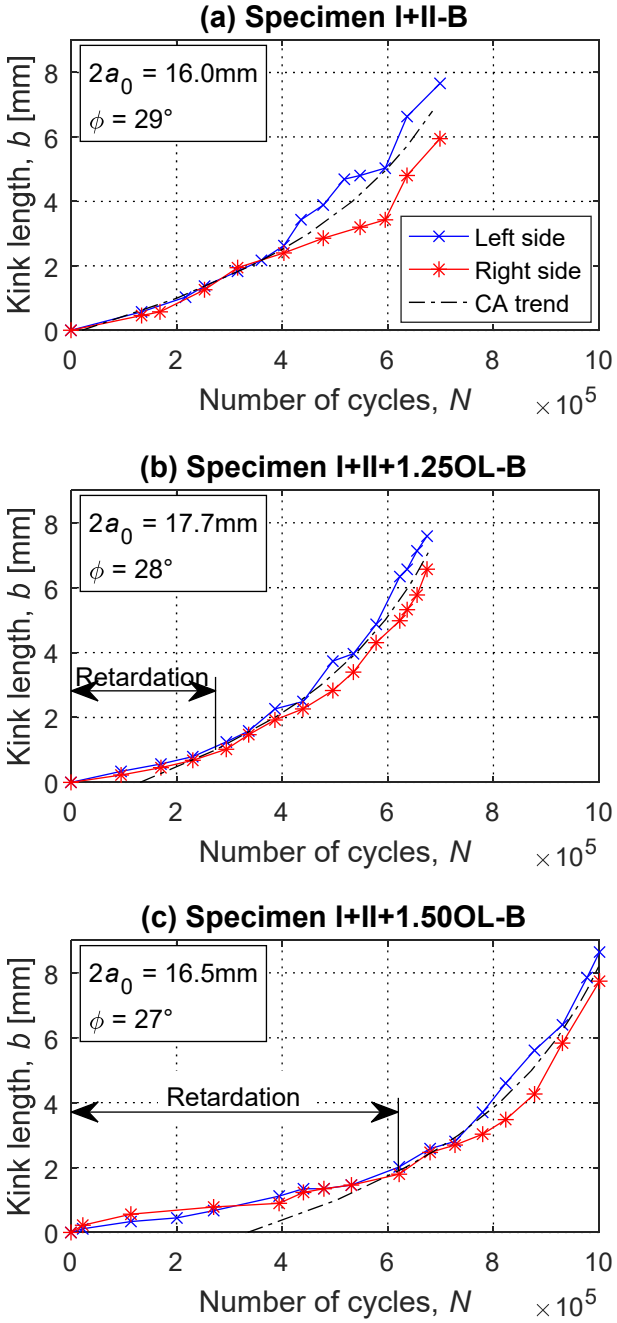


Figure 9.15(a–c) – Fatigue crack propagation histories for specimen groups B. The cyclic loads were $\Delta P = 22.5$ kN and $\Delta T = 234$ Nm for all these specimens

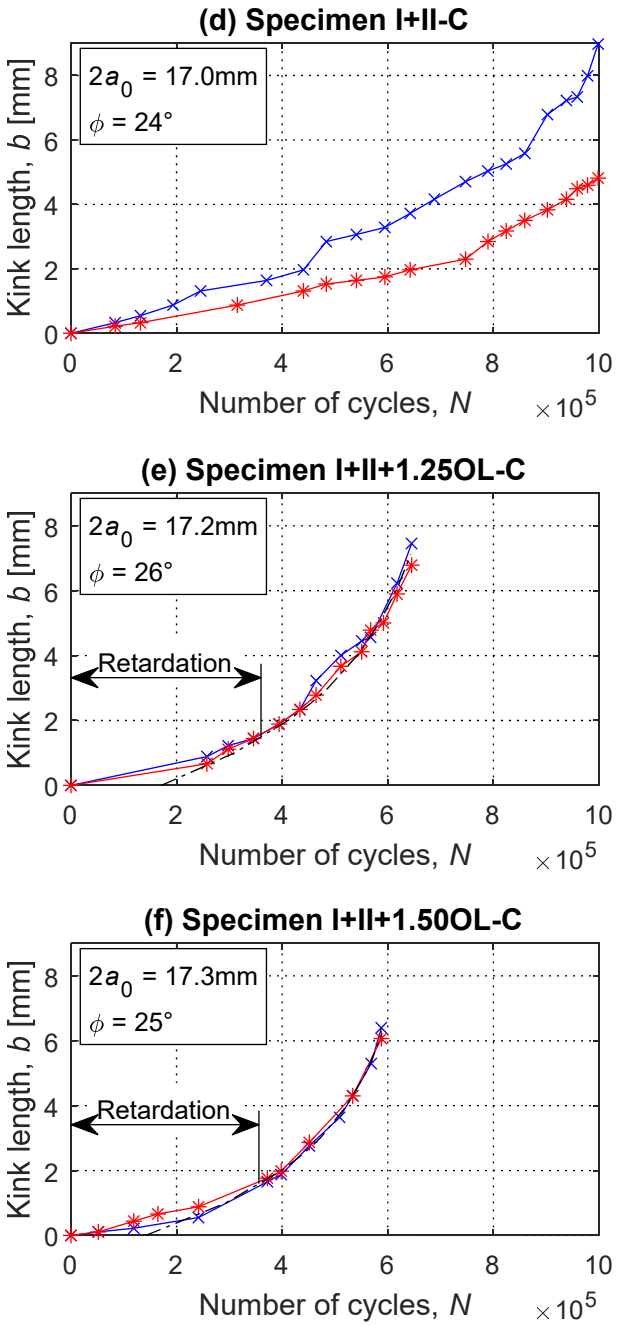


Figure 9.15(d–f) – Fatigue crack propagation histories for specimen groups C. The cyclic loads were $\Delta P$ = 22.5 kN and $\Delta T$ = 234 Nm for all these specimens

Amzallag, 2002), which is considerably lower than the stress intensity factor range applied here. Furthermore, the fact that close to none retardation may be observed for the specimens without an applied overload strengthens the theory that the overloads are responsible for the observed retardation.

The extent of the plastic zone caused by the overload, at the mid-thickness of each specimen, in the direction of the proceeding crack propagation, was computed using the finite element models, assuming a yield stress of 356 MPa (see Table 9.2). An example of the resulting von Mises stress distribution near the crack tip is shown in Figure 9.16. This provides us with a linear elastic estimate of the plastic zone size, corresponding to the left end of the blue bars in Figure 9.17. By instead using the analytical expression by Golos and Wasiluk (2000) together with stress intensity factors obtained from the finite element model, the estimate was found to be between 0.07 and 0.10 mm larger for the overloads considered here. Due to the strain-hardening property of 316L

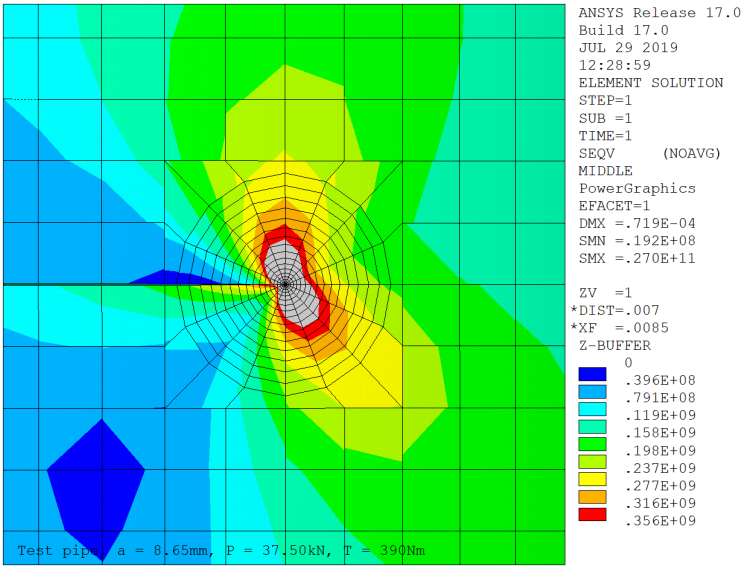


Figure 9.16 – Computed mid-thickness von Mises stress distribution near the right crack tip in specimen I+II+1.50OL-C at the application of the overload. Images used courtesy of ANSYS, Inc.

steel, the actual plastic zone size will be larger than the linear elastic estimate. A rough estimate of the extent of the plastic zone in an elastic-perfectly plastic material is taken as twice of the linear elastic estimate (see Section 9.3.2), and corresponds to the right end of the blue bars in Figure 9.17. Under mode I conditions, the retardation typically lasts over a length which is somewhere in between these estimates (Guerra-Rosa, Moura Branco and Radon, 1984; Sheu, Song and Hwang, 1995; Yuen and Taheri, 2006). However, for the mixed-mode conditions studied in the current work, the retardation length obtained from the experimental data in Figures 9.13–9.15 exceeds these plastic zone estimates considerably, as illustrated in Figure 9.17. A similar observation has recently been made also for a fatigue crack propagating in mode I under biaxial cyclic loading (Datta et al., 2018). This indicates that current variants of the conventional Wheeler model are not readily applicable for predicting the retardation under mixed-mode conditions. It is possible that a better estimate of the mixed-mode plastic zone in a strain-

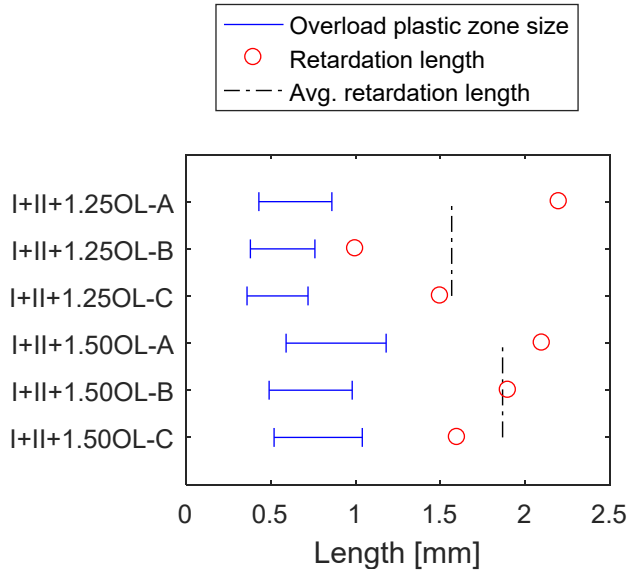


Figure 9.17 – Estimations of the overload plastic zone size in the direction of proceeding crack propagation, compared to observed retardation lengths

hardening material can help to explain the observed retardation length. It would also be interesting to check whether a plasticity-induced closure model would be able to predict the observed retardation lengths, but such an analysis is beyond the scope of the current study.

Figure 9.18 – Left-hand side of the crack in specimen I+II+1.50OL-C. The main crack propagates downwards to the left, while a small branch points upwards

As expected, the average retardation length was found to be larger for the specimens subjected to a 50 % overload, than for the specimens subjected to a 25 % overload. For mode I conditions, it is well known from experiments that a higher overload also leads to a lower crack propagation rate (Ding et al., 2017; Li et al., 2018). This is also observed in Figure 9.13, where the crack propagation rate is observed to be slightly lower after the 50 % overload than after the 25 % overload. The difference is most marked in specimen group B, while for groups A and C the difference between the overloads is not as marked. It is likely that a larger difference between the applied overload magnitudes would have resulted in a more evident trend. Still, one notable difference between the two overload magnitudes was observed: The crack in all the specimens subjected to a 50 % overload was branched at the application of the overload, as shown in Figure 9.18, whereas none of the other specimens experienced macroscopic crack branching (see Figure 9.11). It is well known that applying an overload to a mode I fatigue crack can cause crack branching (Pavlou et al., 2004), and it was also observed by Lee and Choi (2009) for mixed-mode conditions. The branching was not included is the finite element model, but it is likely to reduce the stress

intensity factor of the main crack slightly (see Kitagawa, Yuuki and Ohira (1975) for a mode I crack), thereby being a contributing factor to the retardation.

## 9.5 Conclusions

Experimental results from mixed-mode fatigue crack propagation tests, with and without overloads, have been presented. The tests were performed using tubular specimens made of 316L austenitic stainless steel. Finite element models were used to obtain the stress intensity factors of the propagating crack, allowing the crack propagation to be analysed. The following observations were made:

1. The constant amplitude fatigue crack propagation data agreed quite well with literature data, but displayed considerable scatter between the specimens, possibly due to the fabrication method used in the current study. Still, the experienced scatter would be representable for actual structural details.
2. Applying a mixed-mode overload caused a retardation of the proceeding mixed-mode fatigue crack propagation.
3. The observed retardation length was more than two times longer than the extent of the overload crack tip plastic zone estimated using a linear elastic solution.
4. The 50 % overloads led to a longer average retardation length, and a lower crack propagation rate, than the 25 % overloads.
5. Macroscopic crack branching occurred after the 50 % overload, but not after the 25 % overload, and may have influenced the retardation.

## Acknowledgements

This work was supported by the Norwegian Ministry of Education and Research; and Department of Mechanical and Structural Engineering and Materials Science, University of Stavanger. The authors would like to thank M. Bae for helpful discussions on specimen design and

fabrication. In addition, the authors express gratitude to everyone who assisted during the fatigue tests, including M.A. Atteya, J.O. Rydland, X. Huang, E.S. Kristiansen and A. Aeran.

# 10 Conclusions

In this work, load sequence effects and mixed-mode fatigue crack growth have been studied. It has been illustrated that more realistic fatigue lives may be estimated if these effects are taken into account. This can be useful when operating existing offshore structures beyond their original design life, in which case the conservative approximations used in design may not be able to document sufficient fatigue lives, thereby justifying the use of more accurate models.

For fatigue crack initiation, i.e. fatigue life estimation using *S*-*N* curves, a large number of models have been proposed for including the load sequence effects, and many of them are able to provide reasonable estimates for two-stress level fatigue tests. The comparison presented in Paper II indicated that especially the double linear damage rule and the model presented in the present work seem to be promising candidates. Further study is still required to ensure that they do also perform equally well or better than the Palmgren-Miner rule under spectrum loading (i.e. loading patterns which represent actual service conditions). It is also necessary to study how load cycles below the constant amplitude fatigue limit should be included in these models. The Haibach modification, which is used together with the Palmgren-Miner rule, is a simplification which possibly can be improved when load sequence effects are taken into account.

It should be noted that load sequence effects in fatigue may be very important to consider when a mobile offshore structure is relocated to a new location with a different environment. If the structure is moved from a location with a harsh environment to a location with a benign environment, an increased fatigue life will be expected, due to the lower loads. If the Palmgren-Miner rule is used to estimate the beneficial effect of the relocation, its prediction will most likely be non-conservative, due to the strong load sequence effects which would manifest. In this case,

the beneficial effect should always also be assessed using a nonlinear model which takes the load sequence effects into account.

The literature study showed that a number of models are available also for taking the load sequence effects in mode I fatigue crack propagation into account. Some of the models are in practical use, especially in aerospace and astronautics. These models have also been suggested for predicting mixed-mode fatigue crack propagation histories. For instance, Boljanović and Maksimović (2014; 2017), and Dirik and Yalçinkaya (2018) have suggested the application of the Wheeler and Willenborg models to mixed-mode fatigue, but very few experimental studies have been carried out which can justify this suggestion. This gap has been addressed in this thesis, and it was found that the experimental results obtained did not agree with the basic assumption of these models. The applied mixed-mode overloads were found to cause a retardation to the proceeding constant amplitude mixed-mode fatigue crack propagation, which lasted longer than the estimated overload plastic zone size. This is in direct contradiction to these models, indicating that the models developed for mode I conditions are not readily applicable to mixed-mode I and II conditions. It is possible that models based on plasticity-induced closure are able to explain the observed retardation, but this requires time-consuming elastic-plastic finite element analysis, which could not be included in the scope of this work.

It is interesting to note that the models predict that a single overload will have a different effect in fatigue crack initiation than in fatigue crack propagation. In variable amplitude fatigue crack initiation models, an overload will contribute to the fatigue damage, and decrease the crack initiation life, whereas in variable amplitude fatigue crack propagation models it will cause fatigue crack growth retardation, thereby increasing the crack propagation life. Both predictions are justified by sound physical explanations (see Chapter 2), but this leads to some inconsistency when using nonlinear variable amplitude fatigue models together with the current fatigue analysis rules for welded structures,

where a single *S*-*N* curve is used to predict the sum of the crack initiation life and the crack growth until the crack extends through the material thickness (see Figure 2.2). It is evident that this inconsistency needs to be further studied.

While much research has been directed at mixed-mode fatigue crack propagation, no study has concluded on whether the Tanaka or the Richard effective stress intensity factor is best suited for predicting the mixed-mode fatigue crack propagation rate, mainly due to the small difference between them. The two models have been compared in Figure 7.4, and it was found that the Richard effective stress intensity factor is more conservative in most practical cases. According to the literature study, the crack path can usually be well predicted using the criterion of maximum tangential stress. In Paper VI, it was shown that if the loading direction is only changed once, it is possible to model the resulting crack as a kinked crack (Figure 9.2), where the kink angle is set to the direction which yields $K_{II} = 0$. A mixed-mode fatigue crack generally tends to a path where $K_{II} = 0$ (Cotterell and Rice, 1980), which also explains the observation made in Paper IV, that the value of $K_{II}$ should not be included in the effective stress intensity factor when this kind of crack is approximated as a straight line.

Mixed-mode cracks usually have to be modelled using some computational method. The review presented in Paper III revealed that the boundary element method may be more efficient, but practicing engineers are usually more familiar with the finite element method (FEM), which is also readily available in commercial software codes. The extended finite element method (XFEM) makes the modelling of fatigue crack propagation more convenient, but so far its availability in commercial software is limited. Fatigue crack growth simulations can be solved faster using XFEM, but the current limitation to first-order elements in ANSYS and Abaqus makes it less accurate than FEM (Bjørheim, 2019). However, it is likely that XFEM with second-order elements will eventually be implemented in these software.

In Chapter 6, it was shown that the domain integral method is an excellent technique for extracting the stress intensity factor from a finite element solution, but it is not available for all element types in commercial software. Therefore, it is necessary to know the capabilities and limitations of alternative techniques. It has been shown that care should be taken when the quarter-point displacement technique (QPDT), the displacement correlation technique (DCT) and the modified crack closure integral (MCCI) are used. While these techniques are popular, they do not necessarily converge as the crack tip mesh is refined. The displacement extrapolation technique was found to be significantly less sensitive to the crack tip mesh density, but in some cases it can be challenging to choose the correct nodes for extrapolation.

Often, it can be useful to do an initial assessment of a detected crack using available stress intensity factor solutions. In Paper V, the stress intensity factor for a long circumferential through-wall crack in a cylindrical shell subjected to torsion was determined using FEM. The computed solution was found to be significantly higher than the available analytical solution, which was derived for short cracks, and can be used to assess this crack geometry under mixed-mode conditions.

No matter which kind of model is used to estimate the fatigue life, the predictions will always be limited by the agreement between the analysed stress history, and the actual stress history acting at the critical spots. In Paper I, it was shown that fluid-structure interaction simulations can be used to obtain more realistic stress histories for flexible structures subjected to fluid flow. This can be very useful if one or a few relatively short vibration responses may be extrapolated to represent the full vibration history of the structure. Yet, the computational effort was found to be quite large if the basic large-eddy simulation turbulence model is used.

## 10.1 Recommendations for further study

In order to fairly compare all the different models for variable amplitude fatigue crack initiation, it would be useful to compile a diverse set of experimental data which could be compared to model predictions. Due to the scatter in the experimental data, a few test results are not sufficient to assess the models. It is very expensive to conduct an experimental study on the scale of the study by Manson, Freche and Ensign (1967), and it is therefore necessary to compile data from a number of studies. The data set should naturally also include specimens subjected to multi-stress level loading and spectrum loading. Then, it could be possible to compare the mean value and standard deviation of the ratio of predicted-to-experimental fatigue lives for the different models under different loading conditions. It is also necessary to study whether these models can be applied with *S*-*N* curves for welded joints, which also include a crack propagation phase, as mentioned above. In addition, the modelling of fatigue damage accumulation due to cycles below the constant amplitude fatigue limit, and under multiaxial fatigue loading, requires further study.

In order to verify the conclusions reached about variable amplitude mixed-mode fatigue crack propagation, it is necessary to carry out additional experiments. It would be convenient to choose a specimen which is cheaper to fabricate and simpler to analyse than the one used in the present work. In addition, it would be better to choose a material with higher yield strength and lower toughness, thereby allowing higher crack propagation rates. The 316L steel, which was used in the present work, is a very common stainless steel, and was chosen mainly because it is easier to observe the crack in a stainless steel than in a carbon steel. If new experiments confirm the conclusions reached here, the next step would be to make a predictive model for variable amplitude mixed-mode fatigue crack propagation. It is evident that a significant research effort is required in order to reach this goal.

When it comes to constant amplitude mixed-mode fatigue crack propagation, it would be interesting to conduct experiments which could help us choose between the Tanaka and the Richard effective stress intensity factor. From Figure 7.4 it is possible to choose a mode mixity where the difference between the models is large. With the increasing availability of biaxial fatigue testing machines, it is possible to change the loading direction multiple times during a single test, and the same mode mixity could be repeated multiple times during the test. This kind of experiment would require an accurate crack length measurement method, preferably automatic optical crack length measurements with image analysis hardware and software. This would naturally also be the preferred measurement method for studying variable amplitude mixed-mode fatigue crack propagation.

# Reference list

Abosrra, L., Ashour, A.F., Mitchell, S.C. and Youseffi, M. (2009) Corrosion of mild steel and 316L austenitic stainless steel with different surface roughness in sodium chloride saline solutions, in Brebbia, C.A. and Adey, R.A. (eds.) *Electrochemical Process Simulation III, WIT Transactions on Engineering Sciences Vol. 65*. Southampton: WIT Press, pp. 161–172. doi: 10.2495/ECOR090161

Adedipe, O., Brennan, F. and Kolios, A. (2016) Review of corrosion fatigue in offshore structures: Present status and challenges in the offshore wind sector. *Renewable and Sustainable Energy Reviews*, 61, pp. 141–154. doi: 10.1016/j.rser.2016.02.017

Aeran, A., Siriwardane, S.C., Mikkelsen, O. and Langen, I. (2017) A framework to assess structural integrity of ageing offshore jacket structures for life extension, *Marine Structures*, 56, pp. 237–259. doi: 10.1016/j.marstruc.2017.08.002

Aguilar Espinosa, A.A., Fellows, N.A., Durodola, J.F. and Fellows, L.J. (2017a) Development of numerical model for the determination of crack opening and closure loads, for long cracks, *Fatigue & Fracture of Engineering Materials & Structures*, 40(4), pp. 571–585. doi: 10.1111/ffe.12532

Aguilar Espinosa, A.A., Fellows, N.A., Durodola, J.F. and Fellows, L.J. (2017b) Determination of crack growth for 6082-T6 aluminium subjected to periodic single and block overloads and underloads using a two dimensional finite element model, *International Journal of Fatigue*, 105, pp. 244–261. doi: 10.1016/j.ijfatigue.2017.08.018

Aid, A., Amrouche, A., Bachir Bouiadjra, B., Benguediab, M. and Mesmacque, G. (2011) Fatigue life prediction under variable loading based on a new damage model, *Materials and Design*, 32(1), pp. 183–191. doi: 10.1016/j.matdes.2010.06.010

Alegre, J.M. and Cuesta, I.I. (2010) Some aspects about the crack growth FEM simulations under mixed-mode loading, *International Journal of Fatigue*, 32(7), pp. 1090–1095. doi: 10.1016/j.ijfatigue.2009.12.002

Andersen, I. (2017) Statoil investerer 20 milliarder på Njord og Bauge, *TU.no*. Available at: https://www.tu.no/artikler/378734 (accessed: 27 March 2017).

Anderson, T.L. (2005) *Fracture mechanics: Fundamentals and applications*. 3rd edn. Boca Raton: CRC Press.

ANSYS, Inc. (2015) ANSYS® Academic Research Mechanical, Release 17.0, Help System, Mechanical APDL. ANSYS, Inc.

Arrayago, I., Real, E. and Gardner, L. (2015) Description of stress-strain curves for stainless steel alloys, *Materials & Design*, 87, pp. 540–552. doi: 10.1016/j.matdes.2015.08.001

ASTM International (2016) *ASTM E647 - 15e1 Standard test method for measurement of fatigue crack growth rates*. doi: 10.1520/E0647-15E01

Ayatollahi, M.R., Razavi, S.M.J. and Chamani, H.R. (2014) Fatigue life extension by crack repair using stop-hole technique under pure mode-I and pure mode-II loading conditions, *Procedia Engineering*, 74, pp. 18–21. doi: 10.1016/j.proeng.2014.06.216

Ayatollahi, M.R., Razavi, S.M.J., Sommitsch, C. and Moser, C. (2016) Fatigue life extension by crack repair using double stop-hole technique, *Materials Science Forum*, 879, pp. 3–8. doi: 10.4028/www.scientific.net/MSF.879.3

Ayatollahi, M.R., Razavi, S.M.J. and Yahya, M.Y. (2015) Mixed mode fatigue crack initiation and growth in a CT specimen repaired by stop hole technique, *Engineering Fracture Mechanics*, 145, pp. 115–127. doi: 10.1016/j.engfracmech.2015.03.027

Banks, T.M. and Garlick, A. (1984) The form of crack tip plastic zones, *Engineering Fracture Mechanics*, 19(3), pp. 571–581. doi: 10.1016/0013-7944(84)90012-2

Banks-Sills, L. (2010) Update: Application of the finite element method to linear elastic fracture mechanics, *Applied Mechanics Reviews*, 63(2), 020803. doi: 10.1115/1.4000798

Barsoum, R.S. (1976) On the use of isoparametric finite elements in linear fracture mechanics, *International Journal for Numerical Methods in Engineering*, 10(1), pp. 25–37. doi: 10.1002/nme.1620100103

Beaudoin, M. and Jasak, H. (2008) Development of a generalized grid interface for turbomachinery simulations with OpenFOAM, *Open Source CFD International Conference 2008*. Berlin, December 4–5, 2008.

Belytschko, T. and Black, T. (1999) Elastic crack growth in finite elements with minimal remeshing, *International Journal for Numerical Methods in Engineering*, 45(5), pp. 601–620. doi: 10.1002/(SICI)1097-0207(19990620)45:5<601::AID-NME598>3.0.CO;2-S

Belytschko, T., Liu, W.K., Moran, B. and Elkhodary, K.I. (2014) *Nonlinear finite elements for continua and structures*. 2nd edn. Chichester: Wiley.

Benra, F.-K., Dohmen, H.J., Pei, J., Schuster, S. and Wan, B. (2011) A comparison of one-way and two-way coupling methods for numerical analysis of fluid-structure interactions, *Journal of Applied Mathematics*, 2011, 853560. doi: 10.1155/2011/853560

Bergara, A., Dorado, J.I., Martin-Meizoso, A. and Martínez-Esnaola, J.M. (2017) Fatigue crack propagation in complex stress fields: Experiments and numerical simulations using the extended finite element method (XFEM), *International Journal of Fatigue*, 103, pp. 112–121. doi: 10.1016/j.ijfatigue.2017.05.026

Bian, L. and Taheri, F. (2011) A proposed maximum ratio criterion applied to mixed mode fatigue crack propagation, *Materials and Design*, 32(4), pp. 2066–2072. doi: 10.1016/j.matdes.2010.11.053

Bittencourt, T.N., Wawrzynek, P.A., Ingraffea, A.R. and Sousa, J.L. (1996) Quasi-automatic simulation of crack propagation for 2D LEFM problems, *Engineering Fracture Mechanics*, 55(2), pp. 321-334. doi: 10.1016/0013-7944(95)00247-2

Bjørheim, F. (2019) *Practical comparison of crack meshing in ANSYS mechanical APDL 19.2*. Master's thesis, University of Stavanger.

Blasón, S., Correia, J.A.F.O., de Jesus, A.M.P., Calçada, R.A.B. and Fernández-Canteli, A. (2016) A probabilistic analysis of Miner's law for different loading conditions, *Structural Engineering and Mechanics*, 60(1), pp. 71–90. doi: 10.12989/sem.2016.60.1.071

Boljanović, S. and Maksimović, S. (2014) Mixed mode crack growth simulation with/without overloads, *International Journal of Fatigue*, 67, pp. 183–190. doi: 10.1016/j.ijfatigue.2013.11.011

Boljanović, S. and Maksimović, S. (2017) Computational mixed mode failure analysis under fatigue loadings with constant amplitude and overload, *Engineering Fracture Mechanics*, 174, pp. 168–179. doi: 10.1016/j.engfracmech.2016.12.017

Bordas, S., Rabczuk, T. and Zi, G. (2008) Three-dimensional crack initiation, propagation, branching and junction in non-linear materials by an extended meshfree method without asymptotic enrichment, *Engineering Fracture Mechanics*, 75(5), pp. 943–960. doi: 10.1016/j.engfracmech.2007.05.010

Borrego, L.P., Antunes, F.V., Costa, J.M. and Ferreira, J.M. (2006) Mixed-mode fatigue crack growth behaviour in aluminium alloy, *International Journal of Fatigue*, 28(5–6), pp. 618–626. doi: 10.1016/j.ijfatigue.2005.07.047

Boyer, H.E. (ed.) (1986) *Atlas of fatigue curves*. Ohio: ASM International.

Branco, R., Antunes, F.V. and Costa, J.D. (2015) A review on 3D-FE adaptive remeshing techniques for crack growth modelling, *Engineering Fracture Mechanics*, 141, pp. 170–195. doi: 10.1016/j.engfracmech.2015.05.023

British Standards Institution (2015) *BS 7910:2013+A1:2015 Guide to methods for assessing the acceptability of flaws in metallic structures*.

Budynas, R.G. and Nisbett, J.K. (2015) *Shigley's mechanical engineering design*. 10th edn SI units. New York: McGraw-Hill.

Campbell, R.L. and Paterson, E.G. (2011) Fluid-structure interaction analysis of flexible turbomachinery, *Journal of Fluids and Structures*, 27(8), pp. 1376–1391. doi: 10.1016/j.jfluidstructs.2011.08.010

Cardiff, P. (2012) *Development of the finite volume method for hip joint stress analysis*. Doctoral thesis, University College Dublin. Available at: http://hdl.handle.net/10197/7919 (accessed: 17 February 2017).

Castro, J.T.P., Meggiolaro, M.A., Miranda, A.C.O. et al. (2012) Prediction of fatigue crack initiation lives at elongated notch roots using short crack concepts, *International Journal of Fatigue*, 42, pp. 172–182. doi: 10.1016/j.ijfatigue.2011.10.010

Cesur, A., Carlsson, C., Feymark, A., Fuchs, L. and Revstedt, J. (2014) Analysis of the wake dynamics of stiff and flexible cantilever beams using POD and DMD, *Computers & Fluids*, 101, pp. 27–41. doi: 10.1016/j.compfluid.2014.05.012

Chan, S.K., Tuba, I.S. and Wilson, W.K. (1970) On the finite element method in linear fracture mechanics, *Engineering Fracture Mechanics*, 2(1), pp. 1–17. doi: 10.1016/0013-7944(70)90026-3

Chen, N.-Z. (2016) A stop-hole method for marine and offshore structures, *International Journal of Fatigue*, 88, pp. 49–57. doi: 10.1016/j.ijfatigue.2016.03.010

Chen, W. and Landet, E. (2001) Stress analysis of cutouts with and without reinforcement, *Proceedings of the 20th International Conference on Offshore Mechanics and Arctic Engineering*. Rio de Janeiro, June 3–8, 2001. New York: ASME, vol. 3, pp. 17–23.

Colombo, D. and Giglio, M. (2006) A methodology for automatic crack propagation modelling in planar and shell FE models, *Engineering Fracture Mechanics*, 73(4), pp. 490–504. doi: 10.1016/j.engfracmech.2005.08.007

Cook, R.D., Malkus, D.S., Plesha, M.E. and Witt, R.J. (2002) *Concepts and applications of finite element analysis*. 4th edn. Hoboken: Wiley

Correia, J.A.F.O., Jesus, A., Blasón, S., Calvente, M. and Fernández-Canteli, A. (2016) Probabilistic non-linear cumulative fatigue damage of the P355NL1 pressure vessel steel, *Proceedings of the ASME 2016 Pressure Vessels and Piping Conference*. Vancouver, July 17–21, 2016. New York: ASME, vol. 6A, pp. V06AT06A034. doi: 10.1115/PVP2016-63920

Correia, J.A.F.O., Raposo, P., Muniz-Calvente, M. et al. (2017) A generalization of the fatigue Kohout-Věchet model for several fatigue damage parameters, *Engineering Fracture Mechanics*, 185, pp. 284–300. doi: 10.1016/j.engfracmech.2017.06.009

Cotterell, B. (2010) *Fracture and life*. London: Imperial College Press.

Cotterell, B. and Rice, J.R. (1980) Slightly curved or kinked cracks, *International Journal of Fracture*, 16(2), pp. 155–169. doi: 10.1007/BF00012619

Courtin, S., Gardin, C., Bézine, G. and Ben Hadj Hamouda, H. (2005) Advantages of the *J*-integral approach for calculating stress intensity factors when using the commercial finite element software ABAQUS, *Engineering Fracture Mechanics*, 72(14), pp. 2174–2185. doi: 10.1016/j.engfracmech.2005.02.003

Cui, W., Wang, F. and Huang, X. (2011) A unified fatigue life prediction method for marine structures, *Marine Structures*, 24(2), pp. 153–181. doi: 10.1016/j.marstruc.2011.02.007

Dalløkken, P.E. (2018) Havarikommisjonen: Slik girboksen er konstruert kan en lignende ulykke skje på nytt, *TU.no*. Available at: https://www.tu.no/artikler/441616 (accessed: 4 June 2019).

Dassault Systèmes (2016) SIMULIA User Assistance 2017, Abaqus. Dassault Systèmes Simulia Corp.

Datta, S., Chattopadhyay, A., Iyyer, N. and Phan, N. (2018) Fatigue crack propagation under biaxial fatigue loading with single overloads, *International Journal of Fatigue*, 109, pp. 103–113. doi: 10.1016/j.ijfatigue.2017.12.018

Dattoma, V., Giancane, S., Nobile, R. and Panella, F.W. (2006) Fatigue life prediction under variable loading based on a new non-linear continuum damage mechanics model, *International Journal of Fatigue*, 28(2), pp. 89–95. doi: 10.1016/j.ijfatigue.2005.05.001

Dekker, R., van der Meer, F.P., Maljaars, J. and Sluys, L.J. (2019) A cohesive XFEM model for simulating fatigue crack growth under mixed-mode loading and overloading, *International Journal for Numerical Methods in Engineering*, 118(10), pp. 561–577. doi: 10.1002/nme.6026

deLorenzi, H.G. (1985) Energy release rate calculations by the finite element method, *Engineering Fracture Mechanics*, 21(1), pp. 129–143. doi: 10.1016/0013-7944(85)90060-8

Demir, O., Ayhan, A.O. and İriç, S. (2017) A new specimen for mixed mode-I/II fracture tests: Modeling, experiments and criteria development, *Engineering Fracture Mechanics*, 178, pp. 457–476. doi: 10.1016/j.engfracmech.2017.02.019

Ding, P. and Wang, X. (2017) Three-dimensional mixed mode (I and II) crack-front fields in ductile thin plates — effects of T-stress, *Fatigue & Fracture of Engineering Materials & Structures*, 40(3), pp. 349–363. doi: 10.1111/ffe.12498

Ding, Z., Wang, X., Gao, Z. and Bao, S. (2017) An experimental investigation and prediction of fatigue crack growth under

overload/underload in Q345R steel, *International Journal of Fatigue*, 98, pp. 155–166. doi: 10.1016/j.ijfatigue.2017.01.024

Dirik, H. and Yalçinkaya, T. (2018) Crack path and life prediction under mixed mode cyclic variable amplitude loading through XFEM, *International Journal of Fatigue*, 114, pp. 34–50. doi: 10.1016/j.ijfatigue.2018.04.026

DNV GL (2015) *DNVGL-RP-C210 Probabilistic methods for planning of inspection for fatigue cracks in offshore structures*.

DNV GL (2016) *DNVGL-RP-C203 Fatigue design of offshore structures*.

Dong, L. and Atluri, S.N. (2013a) Fracture & fatigue analyses: SGBEM-FEM or XFEM? Part 1: 2D structures, *Computer Modeling in Engineering & Sciences*, 90(2), pp. 91–146. doi: 10.3970/cmes.2013.090.091

Dong, L. and Atluri, S.N. (2013b) Fracture & fatigue analyses: SGBEM-FEM or XFEM? Part 2: 3D solids, *Computer Modeling in Engineering & Sciences*, 90(5), pp. 379–413. doi: 10.3970/cmes.2013.090.379

Dowling, N.E. (1979) Notched member fatigue life predictions combining crack initiation and propagation, *Fatigue of Engineering Materials and Structures*, 2(2), pp. 129–138. doi: 10.1111/j.1460-2695.1979.tb01349.x

Dowling, N.E. (2013) *Mechanical behavior of materials: engineering methods for deformation, fracture, and fatigue*. 4th int edn. Harlow: Pearson.

Dowling, N.E., Calhoun, C.A. and Arcari, A. (2009) Mean stress effects in stress-life fatigue and the Walker equation, *Fatigue & Fracture of Engineering Materials & Structures*, 32(3), pp. 163–179. doi: 10.1111/j.1460-2695.2008.01322.x

DuPont, J., Yamada, Y., Lacy, T.E. and Newman, J.C. Jr. (2017) Prediction of fatigue-crack growth for 7075-T7351 aluminum alloy

under various flight-load spectra, *Engineering Fracture Mechanics*, 177, pp. 79–94. doi: 10.1016/j.engfracmech.2017.03.023

Elber, W. (1970) Fatigue crack closure under cyclic tension, *Engineering Fracture Mechanics*, 2(1), pp. 37–45. doi: 10.1016/0013-7944(70)90028-7

Elguedj, T., Gravouil, A. and Combescure, A. (2006) Appropriate extended functions for X-FEM simulation of plastic fracture mechanics, *Computer Methods in Applied Mechanics and Engineering*, 195(7–8), pp. 501–515. doi: 10.1016/j.cma.2005.02.007

Elias, Z.M. (1967) *On the derivation of Vlasov's shallow shell equations and their application to non shallow shells*. (NASA-CR-94591). The National Aeronautics and Space Administration. Available at: http://hdl.handle.net/2060/19680014653 (accessed: 15 October 2018).

Erdogan, F. and Ratwani, M. (1972) A circumferential crack in a cylindrical shell under torsion, *International Journal of Fracture Mechanics*, 8(1), pp. 87–95. doi: 10.1007/BF00185200

Erdogan, F. and Sih, G.C. (1963) On the crack extension in plates under plane loading and transverse shear, *Journal of Basic Engineering*, 85(4), pp. 519–527. doi: 10.1115/1.3656897

Ersdal, G., Sharp, J.V. and Stacey, A. (2019) *Ageing and life extension of offshore structures*. Hoboken: Wiley.

Fatemi, A. and Yang, L. (1998) Cumulative fatigue damage and life prediction theories: a survey of the state of the art for homogeneous materials, *International Journal of Fatigue*, 20(1), pp. 9–34. doi: 10.1016/S0142-1123(97)00081-9

Fernández-Canteli, A., Blasón, S., Correia, J.A.F.O. and de Jesus, A.M.P. (2014) A probabilistic interpretation of the Miner number for fatigue life prediction, *Frattura ed Integrità Strutturale*, 8(30), pp. 327–339. doi: 10.3221/IGF-ESIS.30.40

Fines, S. (1985) Loads on ocean structures, in Almar-Næss, A. (ed.) *Fatigue handbook: offshore steel structures*. Trondheim: Tapir, pp. 39–90.

Finnemore, E.J. and Franzini, J.B. (2002) *Fluid mechanics with engineering applications*. 10th edn. New York: McGraw-Hill.

Fissolo, A., Gourdin, C., Chen, Y., Perez, G. and Stelmaszyk, J.M. (2015) Investigations into the cumulative fatigue life of an AISI 304L austenitic stainless steel used for pressure water reactors: Application of a double linear damage rule, *International Journal of Fatigue*, 77, pp. 199–215. doi: 10.1016/j.ijfatigue.2015.02.010

Folias, E.S. (1965) A finite line crack in a pressurized spherical shell, *International Journal of Fracture Mechanics*, 1(1), pp. 20–46. doi: 10.1007/BF00184151

Forman, R.G., Hickman, J.C. and Shivakumar, V. (1985) Stress intensity factors for circumferential through cracks in hollow cylinders subjected to combined tension and bending loads, *Engineering Fracture Mechanics*, 21(3), pp. 563–571. doi: 10.1016/S0013-7944(85)80049-7

Forman, R.G. and Mettu, S.R. (1992) Behavior of surface and corner cracks subjected to tensile and bending loads in a Ti-6Al-4V alloy, in Ernst, H.A., Saxena, A. and McDowell, D.L. (eds.) *Fracture mechanics: twenty-second symposium (volume I), ASTM STP 1131*. Philadelphia: American Society for Testing and Materials, pp. 519–546.

Fremy, F., Pommier, S., Galenne, E. and Courtin, S. (2012) A scaling approach to model history effects in fatigue crack growth under mixed mode I + II + III loading conditions for a 316L stainless steel, *International Journal of Fatigue*, 42, pp. 207–216. doi: 10.1016/j.ijfatigue.2011.10.013

Fries, T.-P. and Belytschko, T. (2010) The extended/generalized finite element method: An overview of the method and its applications

*International Journal for Numerical Methods in Engineering*, 84(3), pp. 253–304. doi: 10.1002/nme.2914

Fu, P., Johnson, S.M., Settgast, R.R. and Carrigan, C.R. (2012) Generalized displacement correlation method for estimating stress intensity factors, *Engineering Fracture Mechanics*, 88, pp. 90–107. doi: 10.1016/j.engfracmech.2012.04.010

Gao, H., Huang, H.-Z., Zhu, S.-P., Li, Y.-F. and Yuan, R. (2014) A modified nonlinear damage accumulation model for fatigue life prediction considering load interaction effects, *The Scientific World Journal*, 2014, 164378. doi: 10.1155/2014/164378

Gao, H., Shen, S. and Yun, Y. (2012) Fatigue crack length real time measurement method based on camera automatically tracking and positioning, *Applied Mechanics and Materials*, 130–134, pp. 3111–3118. doi: 10.4028/www.scientific.net/AMM.130-134.3111

Gao, H.-Y., Zuo, F.-J., Lü, Z.-Q., Zhu, S.-P. and Huang, H.-Z. (2015) Residual life prediction based on nonlinear fatigue damage accumulation model, *Journal of Shanghai Jiaotong University (Science)*, 20(4), pp. 449–453. doi: 10.1007/s12204-015-1647-2

García-Collado, A., Vasco-Olmo, J.M. and Díaz, F.A. (2017) Numerical analysis of plasticity induced crack closure based on an irreversible cohesive zone model, *Theoretical and Applied Fracture Mechanics*, 89, pp. 52–62. doi: 10.1016/j.tafmec.2017.01.006

Gates, N.R. and Fatemi, A. (2017) Experimental fatigue crack growth behavior and predictions under multiaxial variable amplitude service loading histories, *Engineering Fracture Mechanics*, 174, pp. 80–103. doi: 10.1016/j.engfracmech.2016.11.023

Ghaffari, M.A. and Hosseini-Toudeshky, H. (2013) Fatigue crack propagation analysis of repaired pipes with composite patch under cyclic pressure, *Journal of Pressure Vessel Technology*, 135(3), 031402. doi: 10.1115/1.4023568

Gillebaart, T., Blom, D.S., van Zuijlen, A.H. and Bijl, H. (2016) Time consistent fluid structure interaction on collocated grids for

incompressible flow, *Computer Methods in Applied Mechanics and Engineering*, 298, pp. 159–182. doi: 10.1016/j.cma.2015.09.025

Gintalas, M., Ainsworth, R.A. and Scenini, F. (2017) T-stress solutions for through-wall circumferential cracks in straight pipes under bending, *International Journal of Pressure Vessels and Piping*, 152, pp. 27–37. doi: 10.1016/j.ijpvp.2017.04.004

Golos, K. and Wasiluk, B. (2000) Role of plastic zone in crack growth direction criterion under mixed mode loading, *International Journal of Fracture*, 102(4), pp. 341–353. doi: 10.1023/A:1007663728926

Greenshields, C.J. (2016) *OpenFOAM user guide version 4.0*. OpenFOAM Foundation Ltd.

Guerra-Rosa, L., Moura Branco, C. and Radon, J.C. (1984) Monotonic and cyclic crack tip plasticity, *International Journal of Fatigue*, 6(1), pp. 17–24. doi: 10.1016/0142-1123(84)90004-5

Guinea, G.V., Planas, J. and Elices, M. (2000) $K_I$ evaluation by the displacement extrapolation technique, *Engineering Fracture Mechanics*, 66(3), pp. 243–255. doi: 10.1016/S0013-7944(00)00016-3

Guzman-Leong, C.E. and Udyawar, A. (2017) Technical basis for ASME code section XI nonmandatory appendix C update, *Proceedings of the ASME 2017 Pressure Vessels and Piping Conference*. Waikoloa, July 16–20, 2017. New York: ASME, vol. 1A, pp. V01AT01A004. doi: 10.1115/PVP2017-65058

Haagensen, P.J. (1994) Methods for fatigue strength improvement and repair of welded offshore structures, *Proceedings of the 13th International Conference on Offshore Mechanics and Arctic Engineering*. Houston, February 27–March 3, 1994. New York: ASME, vol. 3, pp. 419–427.

Haagensen, P.J., Larsen, J.E. and Vårdal, O.T. (2015) Long term effectiveness of life extension methodologies applied to offshore structures, *Engineering Failure Analysis*, 58(2), pp. 499–513. doi: 10.1016/j.engfailanal.2015.08.045

Han, Q., Wang, Y., Yin, Y. and Wang, D. (2015) Determination of stress intensity factor for mode I fatigue crack based on finite element analysis, *Engineering Fracture Mechanics*, 138, pp. 118–126. doi: 10.1016/j.engfracmech.2015.02.019

Harrop, L.P. (1982) The optimum size of quarter-point crack tip elements, *International Journal for Numerical Methods in Engineering*, 18(7), pp. 1101–1103. doi: 10.1002/nme.1620180713

Hasegawa, K., Li, Y. and Osakabe, K. (2014) Collapse loads for circumferentially through-wall cracked pipes subjected to combined torsion and bending moments, *Engineering Fracture Mechanics*, 123, pp. 77–85. doi: 10.1016/j.engfracmech.2013.12.013

Hashin, Z. and Rotem, A. (1978) A cumulative damage theory of fatigue failure, *Materials Science and Engineering*, 34(2), pp. 147–160. doi: 10.1016/0025-5416(78)90045-9

He, W., Liu, J. and Xie, D. (2014) Numerical study on fatigue crack growth at a web-stiffener of ship structural details by an object-oriented approach in conjunction with ABAQUS, *Marine Structures*, 35, pp. 45–69. doi: 10.1016/j.marstruc.2013.12.001

Heinrich, C., Khalil, M., Martynov, K. and Wever, U. (2019) Online remaining lifetime estimation for structures, *Mechanical Systems and Signal Processing*, 119, pp. 312–327. doi: 10.1016/j.ymssp.2018.09.028

Hellen, T.K. (1975) On the method of virtual crack extensions, *International Journal for Numerical Methods in Engineering*, 9(1), pp. 187–207. doi: 10.1002/nme.1620090114

Henshell, R.D. and Shaw, K.G. (1975) Crack tip finite elements are unnecessary, *International Journal for Numerical Methods in Engineering*, 9(3), pp. 495–507. doi: 10.1002/nme.1620090302

Heyerdahl, S. (2017) Statoil og partnere investerer 20 milliarder kroner på gamle oljefelt, *NRK.no*. Available at: https://www.nrk.no/norge/1.13446612 (accessed: 27 March 2017).

Hjertager, B.H. (2009) *Lecture notes in OpenFOAM*. Stavanger: University of Stavanger.

Hjertager, B.H. (2014) *Computational analysis of fluid flow processes*. Stavanger: University of Stavanger.

Hojo, K., Watanabe, D., Kawabata, S. and Ametani, Y. (2014) Ductile crack propagation simulation of a cylinder with a through-wall circumferential flaw under excessive cyclic torsion loading, *Proceedings of the ASME 2014 Pressure Vessels & Piping Conference*. Anaheim, July 20–24, 2014. New York: ASME, vol. 1, pp. V001T01A109. doi: 10.1115/PVP2014-28093

Holmes, S., Oakley, O.H. Jr. and Constantinides, Y. (2006) Simulation of riser VIV using fully three dimensional CFD simulations, *Proceedings of the 25th International Conference on Offshore Mechanics and Arctic Engineering*. Hamburg, June 4–9, 2006. New York: ASME, vol. 4, pp. 563–570. doi: 10.1115/OMAE2006-92124

Hu, X., Bui, T.Q., Wang, J. et al. (2017) A new cohesive crack tip symplectic analytical singular element involving plastic zone length for fatigue crack growth prediction under variable amplitude cyclic loading, *European Journal of Mechanics A/Solids*, 65, pp. 79–90. doi: 10.1016/j.euromechsol.2017.03.008

Huang, X., Moan, T. and Cui, W. (2008) An engineering model of fatigue crack growth under variable amplitude loading, *International Journal of Fatigue*, 30(1), pp. 2–10. doi: 10.1016/j.ijfatigue.2007.03.004

Hübner, B., Walhorn, E. and Dinkler, D. (2004) A monolithic approach to fluid-structure interaction using space-time finite elements, *Computer Methods in Applied Mechanics and Engineering*, 193(23–26), pp. 2087–2104. doi: 10.1016/j.cma.2004.01.024

Huffman, P.J., Ferreira, J, Correia, J.A.F.O. et al. (2017) Fatigue crack propagation prediction of a pressure vessel mild steel based on a strain energy density model, *Frattura ed Integrità Strutturale*, 11(42), pp. 74–84. doi: 10.3221/IGF-ESIS.42.09

Huh, N.-S., Shim, D.-J., Choi, S., Wilkowski, G.M. and Yang, J.-S. (2008) Stress intensity factors for slanted through-wall cracks based on elastic finite element analyses, *Fatigue & Fracture of Engineering Materials & Structures*, 31(2), pp. 197–208. doi: 10.1111/j.1460-2695.2008.01215.x

Hussain, M.A., Pu, S.L. and Underwood, J. (1974) Strain energy release rate for a crack under combined mode I and mode II, in *Fracture analysis, ASTM STP 560*. Philadelphia: American Society for Testing and Materials, pp. 2–28. doi: 10.1520/STP33130S

Højfeldt, E. and Østervig, C.B. (1986) Fatigue crack propagation in shafts with shoulder fillets, *Engineering Fracture Mechanics*, 25(4), 421–427. doi: 10.1016/0013-7944(86)90256-0

Hörnlund, E., Ersdal, G., Hinderaker, R.H., Johnsen, R. and Sharp, J. (2011) Material issues in ageing and life extension, *Proceedings of the ASME 2011 30th International Conference on Ocean, Offshore and Arctic Engineering*. Rotterdam, June 19–24, 2011. New York: ASME, vol. 3, pp. 261–267. doi: 10.1115/OMAE2011-49363

Irwin, G.R. (1960) Plastic zone near a crack and fracture toughness, *Mechanical and metallurgical behavior of sheet materials: Proceedings of the 7th Sagamore Ordnance Materials Research Conference*. Raquette Lake, August 16–19, 1960. Syracuse: Syracuse University Research Institute, pp. IV-63–78.

Jasak, H. and Tuković, Ž. (2006) Automatic mesh motion for the unstructured finite volume method, *Transactions of FAMENA*, 30(2), pp. 1–20.

Jasak, H. and Tuković, Ž. (2010) Dynamic mesh handling in OpenFOAM applied to fluid-structure interaction simulations, *V European Conference on Computational Fluid Dynamics. Lisbon*, June 14–17, 2010. Barcelona: ECCOMAS.

Jeelani, S. and Musial, M. (1986) A study of cumulative fatigue damage in AISI 4130 steel, *Journal of Materials Science*, 21(6), pp. 2109–2113. doi: 10.1007/BF00547954

Johnson, W.S. (1981) Multi-parameter yield zone model for predicting spectrum crack growth, in Chang, J.B. and Hudson, C.M. (eds.) *Methods and models for predicting fatigue crack growth under random loading, ASTM STP 748*. Philadelphia: American Society for Testing and Materials, pp. 85–102. doi: 10.1520/STP28335S

Kajolli, R., Siriwardane, S.C. and Gudmestad, O.T. (2015) Application of new damage indicator-based sequential law to estimate fatigue life of offshore jacket structures, *COMPDYN 2015, 5th International Conference on Computational Methods in Structural Dynamics and Earthquake Engineering*. Crete, May 25–27, 2015. Athens: National Technical University of Athens, vol. 2, pp. 4690–4701.

Kamble, C. and Chen, H.-C. (2016) 3D VIV fatigue analysis using CFD simulation for long marine risers, *Proceedings of the Twenty-sixth (2016) International Ocean and Polar Engineering Conference*. Rhodes, June 26–July 1, 2016. Cupertino: ISOPE, vol. 3, pp. 1094–1100.

Keprate, A., Ratnayake, R.M.C. and Sankararaman, S. (2017a) Minimizing hydrocarbon release from offshore piping by performing probabilistic fatigue life assessment, *Process Safety and Environmental Protection*, 106, pp. 34–51. doi: 10.1016/j.psep.2016.11.019

Keprate, A., Ratnayake, R.M.C. and Sankararaman, S. (2017b) Adaptive Gaussian process regression as an alternative to FEM for prediction of stress intensity factor to assess fatigue degradation in offshore pipeline, *International Journal of Pressure Vessels and Piping*, 153, pp. 45–58. doi: 10.1016/j.ijpvp.2017.05.010

Keryk, C., Sabatini, R., Kourousis, K., Gardi, A. and Silva, J.M. (2018) An innovative structural fatigue monitoring solution for general aviation aircraft, *Journal of Aerospace Technology and Management*, 10, e0518. doi: 10.5028/jatm.v10.779

Kitagawa, H., Yuuki, R. and Ohira, T. (1975) Crack-morphological aspects in fracture mechanics, *Engineering Fracture Mechanics*, 7(3), pp. 515–529. doi: 10.1016/0013-7944(75)90052-1

Kłysz, S. and Leski, A. (2012) Good practice for fatigue crack growth curves description, in Belov, A. (ed.) *Applied fracture mechanics*. IntechOpen, pp. 197–228. doi: 10.5772/52794

Knezevic, D.J., Kang, H.Y., Sharma, P., Malinowski, G. and Nguyen, T.T. (2018) Structural integrity management of offshore structures via RB-FEA and fast full load mapping based digital twins, *Proceedings of the Twenty-eighth (2018) International Ocean and Polar Engineering Conference*. Sapporo, June 10–15, 2018. Cupertino: ISOPE, vol. 1, pp. 1786–1792.

Knight, N.F. Jr., Ransom, J.B., Griffin, O.H. Jr. and Thompson, D.M. (1991) Global/local methods research using a common structural analysis framework, *Finite Elements in Analysis and Design*, 9(2), pp. 91–112. doi: 10.1016/0168-874X(91)90053-2

Košút, J. (2002) History influence exponent in cumulative fatigue damage determined using two-step loading experiments, *Fatigue & Fracture of Engineering Materials & Structures*, 25(6), pp. 575–586. doi: 10.1046/j.1460-2695.2002.00507.x

Krueger, R. (2004) Virtual crack closure technique: History, approach, and applications, *Applied Mechanics Reviews*, 57(2), pp. 109–143. doi: 10.1115/1.1595677

Kumosa, M. and Hull, D. (1989) Finite element analysis of a circumferentially cracked cylindrical shell loaded in torsion, *Engineering Fracture Mechanics*, 32(1), pp. 123–136. doi: 10.1016/0013-7944(89)90210-5

Kuna, M. (2013) *Finite elements in fracture mechanics*. Dordrecht: Springer.

Kwofie, S. and Rahbar, N. (2013) A fatigue driving stress approach to damage and life prediction under variable amplitude loading,

*International Journal of Damage Mechanics*, 22(3), pp. 393–404. doi: 10.1177/1056789512449638

Lacire, M.H., Chapuliot, S. and Marie, S. (1999) Stress intensity factors of through wall cracks in plates and tubes with circumferential cracks, *PVP-Vol. 388, Fracture, Design Analysis of Pressure Vessels, Heat Exchangers, Piping Components and Fitness for Service – 1999*. Boston, August 1–5, 1999. New York: ASME, pp. 13–21.

Lakshminarayana, H.V. and Murthy, M.V.V. (1976) On stresses around an arbitrarily oriented crack in a cylindrical shell, *International Journal of Fracture*, 12(4), pp. 547–566. doi: 10.1007/BF00034641

Lassen, T. and Recho, N. (2009) Proposal for a more accurate physically based S-N curve for welded steel joints, *International Journal of Fatigue*, 31(1), pp. 70–78. doi: 10.1016/j.ijfatigue.2008.03.032

Lee, J.-M. and Choi, B.-H. (2009) Experimental observation and modeling of the retardation of fatigue crack propagation under the combination of mixed-mode single overload and constant amplitude loads, *International Journal of Fatigue*, 31(11–12), pp. 1848–1857. doi: 10.1016/j.ijfatigue.2009.01.022

Lee, Y.-L., Pan, J., Hathaway, R.B. and Barkey, M.E. (2005) *Fatigue testing and analysis: Theory and practice*. Burlington: Butterworth-Heinemann.

Lesiuk, G. (2019) Mixed mode (I + II, I + III) fatigue crack growth rate description in P355NL1 and 18G2A steel using new energy parameter based on J-integral approach, *Engineering Failure Analysis*, 99, pp. 263–272. doi: 10.1016/j.engfailanal.2019.02.019

Lesiuk, G., Szata, M., Rozumek, D. et al. (2018) Energy response of S355 and 41Cr4 steel during fatigue crack growth process, *The Journal of Strain Analysis for Engineering Design*, 53(8), pp. 663–675. doi: 10.1177/0309324718798234

L'Hostis, D., van der Cammen, J., Hageman, R. and Aalberts, P. (2013) Overview of the Monitas II Project, *Proceedings of the Twenty-third*

*(2013) International Offshore and Polar Engineering Conference*. Anchorage, June 30–July 5, 2013. Cupertino: ISOPE, vol. 4, pp. 378–385.

Li, S., Zhang, Y., Qi, L. and Kang, Y. (2018) Effect of single tensile overload on fatigue crack growth behavior in DP780 dual phase steel, *International Journal of Fatigue*, 106, pp. 49–55. doi: 10.1016/j.ijfatigue.2017.09.018

Li, Y., Hasegawa, K., Miura, N. and Hoshino, K. (2017) Experimental study on failure estimation method for circumferentially cracked pipes subjected to multi-axial loads, *Journal of Pressure Vessel Technology*, 139(1), 011204. doi: 10.1115/1.4033531

Lie, A.M., Sune, R., Dunsæd, G.W., Sørensen, E. and Andreassen, S. (2017) Undesirable incident with HTV Eagle pipehandling crane – Statoil Gullfaks B – 7 March 2017. (Investigation report 001050062). Stavanger: Petroleumstilsynet. Available at: https://www.ptil.no/contentassets/1af8997a6d78482facec101eb7cccd38/investigation-report---statoil---gullfaks-b.pdf (accessed: 26 June 2019).

Lim, I.L., Johnston, I.W. and Choi, S.K. (1992) Comparison between various displacement-based stress intensity factor computation techniques, *International Journal of Fracture*, 58(3), pp. 193–210. doi: 10.1007/BF00015615

Liu, Y., Venkatesan, K.R. and Zhang, W. (2017) Time-based subcycle formulation for fatigue crack growth under arbitrary random variable loadings, *Engineering Fracture Mechanics*, 182, pp. 1–18. doi: 10.1016/j.engfracmech.2017.07.005

Lotsberg, I. (2009) Stress concentrations due to misalignment at butt welds in plated structures and at girth welds in tubulars, *International Journal of Fatigue*, 31(8–9), pp. 1337–1345. doi: 10.1016/j.ijfatigue.2009.03.005

Lotsberg, I. (2016) *Fatigue design of marine structures*. New York: Cambridge University Press.

Lotsberg, I. (2019) Development of fatigue design standards for marine structures, *Journal of Offshore Mechanics and Arctic Engineering*, 141(3), pp. 031301. doi: 10.1115/1.4041993

Lotsberg, I., Sigurdsson, G., Fjeldstad, A. and Moan, T. (2016) Probabilistic methods for planning of inspection for fatigue cracks in offshore structures, *Marine Structures*, 46, pp. 167–192. doi: 10.1016/j.marstruc.2016.02.002

Lv, Z., Huang, H.-Z., Zhu, S.-P., Gao, H. and Zuo, F. (2015) A modified nonlinear fatigue damage accumulation model, *International Journal of Damage Mechanics*, 24(2), pp. 168–181. doi: 10.1177/1056789514524075

Maddox, S.J. (2011) Fatigue design rules for welded structures, in Macdonald, K.A. (ed.) *Fracture and fatigue of welded joints and structures*. Cambridge: Woodhead Publishing, pp. 168–207. doi: 10.1533/9780857092502.2.168

Mai, Q.A., Sørensen, J.D. and Rigo, P. (2016) Updating failure probability of a welded joint in offshore wind turbine substructures, *Proceedings of the ASME 2016 35th International Conference on Ocean, Offshore and Arctic Engineering*. Busan, June 19–24, 2016. New York: ASME, vol. 3, pp. V003T02A059. doi: 10.1115/OMAE2016-54232

Malekan, M. and Carvalho, H. (2018) Analysis of a main fatigue crack interaction with multiple micro-cracks/voids in a compact tension specimen repaired by stop-hole technique, *The Journal of Strain Analysis for Engineering Design*, 53(8), pp. 648–662. doi: 10.1177/0309324718771124

Manson, S.S. (1966) Interfaces between fatigue, creep, and fracture, *International Journal of Fracture Mechanics*, 2(1), pp. 327–363. doi: 10.1007/BF00698478

Manson, S.S., Freche, J.C. and Ensign, C.R. (1967) Application of a double linear damage rule to cumulative fatigue, in *Fatigue crack*

*propagation, ASTM STP 415*. Philadelphia: American Society for Testing and Materials, pp. 384–412. doi: 10.1520/STP47237S

Manson, S.S. and Halford, G.R. (1981) Practical implementation of the double linear damage rule and damage curve approach for treating cumulative fatigue damage, *International Journal of Fracture*, 17(2), pp. 169–192. doi: 10.1007/BF00053519

Marquis, G.B. (2011) Fatigue assessment methods for variable amplitude loading of welded structures, in Macdonald, K.A. (ed.) *Fracture and fatigue of welded joints and structures*. Cambridge: Woodhead Publishing, pp. 208–238. doi: 10.1533/9780857092502.2.208

Marzban, A., Lakshmiraju, M., Richardson, N. et al. (2012) Offshore platform fluid structure interaction simulation, *Proceedings of the ASME 2012 31st International Conference on Ocean, Offshore and Arctic Engineering*. Rio de Janeiro, July 1–6, 2012. New York: ASME, vol. 2, pp. 235–242. doi: 10.1115/OMAE2012-83472

Mehl, M., Uekermann, B., Bijl, H. et al. (2016) Parallel coupling numerics for partitioned fluid-structure interaction simulations, *Computers & Mathematics with Applications*, 71(4), pp. 869–891. doi: 10.1016/j.camwa.2015.12.025

Menandro, F.C.M., Moyer, E.T. Jr. and Liebowitz, H. (1995) A methodology for crack tip mesh design, *Engineering Fracture Mechanics*, 50(5–6), pp. 713–726. doi: 10.1016/0013-7944(94)E0056-M

Menter, F., Sharkey, P., Yakubov, S. and Kuntz, M. (2006) Overview of fluid-structure coupling in ANSYS-CFX, *Proceedings of the 25th International Conference on Offshore Mechanics and Arctic Engineering*. Hamburg, June 4–9, 2006. New York: ASME, vol. 4, pp. 579–585. doi: 10.1115/OMAE2006-92145

Mesmacque, G., Garcia, S., Amrouche, A. and Rubio-Gonzalez, C. (2005) Sequential law in multiaxial fatigue, a new damage indicator,

*International Journal of Fatigue*, 27(4), pp. 461–467. doi: 10.1016/j.ijfatigue.2004.08.005

Mi, Y. and Aliabadi, M.H. (1994) Three-dimensional crack growth simulation using BEM, *Computers & Structures*, 52(5), pp. 871–878. doi: 10.1016/0045-7949(94)90072-8

Miao, X.-T., Zhou, C.-Y. and He, X.-H. (2017) An investigation of I-II mixed mode structures with stop hole technique based on extended finite element method, *Proceedings of the ASME 2017 Pressure Vessels and Piping Conference*. Waikoloa, July 16–20, 2017. New York: ASME, vol. 3B, pp. V03BT03A022. doi: 10.1115/PVP2017-65132

Micone, N. and De Waele, W. (2017a) On the application of infrared thermography and potential drop for the accelerated determination of an S-N curve, *Experimental Mechanics*, 57(1), pp. 143–153. doi: 10.1007/s11340-016-0194-6

Micone, N. and De Waele, W. (2017b) Evaluation of methodologies to accelerate corrosion assisted fatigue experiments, *Experimental Mechanics*, 57(4), pp. 547–557. doi: 10.1007/s11340-016-0241-3

Mikkelsen, O., Rege, K., Hemmingsen, T. and Pavlou, D.G. (2017) Numerical estimation of the stop holes-induced fatigue crack growth retardation in offshore structures taking into account the corrosion effect, *Proceedings of the Twenty-seventh (2017) International Ocean and Polar Engineering Conference*. San Francisco, June 25–30, 2017. Cupertino: ISOPE, vol. 4, pp. 451–458.

Miller, K.J. and Zachariah, K.P. (1977) Cumulative damage laws for fatigue crack initiation and stage I propagation, *Journal of Strain Analysis*, 12(4), pp. 262–270. doi: 10.1243/03093247V124262

Miner, M.A. (1945) Cumulative damage in fatigue, *Journal of Applied Mechanics*, 12(3), pp. A159–A164.

Miranda, A.C.O., Meggiolaro, M.A., Castro, J.T.P., Martha, L.F. and Bittencourt, T.N. (2003) Fatigue life and crack path predictions in generic 2D structural components, *Engineering Fracture*

*Mechanics*, 70(10), pp. 1259–1279. doi: 10.1016/S0013-7944(02)00099-1

Miranda, A.C.O., Meggiolaro, M.A., Martha, L.F. and Castro, J.T.P. (2012) Stress intensity factor predictions: Comparison and round-off error, *Computational Materials Science*, 53(1), pp. 354–358. doi: 10.1016/j.commatsci.2011.09.033

Moan, T. (2017) Integrity management of offshore structures and its implication on computation of structural action effects and resistance, *IOP Conference Series: Materials Science and Engineering*, 276, 012033. doi: 10.1088/1757-899X/276/1/012033

Moës, N., Dolbow, J. and Belytschko, T. (1999) A finite element method for crack growth without remeshing, *International Journal for Numerical Methods in Engineering*, 46(1), pp. 131–150. doi: 10.1002/(SICI)1097-0207(19990910)46:1<131::AID-NME726>3.0.CO;2-J

Mohanty, J.R, Verma, B.B. and Ray, P.K. (2009) Prediction of fatigue life with interspersed mode-I and mixed-mode (I and II) overloads by an exponential model: Extensions and improvements, *Engineering Fracture Mechanics*, 76(3), pp. 454–468. doi: 10.1016/j.engfracmech.2008.12.001

Mok, D.P. (2001) *Partitionierte Lösungsansätze in der Strukturdynamik und der Fluid-Struktur-Interaktion*. Dr.-Ing. dissertation, University of Stuttgart. doi: 10.18419/opus-147

Mokhtarishirazabad, M., Lopez-Crespo, P., Moreno, B., Lopez-Moreno, A. and Zanganeh, M. (2017) Optical and analytical investigation of overloads in biaxial fatigue cracks, *International Journal of Fatigue*, 100, pp. 583–590. doi: 10.1016/j.ijfatigue.2016.12.035

Mshana, Y., Kam, J.C.P. and McDiarmid, D.L. (1992) Fatigue crack growth of welded tubular joints under sequential multiple axis loading, *Proceedings of the 11th International Conference on Offshore Mechanics and Arctic Engineering*. Calgary, June 7–12, 1992. New York: ASME, vol. 3B, pp. 257–265.

Münsch, M. and Breuer, M. (2010) Numerical simulation of fluid-structure interaction using eddy-resolving schemes, in Bungartz, H.-J., Mehl, M. and Schäfer, M. (eds.) *Fluid structure interaction II, lecture notes in computational science and engineering 73*. Berlin/Heidelberg: Springer, pp. 221–253. doi: 10.1007/978-3-642-14206-2_9

Nasri, K. and Zenasni, M. (2017) Fatigue crack growth simulation in coated materials using X-FEM, *Comptes Rendus Mecanique*, 345(4), pp. 271–280. doi: 10.1016/j.crme.2017.02.005

Nebenführ, B. and Davidson, L. (2017) Prediction of wind-turbine fatigue loads in forest regions based on turbulent LES inflow fields, *Wind Energy*, 20(6), pp. 1003–1015. doi: 10.1002/we.2076

Newman, J.C. Jr. (1981) A crack-closure model for predicting fatigue crack growth under aircraft spectrum loading, in Chang, J.B. and Hudson, C.M. (eds.) *Methods and models for predicting fatigue crack growth under random loading, ASTM STP 748*. Philadelphia: American Society for Testing and Materials, pp. 53–84. doi: 10.1520/STP28334S

Newman, J.C. Jr. and Raju, I.S. (1986) Stress-intensity factor equations for cracks in three-dimensional finite bodies subjected to tension and bending loads, in Atluri, S.N. (ed.) *Computational methods in the mechanics of fracture*. Amsterdam: Elsevier, pp. 311–334.

Nguyen, O., Repetto, E.A., Ortiz, M. and Radovitzky, R.A. (2001) A cohesive model of fatigue crack growth, *International Journal of Fracture*, 110(4), pp. 351–369. doi: 10.1023/A:1010839522926

Nguyen, V.-T. and Nguyen, H.H. (2016) Detached eddy simulations of flow induced vibrations of circular cylinders at high Reynolds numbers, *Journal of Fluids and Structures*, 63, pp. 103–119. doi: 10.1016/j.jfluidstructs.2016.02.004

Nikishkov, G.P., Park, J.H. and Atluri, S.N. (2001) SGBEM-FEM alternating method for analyzing 3D non-planar cracks and their growth in structural components, *Computer Modeling in*

*Engineering & Sciences*, 2(3), pp. 401–422. doi: 10.3970/cmes.2001.002.401

Nilsson, K.F., Dolci, F., Seldis, T. et al. (2016) Assessment of thermal fatigue life for 316L and P91 pipe components at elevated temperatures, *Engineering Fracture Mechanics*, 168, pp. 73–91. doi: 10.1016/j.engfracmech.2016.09.006

Nilsson, P., Lillberg, E. and Wikström, N. (2012) LES with acoustics and FSI for deforming plates in gas flow, *Nuclear Engineering and Design*, 253, pp. 387–395. doi: 10.1016/j.nucengdes.2011.10.071

Paczkowski, K.W., Zhang, P., Rogers, R. and Richardson, N. (2014) Fluid-structure interaction study on dynamic response of a capped drilling riser filled with mud, *Proceedings of the ASME 2014 33rd International Conference on Ocean, Offshore and Arctic Engineering*. San Francisco, June 8–13, 2014. New York: ASME, vol. 2, pp. V002T08A018. doi: 10.1115/OMAE2014-23329

Palmgren, A. (1924) Die Lebensdauer von Kugellagern, *Zeitschrift des Vereines Deutscher Ingenieure*, 68(14), pp. 339–341.

Paris, P. and Erdogan, F. (1963) A critical analysis of crack propagation laws, *Journal of Basic Engineering*, 85(4), pp. 528–533. doi: 10.1115/1.3656900

Paris, P.C., Gomez, M.P. and Anderson, W.E. (1961) A rational analytic theory of fatigue, *The Trend in Engineering*, 13, pp. 9–14.

Parks, D.M. (1974) A stiffness derivative finite element technique for determination of crack tip stress intensity factors, *International Journal of Fracture*, 10(4), pp. 487–502. doi: 10.1007/BF00155252

Pavlou, D.G. (2000) Prediction of fatigue crack growth under real stress histories, *Engineering Structures*, 22(12), pp. 1707–1713. doi: 10.1016/S0141-0296(99)00069-3

Pavlou, D.G. (2002) A phenomenological fatigue damage accumulation rule based on hardness increasing, for the 2024-T42 aluminum,

*Engineering Structures*, 24(11), pp. 1363–1368. doi: 10.1016/0141-0296(02)00055-X

Pavlou, D.G. (2017) Loading sequence effects on fatigue damage accumulation of offshore structures: A deterministic approach, *Proceedings of the ASME 2017 36th International Conference on Ocean, Offshore and Arctic Engineering*. Trondheim, June 25–30, 2017. New York: ASME, vol. 4, pp. V004T03A010. doi: 10.1115/OMAE2017-61733

Pavlou, D.G. (2018) Mode I+II fatigue crack growth delay by stop-holes, *Journal of Aerospace Technology and Management*, 10, e1518. doi: 10.5028/jatm.v10.808

Pavlou, D.G., Labeas, G.N., Vlachakis, N.V. and Pavlou, F.G. (2003) Fatigue crack propagation trajectories under mixed-mode cyclic loading, *Engineering Structures*, 25(7), pp. 869–875. doi: 10.1016/S0141-0296(03)00018-X

Pavlou, D.G., Vlachakis, N.V., Pavlou, M.G. and Vlachakis, V.N. (2004) Estimation of fatigue crack growth retardation due to crack branching, *Computational Materials Science*, 29(4), pp. 446–452. doi: 10.1016/j.commatsci.2003.12.003

Peixoto, D.F.C. and de Castro, P.M.S.T. (2017) Fatigue crack growth of a railway wheel, *Engineering Failure Analysis*, 82, pp. 420–434. doi: 10.1016/j.engfailanal.2017.07.036

Peng, X., Atroshchenko, E., Kerfriden, P. and Bordas, S.P.A. (2017) Isogeometric boundary element methods for three dimensional static fracture and fatigue crack growth, *Computer Methods in Applied Mechanics and Engineering*, 316, pp. 151–185. doi: 10.1016/j.cma.2016.05.038

Pereira, H.F.S.G., de Jesus, A.M.P., Ribeiro, A.S. and Fernandes, A.A. (2008) Influence of loading sequence and stress ratio on fatigue damage accumulation of a structural component, *Ciência e Tecnologia dos Materiais*, 20(1–2), pp. 60–67.

Pereira, M. (2004) *Growth of through-wall fatigue cracks in brace members*. (HSE research report 224). Sudbury, Suffolk: Health & Safety Executive. Available at: http://www.hse.gov.uk/research/rrpdf/rr224.pdf (accessed: 30 May 2018).

Pereira Gomes, J. and Lienhart, H. (2010) Experimental benchmark: Self-excited fluid-structure interaction test cases, in Bungartz, H.-J., Mehl, M. and Schäfer, M. (eds.) *Fluid structure interaction II, lecture notes in computational science and engineering 73*. Berlin/Heidelberg: Springer, pp. 383–411. doi: 10.1007/978-3-642-14206-2_14

Phan, A.-V. (no date) *ANSYS tutorial – 2-D fracture analysis*. University of South Alabama. Available at: http://www.southalabama.edu/engineering/mechanical/faculty/phan/ANSYS_LEFM01.pdf (accessed 25 January 2018).

Ponweiser, T., Stadelmeyer, P. and Karásek, T. (2014) *Fluid-structure simulations with OpenFOAM for aircraft designs*. (PRACE white paper 172). Brussels: Partnership for Advanced Computing in Europe. Available at: http://www.prace-ri.eu/IMG/pdf/wp172.pdf (accessed: 6 February 2017).

Pook, L.P., Kam, J.C.P. and Mshana, Y. (1992) On mixed mode fatigue crack growth in tubular welded joints, *Proceedings of the 11th International Conference on Offshore Mechanics and Arctic Engineering*. Calgary, June 7–12, 1992. New York: ASME, vol. 3B, pp. 251–256.

Predan, J., Močilnik, V. and Gubeljak, N. (2013) Stress intensity factors for circumferential semi-elliptical surface cracks in a hollow cylinder subjected to pure torsion, *Engineering Fracture Mechanics*, 105, pp. 152–168. doi: 10.1016/j.engfracmech.2013.03.033

Priddle, E.K. (1978) The influence of grain size on threshold stress intensity for fatigue crack growth in AISI 316 stainless steel, *Scripta*

*Metallurgica*, 12(1), pp. 49–56. doi: 10.1016/0036-9748(78)90226-0

Qian, G., Gonzalez-Albuixech, V.F. and Niffenegger, M. (2014) In-plane and out-of-plane constraint effects under pressurized thermal shocks, *International Journal of Solids and Structures*, 51(6), pp. 1311–1321. doi: 10.1016/j.ijsolstr.2013.12.021

Qian, G., González-Albuixech, V.F., Niffenegger, M. and Giner, E. (2016) Comparison of $K_I$ calculation methods, *Engineering Fracture Mechanics*, 156, pp. 52–67. doi: 10.1016/j.engfracmech.2016.02.014

Qian, J. and Fatemi, A. (1996) Mixed mode fatigue crack growth: A literature survey, *Engineering Fracture Mechanics*, 55(6), pp. 969–990. doi: 10.1016/S0013-7944(96)00071-9

Raju, I.S. (1987) Calculation of strain-energy release rates with higher order and singular finite elements, *Engineering Fracture Mechanics*, 28(3), pp. 251–274. doi: 10.1016/0013-7944(87)90220-7

Raposo, P., Correia, J.A.F.O., De Jesus, A.M.P. et al. (2017) Probabilistic fatigue S-N curves derivation for notched components, *Frattura ed Integrità Strutturale*, 11(42), pp. 105–118. doi: 10.3221/IGF-ESIS.42.12

Razavi, S.M.J., Ayatollahi, M.R., Sommitsch, C. and Moser, C. (2017) Retardation of fatigue crack growth in high strength steel S690 using a modified stop-hole technique, *Engineering Fracture Mechanics*, 169, pp. 226–237. doi: 10.1016/j.engfracmech.2016.11.013

Rege, K. and Lemu, H.G. (2017) A review of fatigue crack propagation modelling techniques using FEM and XFEM, *IOP Conference Series: Materials Science and Engineering*, 276, 012027. doi: 10.1088/1757-899X/276/1/012027

Rege, K. and Pavlou, D.G. (2017) A one-parameter nonlinear fatigue damage accumulation model, *International Journal of Fatigue*, 98, pp. 234–246. doi: 10.1016/j.ijfatigue.2017.01.039

Rege, K. and Pavlou, D.G. (2019a) Effect of stop holes on structural integrity of offshore structures: a numerical model, *Proceedings of the Institution of Civil Engineers – Maritime Engineering*, 172(1), pp. 3–14. doi: 10.1680/jmaen.2018.34

Rege, K. and Pavlou, D.G. (2019b) Stress intensity factors for circumferential through-wall cracks in thin-walled cylindrical shells subjected to tension and torsion, *Fatigue & Fracture of Engineering Materials & Structures*, 42(5), pp. 1062–1074. doi: 10.1111/ffe.12970

Ren, X. and Guan, X. (2017) Three dimensional crack propagation through mesh-based explicit representation for arbitrarily shaped cracks using the extended finite element method, *Engineering Fracture Mechanics*, 177, pp. 218–238. doi: 10.1016/j.engfracmech.2017.04.007

Rhee, H.C. (1989) Fatigue crack growth analyses of offshore structural tubular joint, *Journal of Offshore Mechanics and Arctic Engineering*, 111(1), pp. 49–55. doi: 10.1115/1.3257138

Riahi, H., Bressolette, Ph., Chateauneuf, A., Bouraoui, Ch. and Fathallah, R. (2011) Reliability analysis and inspection updating by stochastic response surface of fatigue cracks in mixed mode, *Engineering Structures*, 33(12), pp. 3392–3401. doi: 10.1016/j.engstruct.2011.07.003

Rice, J.R. (1966) Plastic yielding at a crack tip, *Proceedings of the 1st International Conference on Fracture*. Sendai, September 12–17, 1965. Tokyo: Japanese Society for Strength and Fracture of Materials, vol. 1, pp. 283–308.

Rice, J.R. (1967) Mechanics of crack tip deformation and extension by fatigue, in *Fatigue crack propagation, ASTM STP 415*. Philadelphia: American Society for Testing and Materials, pp. 247–311. doi: 10.1520/STP47234S

Rice, J.R. (1968) A path independent integral and the approximate analysis of strain concentration by notches and cracks, *Journal of Applied Mechanics*, 35(2), pp. 379–386. doi: 10.1115/1.3601206

Richard, H.A. (1989) Specimens for investigating biaxial fracture and fatigue processes, in Brown, M.W. and Miller, K.J. (eds.) *Biaxial and multiaxial fatigue, EGF 3*. London: Mechanical Engineering Publications, pp. 217–229.

Richard, H.A., Schramm, B. and Schirmeisen, N.H. (2014) Cracks on mixed mode loading – theories, experiments, simulations, *International Journal of Fatigue*, 62, pp. 93–103. doi: 10.1016/j.ijfatigue.2013.06.019

Richter, Th. (2012) Goal-oriented error estimation for fluid-structure interaction problems, *Computer Methods in Applied Mechanics and Engineering*, 223–224, pp. 28–42. doi: 10.1016/j.cma.2012.02.014

Rozumek, D., Marciniak, Z., Lesiuk, G., Correia, J.A. and de Jesus, A.M.P. (2018) Experimental and numerical investigation of mixed mode I + II and I + III fatigue crack growth in S355J0 steel, *International Journal of Fatigue*, 113, pp. 160–170. doi: 10.1016/j.ijfatigue.2018.04.005

Rybicki, E.F. and Kanninen, M.F. (1977) A finite element calculation of stress intensity factors by a modified crack closure integral, *Engineering Fracture Mechanics*, 9(4), pp. 931–938. doi: 10.1016/0013-7944(77)90013-3

Saeed, R.A., Galybin, A.N. and Popov, V. (2010) Modelling of flow-induced stresses in a Francis turbine runner, *Advances in Engineering Software*, 41(12), pp. 1245–1255. doi: 10.1016/j.advengsoft.2010.09.001

Salimi-Majd, D., Shahabi, F. and Mohammadi, B. (2016) Effective local stress intensity factor criterion for prediction of crack growth trajectory under mixed mode fracture conditions, *Theoretical and Applied Fracture Mechanics*, 85(B), pp. 207–216. doi: 10.1016/j.tafmec.2016.01.009

Salvati, E., Zhang, H., Fong, K.S., Song, X. and Korsunsky, A.M. (2017) Separating plasticity-induced closure and residual stress contributions to fatigue crack retardation following an overload, *Journal of the Mechanics and Physics of Solids*, 98, pp. 222–235. doi: 10.1016/j.jmps.2016.10.001

Sanches, R.F., de Jesus, A.M.P., Correia, J.A.F.O., da Silva, A.L.L. and Fernandes, A.A. (2015) A probabilistic fatigue approach for riveted joints using Monte Carlo simulation, *Journal of Constructional Steel Research*, 110, pp. 149–162. doi: 10.1016/j.jcsr.2015.02.019

Sander, M. and Richard, H.A. (2006) Experimental and numerical investigations on the influence of the loading direction on the fatigue crack growth, *International Journal of Fatigue*, 28(5–6), pp. 583–591. doi: 10.1016/j.ijfatigue.2005.05.012

Sanders, J.L. Jr. (1982) Circumferential through-cracks in cylindrical shells under tension, *Journal of Applied Mechanics*, 49(1), pp. 103–107. doi: 10.1115/1.3161948

Santecchia, E., Hamouda, A.M.S., Musharavati, F. et al. (2016) A review on fatigue life prediction methods for metals, *Advances in Materials Science and Engineering*, 2016, 9573524. doi: 10.1155/2016/9573524

Sarrazin-Baudoux, C., Petit, J. and Amzallag, C. (2002) Near-threshold fatigue crack propagation in austenitic stainless steels, *Fracture mechanics beyond 2000. Proceedings of the 14th Bienniel Conference on Fracture*. Krakow, September 8–13, 2002. Sheffield: EMAS Publishing, vol. 3, pp. 187–194.

Schoenborn, S., Kaufmann, H., Sonsino, C.M. and Heim, R. (2015) Cumulative damage of high-strength cast iron alloys for automotive applications, *Procedia Engineering*, 101, pp. 440–449. doi: 10.1016/j.proeng.2015.02.053

Schöllmann, M., Fulland, M. and Richard, H.A. (2003) Development of a new software for adaptive crack growth simulations in 3D

structures, *Engineering Fracture Mechanics*, 70(2), pp. 249–268. doi: 10.1016/S0013-7944(02)00028-0

Šekutkovski, B., Kostić, I., Simonović, A., Cardiff, P. and Jazarević, V. (2016) Three-dimensional fluid-structure interaction simulation with a hybrid RANS-LES turbulence model for applications in transonic flow domain, *Aerospace Science and Technology*, 49, pp. 1–16. doi: 10.1016/j.ast.2015.11.028

Shang, D.-G. and Yao, W.-X. (1999) A nonlinear damage cumulative model for uniaxial fatigue, *International Journal of Fatigue*, 21(2), pp. 187–194. doi: 10.1016/S0142-1123(98)00069-3

Shepherd, J.E. and Inaba, K. (2010) Shock loading and failure of fluid-filled tubular structures, in Shukla, A., Ravichandran, G. and Rajapakse, Y.D.S. (eds.) *Dynamic failure of materials and structures*. New York: Springer, pp. 153–190. doi: 10.1007/978-1-4419-0446-1_6

Sheu, B.C., Song, P.S. and Hwang, S. (1995) Shaping exponent in Wheeler model under a single overload, *Engineering Fracture Mechanics*, 51(1), pp. 135–143. doi: 10.1016/0013-7944(94)00250-L

Shih, C.F. and Asaro, R.J. (1988) Elastic-plastic analysis of cracks on bimaterial interfaces: part I—small scale yielding, *Journal of Applied Mechanics*, 55(2), pp. 299–316. doi: 10.1115/1.3173676

Shih, C.F., deLorenzi, H.G. and German, M.D. (1976) Crack extension modeling with singular quadratic isoparametric elements, *International Journal of Fracture*, 12(4), pp. 647–651. doi: 10.1007/BF00034654

Shih, C.F., Moran, B. and Nakamura, T. (1986) Energy release rate along a three-dimensional crack front in a thermally stressed body, *International Journal of Fracture*, 30(2), pp. 79–102. doi: 10.1007/BF00034019

Shim, D.-J., Xu, S. and Lee, D. (2014) Closed-form stress intensity factor solutions for circumferential through-wall cracks in cylinder,

*Proceedings of the ASME 2014 Pressure Vessels & Piping Conference*. Anaheim, July 20–24, 2014. New York: ASME, vol. 1, pp. V001T01A011. doi: 10.1115/PVP2014-28049

Sih, G.C. (1974) Strain-energy-density factor applied to mixed mode crack problems, *International Journal of Fracture*, 10(3), pp. 305–321. doi: 10.1007/BF00035493

Sih, G.C. and Barthelemy, B.M. (1980) Mixed mode fatigue crack growth predictions, *Engineering Fracture Mechanics*, 13(3), pp. 439–451. doi: 10.1016/0013-7944(80)90076-4

Silva, A.L.L., de Jesus, A.M.P., Xavier, J., Correia, J.A.F.O. and Fernandes, A.A. (2017) Combined analytical-numerical methodologies for the evaluation of mixed-mode (I + II) fatigue crack growth rates in structural steels, *Engineering Fracture Mechanics*, 185, pp. 124–138.
doi: 10.1016/j.engfracmech.2017.04.016

Siriwardane, S., Ohga, M., Dissanayake, R. and Taniwaki, K. (2008) Application of new damage indicator-based sequential law for remaining fatigue life estimation of railway bridges, Journal of *Constructional Steel Research*, 64(2), pp. 228–237.
doi: 10.1016/j.jcsr.2007.06.002

Siriwardane, S., Ohga, M., Kaita, T. and Dissanayake, R. (2009) Grain-scale plasticity based fatigue model to estimate fatigue life of bridge connections, *Journal of Constructional Steel Research*, 65(10–11), pp. 1942–1953. doi: 10.1016/j.jcsr.2009.05.002

Smith, K.N., Watson, P. and Topper, T.H. (1970) A stress-strain function for the fatigue of metals, *Journal of Materials*, 5(4), pp. 767–778.

Socie, D.F., Dowling, N.E. and Kurath, P. (1984) Fatigue life estimation of notched members, in Sanford, R.J. (ed.) *Fracture mechanics: Fifteenth symposium, ASTM STP 833*. Philadelphia: American Society for Testing and Materials, pp. 284–299.
doi: 10.1520/STP32560S

Solanki, K., Daniewicz, S.R. and Newman, J.C. Jr. (2004) Finite element analysis of plasticity-induced fatigue crack closure: an overview, *Engineering Fracture Mechanics*, 71(2), pp. 149–171. doi: 10.1016/S0013-7944(03)00099-7

Spagnoli, A., Vantadori, S. and Carpinteri, A. (2015) Interpreting some experimental evidences of fatigue crack size effects through a kinked crack model, *Fatigue & Fracture of Engineering Materials and Structures*, 38(2), pp. 215–222. doi: 10.1111/ffe.12185

Srivatsavan, R. and Subramanyan, S. (1978) A cumulative damage rule based on successive reduction in fatigue limit, *Journal of Engineering Materials and Technology*, 100(2), pp. 212–214. doi: 10.1115/1.3443474

Stacey, A. (2011) KP4: Ageing & life extension inspection programme for offshore installations, *Proceedings of the ASME 2011 30th International Conference on Ocean, Offshore and Arctic Engineering*. Rotterdam, June 19–24, 2011. New York: ASME, vol. 3, pp. 33–48. doi: 10.1115/OMAE2011-49089

Stacey, A., Birkinshaw, M. and Sharp, J.V. (2008) Life extension issues for ageing offshore installations, *Proceedings of the 27th International Conference on Offshore Mechanics and Arctic Engineering*. Estoril, June 15–20, 2008. New York: ASME, vol. 5, pp. 199–215. doi: 10.1115/OMAE2008-57411

Standards Norway (2010) *NS-EN 1993-1-9:2005+NA:2010 Eurocode 3: Design of steel structures Part 1-9: Fatigue*.

Standards Norway (2013) *NORSOK N-004 Design of steel structures. Rev. 3, February 2013*.

Standards Norway (2015) *NORSOK N-006:2015 Assessment of structural integrity for existing offshore load-bearing structures. Edition 2, April 2015*.

Stazi, F.L., Budyn, E., Chessa, J. and Belytschko, T. (2003) An extended finite element method with higher-order elements for curved cracks,

*Computational Mechanics*, 31(1–2), pp. 38–48. doi: 10.1007/s00466-002-0391-2

Stolarska, M., Chopp, D.L., Moës, N. and Belytschko, T. (2001) Modelling crack growth by level sets in the extended finite element method, *International Journal for Numerical Methods in Engineering*, 51(8), pp. 943–960. doi: 10.1002/nme.201

Subramanya, H.Y., Viswanath, S. and Narasimhan, R. (2005) A three-dimensional numerical study of mixed mode (I and II) crack tip fields in elastic-plastic solids, *International Journal of Fracture*, 136(1–4), pp. 167–185. doi: 10.1007/s10704-005-5422-5

Subramanyan, S. (1976) A cumulative damage rule based on the knee point of the S-N curve, *Journal of Engineering Materials and Technology*, 98(4), pp. 316–321. doi: 10.1115/1.3443383

Sukumar, N., Chopp, D.L. and Moran, B. (2003) Extended finite element method and fast marching method for three-dimensional fatigue crack propagation, *Engineering Fracture Mechanics*, 70(1), pp. 29–48. doi: 10.1016/S0013-7944(02)00032-2

Suresh, S. (1998) *Fatigue of materials*. 2nd edn. Cambridge: Cambridge University Press.

Søndeland, G. and Seglem, E. (2017) Én centimeter kostet 13 personer livet, *Stavanger Aftenblad*, April 28, p. 22.

Tada, H., Paris, P.C. and Irwin, G.R. (2000) *The stress analysis of cracks handbook*. 3rd edn. Bury St. Edmunds: Professional Engineering Publishing.

Taheri, F., Trask, D. and Pegg, N. (2003) Experimental and analytical investigation of fatigue characteristics of 350WT steel under constant and variable amplitude loadings, *Marine Structures*, 16(1), pp. 69–91. doi: 10.1016/S0951-8339(02)00004-7

Takahashi, Y. (2002) Evaluation of leak-before-break assessment methodology for pipes with a circumferential through-wall crack. Part I: stress intensity factor and limit load solutions, *International*

*Journal of Pressure Vessels and Piping*, 79(6), pp. 385–392. doi: 10.1016/S0308-0161(02)00036-4

Tanaka, K. (1974) Fatigue crack propagation from a crack inclined to the cyclic tensile axis, *Engineering Fracture Mechanics*, 6(3), pp. 493–507. doi: 10.1016/0013-7944(74)90007-1

Theil, N. (2016) Fatigue life prediction method for the practical engineering use taking in account the effect of overload blocks, *International Journal of Fatigue*, 90, pp. 23–35. doi: 10.1016/j.ijfatigue.2016.04.006

Theocaris, P.S. and Andrianopoulos, N.P. (1982a) The T-criterion applied to ductile fracture, *International Journal of Fracture*, 20(4), pp. R125–R130. doi: 10.1007/BF01130617

Theocaris, P.S. and Andrianopoulos, N.P. (1982b) The Mises elastic-plastic boundary as the core region in fracture criteria, *Engineering Fracture Mechanics*, 16(3), pp. 425–432. doi: 10.1016/0013-7944(82)90120-5

Tian, X., Ong, M.C., Yang, J. and Myrhaug, D. (2014) Large-eddy simulation of the flow normal to a flat plate including corner effects at a high Reynolds number, *Journal of Fluids and Structures*, 49, pp. 149–169. doi: 10.1016/j.jfluidstructs.2014.04.008

Tijsseling, A.S. (1996) Fluid-structure interaction in liquid-filled pipe systems: A review, *Journal of Fluids and Structures*, 10(2), pp. 109–146. doi: 10.1006/jfls.1996.0009

Toribio, J., Matos, J.-C. and González, B. (2017) Aspect ratio evolution in embedded, surface, and corner cracks in finite-thickness plates under tensile fatigue loading, *Applied Sciences*, 7(7), 746. doi: 10.3390/app7070746

Tracey, D.M. (1971) Finite elements for determination of crack tip elastic stress intensity factors, *Engineering Fracture Mechanics*, 3(3), pp. 255–265. doi: 10.1016/0013-7944(71)90036-1

Trim, A.D., Braaten, H., Lie, H. and Tognarelli, M.A. (2005) Experimental investigation of vortex-induced vibration of long marine risers, *Journal of Fluids and Structures*, 21(3), 335–361. doi: 10.1016/j.jfluidstructs.2005.07.014

Tuković, Ž., Cardiff, P., Karač, A., Jasak, H. and Ivanković, A. (2014) OpenFOAM library for fluid structure interaction, *9th OpenFOAM Workshop*. Zagreb, June 23–26, 2014.

Tuković, Ž. and Jasak, H. (2007) Updated Lagrangian finite volume solver for large deformation dynamic response of elastic body, *Transactions of FAMENA*, 31(1), pp. 55–70.

Tuković, Ž. and Jasak, H. (2012) A moving mesh finite volume interface tracking method for surface tension dominated interfacial fluid flow, *Computers & Fluids*, 55, pp. 70–84. doi: 10.1016/j.compfluid.2011.11.003

Turek, S. and Hron, J. (2006) Proposal for numerical benchmarking of fluid-structure interaction between an elastic object and laminar incompressible flow, in Bungartz, H.-J. and Schäfer, M. (eds.) *Fluid structure interaction, lecture notes in computational science and engineering 53*. Berlin/Heidelberg: Springer, pp. 371–385. doi: 10.1007/3-540-34596-5_15

Tweed, J. and Rooke, D.P. (1973) The distribution of stress near the tip of a radial crack at the edge of a circular hole, *International Journal of Engineering Science*, 11(11), pp. 1185–1195. doi: 10.1016/0020-7225(73)90084-0

van Driest, E.R. (1956) On turbulent flow near a wall, *Journal of Aeronautical Sciences*, 23(11), pp. 1007–1011.

van Zuijlen, A.H. and Bijl, H. (2010) Multi-level accelerated sub-iterations for fluid-structure interaction, in Bungartz, H.-J., Mehl, M. and Schäfer, M. (eds.) *Fluid structure interaction II, lecture notes in computational science and engineering 73*. Berlin/Heidelberg: Springer, pp. 1–25. doi: 10.1007/978-3-642-14206-2_1

Versteeg, H.K. and Malalasekera, W. (2007) *An introduction to computational fluid dynamics*. 2nd edn. Essex: Pearson.

Vestli, H., Lemu, H.G., Svendsen, B.T., Gabrielsen, O. and Siriwardane, S.C. (2017) Case studies on structural health monitoring of offshore bottom-fixed steel structures, *Proceedings of the Twenty-seventh (2017) International Ocean and Polar Engineering Conference*. San Francisco, June 25–30, 2017. Cupertino: ISOPE, vol. 1, pp. 965–972.

Vigneron, L.M., Duflot, M.P., Robe, P.A., Warfield, S.K. and Verly, J.G. (2009) 2D XFEM-based modeling of retraction and successive resections for preoperative image update, *Computer Aided Surgery*, 14(1–3), pp. 1–20. doi: 10.3109/10929080903052677

Viz, M.J., Potyondy, D.O., Zehnder, A.T., Rankin, C.C. and Riks, E. (1995) Computation of membrane and bending stress intensity factors for thin, cracked plates, *International Journal of Fracture*, 72(1), pp. 21–38. doi: 10.1007/BF00036927

Votsis, R.A., Michailides, C., Tantele, E.A., Onoufriou, T. (2018) Review of technologies for monitoring the performance of marine structures, *Proceedings of the Twenty-eighth (2018) International Ocean and Polar Engineering Conference*. Sapporo, June 10–15, 2018. Cupertino: ISOPE, vol. 1, pp. 1378–1385.

Weller, H.G., Tabor, G., Jasak, H. and Fureby, C. (1998) A tensorial approach to computational continuum mechanics using object-oriented techniques, *Computers in Physics*, 12(6), pp. 620–631. doi: 10.1063/1.168744

Wheeler, O.E. (1972) Spectrum loading and crack growth, *Journal of Basic Engineering*, 94(1), pp. 181–186. doi: 10.1115/1.3425362

Willenborg, J., Engle, R.M. and Wood, H.A. (1971) *A crack growth retardation model using an effective stress concept*. (Technical Memorandum 71-1-FBR). Ohio: Air Force Flight Dynamics Laboratory. Available at: https://apps.dtic.mil/dtic/tr/fulltext/u2/a956517.pdf (accessed: 7 September 2017).

Woldemariam, E.T. and Lemu, H.G. (2016) Comparative analysis of computational methods in fluid-structure interaction: Temporal discretization and coupling techniques, *Proceedings of the 6th International Workshop of Advanced Manufacturing and Automation*. Manchester, November 10–11, 2016. Atlantis Press, pp. 144–150. doi: 10.2991/iwama-16.2016.26

Wu, H., Imad, A., Benseddiq, N., Castro, J.T.P. and Meggiolaro, M.A. (2010) On the prediction of the residual fatigue life of cracked structures repaired by the stop-hole method, *International Journal of Fatigue*, 32(4), pp. 670–677. doi: 10.1016/j.ijfatigue.2009.09.011

Wu, Y., Xu, Y., Guo, X. and Bao, R. (2017) Fatigue life prediction based on equivalent initial flaw size for Al-Li alloy 2297 under spectrum loading, *International Journal of Fatigue*, 103, pp. 39–47. doi: 10.1016/j.ijfatigue.2017.04.015

Xia, T. and Yao, W. (2013) Comparative research on the accumulative damage rules under multiaxial block loading spectrum for 2024-T4 aluminium alloy, *International Journal of Fatigue*, 48, pp. 257–265. doi: 10.1016/j.ijfatigue.2012.11.004

Xing, C. and Zhou, C. (2018) Finite element modeling of crack growth in thin-wall structures by method of combining sub-partition and substructure, *Engineering Fracture Mechanics*, 195, pp. 13–29. doi: 10.1016/j.engfracmech.2018.03.023

Yang, L. and Fatemi, A. (1998) Cumulative fatigue damage mechanisms and quantifying parameters: A literature review, *Journal of Testing and Evaluation*, 26(2), pp. 89–100. doi: 10.1520/JTE11978J

Yang, Z. (2006) Fully automatic modelling of mixed-mode crack propagation using scaled boundary finite element method, *Engineering Fracture Mechanics*, 73(12), pp. 1711–1731. doi: 10.1016/j.engfracmech.2006.02.004

Yau, J.F., Wang, S.S. and Corten, H.T. (1980) A mixed-mode crack analysis of isotropic solids using conservation laws of elasticity,

*Journal of Applied Mechanics*, 47(2), pp. 335–341. doi: 10.1115/1.3153665

Yazid, A., Abdelkader, N. and Abdelmadjid, H. (2009) A state-of-the-art review of the X-FEM for computational fracture mechanics, *Applied Mathematical Modelling*, 33(12), pp. 4269–4282. doi: 10.1016/j.apm.2009.02.010

Yokobori, A.T. Jr., Yokobori, T., Sato, K. and Syoji, K. (1985) Fatigue crack growth under mixed modes I and II, *Fatigue & Fracture of Engineering Materials & Structures*, 8(4), pp. 315–325. doi: 10.1111/j.1460-2695.1985.tb00430.x

Yu, X., Li, L. and Proust, G. (2017) Fatigue crack growth of aluminium alloy 7075-T651 under proportional and non-proportional mixed mode I and II loads, *Engineering Fracture Mechanics*, 174, pp. 155–167. doi: 10.1016/j.engfracmech.2017.01.008

Yuan, R., Li, H., Huang, H.-Z., Zhu, S.-P. and Li, Y.-F. (2013) A new non-linear continuum damage mechanics model for fatigue life prediction under variable loading, *Mechanika*, 19(5), pp. 506–511. doi: 10.5755/j01.mech.19.5.5541

Yuen, B.K.C. and Taheri, F. (2006) Proposed modifications to the Wheeler retardation model for multiple overloading fatigue life prediction, *International Journal of Fatigue*, 28(12), pp. 1803–1819. doi: 10.1016/j.ijfatigue.2005.12.007

Zahoor, A. (1985) Closed form expressions for fracture mechanics analysis of cracked pipes, *Journal of Pressure Vessel Technology*, 107(2), pp. 203–205. doi: 10.1115/1.3264435

Zahoor, A. (1989) *Ductile Fracture Handbook*. (EPRI NP-6301-D). Palo Alto: Electric Power Research Institute.

Zareei, A. and Nabavi, S.M. (2016) Calculation of stress intensity factors for circumferential semi-elliptical cracks with high aspect ratio in pipes, *International Journal of Pressure Vessels and Piping*, 146, pp. 32–38. doi: 10.1016/j.ijpvp.2016.05.008

Zarrinzadeh, H., Kabir, M.Z. and Deylami, A. (2017) Experimental and numerical fatigue crack growth of an aluminium pipe repaired by composite patch, *Engineering Structures*, 133, pp. 24–32. doi: 10.1016/j.engstruct.2016.12.011

Zhan, Z., Hu, W., Li, B. et al. (2017) Continuum damage mechanics combined with the extended finite element method for the total life prediction of a metallic component, *International Journal of Mechanical Sciences*, 124–125, pp. 48–58. doi: 10.1016/j.ijmecsci.2017.03.002

Zhang, Y.-H. and Maddox, S.J. (2009) Investigation of fatigue damage to welded joints under variable amplitude loading spectra, *International Journal of Fatigue*, 31(1), pp. 138–152. doi: 10.1016/j.ijfatigue.2008.04.006

Zhu, X.-K. and Leis, B.N. (2014) Effective methods to determine stress intensity factors for 2D and 3D cracks, *Proceedings of the 2014 10th International Pipeline Conference*. Calgary, September 29–October 3, 2014. New York: ASME, vol. 2, pp. V002T06A047. doi: 10.1115/IPC2014-33120

Zuo, F.-J., Huang, H.-Z., Zhu, S.-P., Lv, Z. and Gao, H. (2015) Fatigue life prediction under variable amplitude loading using a non-linear damage accumulation model, *International Journal of Damage Mechanics*, 24(5), pp. 767–784. doi: 10.1177/1056789514553042

# Appendix A: Creating a graded mesh along a line in ANSYS APDL

In finite element analysis, it is often useful to construct a graded mesh, where the mesh is fine near stress concentrators (such as a crack tip), and coarse in regions of uniform stress. This technique was used when constructing the finite element meshes used in Chapter 6 and Paper IV, see e.g. Figure 6.8. Often, it is desirable that the mesh is graded along a line, as illustrated in Figure A.1. This is possible to accomplish in ANSYS APDL by using the command {`LESIZE, NL1, , , NDIV, SPACE`}, where NL1 is the number of the line, NDIV is the number of element divisions along the line (6 in Figure A.1), and SPACE is the ratio between the last division size to the first division size.

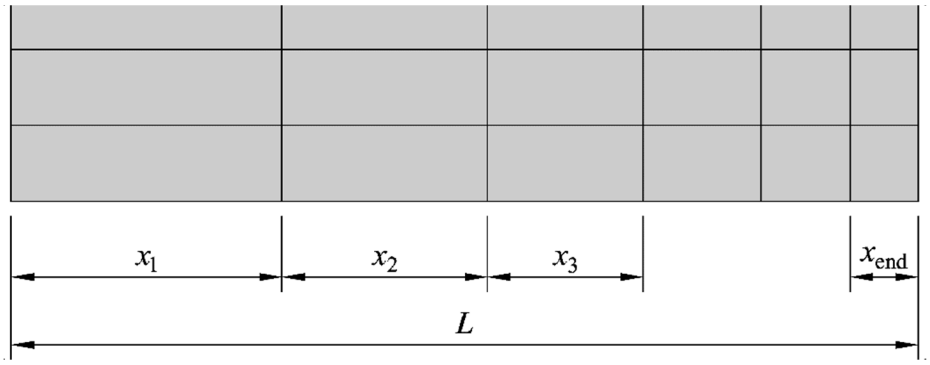


Figure A.1 – A graded mesh with element lengths varying from $x_1$ to $x_{end}$

Often, specific element lengths, $x_1$ and $x_{end}$, are desired at each end of the graded mesh. In this case, the values of $x_1$, $x_{end}$ and $L$ are known. The spacing ratio may be calculated as:

$$\text{SPACE} = \frac{x_{end}}{x_1} \tag{A.1}$$

However, the number of element divisions, NDIV, required to obtain these element lengths, is unknown, and the ANSYS documentation does not provide any guidelines for calculating this value[4]. Therefore, a formula for calculating this value will be derived here.

It was found that the LESIZE command in ANSYS APDL divides the line into a geometric series of element lengths:

$$x_1 + x_2 + x_3 + x_4 + \ldots + x_{\text{end}} = x_1 + x_1 r + x_1 r^2 + x_1 r^3 + \ldots + x_1 r^{\text{NDIV}-1} = L \tag{A.2}$$

where $r$ is the common ratio. The last term of the sum is

$$x_{\text{end}} = x_1 r^{\text{NDIV}-1}, \tag{A.3}$$

which leads to

$$r^{\text{NDIV}-1} = \frac{x_{\text{end}}}{x_1} \tag{A.4}$$

and

$$r^{\text{NDIV}} = r\frac{x_{\text{end}}}{x_1}. \tag{A.5}$$

From Equation (A.4), we can get an expression for NDIV:

$$\text{NDIV} - 1 = \frac{\log\left(x_{\text{end}}/x_1\right)}{\log r} \tag{A.6}$$

or

[4] In other software, e.g. SALOME, it is possible to specify $x_1$ and $x_{\text{end}}$ directly as input parameters, see https://docs.salome-platform.org/latest/gui/SMESH/1d_meshing_hypo.html#start-and-end-length-anchor (accessed 25 September 2019)

$$\mathrm{NDIV} = 1 + \frac{\log x_{\mathrm{end}} - \log x_1}{\log r}. \tag{A.7}$$

We now have an expression for NDIV, but $r$ is still unknown. This problem is solved by introducing the sum of the NDIV terms of the geometric series, Equation (A.2), which is given as:

$$\sum_{k=0}^{\mathrm{NDIV}-1} x_1 r^k = x_1 \frac{1 - r^{\mathrm{NDIV}}}{1 - r} = L \tag{A.8}$$

By combining Equations (A.5) and (A.8), we get:

$$x_1 \frac{1 - r x_{\mathrm{end}} / x_1}{1 - r} = L \tag{A.9}$$

By reordering Equation (A.9), we get:

$$r = \frac{L - x_1}{L - x_{\mathrm{end}}} \tag{A.10}$$

With the aid of Equation (A.10), Equation (A.7) can be rewritten as:

$$\mathrm{NDIV} = 1 + \frac{\log x_{\mathrm{end}} - \log x_1}{\log\left(L - x_1\right) - \log\left(L - x_{\mathrm{end}}\right)} \tag{A.11}$$

This equation can be used to calculate the number of element divisions, NDIV, when the desired element lengths, $x_1$ and $x_{\mathrm{end}}$, in each end of a graded mesh along a line with length $L$ is known. NDIV obviously has to be rounded to an integer.

# Appendix B: Experimental fatigue crack propagation histories

This appendix contains the crack propagation histories obtained from the fatigue tests presented in Paper VI, as well as specifications of the applied loading. A pre-cracking frequency of 10 Hz was used for all specimens. All recorded crack lengths are included, even though a larger crack size measurement interval was used in the analysis presented in Paper VI.

## *Specimen I-A*

Pre-cracking load: Increased from 2–20 kN to 2.5–25 kN to 3–30 kN
Pre-crack length, $2a_0$: 25.7 mm
Number of cycles taken to reach pre-crack length: Not recorded
Overload, tension: None
Overload, torsion: None
Test load, tension: 3–30 kN
Test load, torsion: None
Test load frequency: 10 Hz

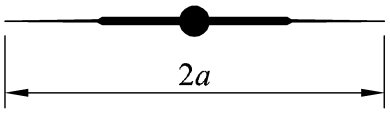


| $N$ | $2a$ [mm] | | $N$ | $2a$ [mm] |
|---|---|---|---|---|
| 0 | 25.7 | | 96 200 | 42.7 |
| 31 200 | 27.8 | | 101 200 | 45.3 |
| 68 590 | 31.8 | | 106 200 | 46.3 |
| 73 580 | 36.2 | | 111 200 | 47.2 |
| 78 200 | 36.9 | | 116 200 | 49.8 |
| 81 200 | 37.8 | | 121 200 | 50.6 |
| 84 200 | 38.5 | | 126 200 | 52.4 |
| 87 200 | 38.6 | | 131 384 | 58.1 |
| 91 200 | 39.7 | | 136 199 | 61.3 |
| | | | 141 464 | 72.0 |

## Specimen I-B

Pre-cracking load: 2.8–28 kN
Pre-crack length, $2a_0$: 18.3 mm
Number of cycles taken to reach pre-crack length: 645 484
Overload, tension: None
Overload, torsion: None
Test load, tension: 2.8–28 kN
Test load, torsion: None
Test load frequency: 10 Hz

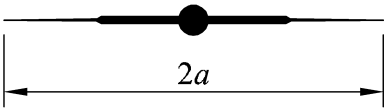


| $N$ | $2a$ [mm] | | $N$ | $2a$ [mm] |
|---|---|---|---|---|
| 0 | 18.3 | | 404 253 | 22.7 |
| 12 600 | 18.8 | | 410 253 | 22.8 |
| 21 600 | 18.9 | | 487 724 | 23.8 |
| 33 600 | 19.2 | | 525 524 | 25.1 |
| 156 028 | 20.2 | | 637 046 | 26.8 |
| 340 053 | 21.4 | | 649 046 | 27.2 |
| 344 253 | 21.5 | | 661 046 | 27.5 |
| 356 253 | 21.6 | | 667 046 | 27.7 |
| 368 253 | 21.7 | | 679 046 | 28.1 |
| 374 253 | 22.1 | | 685 046 | 28.3 |
| 380 253 | 22.4 | | 691 046 | 28.5 |
| 398 253 | 22.6 | | 703 046 | 28.8 |
| | | | 745 064 | 29.9 |

## *Specimen I-C*

Pre-cracking load: 2.8–28 kN
Pre-crack length, $2a_0$: 17.9 mm
Number of cycles taken to reach pre-crack length: 246 975
Overload, tension: None
Overload, torsion: None
Test load, tension: 2.8–28 kN
Test load, torsion: None
Test load frequency: 10 Hz

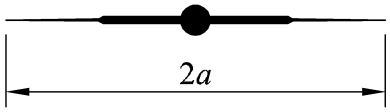


| *N* | 2*a* [mm] | *N* | 2*a* [mm] | *N* | 2*a* [mm] |
|---|---|---|---|---|---|
| 0 | 17.9 | 222 875 | 28.7 | 291 875 | 39.5 |
| 118 475 | 21.6 | 228 875 | 28.9 | 294 275 | 40.4 |
| 120 875 | 21.9 | 234 875 | 29.8 | 294 875 | 40.6 |
| 126 875 | 22.2 | 240 875 | 30.1 | 295 475 | 40.9 |
| 132 875 | 22.5 | 246 875 | 31.2 | 296 075 | 41.0 |
| 138 875 | 23.0 | 252 875 | 32.2 | 296 675 | 41.5 |
| 144 875 | 23.2 | 258 875 | 32.9 | 297 275 | 41.7 |
| 150 875 | 23.9 | 264 875 | 34.0 | 297 875 | 41.8 |
| 156 875 | 24.3 | 270 875 | 35.5 | 298 475 | 41.9 |
| 162 875 | 24.7 | 273 275 | 35.6 | 299 675 | 42.1 |
| 168 875 | 25.1 | 276 875 | 36.8 | 300 275 | 42.3 |
| 174 875 | 25.4 | 277 475 | 37.8 | 300 875 | 42.4 |
| 180 875 | 25.5 | 279 275 | 37.9 | 301 475 | 42.7 |
| 192 875 | 26.4 | 284 075 | 38.0 | 302 675 | 42.8 |
| 198 875 | 27.1 | 286 475 | 38.5 | 303 275 | 43.3 |
| 204 875 | 27.3 | 288 275 | 39.0 | 303 875 | 43.7 |
| 210 875 | 27.6 | 288 875 | 39.1 | 304 475 | 44.0 |
| 216 875 | 28.3 | 290 075 | 39.3 | 305 075 | 44.3 |
| | | | | 306 535 | 44.9 |

## Specimen I+II-A

Pre-cracking load: 2.8–28 kN
Pre-crack length, left side, $x_{0,left}$: 8.6 mm
Pre-crack length, right side, $x_{0,right}$: 8.7 mm
Number of cycles taken to reach pre-crack length: 260 000
Overload, tension: None
Overload, torsion: None
Test load, tension: 2.3–23 kN
Test load, torsion: 25–250 Nm
Test load frequency: 2 Hz
Measured kink angle, $\phi$: 31 ± 2 °

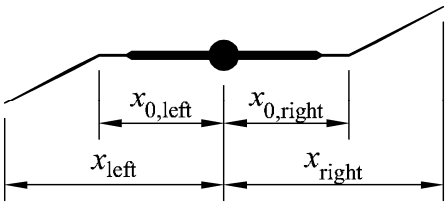


| $N$ | $x_{left}$ [mm] | $x_{right}$ [mm] |
|---|---|---|
| 0 | 8.6 | 8.7 |
| 199 061 | 10.5 | 10.4 |
| 241 037 | 11.0 | 11.2 |
| 271 458 | 11.4 | - |
| 287 754 | 11.8 | 11.9 |
| 304 494 | 12.1 | 12.2 |
| 347 354 | 13.1 | 13.4 |
| 383 566 | 14.0 | 14.4 |

## Specimen I+II-B

Pre-cracking load: 2.8–28 kN
Pre-crack length, left side, $x_{0,\text{left}}$: 8.2 mm
Pre-crack length, right side, $x_{0,\text{right}}$: 7.8 mm
Number of cycles taken to reach pre-crack length: 300 000
Overload, tension: None
Overload, torsion: None
Test load, tension: 2.5–25 kN
Test load, torsion: 26–260 Nm
Test load frequency: 4 Hz
Measured kink angle, $\phi$: 29 ± 2 °

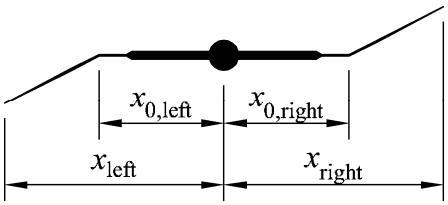


| $N$ | $x_{\text{left}}$ [mm] | $x_{\text{right}}$ [mm] |
|---|---|---|
| 0 | 8.2 | 7.8 |
| 133 813 | 8.7 | 8.2 |
| 168 712 | - | 8.3 |
| 216 952 | 9.1 | - |
| 253 086 | 9.4 | 8.9 |
| 315 540 | 9.8 | 9.5 |
| 360 660 | 10.1 | - |
| 403 302 | 10.5 | 9.9 |
| 435 702 | 11.2 | - |
| 477 743 | 11.6 | 10.3 |
| 517 689 | 12.3 | - |
| 547 580 | 12.4 | 10.6 |
| 595 100 | 12.6 | 10.8 |
| 636 435 | 14.0 | 12.0 |
| 698 872 | 14.9 | 13.0 |

## Specimen I+II-C

Pre-cracking load: 2.8–28 kN
Pre-crack length, left side, $x_{0,left}$: 8.8 mm
Pre-crack length, right side, $x_{0,right}$: 8.2 mm
Number of cycles taken to reach pre-crack length: 397 559
Overload, tension: None
Overload, torsion: None
Test load, tension: 2.5–25 kN
Test load, torsion: 26–260 Nm
Test load frequency: 5 Hz
Measured kink angle, $\phi$: 24 ± 2 °

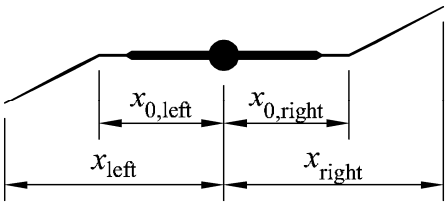


| $N$ | $x_{left}$ [mm] | $x_{right}$ [mm] | | $N$ | $x_{left}$ [mm] | $x_{right}$ [mm] |
|---|---|---|---|---|---|---|
| 0 | 8.8 | 8.2 | | 642 574 | 12.2 | 10.0 |
| 83 699 | 9.1 | 8.4 | | 688 174 | 12.6 | - |
| 131 699 | 9.3 | 8.5 | | 747 234 | 13.1 | 10.3 |
| 193 255 | 9.6 | - | | 789 684 | 13.4 | 10.8 |
| 245 455 | 10.0 | - | | 824 184 | 13.6 | 11.1 |
| 314 995 | - | 9.0 | | 859 520 | 13.9 | 11.4 |
| 370 495 | 10.3 | - | | 902 270 | 15.0 | 11.7 |
| 440 232 | 10.6 | 9.4 | | 938 273 | 15.4 | 12.0 |
| 483 582 | 11.4 | 9.6 | | 958 673 | 15.5 | 12.3 |
| 540 592 | 11.6 | 9.7 | | 978 323 | 16.1 | 12.4 |
| 594 442 | 11.8 | 9.8 | | 998 374 | 17.0 | 12.6 |

## Specimen I+II+1.25OL-A

Pre-cracking load: 2.8–28 kN
Pre-crack length, left side, $x_{0,left}$: 9.5 mm
Pre-crack length, right side, $x_{0,right}$: 9.8 mm
Number of cycles taken to reach pre-crack length: 227 526
Overload, tension: 31.25 kN
Overload, torsion: 325 Nm
Test load, tension: 2.5–25 kN
Test load, torsion: 26–260 Nm
Test load frequency: 5 Hz
Measured kink angle, $\phi$: 25 ± 2 °

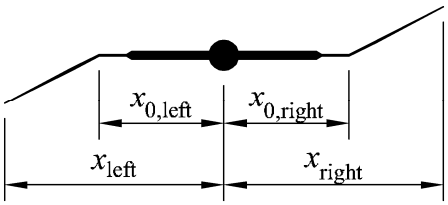


| $N$ | $x_{left}$ [mm] | $x_{right}$ [mm] |
|---|---|---|
| 0 | 9.5 | 9.8 |
| 41 700 | 10.1 | 10.1 |
| 96 968 | 10.6 | 10.8 |
| 139 118 | 11.0 | 11.5 |
| 178 646 | 11.4 | 12.1 |
| 212 546 | 12.5 | 13.2 |
| 239 546 | 13.5 | 13.8 |
| 259 228 | 14.1 | 14.2 |
| 268 824 | 14.4 | 14.8 |
| 280 424 | 14.9 | 15.3 |
| 294 674 | 15.6 | 15.6 |
| 317 209 | 16.9 | 16.8 |

## Specimen I+II+1.25OL-B

Pre-cracking load: 2.8–28 kN
Pre-crack length, left side, $x_{0,\mathrm{left}}$: 9.0 mm
Pre-crack length, right side, $x_{0,\mathrm{right}}$: 8.7 mm
Number of cycles taken to reach pre-crack length: 400 948
Overload, tension: 31.25 kN
Overload, torsion: 325 Nm
Test load, tension: 2.5–25 kN
Test load, torsion: 26–260 Nm
Test load frequency: 5 Hz
Measured kink angle, $\phi$: 28 ± 2 °

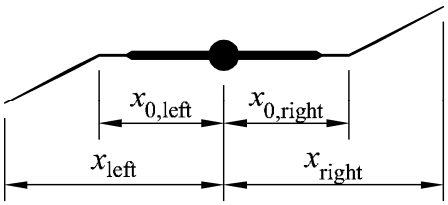


| $N$ | $x_{\mathrm{left}}$ [mm] | $x_{\mathrm{right}}$ [mm] |
|---|---|---|
| 0 | 9.0 | 8.7 |
| 94 904 | 9.3 | 8.9 |
| 170 480 | 9.5 | 9.1 |
| 230 780 | 9.7 | 9.3 |
| 294 276 | 10.1 | 9.6 |
| 336 726 | 10.4 | 10.0 |
| 386 455 | 11.0 | 10.4 |
| 439 466 | 11.2 | 10.7 |
| 496 064 | 12.3 | 11.2 |
| 534 914 | 12.5 | 11.7 |
| 577 993 | 13.3 | 12.5 |
| 622 843 | 14.6 | 13.1 |
| 636 643 | 14.8 | 13.4 |
| 655 393 | 15.3 | 13.8 |
| 674 376 | 15.7 | 14.5 |

## Specimen I+II+1.25OL-C

Pre-cracking load: 2.8–28 kN
Pre-crack length, left side, $x_{0,left}$: 8.8 mm
Pre-crack length, right side, $x_{0,right}$: 8.4 mm
Number of cycles taken to reach pre-crack length: 383 788
Overload, tension: 31.25 kN
Overload, torsion: 325 Nm
Test load, tension: 2.5–25 kN
Test load, torsion: 26–260 Nm
Test load frequency: 5 Hz
Measured kink angle, $\phi$: 26 ± 2 °

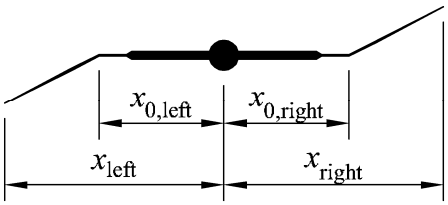


| $N$ | $x_{left}$ [mm] | $x_{right}$ [mm] |
|---|---|---|
| 0 | 8.8 | 8.4 |
| 257 545 | 9.6 | 9.0 |
| 297 745 | 9.9 | 9.4 |
| 345 711 | 10.1 | 9.7 |
| 394 161 | 10.5 | 10.1 |
| 433 611 | 10.9 | 10.5 |
| 464 218 | 11.7 | 10.9 |
| 511 318 | 12.4 | 11.7 |
| 550 618 | 12.8 | 12.1 |
| 567 553 | 12.9 | 12.7 |
| 591 853 | - | 12.9 |
| 617 503 | 14.4 | 13.7 |
| 645 103 | 15.5 | 14.5 |

## Specimen I+II+1.50OL-A

Pre-cracking load: 2.8–28 kN
Pre-crack length, left side, $x_{0,\mathrm{left}}$: 9.2 mm
Pre-crack length, right side, $x_{0,\mathrm{right}}$: 9.4 mm
Number of cycles taken to reach pre-crack length: 177 478
Overload, tension: 37.5 kN
Overload, torsion: 390 Nm
Test load, tension: 2.5–25 kN
Test load, torsion: 26–260 Nm
Test load frequency: 5 Hz
Measured kink angle, $\phi$: 27 ± 2 °

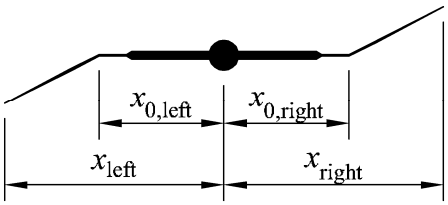


| $N$ | $x_{\mathrm{left}}$ [mm] | $x_{\mathrm{right}}$ [mm] |
|---|---|---|
| 0 | 9.2 | 9.4 |
| 34 655 | 9.3 | 9.5 |
| 81 305 | 9.7 | 9.9 |
| 158 694 | 10.8 | 11.0 |
| 205 794 | 11.4 | 11.7 |
| 228 294 | 12.0 | 12.2 |
| 264 244 | 13.3 | 13.2 |
| 306 713 | 14.8 | 15.2 |

## Specimen I+II+1.50OL-B

Pre-cracking load: 2.8–28 kN
Pre-crack length, left side, $x_{0,left}$: 8.4 mm
Pre-crack length, right side, $x_{0,right}$: 8.1 mm
Number of cycles taken to reach pre-crack length: 302 542
Overload, tension: 37.5 kN
Overload, torsion: 390 Nm
Test load, tension: 2.5–25 kN
Test load, torsion: 26–260 Nm
Test load frequency: 4 Hz
Measured kink angle, $\phi$: 27 ± 2 °

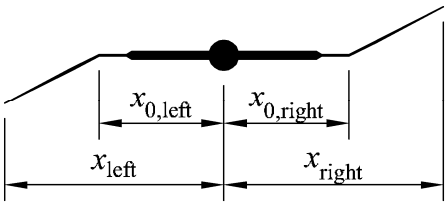


| $N$ | $x_{left}$ [mm] | $x_{right}$ [mm] | $N$ | $x_{left}$ [mm] | $x_{right}$ [mm] |
|---|---|---|---|---|---|
| 0 | 8.4 | 8.1 | 621 569 | 10.2 | 9.7 |
| 22 463 | 8.5 | 8.3 | 680 142 | 10.7 | 10.3 |
| 113 570 | 8.7 | 8.6 | 727 422 | 10.9 | 10.5 |
| 200 659 | 8.8 | - | 779 616 | 11.7 | 10.8 |
| 270 315 | 9.0 | 8.8 | 823 296 | 12.5 | 11.2 |
| 394 324 | 9.4 | 8.9 | 877 825 | 13.4 | 11.9 |
| 440 362 | 9.6 | 9.2 | 930 745 | 14.1 | 13.3 |
| 479 122 | 9.6 | 9.3 | 977 238 | 15.4 | - |
| 531 040 | 9.7 | 9.4 | 1 000 967 | 16.1 | 15.0 |

## Specimen I+II+1.50OL-C

Pre-cracking load: 2.8–28 kN
Pre-crack length, left side, $x_{0,left}$: 8.7 mm
Pre-crack length, right side, $x_{0,right}$: 8.6 mm
Number of cycles taken to reach pre-crack length: 213 914
Overload, tension: 37.5 kN
Overload, torsion: 390 Nm
Test load, tension: 2.5–25 kN
Test load, torsion: 26–260 Nm
Test load frequency: 5 Hz
Measured kink angle, $\phi$: 25 ± 2 °

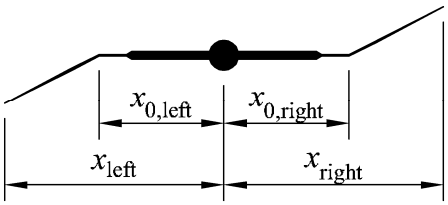


| $N$ | $x_{left}$ [mm] | $x_{right}$ [mm] |
|---|---|---|
| 0 | 8.7 | 8.6 |
| 51 900 | 8.8 | 8.7 |
| 119 028 | 8.9 | 9.0 |
| 164 628 | - | 9.2 |
| 241 616 | 9.2 | 9.4 |
| 371 963 | 10.2 | 10.2 |
| 398 063 | 10.4 | 10.4 |
| 451 379 | 11.2 | 11.2 |
| 508 786 | 12.0 | - |
| 533 504 | 12.6 | 12.5 |
| 568 570 | 13.5 | - |
| 587 770 | 14.5 | 14.1 |